Mass transfer characteristics of trickle bed reactors and their impact on reactor performance of heterogeneous hydrogenations

Jonathan Paul White

Submitted in accordance with the requirements for the degree of
Doctor of Philosophy

The University of Leeds
School of Chemical and Process Engineering

June 2022

The candidate confirms that the work submitted is his/her own and that appropriate credit has been given where reference has been made to the work of others.

The work in Chapters 4 and 5 of the thesis has appeared in the following publication;

Decoupling the relative rate of hydrogen uptake via convection and mass transfer by a single catalytic pellet in a scaled down trickle bed reactor, Jonathan P. White, Thomas W. Chamberlain, Richard A. Bourne, David Taylor, Colin Brennan and Frans L. Muller, Chemical Engineering Journal, volume 394, August 2020,124290.

I can confirm I was responsible for all the work related to the publication, with the other authors comprising of my academic and industrial supervisory team whose role in the publication was advisory.

Acknowledgements

I would first like to acknowledge my supervisor Professor Frans Muller for his exceptional guidance and mentoring over the course of the last four years. I will look back fondly on the many hours spent discussing engineering topics and deciphering pages of notes after a meeting. I would also like to thank Dr Thomas Chamberlain and Dr Richard Bourne for their continued support throughout the project and my time at Leeds. I would also like to acknowledge my industrial supervisors Colin Brennan and David Taylor for their support and making my placement with Syngenta such an enjoyable experience.

Next I would like to thank the Centre of Doctor training in Complex Particulate Products and Processes and EPSRC for providing me with the opportunity to undertake a PhD project and providing numerous opportunities to communicate my research through industrial engagements.

I would like to thank Ilias Stamatiou for the many productive discussions in relation to trickle bed reactors and mass transfer, Matthew Broadbent for making my engineering designs come to life and my iPRD colleagues for making long days in the laboratory more enjoyable.

Finally, I would like to thank my CDT cohort 3 colleagues for making whole experience great, in particular David Austin and Peter Kaskiewicz, who more than most had to bear one of my many rants over a Library “coffee”. My family for supporting all my endeavours and my partner Tara, who’s continued support and inspiration carried me through some of the darkest times of the project – I truly would not have finished without you.

Abstract

Mass transfer is a key process in trickle bed reactors that effects reactor performance, chemical selectivity and scale up of heterogenous hydrogenations. A lack of fundamental knowledge of how the convective and radial diffusive transfer processes contribute to the overall mass transfer rate has hindered uptake of trickle bed reactors for the manufacture of fine chemicals. The complex relationship between the phase hydrodynamics and the transfer processes makes this class of packed bed reactor challenging to study. To circumvent this issue, a methodology has been developed to scale down a trickle bed reactor to a single catalyst pellet to investigate the mass transfer characteristics.

By scaling down, the common hydrodynamic issues encountered at laboratory scale were removed and two mass transfer regimes were isolated by manipulating the extent to which hydrogen saturated the feed. Hydrogen saturated feeds were found to be convection dominating, with the hydrogen uptake rate almost linearly proportional to the molar flow of hydrogen in the liquid. Hydrogen free feeds were observed to be diffusion limited, with thicker liquid films resulting in increased diffusional resistance and hence reduced hydrogen uptake rates.

The convective and radial diffusive transfer processes were successfully decoupled using a two-stage model able to describe mass transfer over both catalytically active and inert surfaces in the scaled down reactor. It was demonstrated that the two processes can be manipulated by altering the process conditions to control the rate at which hydrogen accesses the catalyst surface. Moreover, the provision of an inert surface has been shown to increase reactor performance by enhancing convective transfer.

Two alternative single pellet reactor platforms were fabricated and experimentally evaluated to assess their ability to efficiently screen catalysts and investigate the mass transfer characteristics in gas-liquid-solid systems.

Knowledge of how to control the hydrogen supply could aid in the design, operation and scale up of trickle bed processes for chemical systems where selectivity is key to performance and improve the uptake of this technology in the fine chemical industry.

Table of Contents

List of Tables

List of Figures

Nomenclature

A_b	Surface area of a single glass bead (m^2)
A_{bs}	Total surface area of the film over the inert glass beads (m^2)
A_p	Surface area of the catalyst pellet (m^2)
A_{Pd}	Surface area of a palladium nanoparticle (m^2)
C_B	Boundary concentration of hydrogen (mol m^{-3})
$C_{ethylbenzene}$	Concentration of ethylbenzene (mol m^{-3})
C_f	Average hydrogen concentration of the liquid film flowing over the pellet (mol m^{-3})
$\overline{C_f}$	Characteristic hydrogen concentration of the liquid film flowing over the pellet (mol m^{-3})
C_{in}	Hydrogen concentration in the liquid feed (mol m^{-3})
C_{H_2}	Concentration of hydrogen (mol m^{-3})
C_L	Hydrogen concentration in the liquid phase (mol m^{-3})
C_s	Hydrogen concentration at the surface of the catalyst (mol m^{-3})
C_0	Hydrogen concentration in the liquid at the point where the liquid reaches the pellet in the bed (mol m^{-3})
C^*	Equilibrium concentration of hydrogen in the liquid at the conditions investigated (mol m^{-3})
d_{bs}	Diameter of a single glass bead (m)
d_{Pd}	Palladium nanoparticle diameter (m)
d_{50}	The dimension that 50% of the samples' dimensions are both smaller and larger than
D_{eff}	Effective diffusion rate of hydrogen in palladium on carbon catalysts (m^2 s^{-1})
$\mathbb{D}_{H_2}$	Diffusion coefficient of hydrogen in liquid (m^2 s^{-1})
g	Gravitational acceleration (m s^{-2})
h	Height a plate (falling film derviation) (m)
H	Henry's constant (Pa m^3 mol^{-1})
k_b	Liquid film mass transfer coefficient over the bead section (m s^{-1})
$k_{b.ref}$	Mass transfer coefficient over the beads at the reference flowrate (m s^{-1})
k''_{obs}	Observed rate constant per unit area of pellet (m s^{-1})
k_{obs}^{Vshell}	Observed rate constant within the enriched palladium shell (s^{-1})
l_p	Catalyst pellets' length (m)

l_{unit}	Length of palladium unit cell (nm)
L_{edge}	Length of the nanoparticles' edge (m)
L_{np}	Length of the nanoparticle (m)
L_p	Length of catalyst pellet (m)
MTR''_{B-R},	mass transfer flux from the boundary layer to the palladium surface with subsequent chemical reaction (mol m^{-2} s^{-1})
MTR''_{g-f}	Mass transfer flux from the gas-liquid interface to the liquid film (mol m^{-2} s^{-1})
MTR''_{f-s}	Mass transfer flux from the liquid film to the catalyst surface (mol m^{-2} s^{-1})
MTR''_{f-R}	Mass transfer flux from the liquid film to the catalyst surface and subsequent chemical reaction (mol m^{-2} s^{-1})
MTR''_{H_2}	Overall mass transfer rate of hydrogen (mol m^{-2} s^{-1})
MTR''_{conv}	Convective transport of hydrogen flowing onto the pellet (mol m^{-2} s^{-1})
MTR''_{radial}	Radial transport of hydrogen from the gas phase through the liquid film to the surface of the catalyst (mol m^{-2} s^{-1})
N_{atoms}	Number of palladium atoms per nm^2
N_{bulk}	Total number of palladium atoms in the nanoparticle
N_{bs}	Number of glass beads in the bed prior to the pellet
$\dot{N}_{H_2}$	Number of moles of hydrogen consumed per second at the surface of the catalyst (mol s^{-1})
N_s	Number of palladium surface atoms per nanoparticle
P_{H_2}	Partial pressure of hydrogen (MPa)
$Pd_{\%s}$	Fraction of palladium in the enriched layer
U_{bs}	Liquid velocity over the glass beads (m s^{-1})
r_{core}	Radius of the catalyst up to the enriched palladium shell (m)
r_p	Radius of the catalyst pellet (m)
r_{shell}	Radius equal to the radius of the pellet (m)
R_f	Response factor (au)
$R_{H_2}^{Pd}$	Rate of hydrogen consumption in terms of the catalyst weight (m^3 g^{-1} s^{-1})
S	Cross-sectional area of the reactor (m^2)
$t_{residence\ pellet}$	Residence time of the liquid over the pellet (s)
T	Temperature (K)
V_{core}	Volume of a catalyst pellet not including the enriched shell (m^3)
V_F	Volume of free space when packed (void volume)

V_p	Volume of the pellet (m^3)
V_{p-w}	Volume of liquid between the pellet and reactor wall (m^3)
V_R	Volume of empty reactor
V_{shell}	Volume of a catalyst pellet enriched in palladium (m^3)
V_z	Liquid velocity in the direction of gravitational force, z (m s^{-1})
W	Width of a plate (falling film derivation) (m)
W_p	Quantity of palladium in the pellet (g)
z_B	Packed bed length (m)
$\#_{Pd_{Core}}$	Number of palladium Lα counts per μm^3 in the interior of the pellet
$\#_{Pd_{Shell}}$	Number of palladium Lα counts per μm^3 in the enriched shell of the pellet

Greek letters

α	Fraction of the liquid film that forms the gas to liquid film transport resistance
β	Fraction of the liquid film in which the concentration boundary layer forms
β_{dyn}	Dynamic liquid holdup (m^3 liquid · m^{-3} voids)
β_{st}	Static liquid holdup (m^3 liquid · m^{-3} voids)
γ_1	Gradient of the effect of flowrate on mass transfer to beads
γ_2	Ratio of liquid film thickness over a pellet in a bed vs liquid film thickness (δ) over a pellet stack
γ_3	Liquid bypass factor
δ	Liquid film thickness
δ_b	Liquid film thickness over the glass beads (m)
δ_s	Depth of palladium enriched shell into pellets' interior (µm)
ϵ_B	Bed porosity
μ	Dynamic viscosity (kg m^{-1} s^{-1})
π	Constant; ratio of a circle's circumference to its diameter
ρ	Density of liquid (kg m^{-3})
σ	Surface tension (N / m)
τ	Liquid residence time in the reactor (s)
φ	Volumetric liquid flow rate (m^3 s^{-1})
φ_{ref}	Reference liquid flow condition (m^3 s^{-1})

Ω	Mass transfer resistance
Ω_{B-R}	Resistance associated with both diffusion and chemical reaction
Ω_f	Gas to liquid film transport resistance (s m^{-1})
Ω_{f-s}	Liquid Film to catalyst surface transport resistance (s m^{-1})
Ω_{G-L}	Gas-liquid mass transport resistance (s)
Ω_{L-S}	Liquid-solid mass transport resistance (s)
Ω_R	Chemical reaction resistance (s m^{-1})

Dimensionless numbers

$Re = \frac{\delta \rho V_z}{\mu}$	Reynold's number for a falling film
$Re_{bs} = \frac{\rho U_{bs} N_{bs} d_{bs}}{\mu}$	Reynold's number of the liquid over the length of the glass beads
$Re_f = \frac{\delta V_z \rho}{\mu}$	Reynold's number for a falling film
M_T	Thiele modulus; ratio between the rate of reaction and diffusion in porous media
$Sc = \frac{\mu}{\rho \cdot \mathbb{D}_{H_2}}$	Schmidt number

Chapter 1
Introduction

Trickle bed reactors are an excellent example of a promising continuous technology for the heterogenous hydrogenation of fine chemicals. Driven by the increased pressure to reduce the costs of active ingredients, fine chemical industries have been forced to search for new methods to lower manufacturing costs. One of the ways other chemical industries have successfully overcome this challenge has been to move from traditional batch manufacture to continuous processing technologies, with the commodity chemicals industry being a prime example. Continuous processing is well documented to hold numerous advantages over batch manufacture, with enhanced efficiency, safety and throughput, all reducing the overall manufacturing cost of the active ingredient made. The transition from batch to continuous has not been seamless, with the uptake of continuous technologies impeded by a lack of fundamental understanding of how to assess their applicability for fine chemical manufacture and scalability issues. One such reaction class that has been identified as having the potential to significantly benefit from the shift to continuous processing is heterogenous hydrogenations. Several continuous reactor technologies have been investigated to demonstrate their applicability for heterogenous hydrogenations over the last two decades [1]. These include a range of reactor platforms from commercial packed bed technologies to more custom designed plate or chip microreactors. Both have been utilised to demonstrate the applicability of various substrates for continuous manufacture with double and triple carbon – carbon bonds to imine and amine hydrogenation to name a few.

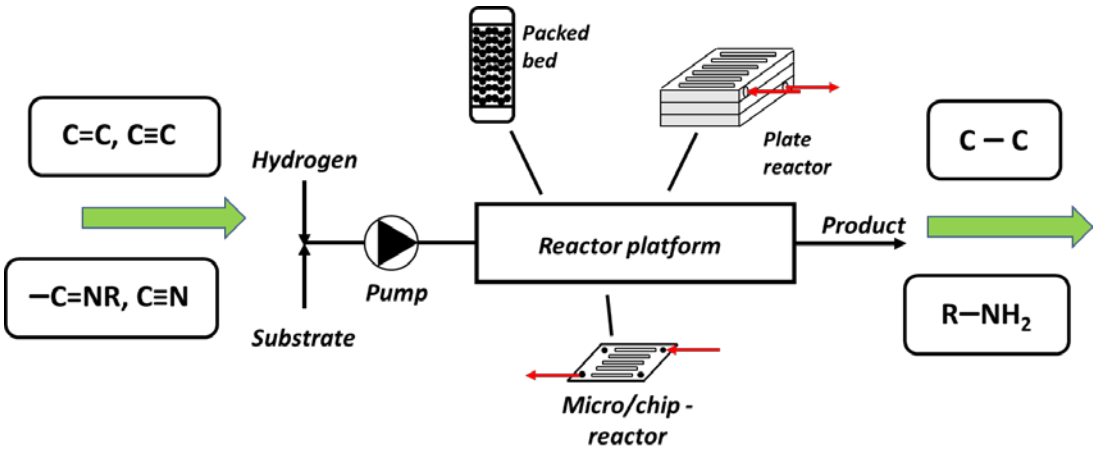

Figure 1.1: Example hydrogenation reactions and continuous reaction platforms

Trickle bed reactors are an excellent example of a promising type of packed bed technology for the heterogenous hydrogenation of fine chemicals, whereby the lack of fundamental knowledge of the mass transfer processes involved have made the empirical assessment of their applicability time and labour intensive. Being a multiphase reactor, understanding of the transfer processes that supply the catalyst with hydrogen is paramount in improving reactor performance and avoiding selectivity issues during development. Where chemical selectivity can be defined as the extent to which a desired chemical species is obtained, avoiding the generation of unwanted chemical species. These systems are not straightforward to study however, having a complex relationship between the mass transfer, kinetics and hydrodynamics making interpretation of experimental data, subsequent modelling and scale up challenging. The aims of this thesis are to design experimental methodologies to study and isolate the effects that the different hydrogen transfer processes have on the reactor performance. This is coupled with mathematical modelling of the three-phase system to understand how the transport processes can be manipulated to control the rate at which hydrogen is supplied to the catalyst.

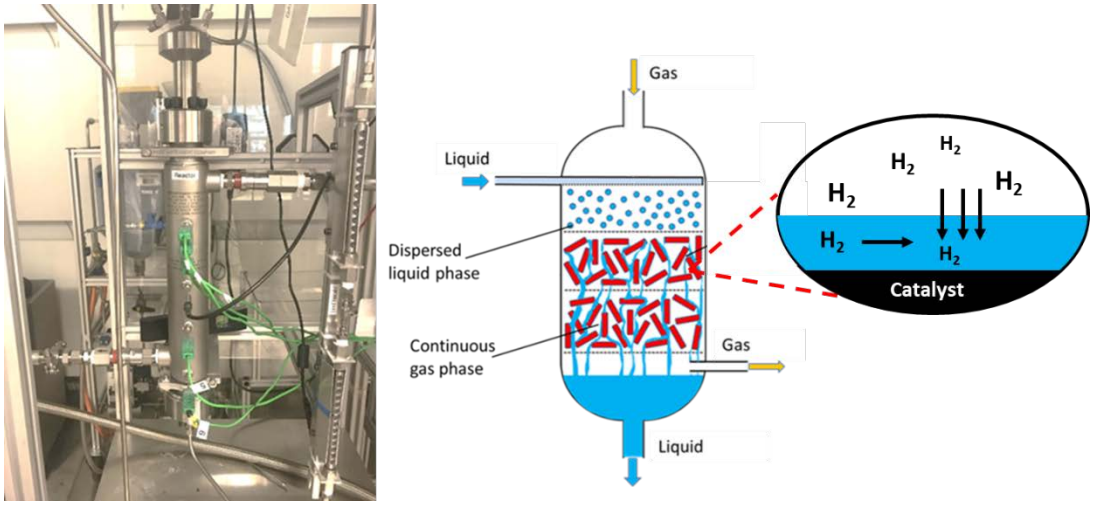

Figure 1.2: A trickle bed reactor and corresponding schematic showing hydrogen mass transfer through the liquid film to the catalyst

Harnessing this knowledge should improve catalyst utility and negate selectivity issues and lay the foundation to develop a methodology to theoretically assess trickle bed reactors applicability as a viable continuous processing technology. This in turn has the potential to significantly promote the uptake of the trickle bed reactor as a potential technology for the manufacture of fine chemicals.

1.1 Batch to continuous

Though the manufacture of relatively simple organic chemicals using efficient continuous flow processes is commonly known, synthesis of fine chemicals using continuous processing on both the laboratory and industrial scale is rarer [2]. More complex molecules such as those used as agrochemicals, inks, drugs, intermediates, additives and other fine chemicals needed for specialised applications are predominantly manufactured in reactors operating in batch or semi-batch mode. However, this is beginning to change over the last decade, with both academic and industrial research centres publishing and patenting more continuous processing technologies for the manufacture of fine chemicals [3, 4]. Reviews of such publications have

highlighted a number of recurring advantages continuous flow technologies hold over more traditional batch manufacturing; reduced amounts of raw materials used (catalyst, solvents, additives), reduced handling of hazardous materials, safer operating conditions, improved yields, lower impurity formation and finally ease of scaling up [2]. It should be mentioned that even though continuous processing offers many benefits, there is still some debate when and where to utilise the technology and there are a number of publications that discuss this decision in-depth [5-8].

It is often the case that though initially only small amounts (milligrams) of a new molecule may be required for testing, the demand can quickly grow to kilograms / tonnes as the development chain progresses. For batch-wise processing this can be problematic as scaling up has numerous challenges including temperature and dilution issues. Manufacturing via continuous flow from early stages in molecule discovery can negate these issues [9]. However, this shift does not come without its own challenges, as the trade-offs between flow rates and transfer regimes can limit the control over the reaction speed and selectivity.

1.2 Continuous hydrogenation & trickle bed reactors

Being one of the largest reaction classes, hydrogenations are estimated to make up nearly 20% of all fine chemical synthesis steps or reactions [10]. In addition to the extent at which hydrogenations feature, they have been identified as a potential process to move to continuous processing in trickle bed reactors for the following reasons [11]:

- Quality of the product; with smaller amounts of liquid in the reactor, hydrogen mass transfer may be more easily controlled. This can reduce impurities and by-products due to hydrogen starvation.
- Improved safety of the process; the use of smaller diameter tanks/pipes offers increased mechanical integrity at higher pressures and continuous processing reduces manual handling of often dangerous catalysts.
- Increased catalyst utility; by reducing the cycle time characteristic to batch operation (charging, activation and filtering), catalyst utility has the potential to be increased from 10 - 20 kg product / kg catalyst to 1000 kg product / kg catalyst.

Being a promising reaction class for continuous processing, there are several different multi-phase reactor technologies that could be used from packed and fluidised beds to continuous stirred tank reactors. Trickle bed reactors are a class of packed bed reactor named after the characteristic liquid flow through the stationary bed of catalyst particles and have been heavily used in the petrochemical industry for hydrocracking and hydrotreating. Trickle bed reactors are usually operated such that the gas phase is the continuous phase and thus, significantly from other types of packed bed reactor such as bubble columns where the catalyst in completely submerged in a continuous liquid phase. The various reactor platforms will be further detailed, and the advantages/disadvantages compared in the subsequent chapters of the thesis. Being simple in design and operating under extreme conditions (high pressure/temperature), trickle beds have many advantages that benefit

selectivity and conversion that make their use for the hydrogenation of fine chemicals industrially viable [12] [13];

- Plug flow behaviour (low back mixing)
- Ability to recycle product streams easily multiple times
- High throughput

Being multiphase reactors, their performance is heavily dependent on the hydrodynamic behaviour, fluid mixing, reaction kinetics, mass and heat transfer [14]. There also exists a complex relationship between the hydrodynamics and transfer phenomena in the reactor that makes the study of these types of reactors challenging. Mass transfer has a significant impact on reactor performance, with the rate of transfer of reactants being dependent on the processing parameters, bed characteristics and phase hydrodynamics. Moreover, it is widely acknowledged that the mass transfer characteristics can strongly influence the selectivity of heterogenous hydrogenations as the rate at which hydrogen is supplied to the catalyst surface will determine the hydrogen concentration at the catalyst surface [15-17]. Selectivity is not always simply enhanced by an increase in hydrogen concentration, in some cases catalyst starvation of hydrogen through mass transfer limitations can enhance selectivity [15]. It is vitally important to understand the effect mass transfer limitations have on the hydrogen concentration gradient (from the gas phase to the catalyst surface), as uncharacterised deviations between the liquid saturation concentration and the catalyst surface concentration can result in selectivity issues. Convectional process design, performance optimisation and scale up has relied on empirical methods, often conducted at laboratory scale, that are not often valid on different reactor scales due to

changes in the hydrodynamics and thus mass transfer behaviour. As can be seen in Figure 1.3, smaller scale reactors are unable to redistribute liquid efficiently and suffer from wall effects, often resulting in laboratory trickle bed reactors being unrepresentative of their commercial scale counterparts. For successful scale up, key design parameters need to be identified and their effects on reactor performance estimated across scales. The hydrodynamic and mass transfer phenomena do not scale linearly with geometry and thus, scale up is time intensive and challenging. This lack of fundamental understanding and scaling issues has hindered the uptake of trickle bed reactors as a continuous processing technology for the manufacture of fine chemicals. Therefore, knowledge of the transport processes by which the catalyst is supplied with hydrogen and the ability to manipulate the rate of transfer would make trickle bed reactors a more viable processing technology in future applications.

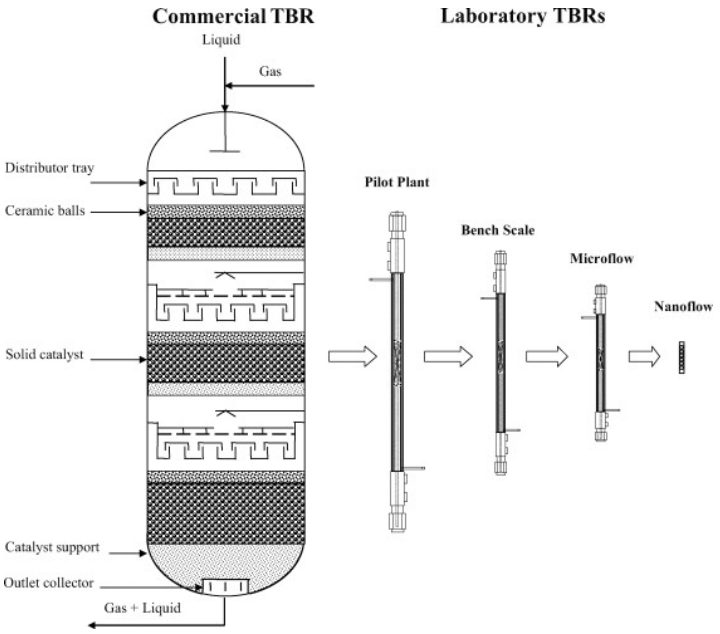

Figure 1.3: Schematic showing scales of trickle bed reactors from commercial to nanoflow. Visually highlighting how quickly liquid distribution and wall effects become an issue (taken from the review by Mederos et al. [18]).

1.3 Trickle bed reactors: A historical perspective

Trickle bed reactors are one of the most widely encountered three phase reactors in the petroleum, petrochemical and bulk chemical industries, with their use being well documented in the literature dating back to the 1970's. Often operated at high temperatures and pressures, commercial trickle beds traditionally bring hydrogen and organic compounds together in the presence of a solid catalyst for various hydrotreatments of bulk chemicals; hydrocracking, hydro-refining and hydrodenitrogenation to name a few [19]. For some perspective, in 1991 Trambouze reported that the petrochemical industry alone had an annual hydrotreatment capacity of an estimated 1.6 billion metric tonnes using trickle beds [20]. By 2004 Robinson and Dolbear had estimated this processing capacity had risen to around 40 million barrels per day (ca. 2.1 billion metric tonnes per annum) for hydrotreatment specifically [21]. Other applications of trickle bed reactors have been demonstrated in the biochemical, waste treatment and electrochemical processing industries. As such between 1970 and the turn of the century there has been a plethora of research conducted on trickle bed reactor operation of which Al-Dahhan *et al*. provide an extensive overview, many of which will be referenced throughout this thesis [19]. Table 1.1 presents some examples of trickle bed reactor applications within the commodity chemical industries that are documented in the literature. Though the list is not exhaustive, it provides and overview of the industries these reactors have been utilised in and some historical perspective.

Table 1.1: Examples of trickle bed usage across various bulk chemical industries

Application/Reaction class	Catalyst information	Conditions	Date reported
Hydrogenation			
Methanol synthesis Pass *et al.* [22]	Cu-Zn-CrO	250°C 71 bar	1990
Hydrogenation of aniline Govindarao and Murthy [23]	Nickel on clay	110-140°C	1975
Glucose Hydrogenation Gallezot *et al.[24]*	Ru/C	100°C 80 bar	1998
Hydrotreatment			
Crude Oil Hydrotreatment Jarullah *et al*. [25]	1 Co-Mo/γ-Al_2O_3	335 °C 100 bar	2011
Hydrodenitrogenation of Quinoline Yang and Satterfield [26]	NiMo/Al_20_3	350-390°C 69 bar	1984
Hydrocracking of Bitumen-Derived Coker Yui and Sanford [27]	NiMo/Al_20_3	350-400°C 70-110 bar	1989
Oxidation			
Oxidation of acetic acid Levec and Smith [28]	3.175 mm iron oxide	252-286°C 67 bar	1976
Wet oxidation of phenol Singha *et al*. [29]	1.58 mm CuO/Al_2O_3	100-130°C 67 bar	2004
Waste processing			
Dichloromethane removal using bioreactor Hartmans and Tramper [30]	Strain DM21	15-30°C 0.47 bar	1991
Bioprocessing			
Ethanol fermentation Jamuna and Ramakrishna [31]	Saccharomyces cerevisiae	25°C	1992
Fisher – Tropsch reaction			
Iliuta and Larachi [32]	Co/MgO	233-250°C 7.9 bar	2018

1.4 Current state of the art in the fine chemical industry

The aim of this section is to the convey the current research interest in continuous hydrogenation of fine chemicals using literature examples and to

summarise the attempts to increase the understanding of mass transfer in trickle bed reactors specifically.

1.4.1 Continuous hydrogenation technologies

1.4.1.1 Continuously stirred tank reactors

In continuously stirred tank reactor (CSTR) processing, materials are continuously fed into a single stirred vessel or a series of vessels and the product/s are continuously collected at the end [33]. There have been numerous instances in the literature whereby CSTRs have been employed for the hydrogenation of various fine chemicals. Hydrogenation of 2,4-dinitrotoluene by Westerterp *et al.* (1991) was an early 'proof of concept' study using a single laboratory scale CSTR [34]. 2,4-dinitrotoluene can react along a series of parallel and subsequent, consecutive reactions which are strongly exothermic, and as expected lower flow rates (increased residence time) and higher pressures increased conversion, but how these factors affect the selectivity was not reported.

Alsten *et al. (2007)* used two CSTR reactors in series to hydrogenate a dinitro pharmaceutical intermediate to the desired diamine product, a smoking cessation drug [11]. The reduction of such aromatic nitro compounds via hydrogenation has been subject to great interest in the literature due to their industrial importance [35]. The two reactors were shown to be operating in different limiting regimes, as reactor one converted over 80% of the substrate (limited by hydrogen mass transfer) and reactor two converting the last 10-20% (dinitro concentration limited).

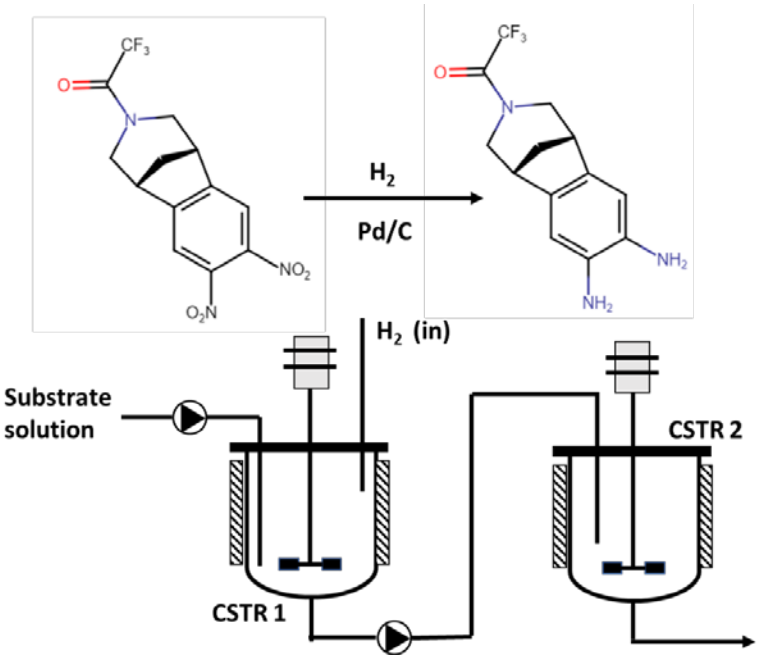

Figure 1.4: Hydrogenation of the dinitro pharmaceutical intermediate to the diamine product and the corresponding two CSTR set up by Alsten et al. (2007).

More recently, Sun *et al.* (2013) selectively hydrogenated benzene to cyclohexene using two CSTRs in series [36], where the partial hydrogenation and isolation of the intermediate rather than complete hydrogenation to cyclohexane is challenging. It was found that as benzene adsorption onto the catalyst was more favourable than cyclohexene, by increasing the flow rate selectivity towards the cyclohexene could be increased, at the expense of overall conversion. The study concluded that by having a CSTR system (rather than batch) the increased volume results in increased benzene feed rates and hence better selectivity.

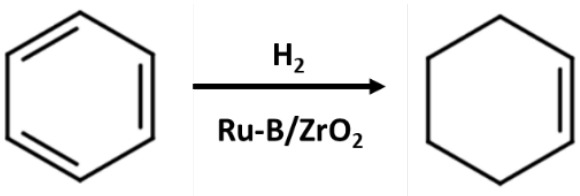

Figure 1.5: Reaction scheme for the partial hydrogenation of benzene to cyclohexene.

1.4.1.2 Packed bed reactors

Fishwick *et al.* (2007) undertook a comparative study to evaluate selective hydrogenation in a structured monolith reactor, a trickle bed and a stirred tank reactor [37]. The partial hydrogenation of 2-butyne-1,4-diol to the alkene intermediate used in the synthesis of vitamin A and B_6 in the pharmaceutical and agrochemical industry is particularly challenging given the many side reaction that can occur. All the reactors used in this study, however, exhibited relatively high selectivity (>85%) to the desired alkene by restricting the residence time to prevent further hydrogenation to the alkane. At 90% conversion, the concentration of side products in the stirred tank reactor was found to be much higher than in the continuous reactors and the authors attributed hydrogen mass transfer and catalyst dispersion as the primary factors that led to this result. Figure 1.6 shows the reaction scheme for the partial hydrogenation of 2-butyne-1, 4-diol in the various three phase reactor configurations investigated in the study.

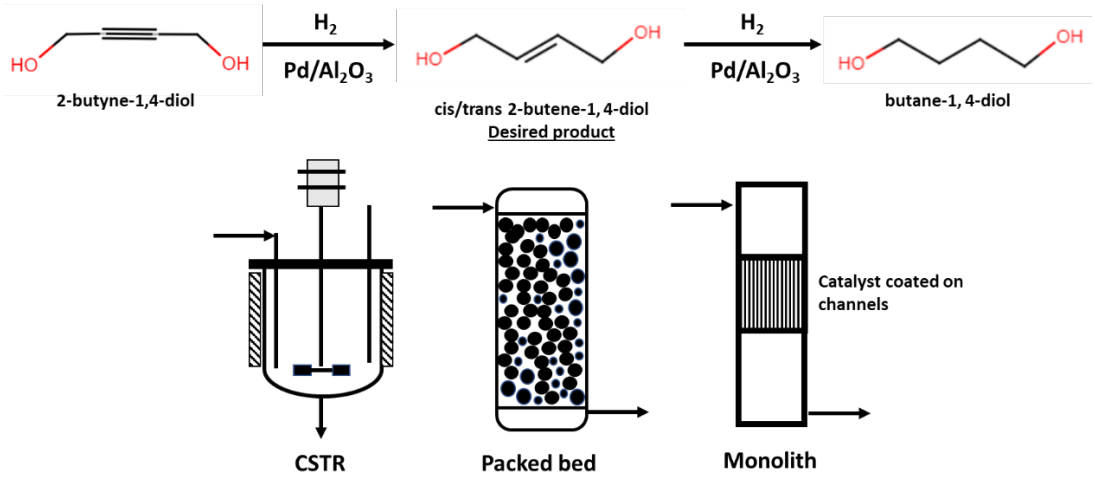

Figure 1.6: Selective hydrogenation of 2-butyne-1,4-diol to 2-butene-1,4-diol and the three types of reactors used by Fishwick et al. (2007).

Stüber and Demlas (2003) investigated the feasibility of operating a trickle bed reactor in counter-current mode to assess selectivity with a consecutive reaction [38]. In this case the partial hydrogenation of 1,5,9-cyclododecatriene (CDT) to cyclododecene (CDE). The influence of operating parameters (hydrogen pressure, cooling temperature, liquid and gas velocity) on the selectivity was studied, and though the parameters did indeed affect the reaction rate, the selectivity was marginally affected. To increase selectivity to the desired 90% whilst maintaining high conversion, the liquid flow rate was increased to minimise axial dispersion. This in turn resulted in the need for an increased reactor length or multiple reactors (in which the hydrogen surface concentration is lower to prevent further reaction). Similar work compared the partial hydrogenation of CDT in trickle beds operated in counter- and concurrent flow [39]. The reported work highlights that though selectivity to CDE is generally higher when operating in counter-current mode, this is only when considering two of the potential products that could be formed. When considering all the products that could be formed selectivity to CDE was higher in concurrent mode. Moreover, the global rate of hydrogenation was higher in concurrent operation.

Traditionally most continuous technologies are designed with steady-state operation in mind, however several researchers have stated the potential performance improvement (regarding both selectivity and conversion) of operating in unsteady-state operation by periodic modulation of gas/liquid flow rates [40]. Liu *et al.* (2005) exhibited this effect during the hydrogenation of 2-ethylanthraquinones (EAQs) in a periodically operated trickle bed reactor [41], with the hydrogenation of 2-ethylanthraquinones being one of the most important steps in hydrogen peroxide manufacture.

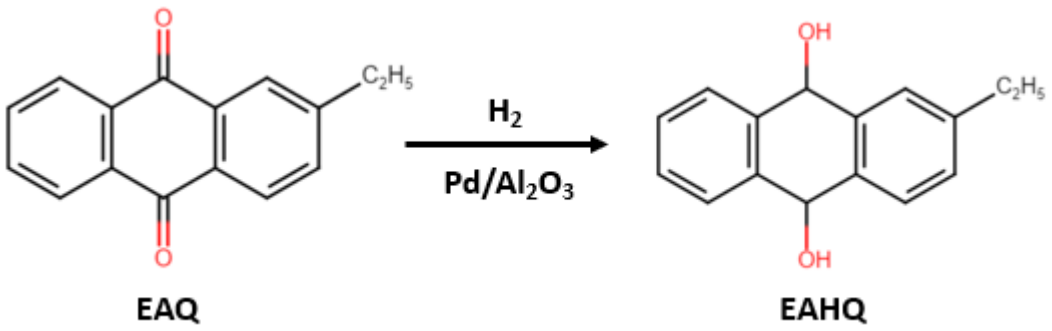

Figure 1.7: Reaction schematic for the hydrogenation of 2-ethylanthraquinone, a vital step in the manufacture of hydrogen peroxide.

Again, being another example of a consecutive reaction whereby only partial hydrogenation is desired, the selectivity and conversion were reported to be enhanced by up to 20% and 12% respectively. It is thought that by modulating the liquid flow, the rate of reaction increases due to higher hydrogen concentration on the surface of the catalyst and improved wettability when liquid flow is on. Conversely when liquid flow is stopped, gas-liquid and liquid-solid mass transfer is improved.

More recently, investigators at GlaxoSmithKline presented a methodology for transferring the hydrogenation of para-substituted nitrobenzenes from batch to continuous processing in a trickle bed reactor [42]. By pre-screening different catalyst particle sizes to assess the effect on selectivity and conversion, the authors successfully hydrogenated the case reaction systems continuously. The study itself focussed heavily on characterisation of the catalyst rather than the transport phenomena and it is suspected that due to the high operating pressure and short reactor length, mass transfer limitations were minimised.

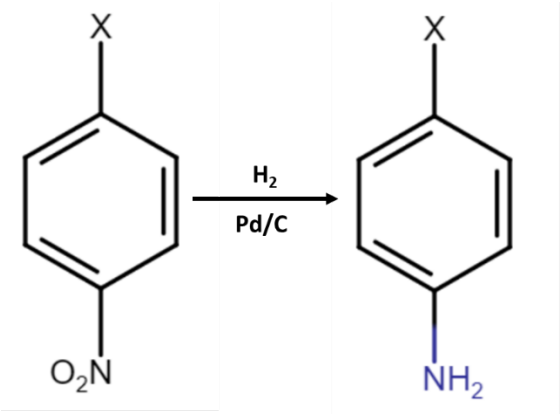

Functional groups (X)
Cl
MeO
CO_2Me
CN

Figure 1.8: Reaction schematic of the hydrogenation of various para-substituted nitrobenzene's investigated by the Chemical development team at GlaxoSmithKline.

1.4.2 Fundamental studies into mass transfer in trickle beds

Nearly all the literature examples discussed in section 1.4.1 were proof of concept studies, with limited focus on isolating and understanding the effect mass transfer has on the selectivity and conversion of the species of interest. Many studies have focused on experimental methods to determine the mass transfer coefficients and intrinsic reaction kinetics under different processing conditions [43]. Though many of these studies have aided in improving the reactor performance, the values are averaged over the catalyst bed and do not describe fully the transport processes by which hydrogen is supplied to the catalyst surface at the pellet scale. Many attempts to model trickle bed reactors have focused on developing reactor models that are able to describe both the hydrodynamic behaviour and transport processes. Authors have then utilised numerical methods and more recently 3D modelling techniques such as CFD to solve the series of underlying equations for these systems [44]. These approaches still rely on empirical correlations to estimate the mass transfer coefficients and other parameters in the model.

An alternative method of investigating mass transfer limitations in trickle bed reactors has been to scale down to a small number of catalyst pellets positioned to form a continuous line of catalyst for liquid to trickle over [45]. First developed by Satterfield *et* al.(1969), using this approach investigators were able to model the transfer of hydrogen by both diffusion normal to the axis of the catalyst support and convective transport of hydrogen present in the liquid for the first time. A schematic of the scaled down reactor that was used and picture detailing the transfer processes are shown in Figure 1.9. The amount of hydrogen supplied to the catalyst by each transport process was not quantified or compared. To the best of the authors knowledge, assessing the individual contribution convection and diffusion has on the overall mass transfer rate of hydrogen has been investigated by relatively few investigators.

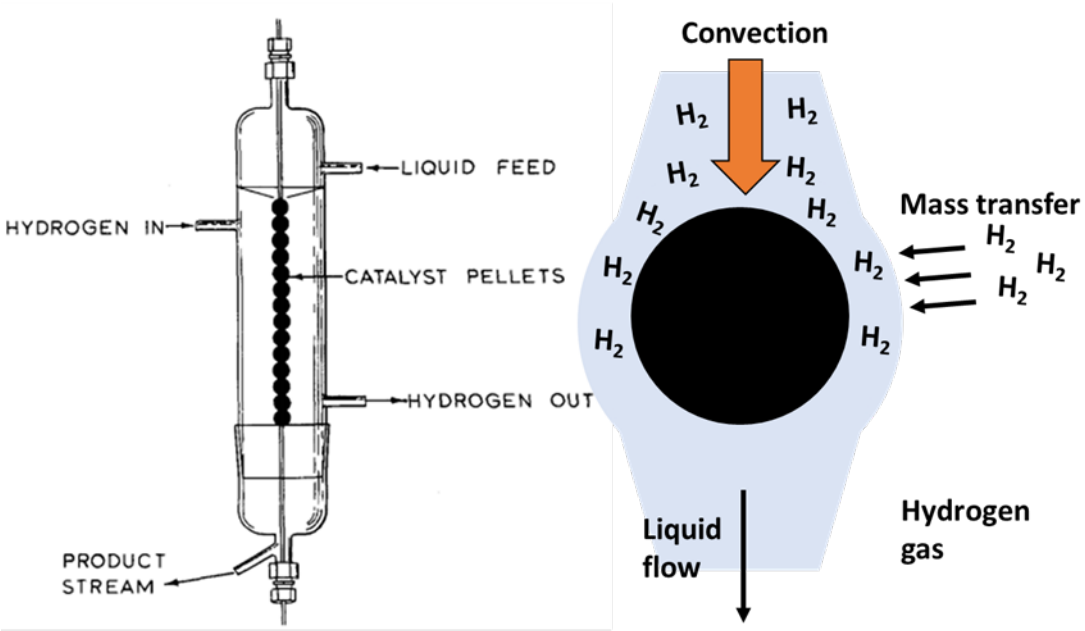

Figure 1.9: The scaled down trickle bed system used by Satterfield et al. (1969). The reactor consisted of a string of catalyst beads (left) and the schematic of the mass transfer processes supplying the catalyst with hydrogen are also shown (right).

Banchero *et al*. considered the initial effect of convective transfer as liquid enters the upper portion of the packed bed in a trickle bed reactor [46]. The authors determined that the effect of this region, where dissolved hydrogen is consumed by the catalyst, influenced the overall mass transfer rate, which became more significant as the bed length decreased. This scaling down methodology has been extended create a new class of reactor systems known as string reactors: single channels containing catalyst particles with sizes close to that of the channel dimensions to create ‘strings’ of successive pellets. The primary drawback of this approach is that the hydrodynamics are not representative when compared to the gas-liquid flow in a trickle bed reactor and thus, the mass transfer differs significantly too. Figure 1.10 shows the string pellet reactor configuration used by Hipolito *et al*. (2010) for catalyst testing and the characteristic slug flow regime observed by Bauer and Haase (2011) [47, 48].

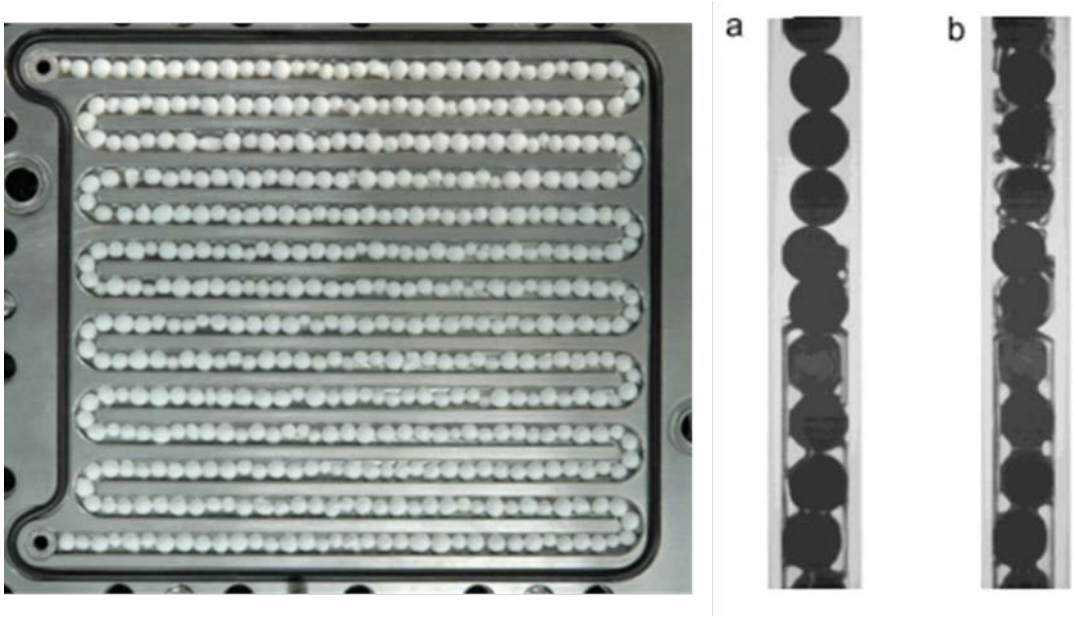

Figure 1.10: The string reactor configuration used by Hipolito et al. (2010). Showing an image of the string of pellets inside the reactor (left) and the slug flow regime characteristic of string pellet reactors identified by Bauer and Haase (2011) (right).

1.4.3 Concluding remarks on the current state of the art

Having reviewed the literature it is evident that the application of continuous technologies for the heterogenous hydrogenation of fine chemicals is relatively small but the number of ‘proof of concept’ publications has started to grow since the turn of the century. Examples of the application of trickle bed reactors are even more limited in number. However, in almost all cases where trickle beds had been employed, increased performance benefits with regards to conversion and selectivity were observed. Though the publications excellently display the potential advantages one can obtain, the drawback from these studies is that all are completely empirical, specific to a case study and are very time intensive. Moreover, fundamental understanding of the relationship between the mass transfer, intrinsic kinetics and hydrodynamics that gives rise to the experimental trends is somewhat limited and lacking thorough interpretation.

In relation to the mass transfer characteristics of trickle bed reactors, they are not simple systems to investigate with challenging hydrodynamic and transport phenomena occurring simultaneously in the bed of catalyst. Fundamental mass transfer research into these systems spans back to the early 1970s and ranges from experimental approaches to determine the mass transfer coefficients to full reactor models. However, to the best of the authors knowledge research into the convection and diffusion mass transfer processes has not been supplemented greatly since Satterfield’s early experiments in 1969. Specifically, there has been little effort to determine the contribution these two processes individually have on the overall mass transfer rate of hydrogen by modelling or experimental methodologies.

1.5 Industrial research motivations

As discussed in Section 1.2, heterogenous hydrogenations are extensively used in the synthesis of fine chemicals. In a recent study published by a team from GlaxoSmithKline, heterogenous hydrogenations accounted for 77% of all gas/liquid transformations in their portfolio [42]. Moreover, the investment and research into continuous processing technologies to manufacture active ingredients is on the rise. The sponsoring company for this work, Syngenta UK Ltd. are a global agribusiness with an estimated agrochemicals revenue of 10 billion USD per annum [49]. As a fine chemicals business, Syngenta are continually searching for the most efficient synthesis routes to manufacture their active ingredients to add value to their customers by providing a good cost-benefit balance. Wanting to build and improve manufacturing capability further, Syngenta have highlighted continuous hydrogenation as an area for future investment. From an economic standpoint, there currently exists the capacity to conduct heterogenous hydrogenations in batch and therefore, any investment into new continuous processing technologies would need assessing to ascertain the cost, safety and quality improvements.

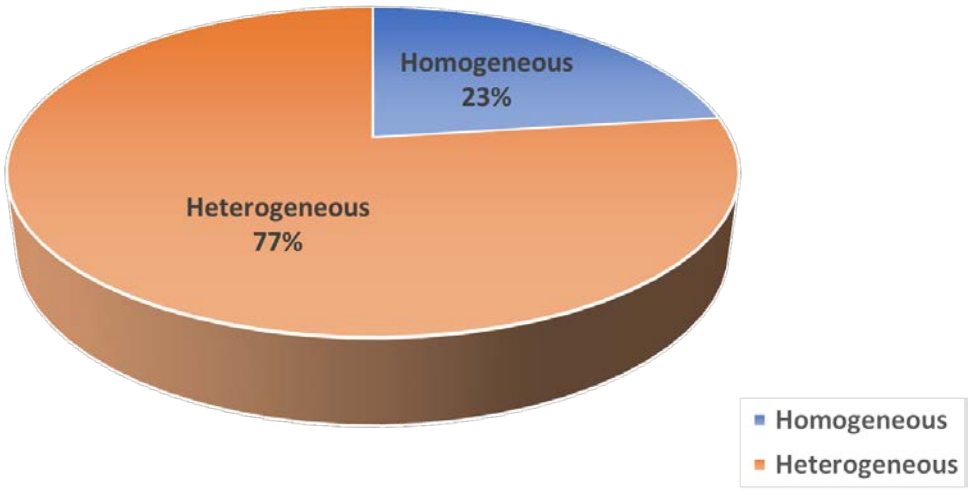

Figure 1. 11: Breakdown of GlaxoSmithKline's hydrogenation portfolio.

By supplementing current knowledge and further demonstrating the applicability of continuous hydrogenation in trickle bed reactors, the work presented in this thesis aims to aid in the drive to move from batch to continuous processing of fine chemicals. Moreover, having a thorough understanding of the mass transfer characteristics will help improve throughput and preventing processing issues during development and scale up.

1.6 Research question

The concluding remarks of the literature review can be summarised as follows:

- The use of trickle bed reactors for fine chemical manufacture has been demonstrated in the literature, but thorough interpretation to understand how mass transfer can be manipulated to control selectivity is limited.
- Understanding of convective and diffusive transfer processes has not been greatly supplemented and there is an opportunity to further explore these transfer processes to assess whether they can measured and quantified to control the rate at which hydrogen reaches the catalyst.

These two statements are inherently linked, as increased knowledge of how to manipulate the transfer processes could be the catalyst in facilitating the move to assessing the applicability of trickle bed reactors for fine chemical synthesis and spur the transition away from batch manufacture. Mass transfer limitations in trickle bed reactors are a significant issue and thus have been identified as a key design parameter for successfully scale up. Investigation

into the convective and diffusive processes and their effect on the surface concentration of hydrogen will lay the foundation to be able to theoretically assess whether a specific chemical reaction's selectivity could be enhanced using a trickle bed reactor. Finally, a more detailed understanding of how to manipulate the two transfer processes may result in reactor performance benefits, improved scalability and increased catalytic productivity. This leads to the primary research question this thesis will aim to answer;

Can we identify, measure and quantify the key mass transport processes that control the design and scaleup of heterogenous hydrogenations in trickle bed reactors?

1.7 Research methodology & thesis layout

As this thesis aims to investigate the mass transfer processes within trickle bed reactors, an interdisciplinary approach is required that will consider all the associated physical and chemical phenomena occurring. To briefly summarise before going into more depth, the scope of this thesis is to;

- Characterise catalyst material properties
- Design a scaled down trickle bed reactor to experimentally study diffusion and convection and the effect of operating conditions
- Model convection and diffusion to assess the contribution each process has on the overall mass transfer rate of hydrogen
- Combine the fundamental knowledge gathered to design bespoke multiphase reactors and model mass transfer in these systems

The physical properties of the catalyst, such as the location of the active catalytic material, and their effects on mass transfer have been well

documented in the literature. It is therefore necessary to first characterise the catalytic material and as will later be detailed throughout the thesis, many of the assumptions in relation to modelling and experimental design were justified by the catalyst characterisation. In a typical trickle bed reactor, there are two transport pathways by which a catalyst pellet is supplied with hydrogen; (i) diffusion of molecular hydrogen normal to the catalyst's surface and (ii) convective transfer of hydrogen already dissolved in the liquid as it flows over the surface of the catalyst pellet. It would be challenging to experimentally isolate the individual effects convection and diffusion have on the overall mass transfer rate of hydrogen in a trickle bed reactor due to both processes happening simultaneously throughout the bed (on hundreds of pellets). To overcome this issue, the system will be scaled down to a single catalyst pellet, where mass transfer characteristics will not be averaged over the whole bed. At this scale the hydrogen uptake rate of the pellet can be closely monitored and studied under different processing conditions. Following the experimental work, the two transport processes in the scaled reactor are mathematically modelled to determine the hydrogen concentration profile at the surface of the catalyst pellet and quantify the contribution made by both diffusion and convection on the hydrogen uptake rate of the pellet. The final section of work focusses on the design and fabrication of novel multiphase reactors that can utilise the fundamental knowledge gained from the experimental and modelling chapters to control the rate at which hydrogen is supplied to the surface of the catalyst. Two novel reactor platforms will be experimentally evaluated to assess their application as hydrogenation technologies for fine chemicals in the future.

1.7.1 Thesis layout

The overall thesis layout is summarised in Figure 1.12. The thesis will start with an overview of the literature and relevant theory, covering all the underlying concepts from heterogenous hydrogenations and hydrogenation reactors to mass transfer models and will include a detailed section on trickle bed reactors (hydrodynamics and transfer behaviour). Chapter 3 is split into two parts; (i) description of the materials and chemical analysis methods used throughout the thesis and (ii) characterisation of the two catalysts of interest. The experimental sections have been omitted and have been included in the relevant chapters as each experimental methodology is specific to each chapter of work. Chapter 4 describes the experimental approach to scaling down a trickle bed reactor to study mass transfer phenomena and isolation of the convective and diffusive processes supplying the catalyst pellet with hydrogen. Mathematical modelling of the mass transfer and kinetics to describe the experimental trends observed in Chapter 4 will be presented in Chapter 5. This will include analysis of the hydrogen concentration profile at the surface of the catalyst and quantification of the contribution convection and diffusion have on the mass transfer rate. Chapter 6 is dedicated to the design of two alterative multiphase reactor platforms and evaluates their potential as a new hydrogenation technology whereby the rate at which hydrogen is supplied to the surface can be controlled. Where appropriate, the mass transfer processes will be mathematically modelled. Chapter 7 will summarise the thesis, detail the research contributions and assess the outcomes in relation to the research question. Chapter 8 will discuss the future perspectives and recommended work leading on from the findings of this thesis.

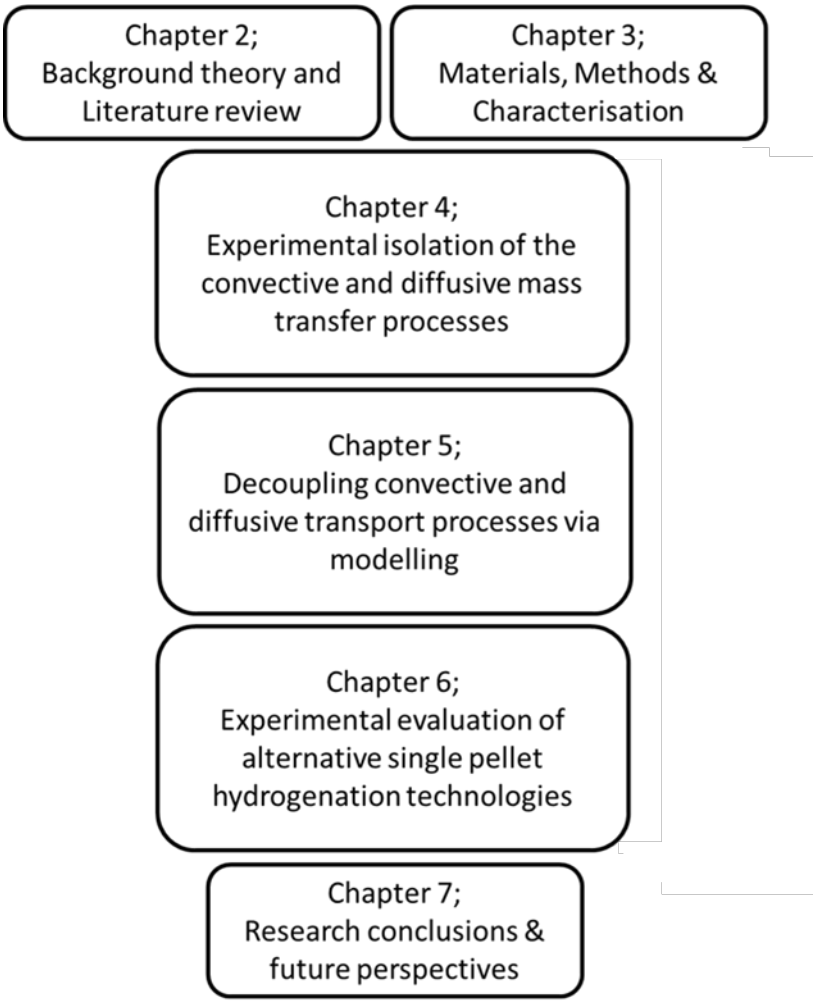

Figure 1.12: Schematic outlining the thesis layout and chapter titles.

Chapter 2
Background Theory and Literature Review

This chapter presents a general overview of the theory and relevant literature associated with the study of mass transfer processes during heterogenous hydrogenations in three phase reactors. Starting with catalysis, heterogenous hydrogenations and the typical reactor platforms used, the chapter will then cover the mass transfer and chemical reaction phenomena associated with describing three phase catalytic reactions. Finally, a brief overview of the hydrodynamic behaviour and mass transfer characteristics associated with trickle bed reactors will be presented.

2.1 Catalysis and heterogenous hydrogenations

The first use of catalysis in an industrial setting was for the manufacture of sulfuric acid in 1746 by John Roebuck, when he showed that by lining the walls of a brick built reactor with lead an increase in efficiency could be obtained [50]. Catalysis is now an integral and extremely important process in modern day society, utilised by a wide range of industrial sectors from oil, coal and gas refining to chemical and polymer manufacture. Moreover, it is approximated that over 85% of all chemicals manufactured worldwide involve catalysis at some stage in their manufacture [51]. By definition, catalysis is usually described as an increase in the rate of a chemical reaction, brought about by the presence of a material that remains chemically unchanged at the reactions end [52]. Materials that have this ability are known as catalysts and are chemical species themselves. Many catalytic materials are compounds containing transition metals such as copper, nickel, palladium and iron. This is due to transition metals having variable oxidation states, meaning they can

be manipulated into accepting or donating an electron relatively easily and can readily absorb other chemical species onto their surface [53].

To understand how a catalyst functions, it is first useful to describe a chemical reaction in terms of the energetics and collisions between molecular species. For a successful reaction to occur, two reacting molecules must first collide with enough energy to overcome a minimum energy barrier known as the activation energy. In a system such as this, the rate at which the reaction takes place will be low, as most molecules will have insufficient energy to react. A catalyst functions by offering an alternate reaction route to the reacting molecules, which has a lower activation energy, this is shown schematically in Figure 2.1. With a lower activation energy, the probability that two molecules will collide with sufficient energy to react is higher and an increase in the overall rate of the reaction is observed [54]. The alternative reaction pathway made available by the catalyst is generally a transition state (or series of transition states) whereby the reactants chemically or physically interact with the catalyst before a subsequent reaction between them forms the desired product which results in regeneration of the catalyst.

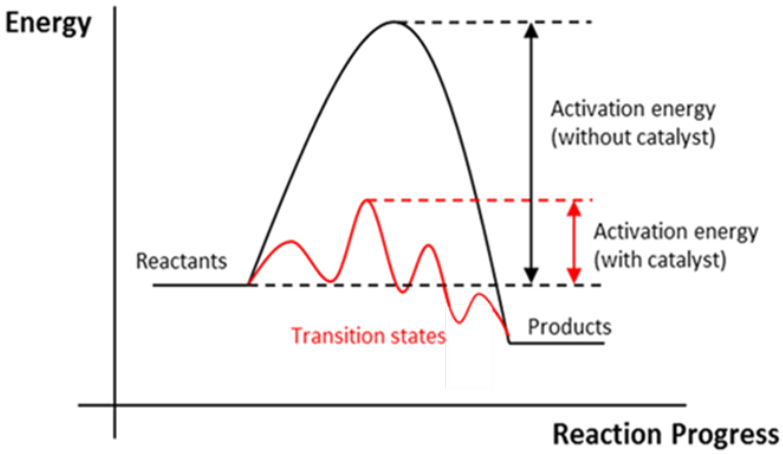

Figure 2.1: A generic potential energy diagram of a reaction with and without a catalyst.

It is generally accepted that catalysts can be divided into two types depending on the phase the catalyst is in within the system relative to the reactants [55]. When the catalyst is in the same phase as the reactants, typically contained in a liquid or gas phase, it is known as a homogeneous catalyst. Conversely, if the catalyst is in a different phase to the reactants, such as a solid powder in the presence of a reacting liquid and gas, it is known as a heterogeneous catalyst. Both types of catalyst offer a range of advantages and disadvantages, however, due to the ease at which the catalyst is separated from the products and their relatively low manufacture cost, heterogeneous catalysts are often preferred for the industrial scale manufacture of chemical species [56]. As a result, heterogeneous catalysis is extensively used in a wide variety of industries from oil and gas to the pharmaceutical and fine chemical industries [57].

2.1.1 Heterogenous catalysts

Industrial heterogenous catalysts vary greatly in both physical appearance and chemical nature but are generally either bulk or supported catalysts. Given the nature of the catalyst used in this work, the literature review will focus only on describing the latter of the two types of catalyst. Supported catalyst generally consist of three components; (i) an active phase, (ii) a carrier material or support and (iii) a promoter [58]. The active phase is typically a metal or metal oxide where the reaction takes place and as the metal catalyst is usually expensive it is dispersed as nanoparticles between 1-50 nm in size on a support material. The distribution of the active phase across the support (often 1-25 wt%) can be influenced during the manufacturing process to produce different catalyst types, the four main types are illustrated in Figure 2.2.

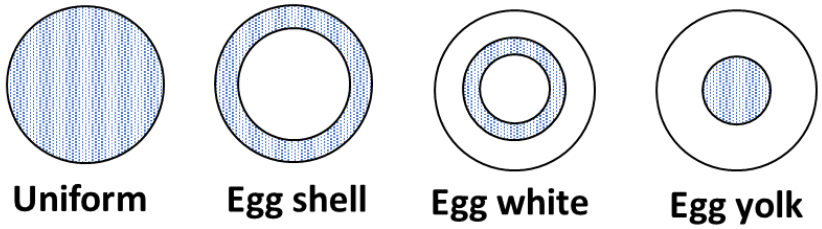

Figure 2.2: Types of heterogenous catalyst based on the location of the active phase. Showing the four ways in which active phase (depicted as blue stripes) is typically distributed through the catalyst support (white).

Each type of catalyst can be effective depending on the reaction conditions used, for example, in a mass transfer limited reaction depositing the active phase on the surface in an egg shell distribution enhances the rate at which reactants can access the active phase by removing the need for pore diffusion.

The size and shape of the metal nanoparticles is also a critical factor that can influence both the reactivity and selectivity during a catalyst reaction [59]. As the nanoparticle size increases, the number of exposed atoms on vertices, edges and planes increases and thus, the catalytic activity can also change. The extent to which reactivity/selectivity is affected by the size and shape is specific to the chemical transformation being studied and hence, there is a plethora of literature covering this topic. Cao *et al*. provides an extensive review illustrating how the size and shape affects the reactivity of several key hydrogenation reactions used in industry [60]. Of the studied systems, the hydrogenation of aromatics, aromatic nitriles and unsaturated aldehydes were all found to be shape and size dependent.

The supporting material stabilises and immobilises the active phase and is typically a porous metal oxide or carbon-based structure with a very large surface area and pore volume [61]. The types of materials employed are

commercially available and relatively cheap, ranging from refractory ceramic materials (alumina, silica) to carbon-based structures. Supports often consist of extensive networks of pores, having both a pore macrostructure and microstructure, which can greatly affect diffusion of reacting species to the active nanoparticles [62]. The material also must have the required mechanical properties to prevent the catalyst being released into the reaction mixture through crushing and abrasion. The support can itself be manufactured in a variety of forms depending on the processing requirements, from powders and pastes through to pellets and spheres. When used in packed bed reactors, the size and shape of the support determines the bed porosity, pressure drop and transport phenomena, and therefore often a comprise is needed to select the most efficient catalyst. For example, a catalyst with a smaller particle size will likely enhance transfer compared to a larger catalyst but the pressure drop will be greater across the bed. An extensive overview detailing the selection of catalyst supports for packed bed reactors is provided by Foumeny and Afandizadeh [63]. The methods and techniques used to manufacture the supports and each type of catalyst are extensively covered in the catalyst literature [58, 64, 65] and thus, will not be covered here.

Finally, additional elements are added at low concentrations to enhance catalytic activity and stability, known as promoters [66]. A well-known example is the inclusion of potassium in iron-based catalysts to increase yield during ammonia synthesis [67]. Though the benefits of utilising promoters are widely recorded in the literature, the mechanistic understanding describing the way in which promoters improve catalyst activity is limited. As the work described in this thesis will solely focus on commercially available catalysts

rather than catalyst preparation, an extensive discussion around the inclusion of promoters in catalyst manufacture will not be included.

2.1.2 Heterogenous hydrogenations

Heterogeneous hydrogenation is a particularly important catalytic chemical process used across many industries [68]. It has been estimated that within the fine chemical industry alone, one in five chemical reactions are catalytic hydrogenations, though it is also heavily used in the agrichemical and petroleum sectors [69].

Heterogeneous hydrogenation can be defined as a reduction process, being the addition of molecular hydrogen (H_2) to a chemical species (usually an organic compound containing a double or triple bond) in the presence of a catalyst [70]. Though the reduction of multi-bond containing species using hydrogen can have its disadvantages, it is industrially viable for two main reasons. Firstly, catalytic hydrogenation can be considered to be a green process, having a high atom efficiency and generally mild reaction conditions (low temperature and pressure) [71]. Secondly, given the extent to which hydrogen is used throughout chemical industry the practical guidelines for its use are well established, meaning it can be implemented and used relatively safely at plant scale [72]. Other methods of reduction involve using stoichiometric inorganic reagents such as metal hydrides or via hydrogen transfer catalysts, which can be potentially difficult to handle, have a poor atom economy and generate large amounts of waste [73, 74].

2.2 Hydrogenation reactors

Reactors used for catalytic hydrogenation are designed to bring together the reacting species, hydrogen gas and catalyst into contact in the absence of

oxygen and come in a range of designs across all scales of processing [75]. Generally, reactors can be split into two categories depending on their modes of operation. In the first category, a catalyst powder or paste is suspended in the continuous liquid medium by some method of agitation and the gas is dispersed within; these are known as slurry reactors. In the second category, the catalyst is stationary and the liquid and gas phases pass through the catalyst bed, these types of reactors are known as packed bed reactors [76].

2.2.1 Slurry reactors

The three phase slurry reactors are prominently used within many chemical processing industries, including catalysis. Within this category of reactor two types of slurry reactors are usually encountered; mechanically agitated and bubble column slurry reactors [77], both illustrated in Figure 2.3. Both types of reactor can be operated in continuous or semi-batch modes [78], however, continuous operation is hindered by challenges associated with separation of the catalyst and handling of the slurry [77].

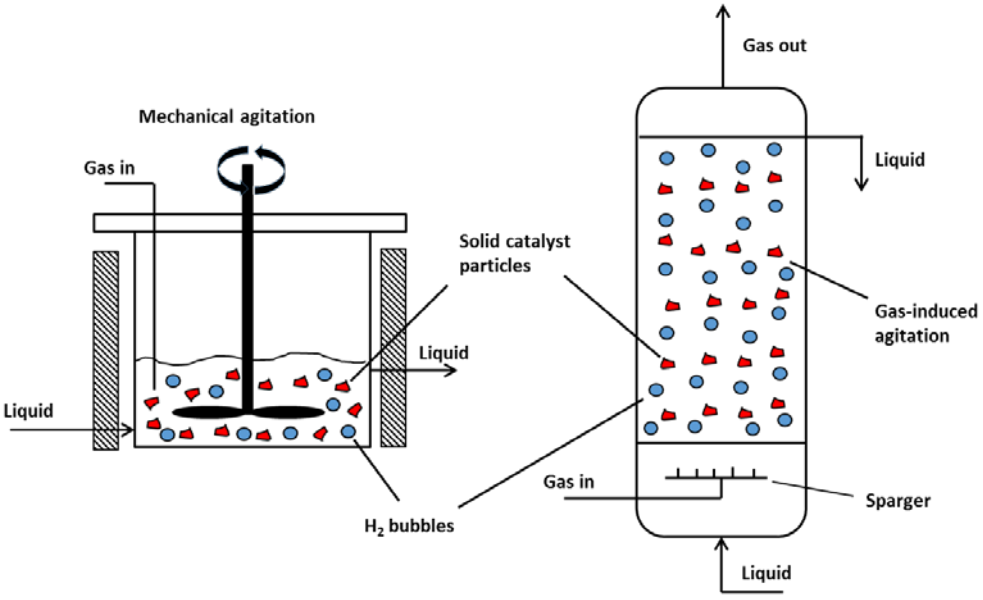

Figure 2.3: The two the types of three phase slurry reactors encountered. Showing a mechanically agitated reactor (left) and a bubble column slurry reactor (right).

Mechanically agitated slurry reactors, in which an impeller is used to suspend a catalyst powder or paste, offer efficient mass and heat transfer and are the preferred option when manufacturing fine chemicals (high quality required) [79]. However, back mixing of the liquid and catalyst attrition can make their use problematic. In bubble columns, the catalyst is suspended in a continuous liquid phase via gas induced agitation. The dispersed gas phase is introduced into the bottom of a vertical cylinder containing catalysts particles and a liquid medium. As the gas phase transitions up the column the catalyst becomes fluidised in the liquid phase resulting in lower mass and heat transfer efficiencies and non-uniform distribution of the catalyst in the reactor [77]. The advantages of using slurry reactors as opposed to packed bed reactors are well documented [80]. For example, as the pressure drop across the reactor is not a primary concern, smaller catalyst particles can be used during operation (1 – 200 μm range) and hence the resistance to intra-particle diffusion is much smaller [81]. Moreover, issues with partial wetting of the catalyst are not readily encountered and fresh catalyst can easily be fed into the reactor without halting processing. The risk of thermal hotspots and temperature runaway are minimised due to the high heat transfer efficiency and heat capacity of the slurry. That said, the use of slurry reactors does not come without some operational challenges [79]. Separation of the catalyst, equipment erosion due to solids and back mixing issues (hindering plug flow) are all technical difficulties commonly seen. Deciding on which reactor type to use depends on the specific process and processing scale required. For the hydrogenation of fatty acids or esters where large volumes of product are desired, a bubble column reactor is preferred in continuous operation. Whereas for a small volume of fine chemicals or pharmaceutical ingredients

mechanically agitated reactors are chosen [76]. Extensive reviews on the reaction kinetics, mass transfer, hydrodynamics and reactor design have been conducted and are presented in the literature for both mechanically agitated and bubble column slurry reactors [43, 76, 82-84] and therefore, will not be subject to discussion in this report.

2.2.2 Packed bed reactors

In packed bed reactors the solid catalyst is held in place whilst either the dispersed liquid phase flows through the bed as seen in trickle bed reactors, or a continuous liquid phase submerges the packed bed and the dispersed gas phase bubbles through the bed, known as packed bubble column reactors [13].

In a trickle bed reactor, both gas and liquid flow concurrently down through a packed bed of catalyst that rests on a sieve plate or wire mesh. A schematic of a typical trickle bed reactor can be seen in Figure 2.4.

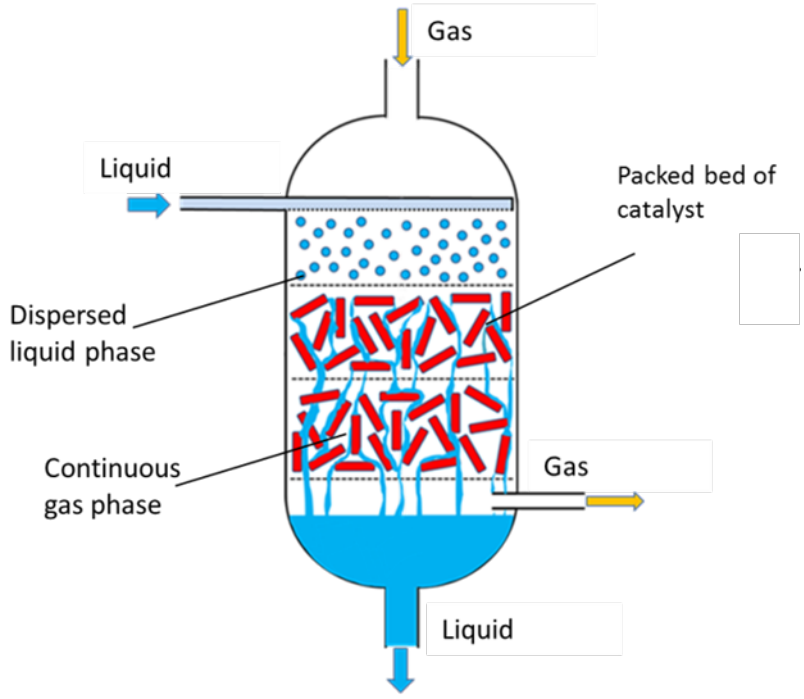

Figure 2.4: Schematic of a trickle bed reactor operating in a concurrent configuration

As liquid trickles through the bed not all catalyst particles are fully wetted and therefore the liquid distribution within the packed bed is integral for efficient heat transfer and reactor performance It is also possible to flow the two phases in a counter-current mode (liquid descends and gas ascends through the bed) [85]. Recent studies into counter-current flow have shown that the contact between the phases can be improved during this mode of operation, though the bed can be prone to flooding (liquid flow reverse) at increased gas velocities and this has decreased its industrial application [86, 87]. Wu *et al* [88] found however, that counter-current operation offers performance benefits over concurrent at high pressures, where the rate of reaction is controlled by the availability of the reactant in the liquid. Conversely, concurrent flow performs better at low operating pressures where the availability of the gas limits the reaction. Trickle bed reactors can be further classified into whether the bed is randomly packed, structured or arranged into micro channels. There is some evidence to suggest that by structuring the packed bed to form small channels for the liquid to regularly flow through, reactor performance can be enhanced over conventional randomly packed beds. However, no benefits regarding selectivity has been observed [47]. Micro-channel reactors can be useful for kinetically fast and exothermic reactions as they offer efficient heat and mass transfer characteristics. However, they are expensive and operationally challenging as they are prone to clogging and difficult to clean [13].

In bubble column reactors the packed bed is completely submerged in the now continuous liquid phase and the dispersed gas phase bubbles through the bed. A schematic of a bubble column packed bed reactor is shown in Figure 2.5.

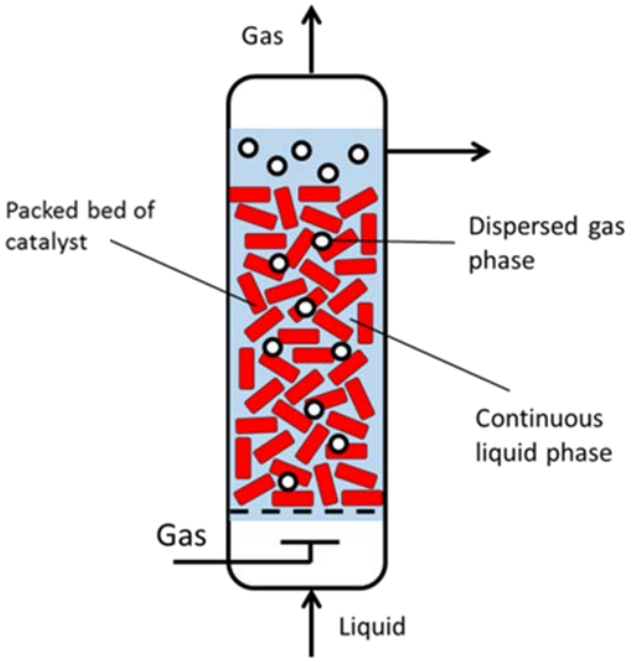

Figure 2.5: Schematic of a packed bubble column reactor

In this mode of operation the catalyst can be easily separated from the other phases, overcoming the disadvantages associated with conventional slurry bubble columns [89]. Catalyst loading generally higher than in trickle beds and as the bed is completely submerged, the whole catalyst surface is utilised resulting in more efficient heat transfer [90]. Table 2.1 compares the performance of both types of packed bed reactors. Due to its simple operation under high pressure and temperature conditions and its ability to easily recycle liquid product streams multiple times (mimicking batch operation), trickle bed reactors are a more viable option for the manufacture of fine chemicals [12]. Moreover, trickle bed reactors have the potential to reach high levels of conversion and selectivity due to plug flow like conditions (low back mixing) [13]. Although partial or incomplete wetting of the catalyst can cause performance issues, homogenous side reactions are reduced due to limited liquid hold-up in the packed bed and areas of purely gas-solid interactions can benefit slower reactions requiring higher catalyst loading.

Table 2.1: Operability assessment and comparison between trickle and bubble packed bed reactors [13, 19].

Parameter	*Trickle Bed Reactor*	*Packed Bed Bubble Column*
Ease of operation	Simple	Simple
Catalyst loading	High	High
Heat transfer	Low (can be problematic for fast exothermic reactions)	Better than trickle bed but still relatively low
Mass transfer	Can be an issue for large catalytic particles	Smaller gas-liquid area for mass transfer to occur
Plug flow (low back mixing)	Low back mixing	Back mixing can be an issue
Ability to use foaming / viscous liquids	Struggles to process viscous liquids	Relatively easy to process viscous liquids
Reactor volume	High throughput	High throughput
Reactor pressure drop	Lower	Higher

2.3 Mass transfer in three phase catalytic reactions

Given the extent to which three phase catalytic reactions have been studied over the years, the understanding of the overall rate of reaction that includes the effect of the various mass transfer steps taking place between the phases is well developed [91]. For a bimolecular reaction occurring within a porous catalyst pellet, the transport steps involved are [92]:

$$A_{gas} \rightarrow A_{liquid} + B_{liquid} \xrightarrow{catalyst\ surface} products$$

- The gaseous reactant *A* must first dissolve into the bulk liquid phase. The quantity of dissolved gas A present in the liquid is proportional to its partial pressure, where the proportional constant is known as by Henry's Law constant, H where:

$$C_{A,\ gas} = H \cdot C_{A,\ liquid}$$

- Reactants *A* and *B* must travel though the bulk liquid to the surface of the catalyst

- Reactants *A* and *B* must then diffuse through the pores of the catalyst to an active site
- *A* and *B* adsorb onto the catalyst, react to form the products and desorb

These steps are schematically shown in Figure 2.6, which highlights the concentration changes driving mass transfer. In cases where a non-porous catalyst is present (the active sites are limited to the external surface of the pellet/particle) pore diffusion and subsequent reaction does not occur and instead a surface catalysed reaction occurs which can be defined in terms of the surface area of the catalyst used [91]. Transport from gas to liquid and across the liquid-solid interface is known as external diffusion whereas transfer through the porous catalyst is referred to as internal diffusion.

2.3.1 External diffusion

Mass transfer is a term that is commonly employed to describe the transference of a component or chemical species within a system from that of a concentrated region to a region of lower concentration [93].

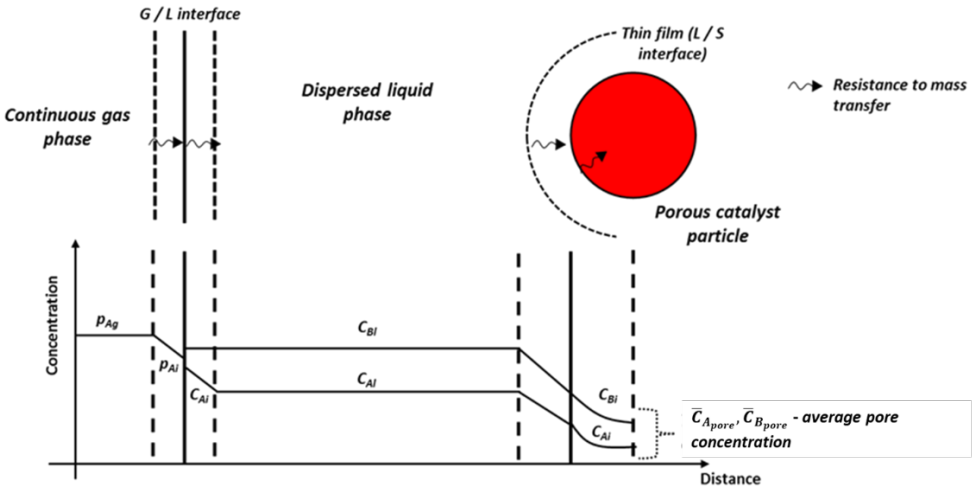

Figure 2.6: Concentration profiles of the gas and liquid reactants in heterogenous reaction. The black wiggly arrows represent resistance to mass transfer as a reactant travels across an interface.

The rate at which mass transfer between regions occurs is dependent on the concentration difference (known as the driving force) and any resistances to mass transfer present in the system. In the case of heterogeneous catalysis, as the catalyst is in a different phase to the reacting components, transfer between two to three phases is required for the reaction to occur. The overall rate of reaction is, therefore, heavily dependent on the mass transfer between all of the phases involved.

One of the simplest examples of mass transfer is diffusion in binary mixtures of gases. Consider two ideal gases, ***A*** and ***B*** contained in a sealed vessel separated by a barrier. If the barrier is suddenly removed the two gases will diffuse into each other. The rate at which molecules of ***A*** diffuse into ***B*** and vice versa is governed by Fick's Law for steady-state diffusion, whereby the driving force is the molar concentration gradient across the system [94]. Assuming the two gases are ideal, steady state diffusion of ***A*** into ***B*** can be expressed as in Eq. (2.1).

$$N_A = -D_{AB}\frac{dC_A}{dy} \tag{2.1}$$

Here N_A is the molar flux of ***A*** (moles per unit area per unit time), C_A the concentration of ***A***, D_{AB} the diffusion coefficient for ***A*** in ***B*** and y the distance in the transfer direction. In this case the mass transfer rates of both gases are equal and opposite, this is known as equimolecular counter-diffusion [95]. In these conditions the differential equation for molar flux of ***A*** can be integrated between the boundary conditions $y = y_1, C_A = C_{A1}$ and $y = y_2, C_A = C_{A2}$, at constant pressure and temperature to give Eq. (2.2).

$$N_A = k(C_{A1} - C_{A2}) \tag{2.2}$$

In this expression C_{A1} and C_{A2} are the concentrations at distances y_1 and y_2 in the direction of diffusion ($y_2 > y_1$). The final term k is the mass transfer coefficient and is expressed as a velocity (length per unit time), where $k = D_{AB} / (y_2-y_1)$. In this case the driving force is expressed as a difference in molar concentration; however, it can be expressed as a difference in partial pressures or mole fractions.

Many processes involve the transfer of mass across a phase boundary. Whether the transfer is between gas and solid or liquid and liquid, material must transfer across an interface. Mathematical theories have been proposed to describe this transfer of mass across a phase boundary and the following section will provide an overview of the most well-established mass transfer theories. In addition, an overview of the resistances in series mass transfer model, which is used to describe transfer across multiple phase boundaries and is used throughout the thesis, will be included.

2.3.1.1 Whitman two-film theory

One of the earliest approaches to try and model mass transfer across a phase boundary was that of Lewis and Whitman who proposed a two-film model when studying gas adsorption [96]. This model assumes that between two stagnant or laminar phases (immiscible liquids or gas-liquid) there exists an interfacial area via which material travels through, driven by a difference in concentration or partial pressure. [97]. A schematic illustrating the model is shown in Figure 2.7. In this theory the following assumptions are made; no material accumulates at the interface, the total resistance to mass transfer originates within the two films and the two phases are in equilibrium at the interface.

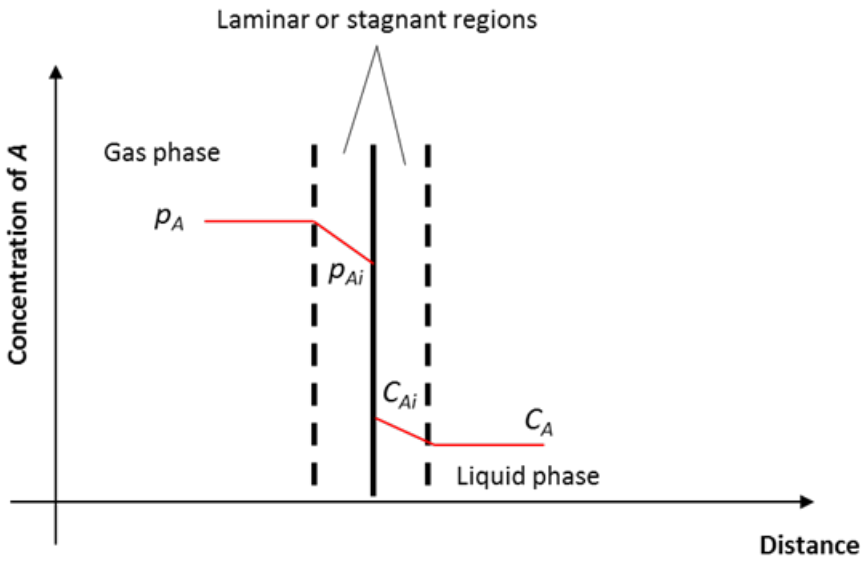

Figure 2.7: Visual representation of Whitman two-film theory for gas adsorption into a liquid. The red line represents the concentration gradient across the interface.

If no accumulation at the interface occurs, the rate of mass transfer from the gas to the interface must be equal to that of the interface to the liquid [93].

$$k_g(p_A - p_{Ai}) = k_L(C_{Ai} - C_A) \quad \textbf{(2.3)}$$

The left-hand side of Eq. (2.3) expresses the flux of ***A*** from the bulk gas to the interface, with k_g being the mass transfer coefficient of the gas film, p_A and p_{Ai} being the partial pressures of ***A*** in the bulk and at the interface respectively. The right-hand side deals with the transference of ***A*** from the interface into the bulk liquid, where k_L is the mass transfer coefficient of the liquid film, C_A the concentration in the bulk and C_{Ai} the concentration at the interface. As the interface is at equilibrium, the relationship between p_{Ai} and C_{Ai} is dependent on the relevant equilibrium function, which for gas adsorption would be Henry's law (the linear relationship between the partial pressure and adsorbed phase concentration, where H_A is the Henry's law constant) [98]. The liquid side mass transfer coefficient, $k_L \sim \frac{D}{\delta}$ suggests that as the liquid film thickness δ increases the mass transfer rate decreases.

2.3.1.2 Penetration theory

In 1935, Ralph Higbie proposed that the mechanism by which mass is transferred across the gas-liquid interface involves turbulent eddies constantly moving fluid “parcels” from the bulk to the interface. Once at the interface unsteady-state diffusion occurs during contact, before being replaced by subsequent fresh bulk fluid [99]. The theory assumes that at the gas-liquid interface equilibrium exists and each portion of liquid in a “parcel” is in contact with the gas phase for the same amount of time. Figure 2.8(a) illustrates a gas bubble rising through a liquid and the path of an eddy as it contacts the interface. Initially, bulk liquid will have a uniform dissolved gas concentration, C_{A0} and is considered internally stagnant in the bulk liquid. As the eddy moves fresh liquid to the interface it contacts the gas phase, where the gas-liquid interface concentration becomes C_A, taken as the equilibrium solubility of the gas in the liquid. Following this theory, it is possible to specify the concentration of solute at a specific depth in the liquid as a function of contact time and thus, is referred to as penetration theory Figure 2.8(b)[100].

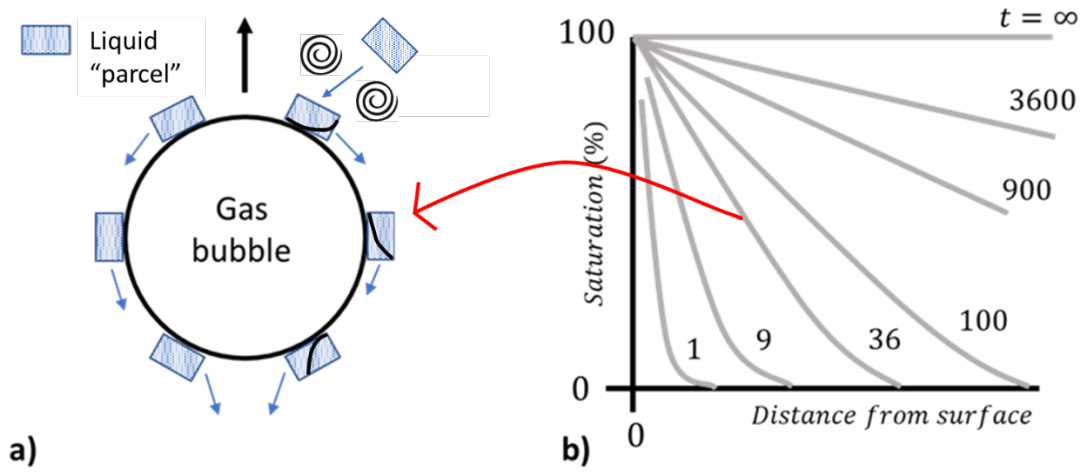

Figure 2.8: A schematic illustrating the visual concepts of penetration theory. Showing the interaction between eddies in the liquid (a) and a gas bubble and the penetration of a solute into a solvent at different exposure times(b).

During the contact time, t, unsteady-state diffusion occurs from the gas to the liquid in the z direction and transfer may be approximated by Fick's second law for unidirectional molecular diffusion;

$$\frac{\partial C_A}{\partial t} = D\frac{\partial^2 C_A}{\partial y^2} \tag{2.4}$$

If diffusion is slow and the eddy contact time short, the solute is thought to be unable to travel the length of the eddy, z_e and z_e is considered infinite. Solving Eq. (2.4) with the following boundary conditions;

$$t = 0 \qquad 0 < y < \infty \qquad C_A = C_{A0}$$

$$t > 0 \qquad y = 0 \qquad C_A = C_{Ai}$$

$$t > 0 \qquad y = \infty \qquad C_A = C_{A0}$$

Gives an expression for the solute concentration C_A as a function as time, t and position, y;

$$\frac{C_A - C_{A0}}{C_{Ai} - C_{A0}} = \mathrm{erf}\left(\frac{y}{2\sqrt{Dt}}\right) \tag{2.5}$$

$$\text{Where erf is the error function: } \mathrm{erf}(x) = \frac{2}{\sqrt{\pi}}\int_x^\infty e^{-x^2}\,dx$$

The concentration gradient is then determined by differentiating Eq. (2.5) with respect to y and the mass transfer rate for the liquid contact time (time the liquid portion has been at the interface before being removed by an eddy), t, is obtained, where the mass transfer coefficient $k_L \sim \sqrt{D/\pi t}$.

$$(N_A)_t = \sqrt{\frac{D}{\pi t}} \cdot (C_{Ai} - C_{A0}) \tag{2.6}$$

2.3.1.3 Surface Renewal theory

When compared to the experimental data penetration theory is generally in good agreement given that the physical model and underlying assumptions

are restrictive [101]. Dankwerts first modified the theory by suggesting eddies or elements of liquid could reside at the interface for different periods of time and thus, there would be a distribution of liquid “parcels” with different exposure/contact times [102]. Moreover, the probability that an eddy could suddenly mix back into the bulk liquid and be replaced by a new eddy was assumed to be independent of the exposure time. To account for these new assumptions Dankwerts introduced the constant, s, which is the fractional rate of liquid surface renewal and showed the age distribution of the eddies at the surface to follow an exponential form [100]. Thus, for a system where the surface is randomly renewed, the overall mass transfer flux of a solute is given Eq.(2.7) where the mass transfer coefficient $k_L \sim \sqrt{D \cdot s}$.

$$N_A = \sqrt{D \cdot s}\,(C_{Ai} - C_{A0}) \tag{2.7}$$

As was observed with penetration theory the transfer rate is proportional to the square of the diffusivity. The fractional rate of surface renewal is difficult to estimate, however, s will increase as the turbulence in the fluid increases and thus, mass transfer will be enhanced.

2.3.1.4 Boundary layer theory

The previous theories describing interphase mass transfer have yet to consider any hydrodynamic properties of the fluid, properties that will have a significant effect on the rate of convective transport [101]. Boundary layer theory incorporates both diffusion and the flow fields of the fluid and therefore, is thought to offer a more realistic description of mass transfer at a phase boundary. The theory is best illustrated in a simple example; fluid flow over a wide flat plate as shown in Figure 2.9.

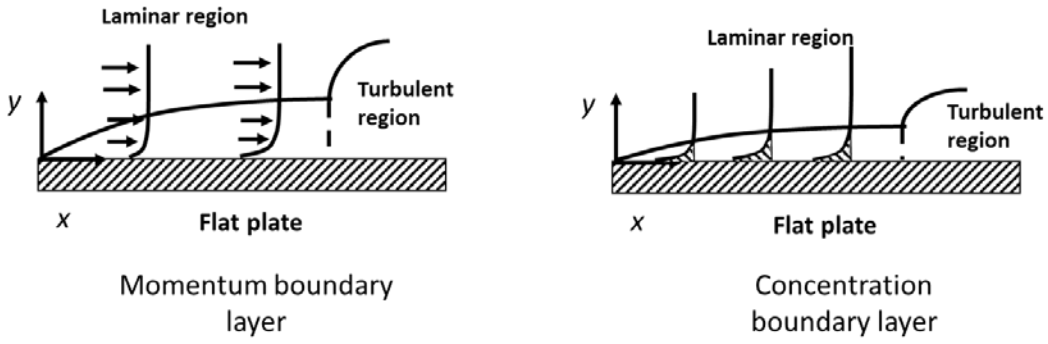

Figure 2.9: Schematic illustrating the momentum and concentration boundary layers in a liquid flowing over a flat plate that is sparing soluble.

The flow of fluid is impeded near the surface of the plate due to drag and forms a region of disruption in the fluid known as the momentum boundary layer [103]. The boundary layer progressively becomes larger as the fluid travels further down the plate, transitioning from a laminar region into a turbulent region. If the plate is sparing soluble, solute will dissolve and diffuse into the liquid. The distance the solute diffuses into the liquid forms a separate boundary layer known as the concentration boundary layer. To determine the rate at which the solute dissolves, it is necessary to understand how the Sherwood number (the ratio of convective and diffusive transfer) is affected by the Reynold's and Schmidt numbers. Derivation of the mass transfer coefficient via boundary layer theory is mathematically rigorous and will not be fully detailed here, the full derivation can easily be found in the literature however [101]. For the flat plate example, an expression for the Sherwood number as a function of the Reynold's and Schmidt numbers is shown in Eq. (2.8).

$$Sh = 0.646 \cdot Re^{\frac{1}{2}} \cdot Sc^{\frac{1}{3}}$$

$$\left(\frac{\bar{k}L}{D}\right) = 0.646 \cdot \left(\frac{LU\rho}{\mu}\right)^{\frac{1}{2}} \cdot \left(\frac{\mu}{\rho D}\right)^{\frac{1}{3}} \quad \textbf{(2.8)}$$

Thus, the averaged mass transfer coefficient, $\bar{k}$, of the film can be determined for a plate of characteristic length, L. It should be noted that this expression holds only for this plate geometry, other geometries will have modified expressions for the Sherwood number specific to the geometry.

2.3.2 Internal diffusion

The intra-particle mass transfer resistance can have a significant effect on the overall rate of reaction depending on the location of the catalyst nanoparticles on the support material. As the internal surface area within the support is significantly larger than that of the external support, the overall rate of reactant can be affected by the ability of the reactants to diffuse to the active sites [104]. The type of diffusion observed is dependent on the size of the pores present in the support, with three modes of diffusion generally being accepted, these are outlined in Table 2.2. For Maxwellian diffusion to be observed, the pore diameter is sufficiently larger than the mean free of the molecule (average distance travelled between a collision) resulting in limited wall interactions. Knudsen diffusion is observed when the pore diameter and mean free path are comparable and the molecule collide with the pore walls. It is postulated that only at low temperatures will surface diffusion considerably affect the overall reaction rate [105]. At high temperatures, reactants are forced into pores due to the total pressure difference across the pore.

Table 2.2: Types of diffusion seen in porous particles.

Diffusion mode	***Condition***	***Comment***
Maxwellian	Pore diameter, d_{pr} >> Mean free path of molecule λ	Similar to external diffusion
Knudsen	$d_{pr} \approx \lambda$	Wall interactions are more frequent than molecular interactions
Surface	d_{pr} ≈ size of diffusing molecule	Diffusion only occurs with the reactant constantly contacting the wall

Ernst Thiele first described the relationship between internal pore diffusion and the rate of reaction within catalyst pellets in 1939 [106]. Following the derivation as described by Levenspiel, for a reactant A diffusing through a cylindrical pore of length L where a first order reaction takes place along its surface, the concentration profile within the pore can be expressed as [92];

$$\frac{C_A}{C_{As}} = \frac{\cosh\sqrt{\frac{k}{\mathcal{D}}}(L-x)}{\cosh\sqrt{\frac{k}{\mathcal{D}}}L} \qquad \textbf{(2.9)}$$

Where C_{As} is the concentration at the entrance of the pore and x the distance which the reactant has travelled. The drop in concentration of A as the reactant diffuses through the pore is dependent on the dimensionless parameter $\sqrt{\frac{k}{\mathcal{D}}}L$ which is known as the Thiele modulus, M_T. At low Thiele modulus values, a uniform concentration gradient is observed in the pore as diffusional resistances are low. As the Thiele modulus increases, pore diffusion causes the concentration profile in the pore to drop progressively more steeply. To describe the extent pore diffusion influences the reaction rate the

effectiveness factor, η, is used by comparing the rates with and without pore diffusion;

$$\eta = \frac{r_{A\ (with\ diffusion\ resistance)}}{r_{A\ (no\ diffusion\ resistance)}} \qquad \textbf{(2.10)}$$

Thiele [106] and Aris [107] related the effectiveness factor to the Thiele modulus for catalyst particles (the relationship is shown in Figure 2.10). At low values of Thiele modulus ($M_T < 0.4$) the pore concentration is almost uniform, and reactant can fully penetrate the pore – known as the diffusion free regime [92]. When strong pore diffusion is present ($M_T > 4$), catalyst present in the centre of the pore is starved of reactant and remains used.

2.3.3 Resistances in series

A mass transfer resistance, Ω, is defined as the ratio between the driving force (which is the concentration difference ΔC) and the mass transfer rate (MTR);

$$Resistance = \frac{driving\ force}{transfer\ rate}$$

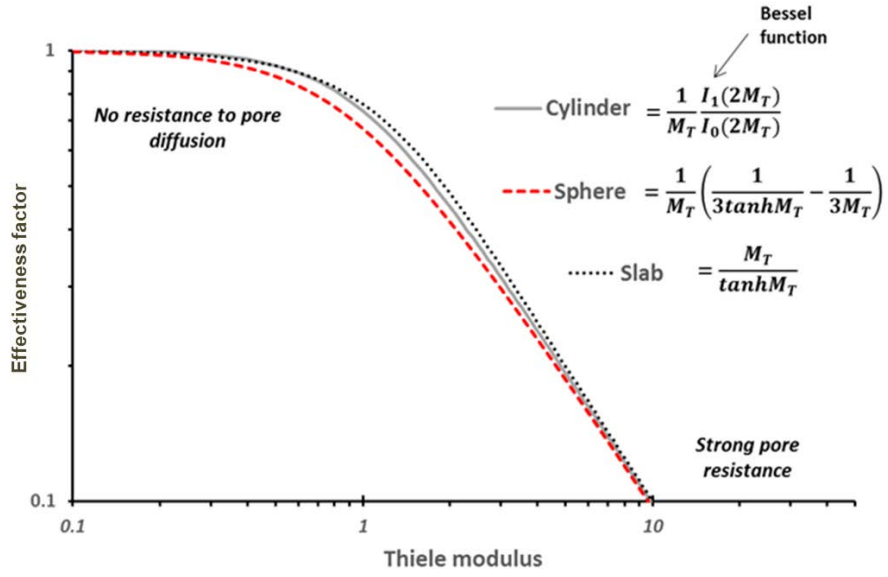

Figure 2.10: Illustrating the relationship between the Thiele modulus and effectiveness factor for cylinder, spherical and slab particle shapes.

Here MTR has units of $mol\ /m^3\ liquid \cdot s$ and is defined as:

$$MTR\ (mol\ /m^3\ s\ ) = k_i \cdot a_i \cdot (C_i - C_b)$$

Where k_i is the mass transfer coefficient (m/s), a_i the interfacial area available for transfer per volume of bed ($m^2\ bed\ \cdot m^{-3}\ bed$) and $(C_i - C_b)$ the concentration difference between the interface and bulk liquid. The resistances in series approach is typically used to mathematically describe the transfer of reactants across multiple interfaces. As the reactant moves from a higher concentration across an interface to a lower concentration there will be an associated resistance to transfer [108]. At steady state the rate of mass transfer between the phases is considered equal, and thus the slowest limiting transfer step will define the overall mass transfer rate. A common analogy used is Ohm's law and current flowing around a circuit containing resistors in series.

Electric circuit	$R = \frac{Voltage}{Current}$	$I \cdot (R1 + R2 + R3) = \Delta V1 + \Delta V2 + \Delta V3$
Mass transfer	$\Omega = \frac{\Delta C}{MTR}$	$MTR \cdot (\Omega 1 + \Omega 2 + \Omega 3) = \Delta C1 + \Delta C2 + \Delta C3$

In the case of three phase catalytic reactions, gas must dissolve into the liquid phase, diffuse to the surface of the catalyst, and then diffuse through the pores of the catalyst support to an active site. Following two-film theory the mass transfer rates between the gas-liquid, liquid-solid and chemical reaction in the pores can be expressed as the following [109];

$$MTR_{G-L} = k_L a_i\ (C_0 - C_L) \qquad C_0 - C_L = \frac{MTR_{G-L}}{k_L a_i}$$

$$MTR_{L-S} = k_s a_s\ (C_L - C_S) \qquad C_L - C_S = \frac{MTR_{L-S}}{k_s a_s}$$

$$MTR_R = k_{obs} C_s \eta a \qquad\qquad C_s = \frac{MTR_R}{k_{obs} C_s \eta f_s}$$

Where k_L is the liquid side mass transfer coefficient, k_s is the solid-liquid mass transfer coefficient, k_{obs} the observed rate constant, η the catalyst effectiveness factor, C_0 the equilibrium concentration of gas in the liquid phase (P/H), C_L the gas concentration in the liquid, C_s the concentration of gas at the surface of the catalyst, a_i the specific surface area of the gas-liquid interface, a_s the specific surface area of the solid-liquid interface and f_s the solid (catalyst) loading. Following the resistance in series principle and taking the sum of the driving force terms shown above leads to an expression for the global mass transfer rate across a three phase system;

$$MTR_{G-L} \approx MTR_{L-S} \approx MTR_R \approx MTR$$

$$MTR \cdot (\Omega_{G-L} + \Omega_{L-S} + \Omega_R) = \Delta C_{G-L} + \Delta C_{L-S} + C_s = C_0$$

$$C_0 = MTR \cdot \frac{1}{k_L a_i} + \frac{1}{k_s a_s} + \frac{1}{k_{obs} \eta f_s}$$

$$MTR = \frac{1}{\frac{1}{k_L a_i} + \frac{1}{k_s a_s} + \frac{1}{k_{obs} \eta f_s}} C_0 \qquad \textbf{(2.11)}$$

2.3.4 Kinetics

The reaction mechanism during heterogeneous catalytic processes can be broken down into a sequence of elementary equations involving several surface intermediates that are often present in very low concentrations. Several mechanisms for describing the reaction rate in term of the adsorption and subsequent desorption of a compound from the catalyst surface have been proposed over the years [110]. However, the two most common

mechanisms: the Langmuir-Hinshelwood and Eley-Rideal mechanisms will be discussed briefly here.

2.3.4.1 Langmuir-Hinshelwood mechanism

This mechanism assumes that reactants are initially chemisorbed onto the surface before any reaction occurs - the most prevailing situation observed in heterogeneous catalysis [111]. The elementary steps for a bimolecular reaction following the Langmuir-Hinshelwood mechanism can be written as follows (here *S* is an active site on the catalyst).

$$A + S \underset{k_{-1}}{\overset{k_1}{\rightleftharpoons}} AS$$

$$B + S \underset{k_{-2}}{\overset{k_2}{\rightleftharpoons}} BS$$

$$AS + BS \xrightarrow{k} products$$

From the adsorption and desorption of both reactants and the reaction itself, five rate constants exist (k_1, k_{-1} ,k_2 ,k_{-2} and k) and assuming Langmuir-Hinshelwood behaviour, the rate equations for the two adsorbing species can be expressed as shown in Eq. (2.12) and Eq. (2.13).

$$k_1(1 - \theta_A - \theta_B)C_A = k_{-1}\theta_A \quad \textbf{(2.12)}$$

$$k_2(1 - \theta_A - \theta_B)C_B = k_{-2}\theta_B \quad \textbf{(2.13)}$$

Where θ_A is the surface coverage of *A*, θ_B is the surface coverage of *B* and *C* is the concentration of the reacting species. If it assumed that the rate limiting step is the irreversible reaction itself and the two reactants compete for sites, setting the rate to to $k\theta_A\theta_B$ solving for θ_A and θ_B gives Eq. (2.14), where the adsorption constants $K_1 = k_1 / k_{-1}$ and $K_2 = k_2 / k_{-2}$.

$$r = k\frac{K_1K_2C_AC_B}{(1 + K_1C_A + K_2C_B)^2} \quad \textbf{(2.14)}$$

2.3.4.2 Eley-Rideal mechanism

If a molecule adsorbs onto the surface and the reactant molecule reacts with it directly from the gas phase without first adsorbing itself, the process is said to follow the Eley-Rideal mechanism [111]. This mechanism is much rarer than the previously discussed Langmuir-Hinshelwood. The elementary steps for this mechanism can be written as;

$$A + S \underset{k_{-1}}{\overset{k_1}{\rightleftharpoons}} AS$$

$$AS + B(g) \xrightarrow{k} product$$

Three rate constants are now present (k_1, k_{-1} and k) and the rate equation for this mechanism can be defined as shown in Eq. (2.15).

$$r = k\theta_A C_B \tag{2.15}$$

Assuming that the reaction is the rate limiting step and that $B(g)$ surface coverage is low, the rate equation can be expressed as shown by Eq. (2.16). The order with respect to *A* depends on the concentration of *A*. When at a low concentration of *A* first order is observed and at high concentrations zero order.

$$r = k\frac{K_1 C_A C_B}{(K_1 C_A + 1)} \tag{2.16}$$

2.3.4.3 The observed rate constant

In the effort to simplify reactions involving two different chemical species (*A* and *B*), it is often assumed that one is in excess of the other. If *B* is in excess, the change in concentration of *B* over time will be negligible and is assumed constant. It is then possible to treat the process as a pseudo first order reaction with the first order rate constant k_{obs}. For the reaction *A+B→P;*

$$-\frac{d[A]}{dt} = k[A][B]$$

Assuming the system is pseudo first order;

$$-\frac{d[A]}{dt} = k_{obs}[A] \; and \; k_{obs}[A] = k[A][B]$$

Then the observed rate constant can be expressed as:

$$k_{obs} = k[B]$$

It is often convenient to utilise observed rate constants in heterogenous catalysis, where complex reaction pathways with multiple elementary steps and unstable intermediates can be challenging to determine. The observed rate constant is therefore complex function that represents contributions from each of the elementary steps involved in the catalysis. He *et al.* employed the observed rate constant method to investigate the transmetalation kinetics in a Sonogashira coupling reaction, a palladium catalysed process that has been extensively studied but where limited mechanistic details currently exist [112].

2.4 Trickle bed reactors; hydrodynamics and mass transfer

Of the hydrogenation reactors discussed in Section 2.2, trickle bed reactors will feature most prominently in the following results chapters. Thus, a brief overview of the hydrodynamic and mass transfer characteristics that need to be considered when operating trickle bed reactors will be given in this section. Given the complex relationship between the hydrodynamics and mass transfer within trickle bed reactors, several parameters need to be either experimentally determined or predicted before successful design and operation can occur. As the mode of operation and observed flow regime will heavily dictate the importance (and determination) of these parameters, it

would be beyond the scope of this report to discuss transport characteristics and hydrodynamic parameters for all flow regimes. Therefore, the discussion will focus on trickle flow as it is the most prevalent mode of operation used in industry and the intended flow regime to be studied in this work.

2.4.1 Hydrodynamics behaviour

In concurrent operation, at least four flow regimes have been identified in trickle bed reactors [113, 114], these are illustrated in the flow regime map in Figure 2.11. The flow regime formed depends on several parameters such as the gas and liquid velocities, physical properties of the phases, size and shape of the catalyst particle and the packing density.

The regime most often operated at industrial level, trickle flow is characteristically achieved at moderate gas and low liquid flow rates [115]. Under these conditions liquid spreading is primarily controlled by capillary pressure (as localised surface forces are stronger than liquid inertia) with the liquid tricking over the catalyst particles as a film or rivulet. As the liquid flow rate increases inertia forces become more dominant and liquid films form over the surface of the catalyst. The operating window in which trickle flow is observed can be widened by either altering the particle size of the catalyst, reducing the surface tension or decreasing the liquid flow rate [116].

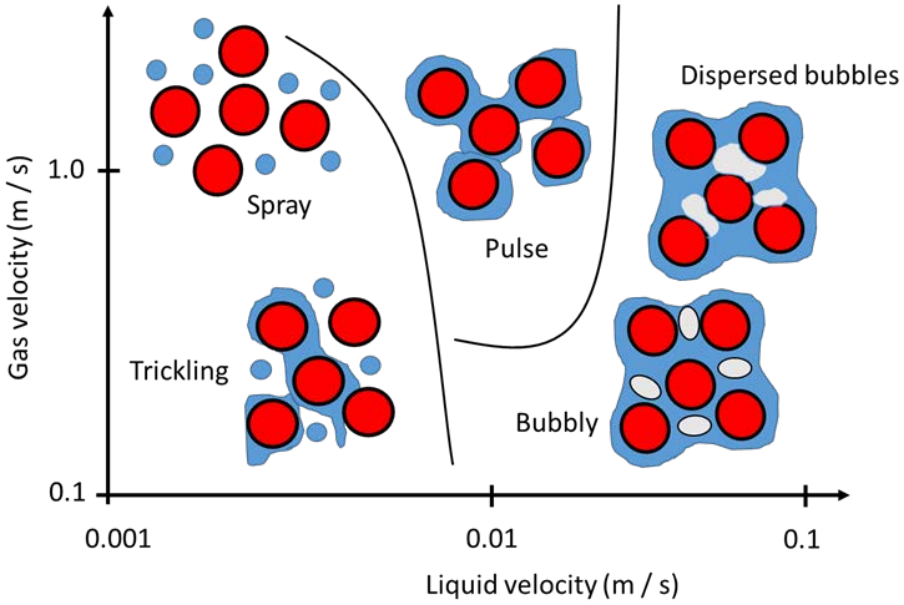

Figure 2.11: Trickle bed reactor flow regime map showing the four flow regimes in concurrent operation [114]

Mass and heat transfer rates are characteristically lower in this regime, however low gas-liquid throughput, pressure drop and catalyst attrition, as well as its ability to process foaming liquid make this regime very advantageous.

As either the gas or liquid flow rate is increased trickle flow transitions to pulsing flow, another regime commonly encountered in the operation of commercial scale reactors. This regime is characterised by having higher rates of mass and heat transfer than trickle flow due to the formation of alternate gas and liquid entrenched zones [117]. Within these pockets of liquid the catalyst is completed wetted, utilising the whole catalyst surface and reducing the likelihood that thermal hotspots will form and preventing catalyst deactivation [13]. In addition, the effect of axial dispersion is lessened due to improved radial mixing and reduced liquid hold-up [118].

During trickle flow, if the liquid flow rate is kept low and the gas flow rate significantly increased to a high flow rate the spray flow regime is obtained [13]. Here the characteristic liquid films formed on the catalyst particles in

trickle flow are put under high shear and the liquid transitions from a semi-continuous film into dispersed droplets. The advantages of operating in this regime are high gas-liquid mass transfer, low liquid holdup and foam-ability, though due to high gas flow rates gas recycling is required. The transition boundary between spray and trickle is mainly dependent on particle size and surface tension. Moreover, it has proved somewhat challenging to experimentally identify and measure the boundary between these two regimes.

At low gas flow and increasingly high liquid flow rates, liquid begins to fill all of the pores within the packed bed and gas now bubbles through the packed bed as the dispersed phase [13]. The characteristic properties of this regime are akin to bubble columns; higher mass and heat transfer rates at the expense of a higher pressure drop and potential back mixing. This regime can benefit highly exothermic reactions or in cases where the availability of the liquid reactant is the limiting component.

2.4.1.1 Liquid holdup

The residence time the liquid resides in the reactor for is affected by the ratio between the liquid volume and the bed volume, otherwise known as the total liquid holdup, ε_L [119]. If liquid volume is being compared to the void volume as opposed to bed volume, liquid holdup is being expressed as the liquid saturation, β_L. The liquid holdup within a reactor can be divided into two fractions; the fraction that moves through the column while operating, known as the dynamic holdup, β_{dyn}, and the fraction of liquid retained near “dead zones” within the column, referred to as the static (or sometimes stagnant) holdup, β_{st} [120]. These two terms are associated with the holdup during operation and as such if the bed was simply filled with liquid another

subdivision can be made. The fraction of liquid remaining in the column that is free to drain out is known as the free-draining holdup, β_{fd}, and the volume of liquid retained in the bed due to capillary forces is the residual holdup, β_{res} [121]. There have been numerous attempts to derive correlations that accurately describe experimentally obtained liquid holdup results with some success, many of which have been already extensively reported and summarised [13, 122-124]. The simplest experimental technique to measure the dynamic and static liquid holdup is the volume draining method [119, 125, 126]. Once steady state has been reached the gas-liquid flow is shut off and the fraction of dynamic liquid holdup freely leaves the reactor and is measured. The remaining liquid fraction in the column is determined by passing heat through the column to evaporate and then condense the gas to determine the static holdup.

2.4.1.2 Wetting efficiency

As liquid passes through the packed bed it is not uncommon for the liquid to flow non-uniformly over the catalyst particles. Consequently, the extent to which a catalyst particle is wetted by the liquid phase can differ particle to particle – this is known as the wetting efficiency [13]. Particles within the bed can be completely, partially or incompletely wetted at any one time. Knowledge of the wetting efficiency is necessary in trickle bed reactors as is important in understanding local reaction kinetics, that are often averaged over the bed to determine reactor performance [127]. In cases where the limiting reactant must travel through the liquid phase, the reaction rate is directly proportional to the fraction of wetting [13]. As the catalyst particles have an associated external and internal surface volume the wetting efficiency of these two surfaces is affected by different micro- and macro-scale

parameters, thus both internal and external wetting efficiencies are independently defined. Liquid distribution has a significant effect on the wetting efficiency, with macro-scale maldistributions being a consequence of particle shape, particle size, superficial liquid velocity, packing but predominantly distributor design. Maiti and Nigam co-authored an excellent in-depth review paper of the various gas-liquid distributors used in commercial and laboratory scale reactors and hence distributor design will not be discussed here [128]. At the particle level, liquid maldistribution has been found to be effected by surface wettability, particle packing, superficial liquid velocity, flow modulations and the start-up procedure [129, 130]. Houwelingen *et al.* investigated different start-up procedures whereby two pre-wetting methods were used to assess the effect on the average wetting efficiency across the packed bed [131]. It was shown that initial pre-wetting of the catalyst by pulsing of the liquid through the bed (Kan pre-wetting) resulted in the whole of the catalyst being utilised. Whereas, when the bed was instead initially flooded and left to drain to ensure internal wetting (Levec pre-wetting), it was observed that the bed was not always fully utilised. Broadly speaking experimental measurement methods can be divided into those that directly measure and those which indirectly measure wetting efficiency. Direct methods commonly involve analysis of cross-sectional images acquired using techniques such as Magnetic resonance imaging (MRI) [132], computed tomography [133] and dye adsorption [129]. However, these techniques are generally expensive or difficult to apply on an industrial scale. Indirect studies are more cost effective and easily implemented on commercial scale and primarily involves using either radioactive tracers [134] or inferences from reaction rate data [135].

2.4.1.3 Axial dispersion

Deviation from ideal (plug-) flow is caused by a number of factors such as non-uniform bed porosity, wall effects, capillary forces, stagnant or dead zones and flow channelling [13]. The consequence of axial dispersion is back-mixing; whereby the retention of the reactant in the reactor increases its effluent concentration and decreases overall conversion [136]. Residence time distribution (RTD) experiments are one of the more successful methods used to identify deviation from ideal flow but for interpretation of the data an axial dispersion model is required (many of which use the dispersion coefficient D_L that accounts for all flow non-idealities), but these fail to completely account for the tailing seen in the RTD curve [120]. Axial dispersion can be minimized by manipulating the bed length to particle diameter ratio (z_B / d_p). Medoras *et al.* (2009) present a concise summary of all the proposed ratios in the literature, with the general consensus being that the ratio needs to greater than 20 [18]. Radial axial dispersion in trickle bed reactors has been researched significantly less but has been identified to be dependent on the reactor diameter to particle diameter ratio (d_R/d_{pe}) [18]. It is minimized by suitable distributor design (multi-point for commercial reactors, single point for laboratory scale) and use of inert fines in laboratory reactors.

2.4.2 Mass transfer in trickle bed reactors

This section will attempt to outline and evaluate methods used for determining the mass transfer coefficients in the literature for trickle bed reactors operating in the trickling flow regime to give an overview of the typical values found in the literature.

2.4.2.1 Gas-liquid mass transfer coefficient

As hydrogen must diffuse through the liquid film, the gas-liquid mass transfer coefficient, k_La is a particular important parameter in trickle beds. Surveying the literature, k_La is significantly affected by the liquid phase velocity and catalyst particle size. With smaller sized catalysts and higher liquid flow rates producing higher valves of k_La. Gas velocity tends to have less of an impact on k_La values in laboratory scale trickle beds, however for micro-packed beds gas flow has a greater effect, likely due to the enhancement of gas-liquid interfacial area. The resistance to mass transfer within the gas film itself is often thought of as negligible compared to that of the liquid and as such investigations in the literature have focused on mass transfer in the liquid film [137]. All the methods evaluated and the associated k_La values determined are shown in Table 2.3.

Generally, experimental methodologies can be split into two approaches; physical adsorption and chemical adsorption [138]. For physical absorption studies, the direct measurement of the dissolution of gases into the liquid phase has been used as a standard since Goto first reported the adsorption/desorption of oxygen into water to calculate k_La [139]. Physical adsorption methods give the advantage of determining k_La under processing conditions, however, most gases have poor solubility in the liquid phase owing to limited resolution [140]. Evran and Özdural further proposed a physical adsorption method for carbon dioxide into water whereby the mass transfer coefficient is calculated by fitting k_La to the experimental data [141]. The difference in k_La results between the two physical methods may stem from the fact carbon dioxide has a relatively higher solubility in water compared to oxygen.

Table 2.3: Examples of the physical adsorption, chemical absorption and reaction methods for determination of k_La in the literature

Physical adsorption methods					
Oxygen adsorption into water – Goto and Smith [139]					
$k_La = \frac{U_L}{z_B} ln\left[\frac{(C_{L,O_2})_e}{(C_{L,O_2})_{e'}}\right]$	CuO . ZnO Raschig rings d_p = 0.54 & 2.91 mm	Z_B = 0.15 m d_R = 0.025 m ε_B = 0.39 & 0.41	25°C 1 bar	Liquid velocity; 0.5 - 5x10^{-3} m s^{-1} Gas velocity: 0 - 8.4x10^{-3} m s^{-1}	2 – 10x10^{-3} s^{-1} k_La increased with increasing liquid flow rate & smaller CuO . ZnO particle size
Z_B = bed height, U_L = liquid velocity, $(C_{L,O_2})_e$ = exit oxygen concentration packed bed and $(C_{L,O_2})_{e'}$= exit oxygen concentration with empty bed					
Hydrogen adsorption into liquid cumene - Turek and Lange **[142]**					
$k_La = \frac{U_L}{z_B} ln\left[\frac{(C^{eq}_{L,H_2} - C^0_{L,H_2})}{(C^{eq}_{L,H_2} - C_{L,H_2})}\right]$	Crushed Pd/Al_2O_3 d_p = 5.7, 9.0 & 30 um	Z_B = 0.72 m d_R = 0.034 m	30°C 1.5 - 4 bar	Liquid velocity; 0.5 – 4.6x10^{-4} m s^{-1} Gas velocity: 2 - 20x10^{-3} m s^{-1}	0.05 – 0.2x10^{-3} s^{-1} k_La increased with increasing liquid flow rate & smaller Pd/Al_2O_3 particle size
Z_B = bed height, U_L = liquid velocity, C^{eq}_{L,H_2}= *equilibrium concentration of hydrogen and* C^0_{L,H_2} *= hydrogen concentration at y = 0 (top of the packed bed)*					
CO_2 adsorption into water - Evren *et al.* **[141]**					
-	Glass Raschig rings d_p = 8 mm	Z_B = 0.335 m d_R = 0.034 m ε_B = 0.27	21°C 1 bar	Liquid velocity; 5.8– 9.1x10^{-3} m s^{-1} Gas velocity: 0.183 m s^{-1}	0.0165 - 0.018 s^{-1} k_La increased with increasing liquid flow rate & & smaller Raschig sizes
Chemical adsorption methods					
CO_2 into methyl diethanolamine/water solution - Zhang *et al.* **[140]**					
$N_{CO_2} = k_La(k_HPx_{CO_2})$	Glass beads d_p = 75 & 250 um	Z_B = 0.1 m d_R = 3.05 & 4.57 mm ε_B = 0.37	20°C 1 bar	Liquid velocity; 0.9 – 7.3x10^{-3} m s^{-1} Gas velocity: 0.03 – 0.12 m s^{-1}	0.24 - 0.58 s^{-1} k_La Increased with increasing liquid and gas flow rates. Smaller sized glass beads gave higher k_La
N_{CO_2} = mass transfer flux of CO_2, k_H = Henry's constant, P = pressure, x_{CO_2}= CO_2 mole fraction,					
CO_2 into bicarbonate/water solutions - Blok *et al.* **[143]**					
$\frac{1}{k_La} = \frac{1}{R_a} - \frac{1}{k_{obs}\beta} + C$	Glass Raschig rings d_p = 2.5 & 4 mm	Z_B = 1 m d_R = 0.05 & 0.1 m	25°C 1 bar	Liquid velocity; 0.009 – 0.02 m s^{-1} Gas velocity: 0.44 - 1.8 m s^{-1}	0.4 -4 s^{-1} k_La Increased with increasing liquid and gas flow rates. Smaller sized glass beads gave higher k_La
R_a = apparent value of k_La when no reaction occurs in the liquid film, pseudo first order rate constant, β = liquid holdup, C = correction term for background CO_2 present in the film.					

CO_2 into diethanolamine/ethylene glycol - Larachi *et al.* **[144]**

	Polypropylene pellets d_p = 3.1 mm	Z_B = 0.4 m d_R = 23 mm ε_B = 0.32-0.39	25°C 3-30 bar	Liquid velocity; 1.7 – 7.7x10^{-3} m s^{-1} Gas velocity: 0.005 - 0.05 m s^{-1}	0.015 - 0.07 s^{-1} k_La Increased with increasing liquid and gas flow rates. Smaller sized glass beads gave higher k_La. Increasing pressure thought to vary k_La through the change in interfacial area

Reaction methods

Hydrogenation of α-methylstyrene **-** Turek and Lange **[142]**

$$\frac{dX_{AMS}}{d\tau} = \frac{(1 - X_{AMS}) \cdot k' K_A C^*_{L,H_2}}{\left[1 + K_A C_{AMS}(1 + \frac{k'}{k_{g-R}a})\right]}$$

Crushed Pd/Al_2O_3 d_p = 0.36 - 3 mm	Z_B = 0.72 m d_R = 0.034 m	15-50°C 1 - 15 bar	Liquid velocity; 0.5 – 3.1x10^{-4} m s^{-1} Gas velocity: 0 – 0.03 m s^{-1}	0.01 - 0.2 s^{-1} $k_{g-R}a$ increased with increasing liquid flow rate & smaller Pd/Al_2O_3 particle size. $k_{g-R}a$ determined from reaction two orders of magnitude larger than k_La from adsorption method

X_{AMS}= conversion of α-methylstyrene, τ = m^3 liquid / g catalyst per minute, k'= intrinsic rate constant 1/s, k_{g-R} = overall mass transfer coefficient from gas to catalyst particle through the liquid film, K_A equilibrium adsorption constant, C^*_{L,H_2}= equilibrium concentration of hydrogen.

Hydrogenation of cyclohexene - Losey *et al.* **[145]**

$$R = \frac{C_{H_2,L}}{\frac{1}{k_La} + \frac{1}{\eta k}}$$

Pd/Al_2O_3 powder d_p = 53 - 75 um	Z_B = 0.2 mm d_R = 625 um	25°C 1 – 1.7 bar	Liquid velocity; 0.001 – 0.01 m s^{-1} Gas velocity: 0.001 – 0.02 m s^{-1}	5 - 15 s^{-1} k_La enhanced through high gas-liquid interfacial area

R = reaction rate, $C_{H_2,L}$ = saturated solubility of hydrogen, k_La overall mass transfer coefficient, η effectiveness factor, k the intrinsic rate constant.

Hydrogenation of Styrene **-** Stamatiou and Muller [108]

$$\Omega^{Tot}_{H_2} = \frac{1}{k_La} + \frac{V_L}{W_{Pd}}\left(\frac{1}{k_sa_s} + \frac{1}{\eta k_{obs}}\right)$$

Glass beads & Pd/C pellets d_p = 3.0 & 1.3 mm	Z_B = 0.32 m d_R = 0.025 m	32°C 3 bar	Liquid velocity; 1.64x10^{-}m s^{-1} Gas velocity: 0.002 m s^{-1}	0.06 s^{-1}

$\Omega^{Tot}_{H_2}$ = overall mass transfer resistance, V_L = liquid volume, W_{Pd} = quantity of palladium in the bed , k_ga_s = liquid solid mass transfer coefficient, η = effectiveness factor, k_{obs} = first order observed rate constant

In chemical adsorption methods, gas adsorption is measured from the amount of gas reacting with a dissolved species within the liquid phase whereby gas-liquid mass transfer is the rate limiting step. By changing the concentration of reacting species both k_La and the interfacial area, a, can be determined [140]. Blok *et al.* measured the adsorption of carbon dioxide into bicarbonate/carbonate buffer solutions and calculated k_La for a trickle bed reactor in pulse flow [143]. Several researchers (Zhang *et al.* and Larachi *et al.* 1998) have applied Danckwerts' penetration model to calculate k_La for chemical adsorption [140, 144, 146]. The k_La values again vary across the three different studies. The higher values found by Blok *et al.* (1984) are likely to be a result of operating the column in pulse flow and Zhang *et al*. (2017) used a micro packed column, both known to enhance mas transfer. Larachi *et al. (*1998) investigated higher pressures and found k_La increased with increasing reactor pressure and gas flow rate.

Losey *et al.* showed that by 'lumping' the mass transfer resistances together k_La can be estimated from the reaction rate, R [145]. Therefore, by knowing the rate of reaction, calculating the intrinsic rate constant and estimating the effectiveness factor, k_La can be determined for any processing conditions. When the gaseous reactants are very soluble in the liquid phase, it has been hypothesised that in fact mass transfer resistance within the liquid film is negligible, and mass transfer in the gas film (k_Ga) plays a significant role [137]. Iliutia *et al.* reported on the distinct lack of literature data for k_Ga values and used both physical and chemical adsorption methods to calculate gas-side mass transfer for carbon dioxide in water and a sodium hydroxide solution respectively. The conclusions from the work were that the resistance

to mass transfer on the gas-side was indeed negligible under the atmospheric conditions investigated.

2.4.2.2 Liquid-solid mass transfer coefficient

Though not exhaustive, Table 2.4 presents $k_S a_s$ values reported in the literature. In all instances solid-liquid transfer was enhanced by increasing the liquid velocity. The effect of gas velocity varies in the literature however, with an increase in $k_a s_a$ at higher gas flow rates observed by many researchers. This is thought to be due to increased turbulence and the reduction in liquid cross-sectional area for flow [147]. For micro-packed beds gas flow rate has been found to have no significant effect on solid-liquid transfer, likely due to its limited effect on the gas-liquid interactions at this scale [148]. In general, smaller sized catalyst particles gave higher rates of solid-liquid mass transfer. The large majority of methods in the literature attempting to quantify liquid-solid mass transfer in trickle bed reactors use either dissolution or electrochemical techniques [149]. Nearly all the techniques discussed reported that $k_S a_s$ increased with liquid flow rate and operating pressure, but gas flow rate had little effect.

Dissolution is used to determine the average volumetric liquid-solid coefficient ($k_S a_S$) by measuring the limit of liquid saturation across a defined section of the packed bed [147]. Sparingly soluble particulate material is preferred (benzoic acid, naphthalene and β-napthal have been employed) to prevent changes in bed characteristics during the experiment and it is imperative that the liquid exiting the column does not become saturated [150]. Al-Dahhan *et al.* reported when attempting measurements at high pressures noticeable losses in dissolved material are observed (caused by flashing or stripping into the gas phase during sampling).

Table 2.4: A selection of values and expressions for determining the liquid-solid mass transfer coefficient for trickle beds within the literature.

Dissolution methods					
Naphthol dissolution in water - Goto and Smith [139]					
$k_s a_s = \frac{U_L}{z_B} ln\left[\frac{\left(C^L_{A,\ sat} - C^L_{A,\ in}\right)}{\left(C^L_{A,\ sat} - C^L_{A,\ out}\right)}\right]$	β-naphthol spheres d_p = 0.54 & 2.41 mm	Z_B = 0.15 m d_R =0.0198 & 0.026 m ε_B = 0.39 & 0.41	22°C 1 bar	Liquid velocity; 0.5 - 5x10^{-3} m s^{-1} Gas velocity: 0 - 8.4x10^{-3} m s^{-1}	0.005 – 0.02 s^{-1} $k_s a_s$ not affected by gas flow rate. $K_s a_s$ increased with higher liquid velocity and longer bed lengths
Z_B = bed height, U_L = liquid velocity, $C^L_{A,\ sat}$ = saturation concentration, $C^L_{A,\ in/out}$ = inlet or outlet concentration					
Copper dissolution in dichromate solution - Cao *et al*. **[151]**					
$k_s a_s = \frac{U_L}{z_B} ln\left[\frac{C_L}{C_0}\right]$	Copper spheres d_p = 53−63 µm	Z_B = 0.022 d_R = 0.6 mm ε_B = 0.33 & 0.36	25°C 1 bar	Liquid velocity; 0.01 – 0.12 m s^{-1} Gas velocity: 0 - 4 m s^{-1}	15 - 45 s^{-1} $k_s a_s$ decreased with increasing gas velocity, attributed to changes in flow regime. $k_s a_s$ increased significantly with higher liquid velocity
Z_B = bed height, U_L = liquid velocity, C_0 = concentration of dichromate anions entering packed bed, C_L = concentration of dichromate anions leaving packed bed					
Benzoic acid dissolution in water – Specchia *et al*. **[152]**					
$k_s a_s = \frac{U_L}{z_B} ln\left[\frac{C_i}{C_i - C_0}\right]$	Benzoic acid cylinders d_p = 3 & 6 mm	Z_B = 0.9 & 0.15 m d_R = 0.038 & 0.08 m	20°C 1 bar	Liquid velocity; 1.6 – 8.3x10^{-3} m s^{-1} Gas velocity: 0.06 – 1.56 m s^{-1}	0.04 – 0.6 s^{-1} $k_s a_s$ increased significantly with increasing gas velocity before slowly beginning to plateau at higher gas flow rates. $k_s a_s$ increased with higher liquid velocity
Z_B = bed height, U_L = liquid velocity, C_o = benzoic acid concentration in liquid outlet, C_i = benzoic acid concentration at the solid-liquid interface					
Electrochemical methods					
Aqueous solution containing iron ions - Highfill *et al.* [147]					
$I_{lim} = nCFA_e f k_s a_s$	Nickel pellet d_p = 3.38 m	Z_B = 0.05 m d_R = 0.02 m	25°C 3.1 – 35.5 bar	Liquid velocity; 0.3 – 3.5x10^{-3} m s^{-1} Gas velocity: 1.1 – 8.0x10^{-2} m s^{-1}	0.04 – 0.2 s^{-1} $k_s a_s$ increased with gas and liquid superficial flow rates.
I_{lim} = limiting current, n = number of electrons involved, C = electrolyte concentration, F = Faraday constant, A_e = area of the electrode, f = wetting efficiency					

Aqueous solution containing iron ions - Joubert and Nicol **[153]**

$I_{lim} = nCFA_e f k_s a_s$	Nickel coated beads d_p = 4.4 m	Z_B = 1 m d_R = 0.012, 0.026 & 0.044 m ε_B = 0.42, 0.4 & 0.36	25°C 1 bar	Liquid velocity; 1 – 5x10^{-3} m s^{-1} Gas velocity: 2x10^{-2} m s^{-1}	0.07 – 0.2 s^{-1} $k_s a_s$ increased with liquid superficial flow rates. Pre-wetting strategies also gave rise to significantly different $k_s a_s$ values.

I_{lim} = limiting current, n = number of electrons involved, C = electrolyte concentration, F = Faraday constant, A_e = area of the electrode, f = wetting efficiency

Adsorption methods

Benzaldehyde adsorption on activated carbon - Tan and Smith **[154]**

$(C_L)_{t=\tau} = C_f exp\left(-\frac{k_s a_s}{U_L} z_B\right)$	Activated carbon d_p = 1.34, 2.4 & 4.1 mm	Z_B = 0.02 – 0.033 m d_R = 0.016 & 0.056 m ε_B = 0.38	25°C 1 bar	Liquid velocity; 0.6 – 7.9x10^{-3} m s^{-1} Gas velocity: 1.47 – 8.0x10^{-2} m s^{-1}	0.02 – 0.8 s^{-1} $k_s a_s$ increased with liquid flow but no change with respect to the gas flow rate was observed. Small particles sizes gave increased mass transfer rates

Z_B = bed height, U_L = liquid velocity, C_f = benzaldehyde concentration at exit of bed, C_L = benzaldehyde concentration in the liquid phase

Operando spectroscopic methods

1-Octene hydrogenation - Zheng *et al.* [148]

$k_S a_S = \frac{X F_L}{C_0 - C_S}$	Pd/Al_2O_3 pellets d_p = 3.7 mm	Z_B = 0.03 m d_R = 0.025 m	21°C 1 bar	Liquid velocity; 0.36 – 6.8x10^{-4} m s^{-1} Gas velocity: 1 – 9.7x10^{-3} m s^{-1}	0.005 – 0.02 s^{-1} $k_s a_s$ increased with liquid flow rate. The effect of gas velocity was not studied.

F_L =molar flow rate of the reacting species in the liquid phase, X = conversion C_0 and C_S = concentration in the liquid and at the catalyst surface respectively

Reaction methods

Hydrogenation of cyclohexene to cyclohexane – Hersicowitz and Abuelhaija **[155]**

$k_S a_S = \frac{r}{C_H - k\eta C_{HS}^{0.5}}$	Pd/Al_2O_3 spheres d_p = 1.7 mm	Z_B = 0.03 m d_R = 0.025 m	30°C 1 bar	Liquid velocity; 1 – 4x10^{-2} m s^{-1} Gas velocity: 0 – 10.4x10^{-3} m s^{-1}	0.07 – 3.1 s^{-1} $k_s a_s$ enhanced with increasing gas and liquid phase velocities. Significant change in $k_s a_s$ observed with transition to high interaction regime.

r = global rate of reaction, C_H = hydrogen equilibrium concentration in the liquid, intrinsic rate constant, η effectiveness factor, C_{HS} = liquid hydrogen concentration at the surface of the particle

Hydrogenation of Styrene **-** Stamatiou and Muller [108]

$\Omega_{H_2}^{Tot} = \frac{1}{k_L a} + \frac{V_L}{W_{Pd}}\left(\frac{1}{k_s a_s} + \frac{1}{\eta k_{obs}}\right)$	Glass beads & Pd/C pellets d_p = 3.0 & 1.3 mm	Z_B = 0.32 m d_R = 0.025 m	32°C 3 bar	Liquid velocity; 1.64x10^{-}m s^{-1} Gas velocity: 0.002 m s^{-1}	0.004 – 0.02 s^{-1} $k_s a_s$ increased as the number of catalystic active pellets in the bed increased

$\Omega_{H_2}^{Tot}$ = overall transfer resistance, V_L = liquid volume, W_{Pd} = quantity of palladium, $k_a a_s$ = liquid-solid transfer coefficient, η = effectiveness factor, k_{obs} = first order observed rate constant

The electrochemical method, also known as the limiting current technique, involves local measurements using microelectrodes to find the $k_S a_S$ of a single particle using an electrolyte solution. Most studies within the literature follow the method used by Sims *et al.* (1993) to investigate mass transfer at the surface of the electrodes [156]. If the voltage applied is such that the rate limiting step in the reaction is the diffusion of the electrolyte solution between electrodes, the surface concentration of the electrolyte can be thought of as zero and $k_S a_S$ can be found.

Other methods of estimating $k_S a_S$ have also been proposed. Tan and Smith (1982) formulated a dynamic method using the adsorption of benzylaldehyde onto porous activated carbon particles at atmospheric pressure [154]. In other instances, magnetic resonance imaging has found to be non-invasive and provide chemically resolved information to estimate $k_S a_S$ *[148]*. Initial studies by Koptyug *et al.* (2004) employed proton MRI to monitor hydrogenation of α-methylstyrene, however, given its narrow chemical-shift range proton MRI can struggle to chemically discriminate between two species in the trickle bed [157]. Sederman *et al.* (2005) proposed the use of carbon-13 (C-13) MRI as a possible alternative to proton MRI and successfully showed it could be employed to monitor the hydrogenation of 1-octene [158]. The same researchers then combined C-13 MRI with the multivariate partial least square regression (PLSR) to determine $k_S a_S$ [148]. Using this method $k_S a_S$ was successfully calculated, however, due to intrinsic mass transfer limitations within the pores, this method likely underestimates concentration of reacting species at the surface.

Chapter 3
Materials, Methods and Catalyst characterisation

The first section of this chapter documents all the materials and the general chemical analysis methods used throughout the project. The specific experimental methodologies will not be presented here, but rather be discussed in the appropriate chapters of work. Moreover, as each experimental results chapter has used a specific and often novel reactor design, reactor experimental set up and methodologies shall also be held in the appropriate chapters. The second portion of the chapter includes relevant characterisation of the catalytic and non-catalytic materials used in both continuous and batch hydrogenations. Though all catalyst materials have been commercially purchased and not synthesised in house, a significant amount of catalyst characterisation is presented. Many of the characterisation techniques have been specifically employed to provide justification for assumptions and/or decisions made in the following chapters and thus, the detailed analysis has been included to support that justification.

3.1 Materials

All reagents and catalysts were used as received without further purification.

3.1.1 Catalysts

All the catalyst materials used throughout the project were purchased from Johnson Matthey. For investigating the interplay between mass transfer and kinetics in continuous flow, 1% palladium on activated carbon (Pd/C) pellets Type 783 (moisture content 0.5%, assay 0.97%) were chosen. In addition, a 5% Pd/C paste Type 87L (moisture content 58.1%, assay 4.99%) was also purchased for comparison to obtain the intrinsic kinetics.

3.1.2 Hydrogenation of styrene

Styrene 99%, methanol 99.9% and n-decane 99% were all purchased from Sigma-Aldrich and used as the substrate, solvent and internal standard respectively for gas chromatography (FID) analysis of the collected samples. Pure compressed hydrogen (UN: 1049) was purchased from BOC. Ethylbenzene 99% was also purchased from Sigma-Aldrich for the gas chromatography calibrations.

3.1.3 Inductively coupled plasma mass spectroscopy reagents

Nitric acid (68 V/V%) and hydrochloric acid (20 V/V%) were purchased from Fisher Chemical to prepare the aqua regia solution. A palladium standard for AAS (1000 mg/L) was purchased from Sigma-Aldrich and used for the calibration standards. Ultra-pure milliQ water was used for all dilutions.

3.1.4 Ancillary packed bed materials

To dilute the catalyst of interest in the packed bed, non-active (palladium free) activated carbon pellets Type 783 were purchased from Johnson Matthey and Ballotini solid soda glass beads (diameter 2.85-3.30 mm) were purchased from Sigmund Lindner GMBH.

3.1.6 Liquid phase physical properties

Methanol was used exclusively throughout this project as the solvent in all of the hydrogenation reactions and the liquid film experiments. Moreover, many of its physical properties were needed for modelling the various transport phenomena and liquid film thickness. A summary of all the physical properties of methanol used in this work are presented in Table 3.1.

Table 3.1: Values of the physical properties of methanol.

Physical property		Value
Density	$\rho, kg/m^3$	790
Dynamic Viscosity at 21 ℃	$\mu, kg/m \cdot s$	$4.88 \cdot 10^{-4}$
Diffusion coefficient of hydrogen in methanol	$\mathbb{D}_{H_2}, m^2/s$	$1.017 \cdot 10^{-8}$
Surface tension at 32 ℃	$\sigma, N/m$	0.0215

3.2 Gas chromatography

Gas-liquid chromatography was used as the main analysis method for quantifying the substrate conversion and is a well-established technique in the separation and quantification of mixtures of volatile compounds [159].

3.2.2 Method and calibration for styrene reduction

The column used to separate and quantify styrene and ethylbenzene was a DB-624: Temp range: -20-260 °C; Length: 30 m; Diameter: 0.25 m; Film thickness: 1.40 µm. The oven temperature ramp is shown in Table 3.2.

The amounts of styrene and ethylbenzene were quantified using the internal standard method, whereby a known quantity of a compound is added. The standard used here, n-decane, was chosen as it did not react with the any of the other reagents or appear to adsorb onto the surface of the catalysts.

Table 3.2: Gas chromatograph temperature ramps for the separation of styrene and ethylbenzene.

Ramp No.	Rate (°C / min)	Final temperature (°C)	Final time (min)
1	1	90	
2	0.1	91	
3	50	200	29.18

The volume of sample injected is very low (≈1 µL) and thus by having the standard in the mixture the volume error associated with each injection is minimised. To calculate a unknown amount of the desired analyte the response factor, R_f, was determined for both styrene and ethylbenzene by plotting the ratio between the peak areas and number of moles of the analyte and internal standard;

$$\frac{Area_{analyte}}{Area_{n-dec}} = R_f \cdot \frac{Mols_{analyte}}{Mols_{n-dec}} \quad \textbf{(3.1)}$$

The calibration curves and response factors for styrene and ethylbenzene are shown in Figure 3.1 between 0-0.2 mol / L. The styrene conversion could then be calculated from the response factor and the known amount of n-decane.

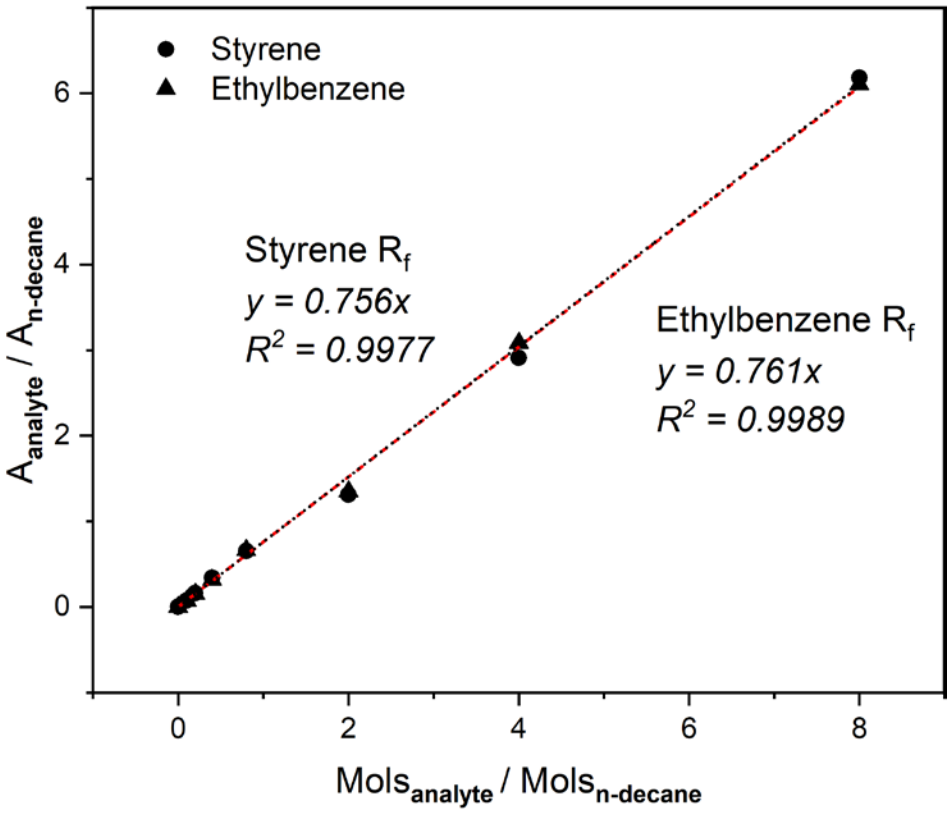

Figure 3.1: Styrene and ethylbenzene calibration curves using the internal standard method and their respective response factors

3.3 Catalyst characterisation

The majority of the work presented throughout this thesis focuses on the 1% Pd/C pellets (shown in Figure 3.2) and thus, the focus will be on the characterisation of this catalytic material. Many of the assumptions and justifications discussed throughout the thesis in relation to the mass transfer and chemical reaction phenomena are based on the physical properties of the catalyst. Therefore, it was deemed necessary to understand such facets as palladium loading distribution, nanoparticle size distribution and location of the nanoparticles on the carbon pellets for example, before pertinent analysis of system could be undertaken.

3.3.1 Experimental procedures

The following section outlines all the experimental methodologies used to characterise the materials of interest.

3.3.1.1 Inductively coupled plasma – mass spectroscopy

ICP-MS was used to determine the Pd content of all catalyst materials. To circumvent issues with digestion of the carbon, the support was first crushed into a fine powder and fully oxidised by thermal degradation [160].

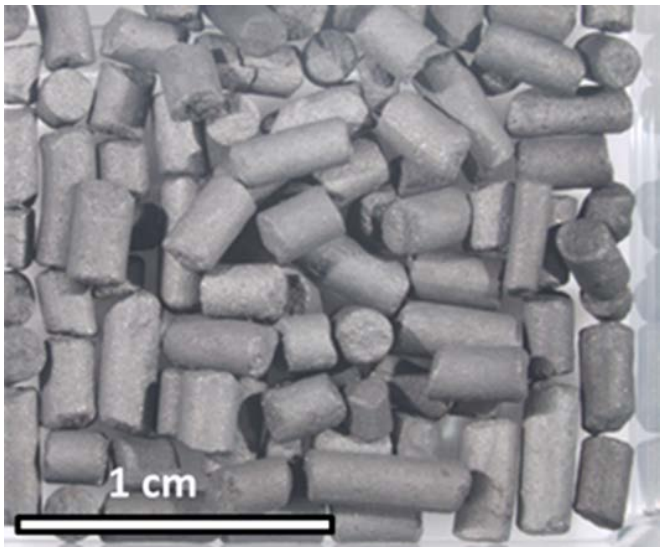

Figure 3.2: Tray containing the 1% Pd/C pellets used throughout the work.

The remaining residual powder was digested in aqua regia overnight under normal temperature and pressure conditions (21 ^{o}C and 1 bara). Ultrapure water (18 mΩ) was added to make up a diluted aqua regia solution (2.5 % v/v) which was subsequently run on a Perkin Elmer SCIEX - ELAN DRC-e, Axial Field Technology ICP-MS. A series of palladium calibration solutions were made (between 0.1-10 mg L^{-1}) with aqua regia in water (2.5 % v/v), yielding a linear plot with an R^2 coefficient of 0.9999 (Figure 3.3).

3.3.1.2 Transition electron microscopy

Transmission electron microscopy (TEM) was used to determine the size of the palladium nanoparticles on the catalyst. To obtain palladium nanoparticles present on the surface of the pellet, the outer layers of carbon on the 1% Pd/C pellets were removed using a scalpel and dispersed in isopropanol (~10 mL) using an ultrasonic bath.

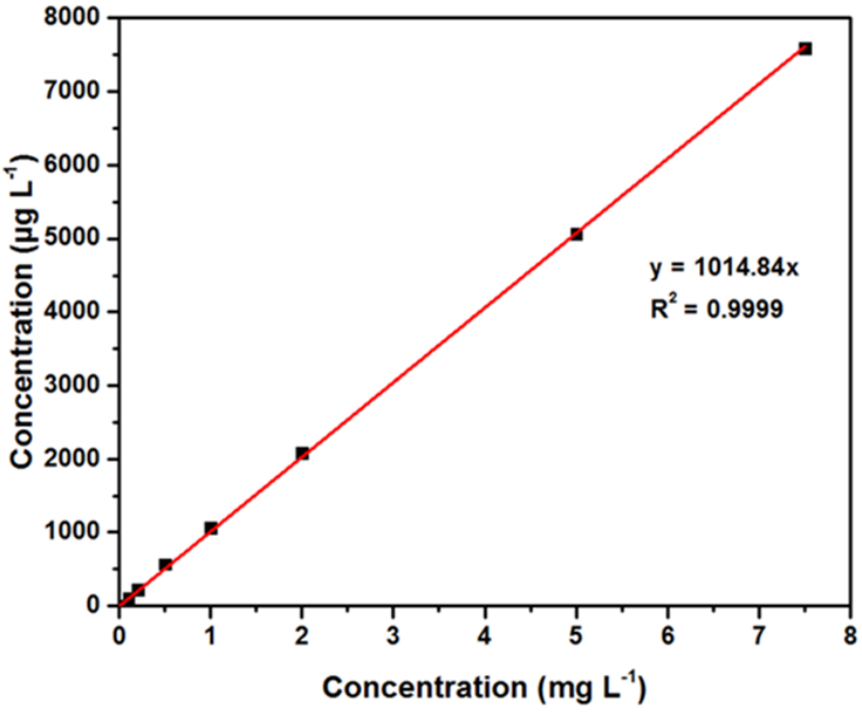

Figure 3.3: ICP-MS calibration curve used to determine the palladium loading in the 1% Pd/C pellets and 5% Pd/C powder.

After 10 minutes, approximately 1 mL of the dispersed carbon suspension was diluted again in isopropanol (~10 mL) and placed in the ultrasonic bath for 10 minutes. This solution was spotted onto a lacey carbon coated copper TEM grid mounted on filter paper until the paper became discoloured and was then left to dry. The 5% Pd/C powder was prepared in a similar manner except, rather than using a scalpel, 1 mg of the powder was dispersed in isopropanol before spotting. A 200 kV FEI Tecnai F20 FEGTEM was used to image the dispersed nanoparticles for subsequent particle sizing using the Gatan microscopy suite software.

3.3.1.3 Scanning electron microscopy/Energy dispersive using X-ray analysis

Scanning electron microscopy (SEM), coupled with energy dispersive X-ray analysis (EDX) was utilised to determine the location of the palladium within the 1% Pd/C pellets. For external surface analysis the 1% Pd/C and non-active carbon pellet were analysed without any sample preparation. To examine a pellets' interior, a pellet was cut in half to obtain two new pellets of roughly equal length using a scalpel. Pellets were cut as such that the a cross-section of the interior surface could be analysed. The broken catalyst pellet was glued onto a SEM stub, making sure that the internal cross section was visible, and analysed using a Hitachi SU8230 Scanning electron microscope 15.0 kV beam to locate the palladium. A series of 1D linescan measurements were made to obtain palladium distributions as a function of beam displacement into the pellet from the surface. In the case of the 5% Pd/C powder catalyst, 1 mg of powder was placed on a SEM grid and analysed.

3.3.1.4 Image analysis (Pellet size distribution)

A sample of the 1% Pd/C and non-active carbon pellets were spread out evenly within three large glass petri dishes. Using a camera, a picture was acquired of each set of petri dishes and the particle size distribution (PSD) via post-processing the images obtained using the ImageJ software. To minimise errors as much as possible, care was taken to ensure the pellets were not touching, as this caused the software to detect a single large particle rather than two or three smaller touching particles. Over 600 individual pellets were analysed from each sample (634 1% Pd/C and 741 non-active pellets) and this was considered to be a large enough to represent the whole batch.

3.3.2 Catalyst external and internal structure

The external and internal pore structure can greatly influence the mass transfer of reactant species to the catalysts' active sites and hence the observed reaction rate in heterogeneous catalysis. To probe the catalyst surface and internal structure of the 1% Pd/C pellets and 5% Pd/C paste scanning electron microscopy was used.

3.3.2.1 1% Pd/C pellets

SEM images showing the external and internal structure of the 1% Pd/C pellets are shown in Figure 3.4. An extensive macro-porous structure exists, resulting from what resemble large aggregates of carbon. This observation is commensurate with what is known of the manufacturing method, whereby the activated carbon powder is combined with a binder and fused together before being extruded, giving rise to a macro-porous structure within the pellet [161]. On further inspection of these aggregates it can be seen that they themselves consist of a meso-scale pore structure.

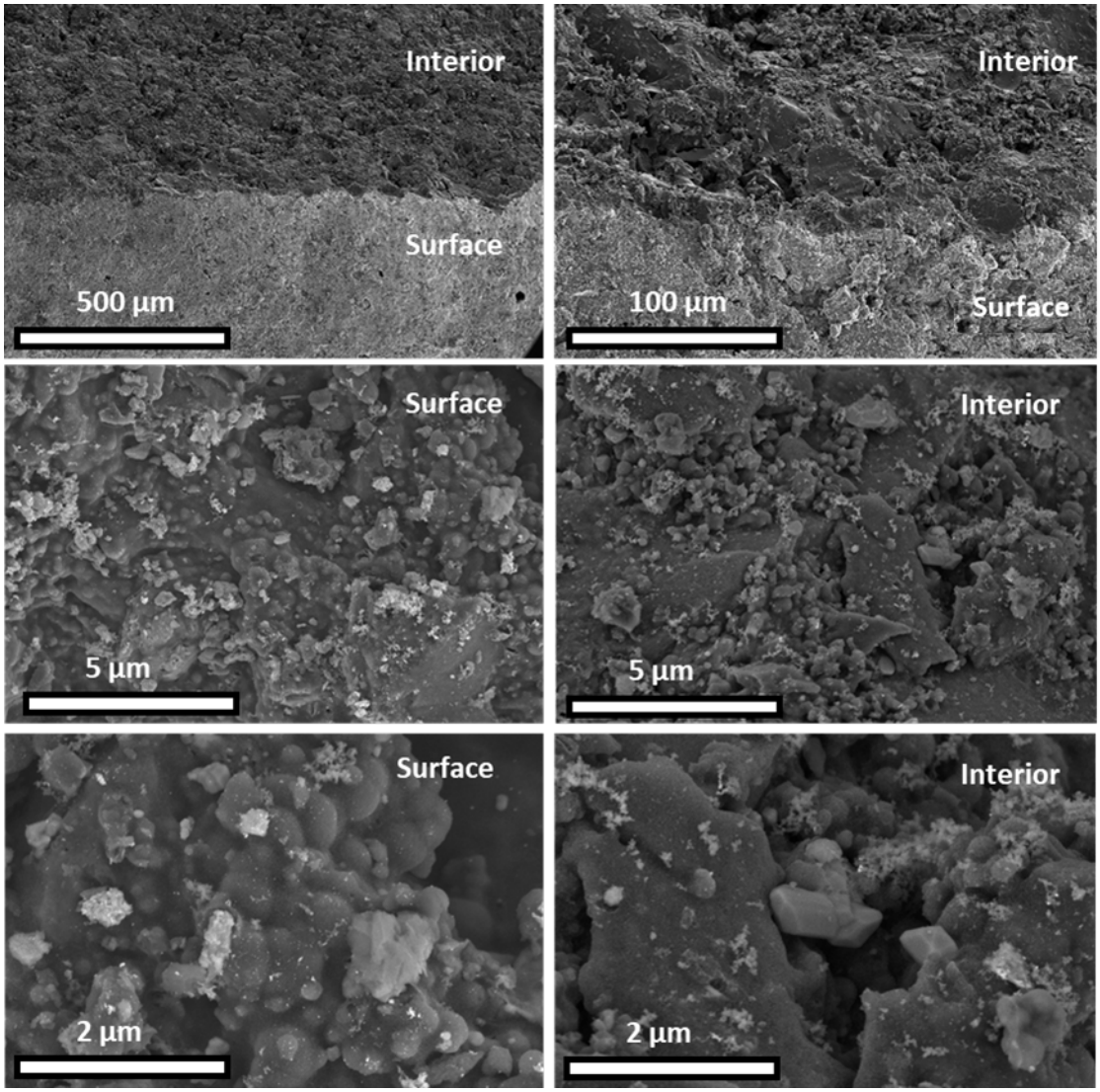

Figure 3.4: Scanning electron microscopy images external and internal structure of the 1% Pd/C pellets.

At an increased magnification (2 µm) another pore network is revealed, showing that micro-pores are present within the internal structure. Evidence of what seems to be some crystalline compounds in the interior images is likely to be a result of residue levels of alumina-silicate used in the manufacture process.

3.3.2.2 5% Pd/C paste

An SEM image of the 5% Pd/C paste is shown in Figure 3.5 and highlights the marked different between the structure of the two catalysts.

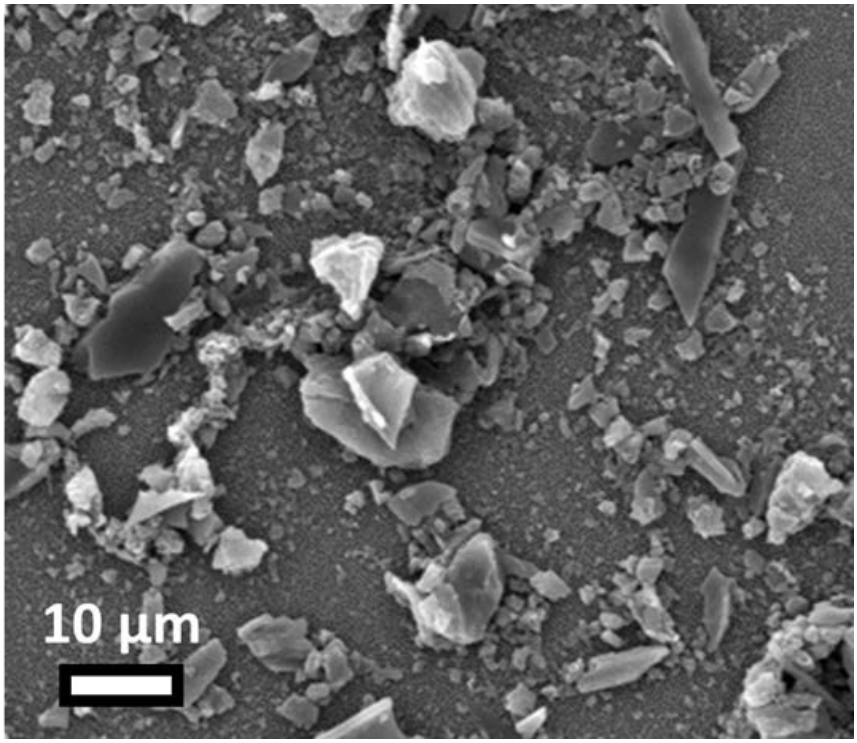

Figure 3.5: SEM image of the 5% palladium on carbon paste

The paste was found to comprise of flat carbon plates and considering the SEM image, appears to have a broad size distribution with the largest particles being roughly 10 µm in diameter and the smallest submicron. Due to the size and shape of the carbon particles it is unlikely that pore resistance would be limiting the reaction, though it could still be occurring.

3.3.3 Palladium percentage loading

Twenty-six Pd/C pellets were analysed by ICP-MS and the palladium percentage loading distribution is shown in Figure 3.6. The average palladium loading and standard deviation for the 1% Pd/C pellets and 5% Pd/C paste are summarised in Table 3.3.

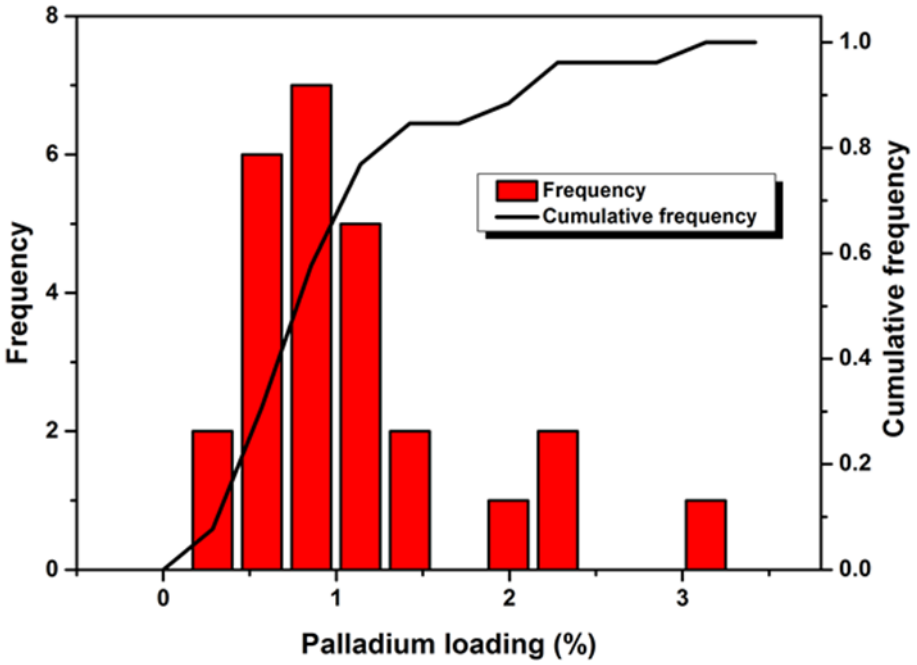

Figure 3.6: Palladium percentage loading distribution and cumulative frequency of the 1% Pd / C pellets analysed by ICP-MS.

Table 3.3: ICP-MS results for palladium loading on the 1% and 5% Pd/C catalysts

Catalyst	Palladium loading (w/w)	Standard deviation
1% Pd/C pellets	0.94	0.64
5% Pd/C paste	4.51	0.78

The percentage loading for both catalysts was found to be slightly lower than the value stated by the supplier. This could be due to incomplete digestion or failure to fully oxidise the carbon (palladium trapped in the support), though no residual carbon was observed in the sample preparation. Though the mean value is close to the percentage value (1%) stated by the supplier, the loading distribution was found to be relatively broad, with some pellets having high (three times that stated by the supplier) and some low palladium loadings. This finding would have to be considered when comparing the hydrogen uptake rate of individual pellets in later chapters of the thesis.

3.3.4 Palladium location on the carbon support

The 1% Pd/C pellets purchased were initially thought to be an egg-shell type catalyst, whereby palladium nanoparticles are specifically deposited on the surface. This removes the need for a reactant to diffuse through the pores to a palladium active site and thus reduces the resistance to internal mass transfer associated with pore diffusion. SEM images of the pellets and their respective elemental maps are shown in Figure 3.7. Both images show the palladium (coloured green) located in high concentration on the surface of the carbon pellet, whilst the interior of the pellet is overwhelmingly made up of carbon (coloured red). There is however, evidence that palladium is located throughout the interior of the pellet in low concentrations.

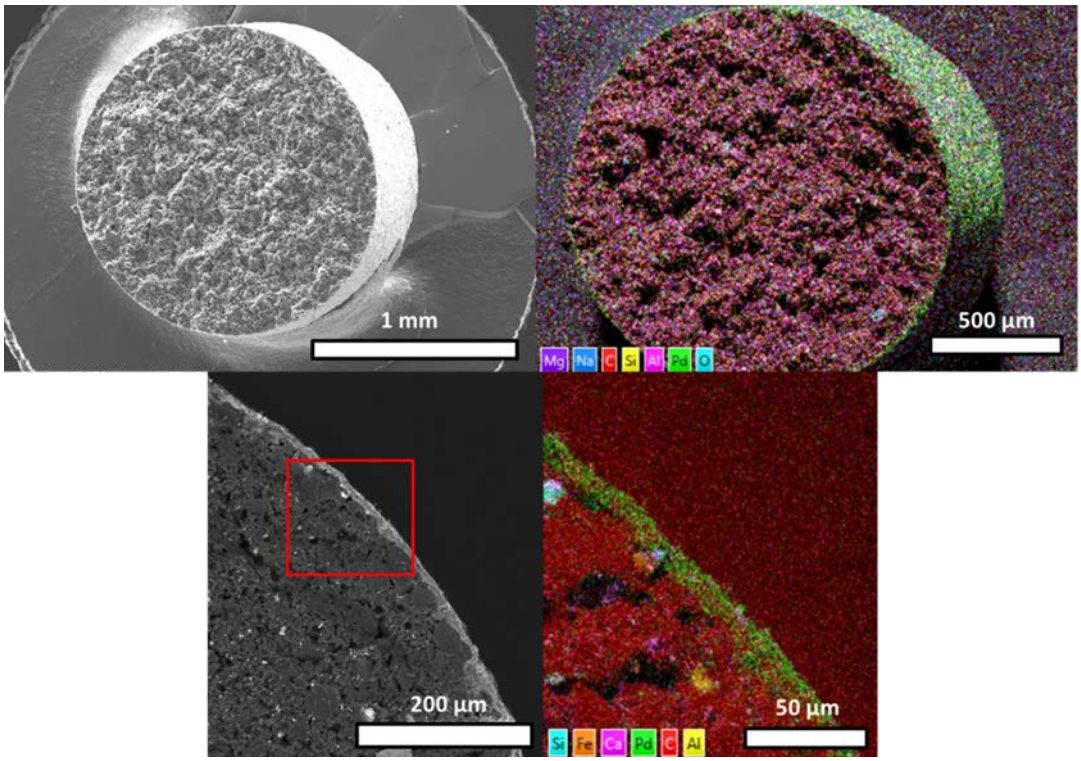

Figure 3.7: SEM images of a 1% Pd/C pellet cross-section and the corresponding EDX map. Showing the palladium (green) distribution over the exterior and interior of a whole pellet (top) and its edge (bottom).

To better quantify where the palladium is located, a series of 1D linescan measurements were made to obtain palladium distribution as a function of depth into the pellet from the surface. A linescan builds a semi-quantitative picture of the quantity of elements present by moving the electron beam across a predetermined path and detecting X-rays produced as the beam interacts with elements in the sample. As the beam hits the sample it scatters forming a teardrop like scattering pattern, this can be seen for a 15 kV beam into carbon in Figure 3.8. Therefore, it is the interaction volume, which for carbon is roughly 0.467 μm^3 (assuming the teardrop to be a cone), rather than the beam diameter that needs to be considered as the linescan is made. The size of the interaction volume depends on the density material being analysed and the beam energy (kV) itself [162]. Palladium linescan profiles for a cross section and surface of a 1% Pd/C pellet and the interior of a non-active carbon pellet are shown in Figure 3.9. Clearly the surface is strongly enriched in palladium.

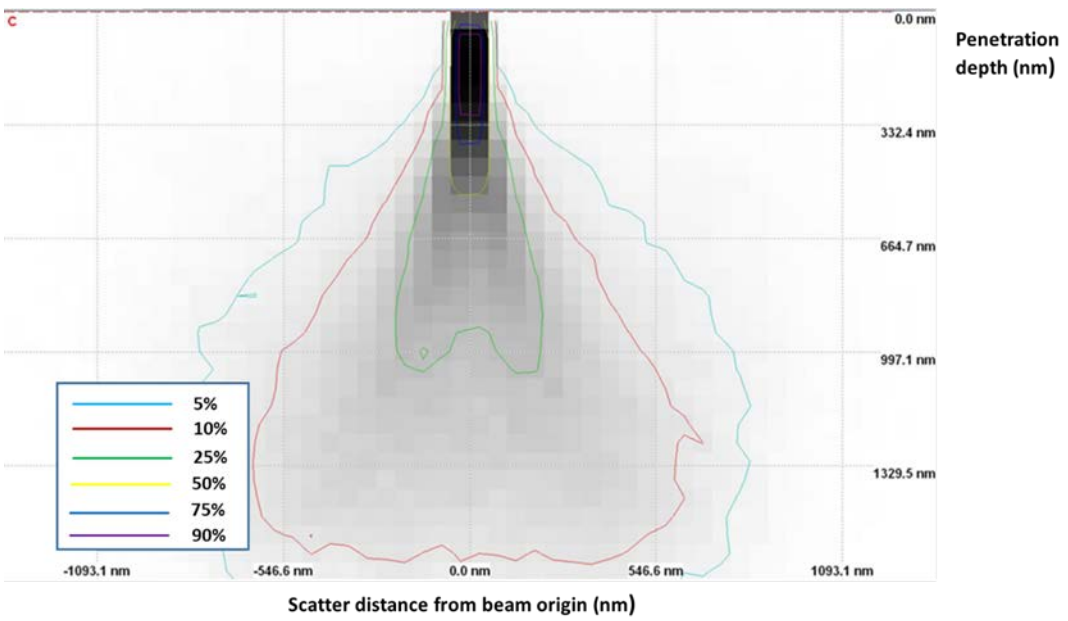

Figure 3.8: Simulated interaction volume as a 15 kV beam interacts with a carbon sample. Quantifying the percentage of electrons able to penetrate and scatter into the sample (kindly provided by Leeds Electron Microscopy and Spectroscopy Centre LEMAS).

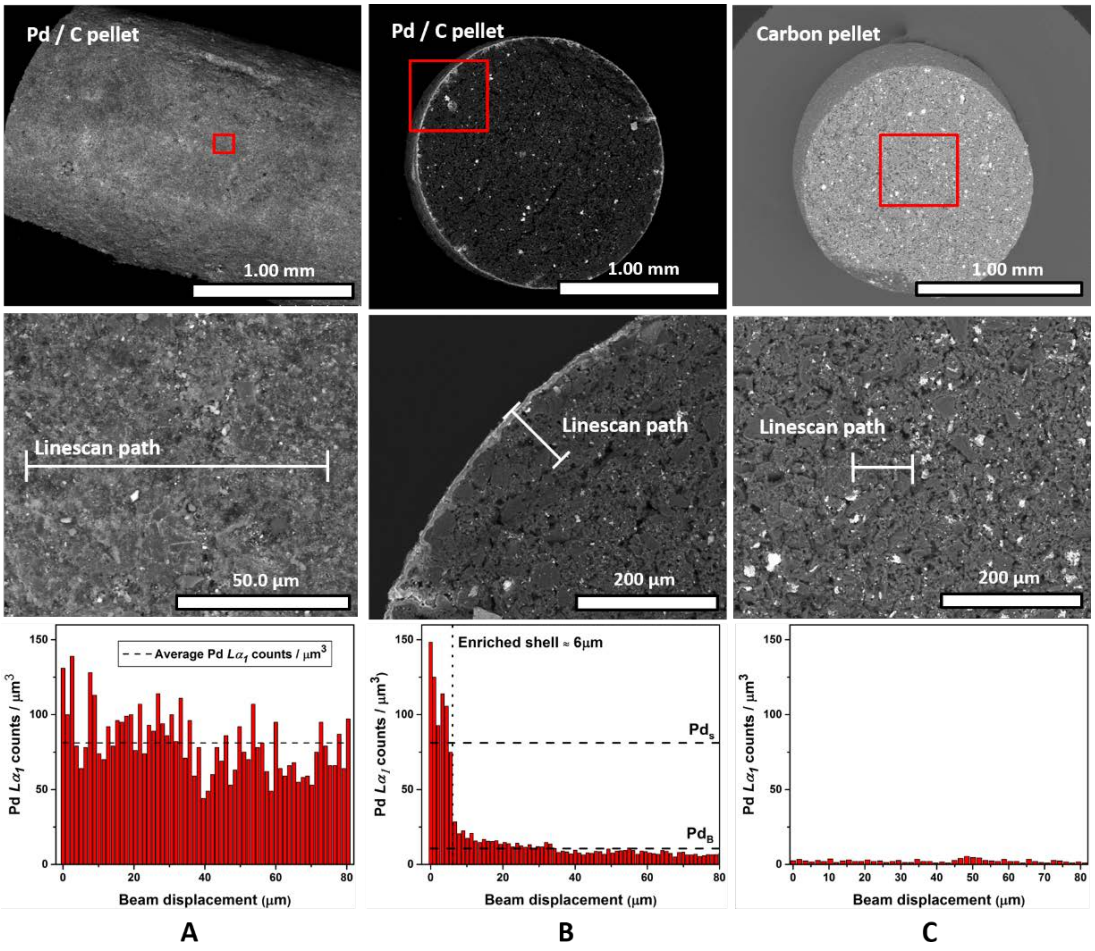

Figure 3.9: SEM images of a 1 wt% Pd/C and non-active carbon pellet..

Showing the surface of the pellet (A), edge of a cross section (B) and centre of a cross section of the interior of an non-active carbon pellet (C). Top: overview of the pellet with the location where a linescan was taken shown in red. Middle: detailed view at the scale of the line scan and Bottom: the respective palladium count line scan profile.

There is some variation over the surface scan, but the count is consistent at ~75. The linescan over the cross section of the pellet shows that the surface concentration is maintained to a depth of $\delta_s = 6\ \mu m$. Further into the pellet the palladium concentration drops sharply by a factor of 4 to 20 counts, and then more gradually as you progress further into the pellet interior. Interestingly, it never reaches the background scatter level that results from the scan of a pellet that is not impregnated with palladium. As the number of counts is directly proportional to the concentration of palladium present [163], the

fraction of palladium in the enriched shell was estimated from the cross-sectional linescan of the pellet. To achieve this, the average number of counts in the enriched shell, $\#_{Pd_{shell}}$ and in the core of the pellet, $\#_{Pd_{core}}$ were first determined. It was assumed that the count intensity remains constant across the diameter of the pellet once past the enriched shell region. The volume of the enriched shell was calculated using the mathematical theory of cylindrical shells, such that $V_{shell} = V_{shell+core} - V_{core}$;

$$V_{shell} = \pi L_p r_{shell+core}^2 - \pi L_p r_{core}^2 = \pi L_p (r_{shell+core} - r_{core})^2$$

$$V_{shell} = \pi L_p (r_{shell+core} + r_{core})(r_{shell+core} - r_{core})$$

$$V_{shell} = 2\pi L_p \left(\frac{1}{2} r_{shell+core} + r_{core}\right)(r_{shell+core} - r_{core})$$

As $r_{shell+core} - r_{core}$ is equal to the thickness of the enriched shell, δ_s and $\frac{1}{2} r_{shell+core} + r_{core}$ the average radius of the shell, the shell volume can be expressed as;

$$V_{shell} = 2\pi r_p L_p \delta_s$$

Thus, the fraction of counts in the enriched shell volume, $Pd_{\#S}$, is the ratio between the total counts per volume of pellet (in the shell plus the core of the pellet) and the enriched shell;

$$Pd_{\%S} = \frac{V_{shell} \cdot \#_{Pd_{shell}}}{V_{shell} \cdot \#_{shell} + V_{core} \cdot \#_{Pd_{core}}}$$

$$Pd_{\#S} = \frac{2\pi r_p L_p \delta_s \cdot \#_{Pd_{shell}}}{2\pi r_p L_p \delta_s \cdot \#_{Pd_{shell}} + \pi r_p^2 L_p \cdot \#_{Pd_{core}}}$$

$$Pd_{\%S} = \frac{2\delta_s \cdot \#_{Pd_{shell}}}{2\delta_s \cdot \#_{Pd_{shell}} + r_P \cdot \#_{Pd_{Core}}} \quad \textbf{(3.2)}$$

Using Eq. (3.2) the proportion of palladium in the shell was estimated to be 15.5% suggesting a large proportion of the palladium metal is located at low

concentration within the interior of the pellet. This result suggests that pore diffusion should not be assumed to be negligible when considering the interplay between the mass transfer and kinetics of the pellet.

3.3.5 Nanoparticle size distributions

To determine the chemical reaction rate within the enriched shell of the 1% Pd/C pellets the intrinsic reaction rate was obtained from the 5% Pd/C in batch. To justify that the intrinsic reaction rate would be the similar for both palladium catalysts the nanoparticles size distributions were measured and compared. The TEM images showing the nanoparticles of the two catalysts used are shown in Figure 3.10. From visual inspection both catalysts appear to have similar shaped and sized nanoparticles (>10 nm), with the 5% Pd/C clearly having a higher concentration of observable nanoparticles in the images. The nanoparticles were individually sized using the Gatan microscopy suit software and are presented as a number frequency (number fraction of particles within a certain size range), percentage weight and available surface atoms of the nanoparticles Figure 3.11.

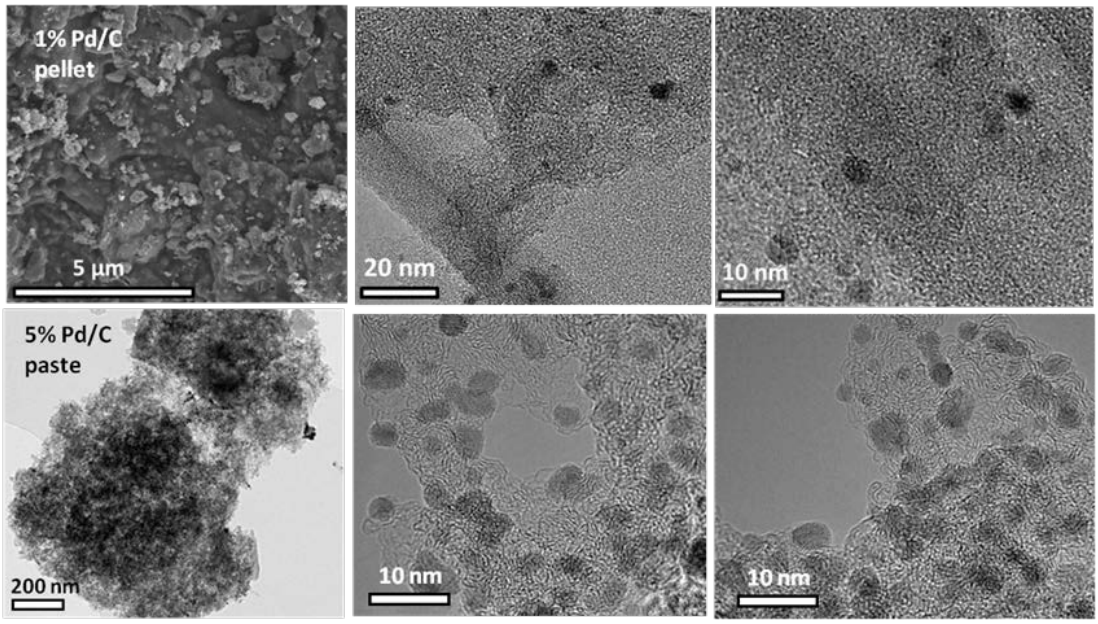

Figure 3.10: TEM images of the nanoparticles for the 1% Pd/C pellets and 5% Pd/C paste.

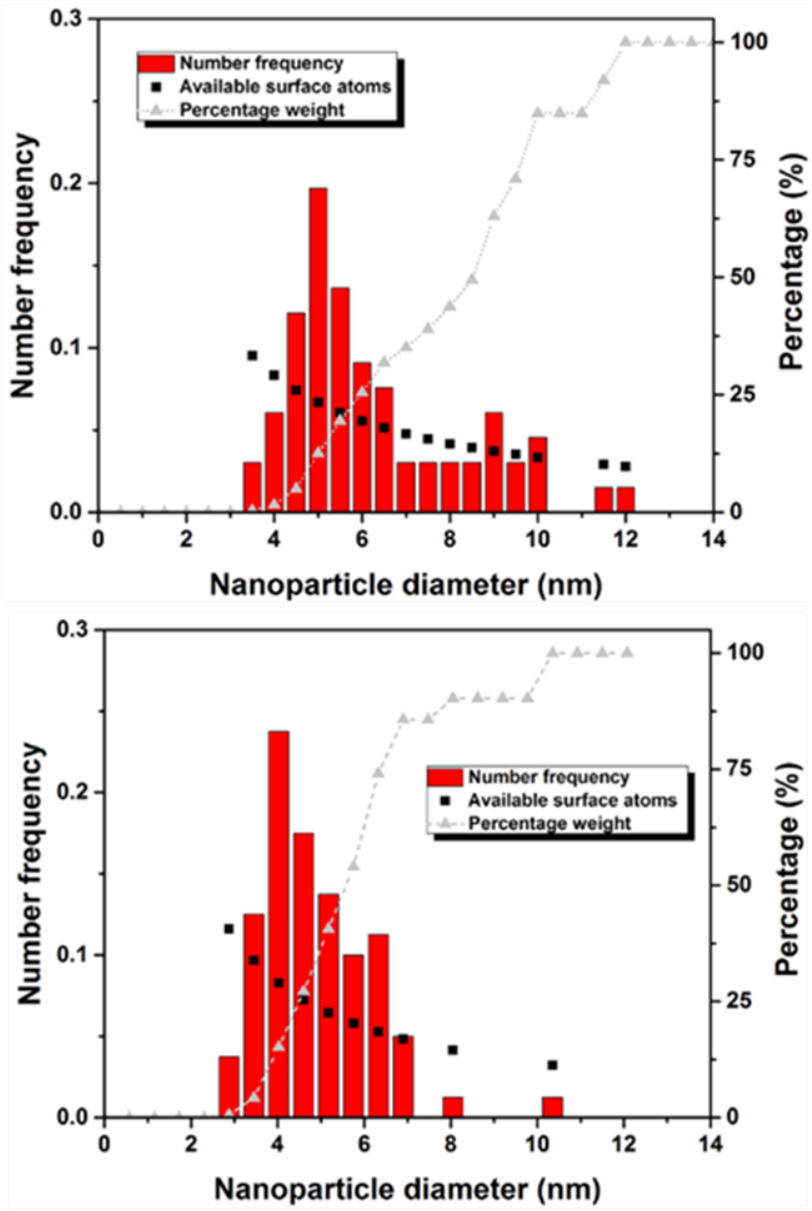

Figure 3.11: Nanoparticle size distributions of the catalysts obtained from TEM analysis. Presented as the number frequency, percentage weight and available surface atoms of the nanoparticles for the 1% Pd/C pellets (top) and 5% Pd/C paste (bottom).

The two size distributions are similar with the 1% Pd/C pellet having a slightly larger and broader distribution (d_{50} pellets = 5.35 ± 1.99 nm) than the 5% Pd/C paste (d_{50} powder = 4.38 ± 1.27 nm).

The distribution affects the number of surface atoms of palladium available to a reacting species. To estimate the number of surface atoms on a single nanoparticle two things are required; (i) the number of palladium

atoms per square nanometre of palladium and (ii) the surface area of the nanoparticle of interest. The number of atoms per nm was determined by considering the top plane of a face centred palladium cubic lattice at the outmost edge of the nanoparticle. As can be seen in Figure 3.12, each unit cell there is an equivalent of two whole atoms; one whole atom in the centre and four quarters of an atom in each corner. Therefore, the number of palladium atoms per nm^2 can be expressed as;

$$N_{atoms\ per\ nm^2} = \frac{2}{(l_{unit})^2} \tag{3.3}$$

Where l_{unit} is the length of a palladium unit cell (0.38907 nm [164]). If the nanoparticles are assumed to be spherical, then the number of surface atoms available for reaction per nanoparticle, N_s can be estimated from the surface area of the nanoparticle, A_{Pd};

$$N_s = A_{Pd} N_{atoms}$$

$$N_s = \pi d_{Pd}^2 \cdot \frac{2}{(l_{unit})^2}$$

$$N_s = 2\pi \left(\frac{d_{Pd}}{l_{unit}}\right)^2 \tag{3.4}$$

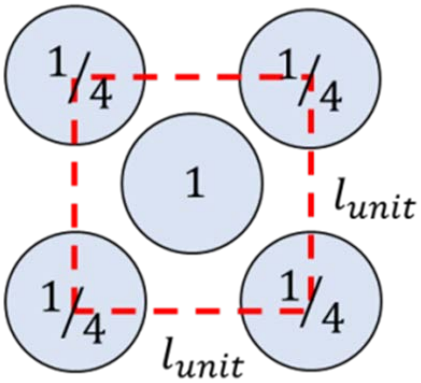

Figure 3.12: Simplistic representation of the top plane of a palladium face centred cubic lattice, showing an equivalent of two palladium atoms in total.

Here N_{atoms} is the number of palladium atoms per nm^2, A_{Pd} is the surface area of the nanoparticle, d_{Pd} the diameter of the nanoparticle. Using Eq. (3.4), the cumulative value of N_S expressed as a ratio to the total number of palladium atoms is given in Figure 3.11. The distribution suggests that the smaller nanoparticles have a higher surface utility, as a larger proportion of palladium atoms are accessible to reacting species on the surface. Larger nanoparticles have a much high proportion of palladium atoms within the interior than on the surface, and therefore as reacting species are limited to reacting on the surface only, the catalyst utility per mass of palladium will decrease. It has been shown in the literature however, that when dealing with small nanoparticles increased catalytic activity is not necessarily directly proportional to increased surface area [165]. It is thought that within a critical size range (1 – 10 nm), changes in the topology, electronic effects (molecular interactions) and metal-support interactions can all determine the effect of particle size has on activity [166].

Though the TEM images showed that the nanoparticles studied here are spherical in nature, other geometries are commonly observed [167]. The effect of particle shape on the available surface atoms was theoretically investigated for tetrahedron, octahedron, cuboctahedron and cubic geometries following the same methodology laid out for the spherical nanoparticles. A more useful measure is the ratio between the number of atoms available on the surface and the total number of atoms in the nanoparticle, N_{bulk}. To calculate the total number of atoms encompassed in the shapes' volume, a method similar to the surface area was used. In a face centred cubic palladium lattice there are a total of four equivalent atoms, which can be expressed as;

$$N_{atoms\ per\ nm^3} = \frac{4}{(l_{unit})^3} \tag{3.5}$$

Using the octahedron geometry as an example, the volume in terms of the edge length, L_{edge} is;

$$V_{oct} = \frac{\sqrt{2}}{3} L_{edge}^3 \tag{3.6}$$

To obtain the volume in terms of the length of the nanoparticle, L_{np}, Pythagoras's theorem can be used;

$$\left(\frac{L_{np}}{2}\right)^2 = \left(\frac{1}{2} L_{edge}\right)^2 + \left(\frac{1}{2} L_{edge}\right)^2$$

$$\frac{1}{\sqrt{2}} L_{np} = L_{edge} \tag{3.7}$$

Substituting Eq. (3.7) into Eq. (3.6) and multiplying by the number of atoms per nm^3 (Eq. (3.5)) yields an expression for the total number of atoms in the nanoparticle;

$$N_{bulk} = \frac{4}{(l_{unit})^3}\ x\ \frac{1}{6}\left(\ L_{np}\right)^3 = \frac{2}{3}\left(\frac{L_{np}}{l_{unit}}\right)^3 \tag{3.8}$$

All mathematical derivations for the shapes' areas, volumes, number of surface atoms and total atoms can be found in Appendix A. The percentage of available surface atoms relative to the total amount of palladium atoms in the nanoparticle is presented in Table 3.4 for each shape. For all calculations, the d_{50} particle size determined from the TEM measurements (5.35 nm) was used. In all cases, surface atoms number less than half of the total number of atoms present in the nanoparticle, however, the tetrahedron and octahedron geometries have a significantly larger percentage on the surface.

Table 3.4: Mathematical derivations for the number of surface atoms and the calculated number of surface atoms for different geometries for the distribution obtained

Shape	Expression for N_s	Expression for N_{bulk}	N_s/N_{bulk} (%)		
			D10	D50	D90
Spherical	$2\pi\left(\frac{d_{Pd}}{l_{unit}}\right)^2$	$\frac{2}{3}\pi\left(\frac{d_p}{l_{unit}}\right)^3$	29	22	13
Cubic	$12\left(\frac{L_{np}}{l_{unit}}\right)^2$	$4\left(\frac{L_{np}}{l_{unit}}\right)^3$	29	22	13
Tetrahedron	$3\sqrt{3}\left(\frac{L_{np}}{l_{unit}}\right)^2$	$\frac{\sqrt{3}}{2}\left(\frac{L_{np}}{l_{unit}}\right)^3$	58	44	26
Octahedron	$2\sqrt{3}\left(\frac{L_{np}}{l_{unit}}\right)^2$	$\frac{2}{3}\left(\frac{L_{np}}{l_{unit}}\right)^3$	50	38	22
Cub-octahedron	$(2\sqrt{3}+6)\left(\frac{L_{np}}{l_{unit}}\right)^2$	$\frac{10}{3}\left(\frac{L_{np}}{l_{unit}}\right)^3$	27	21	12

It is worth noting, that although this may suggest that these geometries are preferential in terms of catalyst utility and activity, a combination of factors that are often specific to the reacting species ultimately effect catalytically activity.

It is evident from assessing the limited amount of experimental studies in the literature involving different palladium shapes, that the geometry with the highest activity can be dependent on the chemical system. Hu *et al.* reported that for cyclohexene hydrogenation, tetrahedron shaped nanoparticles were more catalytically active than spheres [168]. Whilst Jin *et* al. found that for formic acid oxidation, nanoparticles with a cubic geometry exhibited the highest catalytic activity, whereas octahedron nanoparticles exhibited the lowest [169]. Both studies conclude that it is the preferential interactions with the fractions of atoms on the different edges, corners, faces and possible defects that give rise to the observed phenomena.

3.3.6 Ancillary characterisation

The following characterisation results discussed have been compiled into a single section as, though they are important in understanding the physical properties of the materials, they are not used directly in the other chapters presented in the thesis. Specifically, the size distribution, surface area and pore size were compared between the 1% Pd/C and non-active carbon pellets to identify whether the carbon pellets could be used instead of the catalyst pellets during the liquid film thickness (as the catalyst pellets are pyrophoric).

3.3.6.1 Pellet and paste size distributions

Figure 3.13 illustrates the picture analysed using ImageJ and the resulting PSD for the 1% Pd/C and non-active carbon pellets.

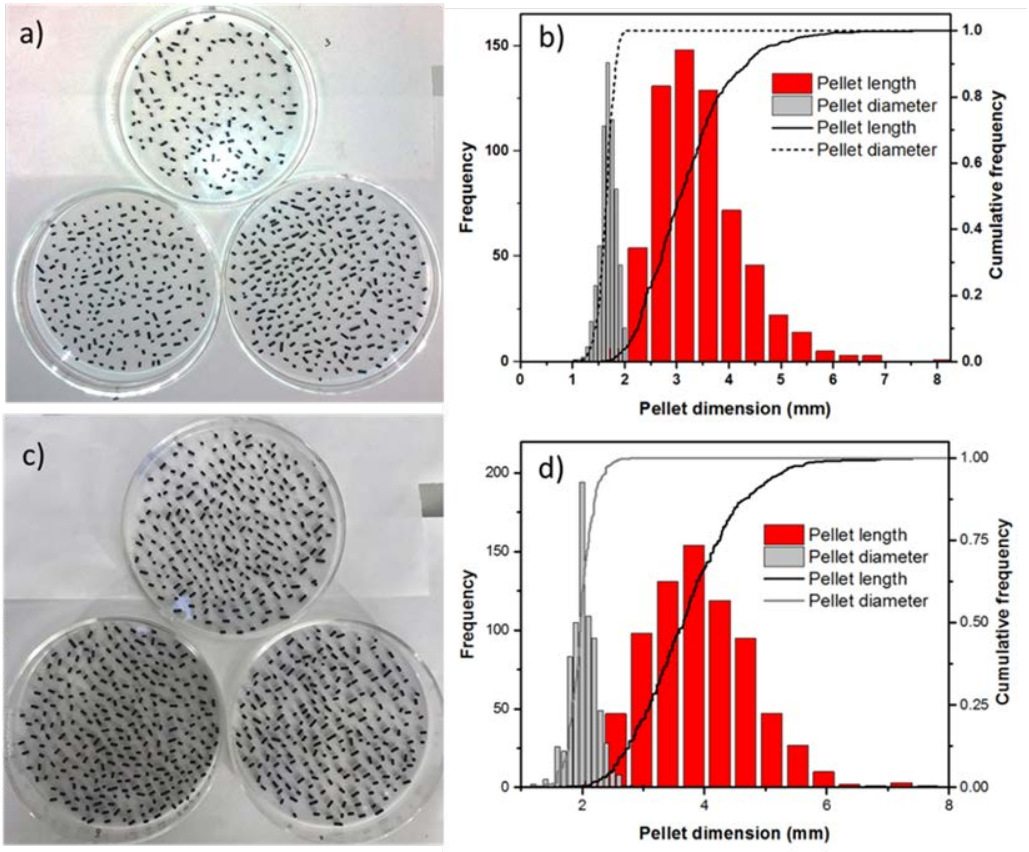

Figure 3.13: Pellet size distribution for the 1% Pd/C and non-active carbon pellets. Showing the picture used in the ImageJ software and the corresponding pellet length and width distributions; a) 1% Pd/C pellets, b) 1% Pd/C PSD, c) non-active carbon pellets and d) non-active carbon pellets PSD.

The 1% Pd/C pellets and non-active carbon pellets were found to have an average diameter of 3.07 ± 0.86 mm and 3.66 ± 0.90 mm, and an average length of 1.65 ± 0.16 mm and 1.97 ± 0.21 mm respectively. Comparing the dimensions, both the length and width are in the same order of magnitude, though the non-active carbon pellets were found to be slightly longer and wider than the 1% Pd/C pellets. The 5% Pd/C paste was found to have a particle size distribution of approximately 17.38 ± 15.02 μm.

3.3.6.2 Surface area

BET adsorption isotherms for the Pd/C and non-active carbon pellets are shown in Figure 3.14. Both adsorption isotherms are characteristic of a Type II adsorption isotherm, whereby the larger plateau region of the curve corresponds to the formation of a gas monolayer and the sharp increase in gas adsorption occurs as the empty voids of the pores are filled by capillary condensation.

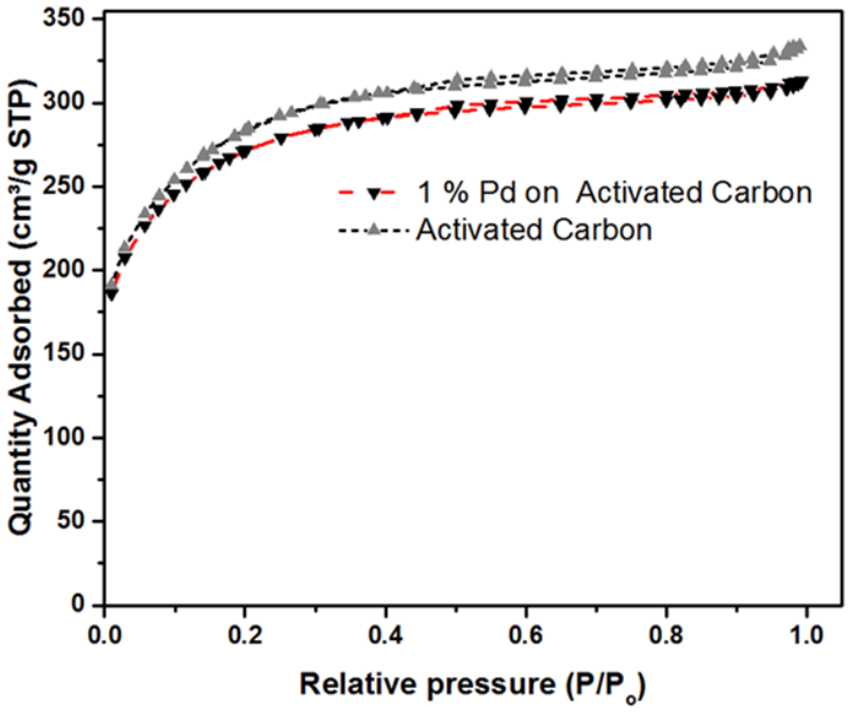

Figure 3.14: Adsorption isotherms of the 1% Pd/C and non-active carbon pellets obtained using BET analysis.

The surface area of the 1% Pd/C and non-active carbon pellet was determined to be 941.22 ± 2.10 m^2/g and 999.03 ± 10.05 m^2/g respectively. The determined specific surface areas are very high (as would be expected for such porous structures) and relatively similar. However, it appears that by loading the carbon with palladium the surface area decreases. This could be attributed to blocked pores but this hypothesis would be difficult to experimentally verify. In comparison, the 5% Pd/C paste was experimentally found to have a surface area of 679.22 ± 33.96 m^2 / g. Though the surface area to volume ratio of the micron sized carbon particles in the paste will be much higher than the pellets, the actual area available for adsorption will be larger in the pellets (due to the extended internal porous structure). It should also be noted that there is some evidence to suggest that BET can overestimate the surface area of micro-porous materials [170], so care needs to be taken when interpreting this data.

3.3.6.3 Pore size distributions

Figure 3.15 presents the pore distributions of both samples and as with the adsorption isotherms the results for the Pd/C and non-active carbon pellets are very similar. The average pore widths are approximately 2 nm for both samples; though these micro-pores are indeed small the model systems used in this work would easily be able to diffuse into even the smallest pores. From the adsorption and pore distribution curves presented, hysteresis can easily be observed and resembles that of a Type-H4 hysteresis loop commonly seen in carbon adsorbents [161].

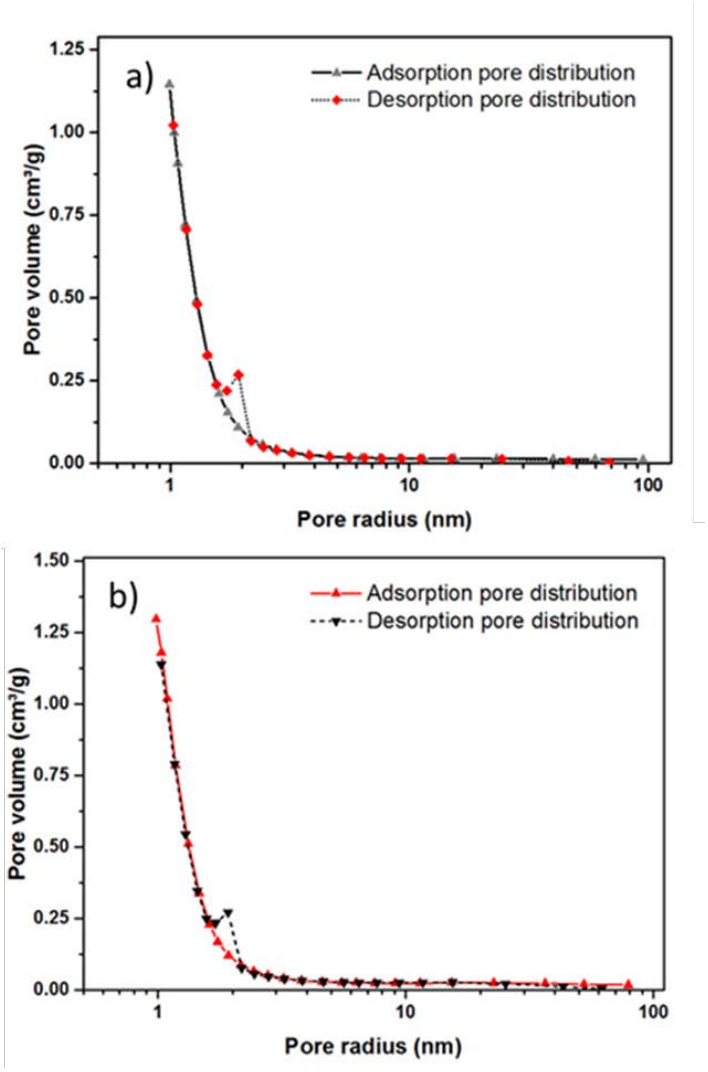

Figure 3.15: Pore size distributions for the 1% Pd/C and non-active carbon pellets.

Calculated from the BET adsorption experiments using BJH theory. Showing; a) 1% Pd/C pellets and b) non-active carbon pellets

Chapter 4

Isolation of the convective and radial diffusive mass transfer processes occurring over a single catalyst pellet in a scaled down trickle bed reactor

As summarized in Chapters 1 and 2, trickle bed reactors are an attractive option for continuous manufacturing due to their simple operation and lower back mixing resulting in enhanced selectivity [13]. However, due to the complex relationship that exists between the kinetics and hydrodynamics, these reactors can be challenging to study at laboratory scale [18]. In addition, the space and mass velocities do not scale linearly with geometry, making both scaling down and up problematic [171]. Consequently, further understanding of the interplay between hydrogen mass transfer and the catalytic reaction is required to facilitate the uptake of such technologies. Thus, the intention of this chapter is to investigate whether the transport processes occurring simultaneously in the bed can be isolated by scaling the process down to a single catalyst pellet. Knowledge of such transfer mechanisms is essential in controlling the rate of supply of hydrogen to the catalyst surface, avoiding scale up issues and potentially manipulating the selectivity of a reaction independent of scale.

4.1 Scaling down to study transport phenomena

Generally, two approaches to scaling down trickle bed reactors have been reported in the literature [172]. The first being the design of a laboratory scale reactor that maintains hydrodynamic similarity, of which Medoras *et al*. presents an extensive review [18]. The second approach is the design of a reactor for the purpose of assessment and manipulation of specific transport

phenomena so as to determine the impact on the reaction. Given the nature of the work to be presented in this study, focus will be on literature in relation to the latter of the two approaches.

The second approach was first demonstrated by Satterfield *et al.* who created a vertical 'string' of fourteen spherical catalyst pellets (d_p = 8 mm) to study the hydrogenation of α-methylstyrene [45]. They compared the experimental hydrogen uptake rates to those predicted by a steady state mass transfer model. The authors found that when using a hydrogen saturated feedstock, liquid flow rate had no significant effect on the reaction rate. Moreover, when complete mixing was assumed in between the pellets, the model was able to reconcile the experimental data well. An alternate concept is that of 'string reactors': single channels containing catalyst particles with sizes similar to the channel dimensions to create 'strings' of successive pellets. Bauer and Hasse used a string reactor (d_p = 1.6 mm) and compared this with a conventional trickle bed reactor using the hydrogenation of α-methylstyrene [47]. The string reactor was shown to outperform the trickle bed reactor, exhibiting a fivefold increase in productivity (rate per unit mass of catalyst). A group from Dresden has looked extensively at the mass transfer characteristics during hydrogenation of α-methylstyrene in string reactors. Using the same palladium on alumina spherical catalyst (d_p = 0.8 mm), different ratios of reactor to particle diameter were studied (1.25 [82], 1.76 [173] and 2.5 [174]). These studies show that the mass transfer rate of hydrogen increases with superficial velocities. At high superficial velocities the mass transfer rates increase significantly with the gas volume fraction. The authors postulate that this is the result of direct transfer from the gas to the solid and demonstrates the significance of the liquid film mass transfer

resistance. Kallinikos and Papayannakos employed a spiral of cylindrical pellets rather than a vertical column for the reduction of benzene [175]. They also showed the impact of the gas volume fraction, though in their case reaction limitation occurred at the higher volume fractions.

There are a relatively small number of reported instances in the literature illustrating the use of a single catalyst pellet or particle to investigate heterogeneous catalysis. With none found outlining the use of a single catalyst pellet to isolate or study the mass transport phenomena occurring in packed beds. Though described as a string pellet reactor, Hipolito *et al.* hydrogenated α-methylstryene using a single pellet immobilised by glass beads in a horizontal pipe [48]. It was identified that by varying the liquid feed rate whilst ensuring a constant liquid hourly space velocity (by varying the catalyst volume in the bed) that the reaction was kinetically limited, as varying the feed rate had no impact on the conversion trends. Many other single pellet studies focus on the internal mass transfer resistances (pore diffusion) in what are described as diffusion reactors [176-178]. All other studies have focussed on the use of single pellets to further understand heat transfer in packed bed reactors. Adaje and Sheintuch suspended a single 3.2 mm catalyst pellet onto a thermocouple to monitor the temperature gradients and compared this to a pellet embedded in a shallow bed of inert pellets [179]. The authors speculate whether single pellet studies are suitable in determining the behaviour of an actual packed bed reactor. Watson and Harold also freely suspended a catalyst pellet via a harness attached to a weighing balance so that the liquid holdup could be continually monitored [180]. The hydrogenation of α-methylstyrene and cyclohexane were chosen as model systems and

vaporisation of the liquid phase due to the reaction was studied from the holdup data.

4.1.1 Aims

There are two transfer processes by which a catalyst pellet in a bed is supplied with hydrogen. The first being the convective transfer of hydrogen already present in the liquid before it contacts the pellet, driven by the bulk flow of the liquid flowing over the surface of the pellet. Hydrogen can also be supplied to the pellet from the gas phase whilst liquid is flowing over the pellet – referred to in this work as the radial diffusive mass transfer process. This process involves a number of transfer steps starting from the gas phase, diffusing across the gas-liquid interface, though the liquid film, across the solid liquid interface and finally arriving at the catalyst nanoparticles (either located on the surface or within the catalyst supports internal structure for which pore diffusion is required). These two transfer processes will be occurring simultaneously within a packed bed of catalyst pellets and thus, would be very challenging to isolate even in a typical laboratory trickle bed reactor.

To circumvent this issue, it was hypothesised that by scaling down to a single catalyst pellet the effect of the two processes could be isolated and observed in the pellets hydrogen uptake rate. In an effort to be as representative of a pellet in a trickle bed reactor as possible, a methodology of scaling a trickle bed reactor down to a single catalyst pellet immobilised in a vertical bed of glass beads was developed and employed. One of the foreseeable issues with the scale at which the hydrogenation was occurring (a single pellet), was whether conversion would be detected for analysis. Therefore, styrene was selected as the model system (the reaction scheme for the hydrogenation of styrene to ethylbenzene in illustrated in Figure 4.1).

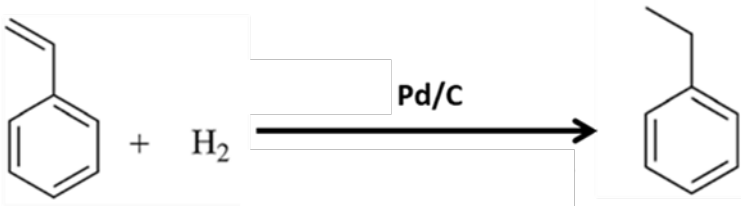

Figure 4.1: Reaction scheme for the hydrogenation of styrene to ethylbenzene.

The intrinsic chemical reaction of the reduction of styrene is kinetically very fast and it is often used to study the external mass transfer processes in three phase catalytic reactions [48].

The initial aim of the work was to ascertain whether the effect of convective mass transfer and radial diffusive mass transfer could be isolated by manipulating the concentration of hydrogen present in the liquid feed. It was hypothesised that by removing the requirement of gas-liquid mass transfer by saturating the feed with hydrogen, convective transfer would dominate and vice versa if the feed was hydrogen free. The effect of flow rate on the hydrogen uptake rate of the pellet would then be investigated for both feed conditions.

The ICP-MS results detailed in Chapter 3 showed that though the percentage loading of palladium was in line with manufacturers specification for the 1% Pd/C pellets (0.94 ± 0.64 wt%). However, the loading distribution across all the pellets tested was observed to be relatively broad (this can also be seen in the percentage error). Thus, the same pellet was used throughout the study to avoid issues when comparing reaction rates between pellets. Moreover, gas velocity and its effect on the mass transfer of hydrogen was not considered here, although it will influence the hydrodynamics of the liquid

flowing though the bed and hence the mass transfer characteristics. Thus, gas flow rate was kept constant throughout the study.

4.2 Experimental

This section details the design, assembly and operation of the scaled down trickle bed reactor, as well as all the materials used in its fabrication.

4.2.1 Design and assembly

The single pellet reactor used throughout this work was constructed from a glass Pasteur pipette (6.5 mm internal diameter and 104 mm length) which contained a single 1% Pd/C pellet (1.49 mm diameter, 5 mm length, 8 mg) immobilised in a bed of Ballotini solid soda glass beads (2.30 g, 80 mm bed height). The tip of the pipette was carefully removed to prevent liquid holdup and subsequent flooding of the bed at higher liquid flow rates. The single pellet was placed roughly 30 mm from the bottom of bed and non-active carbon pellets (0.126 g) were placed on top of the glass beads to reduce liquid maldistribution. The reactor length and the depth the pellet is positioned in the bed was not investigated in this work. A make-shift frit plate was created from cotton wool and used to support the bed in the glass pipette. PTFE tape was then wrapped around the lower section of the pipette. The glass pipette was placed inside a gas condenser and seated, so that the PTFE tape created a seal between the pipette and condenser. The lower section of the glass pipette was bound in PTFE tape and placed inside a gas condenser to form a seal that forced gas flow through the bed. A needle centred directly above the bed was used as a liquid distributor and methanol was pumped into the bed with a HPLC pump (Knauer 100Smartline) from a separate saturation vessel described below. A schematic of the single pellet reactor is illustrated in Figure 4.2.

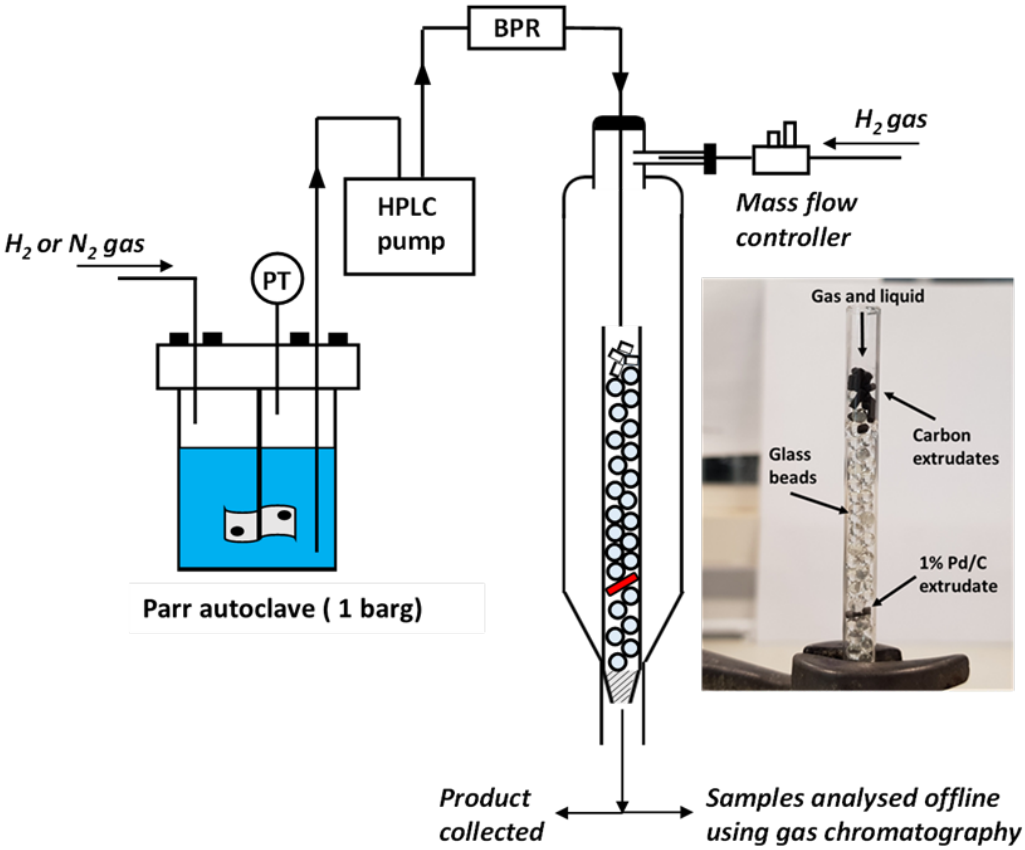

Figure 4.2: A schematic of the single pellet reactor experimental set-up and picture of the 1% Pd/C pellet immobilized in the bed of glass beads.

The hydrogen gas flow rate was regulated using a Bronkhorst mass flow meter and kept constant at 300 mL/min (superficial gas flow rate through the bed = 0.15 m s^{-1}, mass flow rate = 0.012 kg m^{-2} s^{-1}) throughout all experiments. The effect of gas velocity on the mass transfer rate was not examined in this work, though as discussed in Section 2.4.2 is it evident that gas flow is a significant factor that can affect the mass characteristic through changes in the hydrodynamics.

4.2.1.1 Liquid saturation vessel

To saturate the liquid feed with hydrogen before operation, a stainless steel (316 SS) autoclave Parr Instrument 0.6 L stirred tank reactor was used. A gas entrainment impeller agitated the feed and ensured the liquid has been fully saturated with hydrogen. The entrainment impeller consists of four blades,

which have two holes located near the top and bottom of each blade. Gas is drawn into the liquid from a hole higher up the shaft and distributed through the holes in the blades. The impeller was motor driven and capable of agitation speeds between 0-1200 rpm. As the autoclave was pressurised, it became apparent that a 17.2 barg fixed backpressure regulator was required to prevent the pressurised feed passing through the pump head uncontrollably. This in turn was found to greatly increase the precision at which a constant flow rate could be delivered and was not seen to affect the liquid distribution from the needle tip. Pressure in the autoclave was maintained using a pressure transducer and mass flow controller to create an automated control loop and controlled using a Parr Instrument 4871 process controller connected to SpecView software.

4.3.2 Experimental procedure

Assembling the reactor as shown in Figure 4.2, exactly one 1% Pd/C pellet (8 mg, d_p = 1.49 mm, l_p = 5 mm) was placed within the bed of glass beads. The hydrogenation of styrene was conducted as follows;

4.3.2.1 Catalyst activation

To saturate the 1% Pd/C pellets' surface with hydrogen, methanol was used to completely flood the bed and pellet to ensure the catalyst was fully wetted, this procedure was repeated three times. Once fully wetted, methanol (5 mL / min) and hydrogen (300 mL / min) were co-currently passed through the bed at 21 ^{o}C for 20 minutes to completely activate the catalyst.

4.3.2.2 Hydrogen free feed

A styrene solution (0.18 M, 55 mmol) in 0.3 L methanol with n-decane (0.025 M, 7.4 mmol) was fed at 1 mL / min for 10 minutes before being changed to

the desired flow rate. This was found to greatly reduce the time taken for the reactor to reach steady-state at the lower flow rates investigated. Once at the desired flow rate, the reactor was operated for 10 mins before the product stream was sampled (at 5 minute intervals over a 35 minute period). The liquid flow rate through the reactor was manually measured every 10 minutes and an average taken.

4.3.2.3 Hydrogen saturated feed

Methanol (0.3 L) and n-decane (0.025 M, 7.4 mmol) were charged into the liquid saturation vessel and agitated under hydrogen with a gas entrainment impeller at 1000 rpm to fully saturate the liquid with hydrogen (2 bara for 30 minutes). Once fully saturated, the agitation was switched to 200 rpm and styrene was added to the autoclave to obtain a styrene solution in methanol (0.18 M, 55 mmol). The saturated solution was then used in the same manner as the hydrogen free styrene solution.

4.3.2.4 Gas chromatography analysis:

Samples from both experiments were collected and analysed offline via gas chromatography using the column and method described in Section 3.2.

4.3 Reactor characterisation

Before the hydrogenation of styrene could be investigated, the atmospheric reactor was fully characterised to determine the superficial mass velocities to be used and their associated liquid holdup and residence times.

4.3.1 Bed porosity, residence time distribution and liquid holdup

The bed porosity, ϵ_B, was determined by charging the reactor with methanol to calculate the volume of the empty reactor, V_R, and the volume of the free space when the reactor is fully packed, V_F;

$$\varepsilon_B = \frac{V_F}{V_R} \quad \textbf{(4.1)}$$

The bed porosity of the reactor when fully packed was determined to be 0.3. This value is relatively consistent with other studies in trickle bed reactors as can been seen from Table 4.1.

Residence time distribution (RTD) was approximated from the liquid holdup in the reactor [120]. Experiments using a dye were considered, but not undertaken due to the lack of necessary analytical equipment and due to the possible effects of axial dispersion and the subsequent difficult accounting for the tailing observed in the RTD curve. Due to its simplicity, the volume draining method was used to determine the dynamic, β_{dyn}, and static, β_{st}, liquid holdup portions (defined here as the volume of liquid m^3 / reactor void volume m^3 present within the reactor) during operation [119]. The packed glass pipette was first weighed before hydrogen gas and methanol were passed through the column concurrently for 20 minutes to reach a steady-state.

Table 4.1: Comparison of bed porosity determined with trickle bed reactors in the literature.

Packing material	d_p **(mm)**	d_R/d_p	**Bed porosity**	**Reference**
Glass beads	3.0 - 3.3	2.2	0.39	***This work***
Crushed carbon	0.7 - 1.1	3.0	0.36	Colombo *et al.* [181]
Glass beads	3.0 - 3.3	8.5	0.40	Stamatiou and Muller [182]
Glass pellets	1.6 x 3.2	6.5	0.34	Holub *et al.* [183]
Pd/C pellets	1.6 x 4.3	11.0	0.36	Al-Dahhan and Dudukovic´ [184]
Glass beads	3.0	18.0	0.39	Stegeman *et al.* [120]

Gas and liquid flow was then abruptly shut-off and the liquid that freely drained from the reactor was measured and taken as the dynamic portion.To calculate the static liquid holdup the reactor was then re-weighed and the increase in mass was attributed to the portion of liquid remaining within. The residence time, τ was estimated from the holdup data obtained using Eq. (4.2) for liquid flow rates of 0.25 – 4.50 mL / min [120].

$$\tau = \frac{\epsilon_B * [\beta_{Dyn} + \beta_{st}]}{\varphi} * z_B * S \qquad \textbf{(4.2)}$$

Here, φ is the volumetric flow rate, z_B the bed length and S the reactor cross-sectional area. The total liquid holdup and estimated residence times at different superficial and mass velocities is illustrated in Figure 4.3. Liquid holdup generally increased with an increase in liquid flow rate. This is in agreement with the literature, where it has been shown that in trickle beds operating at very low liquid Reynolds numbers (Re_L < *1.2*).

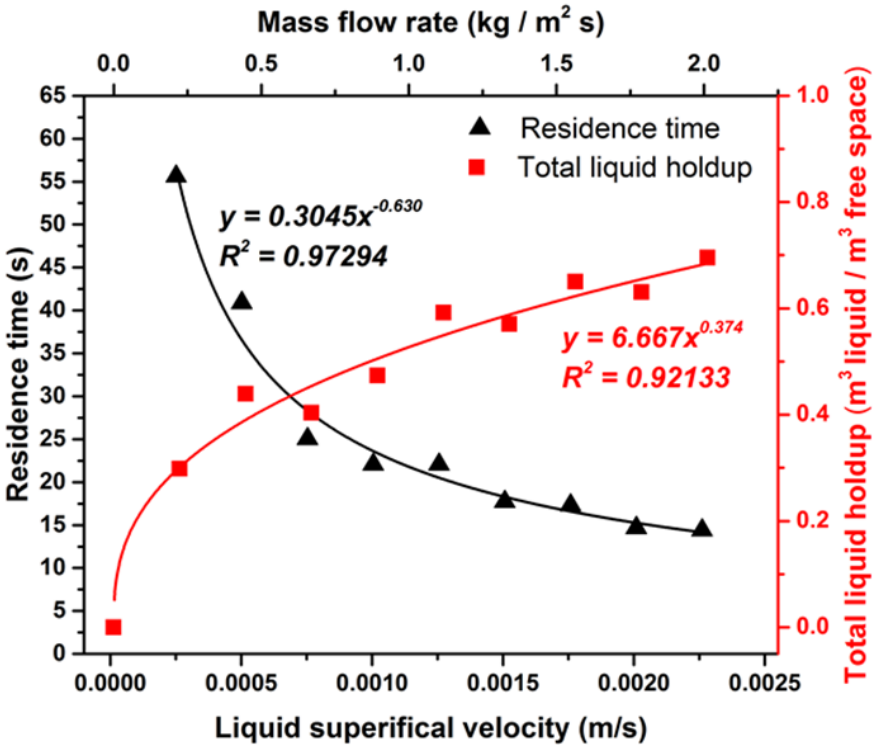

Figure 4.3: Residence time and liquid holdup in the single pellet reactor at flow rates between 0-10 mL / min, conducted at 21 °C, atmospheric pressure and 300 mL / min gas flow rate.

Table 4.2 shows the dynamic and static liquid holdup experimentally determined to approximate the total liquid holdup in the reactor. dynamic holdup increased with increasing liquid flow rates between 0.09 - 0.18 [119]. In the trickle bed literature the static holdup generally increases with higher liquid velocity. Lange *et al*. reported static holdup values between 0.26 – 0.31 for alumina catalyst particles (d_p = 0.73 mm, d_R = 0.034 m, ϵ_B = 0.39) for liquid Reynold's number between 0.1 and 0.5 [119]. In these conditions gas-liquid flow was seen to have little effect on the static .The static hold up values determined here are slightly higher due to increased liquid Reynolds numbers (1.78 – 5) used.

.3.2 Rationale for flow rates investigated

Assessing the literature, Dudukovic *et al.* suggests that generally trickle bed reactors are operated with a liquid holdup of between 0.05-0.25 and liquid mass velocities of up to 50 kg m^2 s^{-1} [127]. From the flow map generated by Sie and Krishna, to operate in the trickling flow regime liquid superficial mass velocities need to be $<$ 10 kg m^2 s^{-1} for the superficial gas flow rate used throughout this work (0.15 m s^{-1}) [116].

Table 4. 2: Dynamic, static and total liquid holdup for the single pellet reactor as a function of liquid flow rate

Liquid flow rate (mL/min)	Dynamic hold-up (m^3 liquid / m^3 free space)	Static hold-up (m^3 liquid / m^3 free space)	Total hold-up (m^3 liquid / m^3 free space)
0.5	0.053	0.245	0.298
1	0.153	0.286	0.439
1.5	0.077	0.326	0.403
2	0.156	0.317	0.473
2.5	0.267	0.325	0.592
3	0.247	0.324	0.571
3.5	0.310	0.340	0.650
4	0.272	0.358	0.630
4.5	0.350	0.346	0.695

It was also visually evident that at liquid flow rates below 1.0 mL / min the flow was characteristic of that of a trickling regime and above 1.0 mL / min the liquid began to pulse through the bed. Therefore, comparing this to the holdup data obtained, superficial liquid mass flow rates up to 0.25 kg m^2 s^{-1} (0.25-1 mL min^{-1}) were investigated during the hydrogenation of styrene.

4.4 Hydrogenation of styrene

Figure 4.4 illustrates the average conversion of styrene by the pellet as a function of the liquid flow rate when the feed was both hydrogen free and saturated. Both trends show that styrene conversion decreases as the liquid flow rate increases. This is expected, given that higher liquid velocities result in shorter residence times and thus lower conversions.

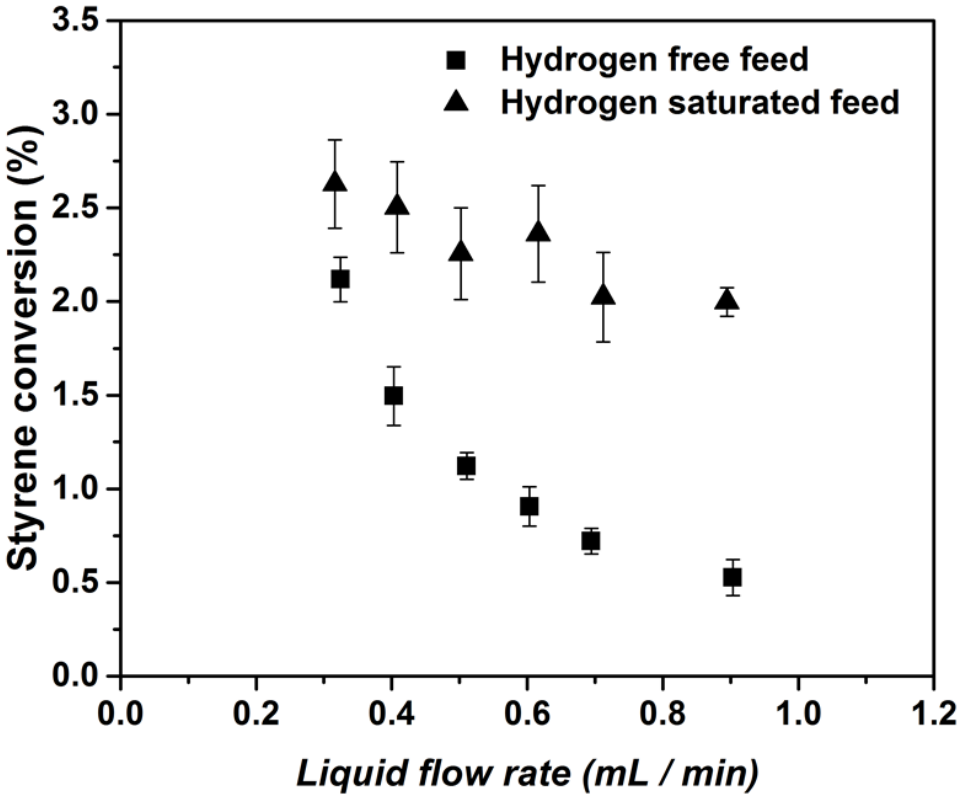

Figure 4.4: Styrene conversion of hydrogen free and saturated feeds at different liquid flow rates. Experimental conditions were 0.18M styrene solution was used at 21 ^oC, atmospheric pressure and 300 mL / min gas flow rate).

However, the extent to which the conversion decreases is markedly different depending on whether hydrogen is present in the liquid feed or not. If it is assumed, for the time being, that when the liquid feed is saturated with hydrogen, convective transfer dominates and the rate at which hydrogen is delivered to the catalyst increases as the flow rate increases. This increased uptake rate is ultimately limited by the time the liquid is in contact with the pellet and thus, the styrene conversion decreases. Following on, if it assumed that when the hydrogen is required to diffuse from the gas phase into the liquid radial diffusion dominates, the increase in liquid velocity over the pellets surface will significantly reduce the amount of hydrogen diffusing to the pellet. This coupled with the decreasing residence time results in the styrene conversion reducing to a much greater extent than that observed in the hydrogen saturated feed case. To the best of the authors' knowledge, there are no examples in the literature where hydrogen saturated / free feeds have been investigated and therefore there are no studies to directly compare these results too.

To account for the time the substrate resides on the pellet, it is more pertinent to present the hydrogen uptake rate of the pellet for the different feed conditions. The experimental uptake rate is the sum of the transport processes and intrinsic chemical reaction rate and thus, it is defined as the overall mass transfer rate of hydrogen (MTR_{H2}) from here on in. The MTR_{H2} (mol / s) is derived from a mass balance over the liquid film as it passes over the pellet;

$$In \pm accumulation = Out$$

$$\varphi C_{H_2}(in) - MTR_{H_2} = \varphi C_{H_2}(Out)$$

$$MTR_{H_2} = \varphi(C_{H_2}(in) - C_{H_2}(Out))$$

Here the change in concentration of hydrogen is equal to the concentration of ethylbenzene formed in the liquid phase by the reaction $(C_{H_2}(in) - C_{H_2}(Out) = \Delta C_{Ethylbenzene})$. Finally, we consider the overall mass transfer over the surface area of the pellet, A_p, to give the overall mass transfer rate as a flux (mol / m^2 pellet . s) so that;

$$MTR''_{H_2} = \frac{QC_{Ethylbenzene}}{A_p} \quad \textbf{(4.3)}$$

Figure 4.5 shows the effect of liquid flow rate on the overall mass transfer rate of hydrogen to the pellet (otherwise referred to as the hydrogen uptake rate of the pellet). In both feed cases the uptake rate was observed to vary significantly with liquid flow, highlighting the effect convective and radial mass transfer processes have on the uptake rate of the pellet.

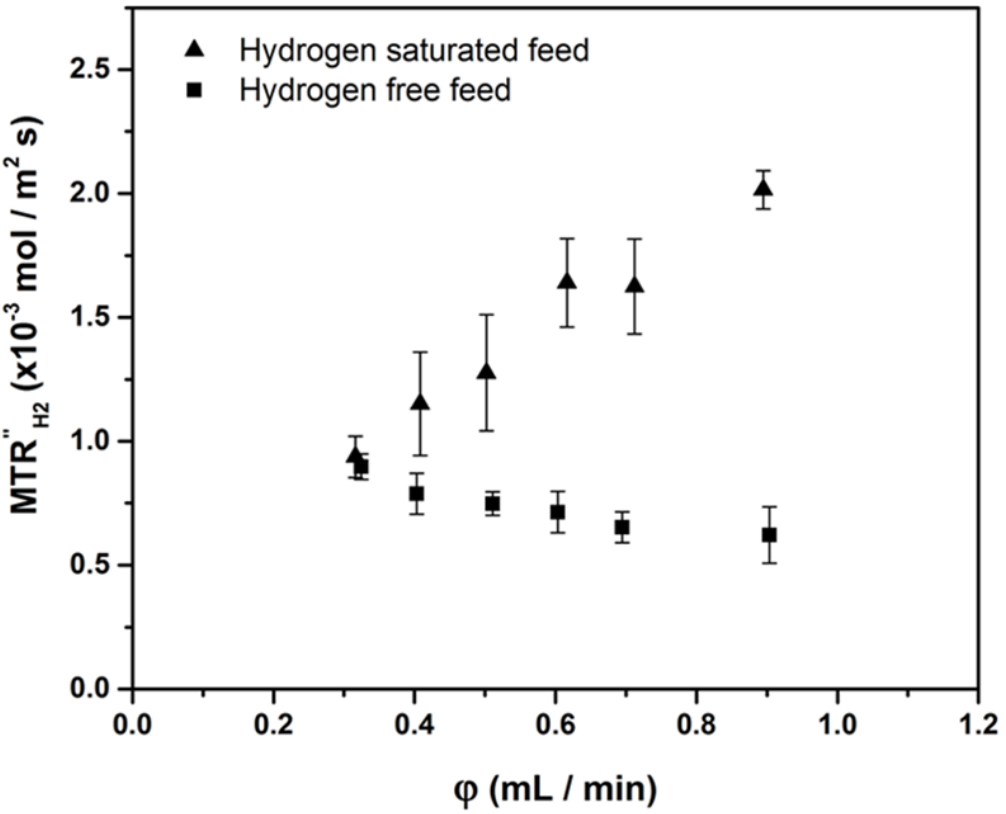

Figure 4.5: The effect of liquid flow rate on the overall mass transfer rate of hydrogen for hydrogen saturated and free feeds (0.18M styrene solution was used at 21 ^{o}C, atmospheric pressure and 300 mL / min gas flow rate).

When hydrogen is present in the feed, the MTR''_{H_2} is almost linearly proportional to liquid flow rate. In other words, the catalyst utility increases at the expense of overall conversion and hence, the concentration of hydrogen present in the liquid as it contacts the pellet is a significant factor in the uptake rate of the pellet. This is thought to be due to the increasing molar flow of hydrogen flowing onto the pellet at higher liquid flow rates. This is strong evidence that convective mass transfer is indeed the dominant transfer process supplying the pellet with hydrogen and results in higher mass transfer rates compared to the hydrogen free feedstock.

The opposite trend is observed when hydrogen is not present in the feed is and is thought to be evidence that radial diffusion is the dominating transfer process in this case. As the liquid flow rate increases the liquid film around the pellet will naturally become thicker and the rate at which hydrogen diffuses through the film to the catalyst support will decrease. To test this hypothesis, it was decided that a series of experiments would be conducted to investigate the effect liquid flow rate had over the film thickness over the catalyst surface. At the lower flow rates investigated, both datasets appear to begin moving towards the same point, suggesting that the film is sufficiently thin that the two transfer processes become comparable. Comparing these results to similar experiments in the literature, the results reported here differ from those of Satterfield *et al.* who studied the atmospheric hydrogenation of α-methylstyrene with a saturated hydrogen feed in a reactor system consisting of 8 mm spherical pellets on a string [45]. They observed dependence of the hydrogen consumption rate on flow rate only at and above 50 ℃. Herskowitz *et al*. observed a similar but less pronounced trend as seen in Figure 4.5 (saturated feed case), where the overall mass transfer rate of α-methylstyrene

increased with increasing liquid flow rate [185]. The authors used a wide, shallow (d_R = 2.35 cm, L = 0.13 cm) bed of 0.75% Pd/Al_2O_3 pellets and a hydrogen saturated liquid feed stock. It is speculated by the authors that the intrinsic kinetics and possibly pore diffusion (internal transfer) are controlling the reaction. This would suggest that convection is the dominating external transfer process supplying hydrogen to the catalyst as the increased molar flow results in a greater hydrogen uptake.

4.5 Determining the liquid film thickness over the pellet

The dispersed liquid phase trickles down through the column passing over the surface of the pellet creating a film that is subject to gravitational and shear forces (from the gas flow). This is somewhat akin to that of a falling film, which are widely encountered in the chemical processing industries [186]. Literature studies involving falling liquid films have been made on planar surfaces, down or inside pipes and on highly curved surfaces, such as wires [187]. Moreover, films in the presence of a gas flow have also been investigated but are somewhat limited in number. Significant attempts have been made to model and theoretically predict the film thickness over a number of geometries with and without gas flow [188-191]. Nearly all these investigations look to further understand and model the complex wave patterns and their formation, something that will not be focused on in this work. Hence, a detailed description of the state-of-the-art will not be featured.

The aim of this study was to estimate the liquid film thickness over the surface of the 1% Pd/C pellets and observe the effect liquid flow rate has on the film thickness. This could then be used to support the reasoning behind the decrease in pellet uptake rate seen in the hydrogen free feed case. The non-active carbon pellets were used to mimic the 1% Pd/C in the film thickness

experiments due to their non-pyrophoric nature and therefore, the two materials physical properties were compared before use. A complete analysis of the pellet size distributions, surface area and pore size distributions are presented in Chapter 3 but are summarised in Table 4.3.

4.5.1 Experimental procedure

To measure the film thickness during flow, a continued surface of material for the liquid to flow down was created by forming a vertical stack of carbon pellets (height = 4.25 mm and diameter = 1.49 mm) using Araldite Standard 2-part epoxy adhesive to bind the pellets together. Under normal temperature and pressure conditions (21 ^{o}C and 1 bara), a HPLC pump (Knauer 100Smartline) was used to distribute methanol from a needle tip over the stack. A Veho VMS-004 Discovery Deluxe USB Microscope filmed the liquid flow over the pellets at the bottom of the stack; this was used as the measurement area throughout the experiment. A schematic of the experimental set-up is shown in Figure 4.6. Liquid flow rates of 0.2-10 mL / min were chosen, which were identified to be within the laminar flow regime using their respective Reynolds numbers ($0 < Re < 60$), no pronounced rippling was visually observed. The methanol continually flowed over the stack for 5-10 mins before recording began to ensure a constant flow regime had been established.

Table 4.3: Comparison of the physical properties of the 1% Pd/C and non-active carbon pellets.

	1% Pd/C	**Non active-carbon pellets**
Surface area (BET) (m^2 / g)	941.22 ± 2.10	999.03 ± 5.02
Average pore Size: (BJH) (nm)	1.992	2.031
Pellet length - d50 (mm)	3.07 ± 0.86	3.66 ± 0.86
Pellet diameter – d50 (mm)	1.65 ± 0.16	1.97 ± 0.21

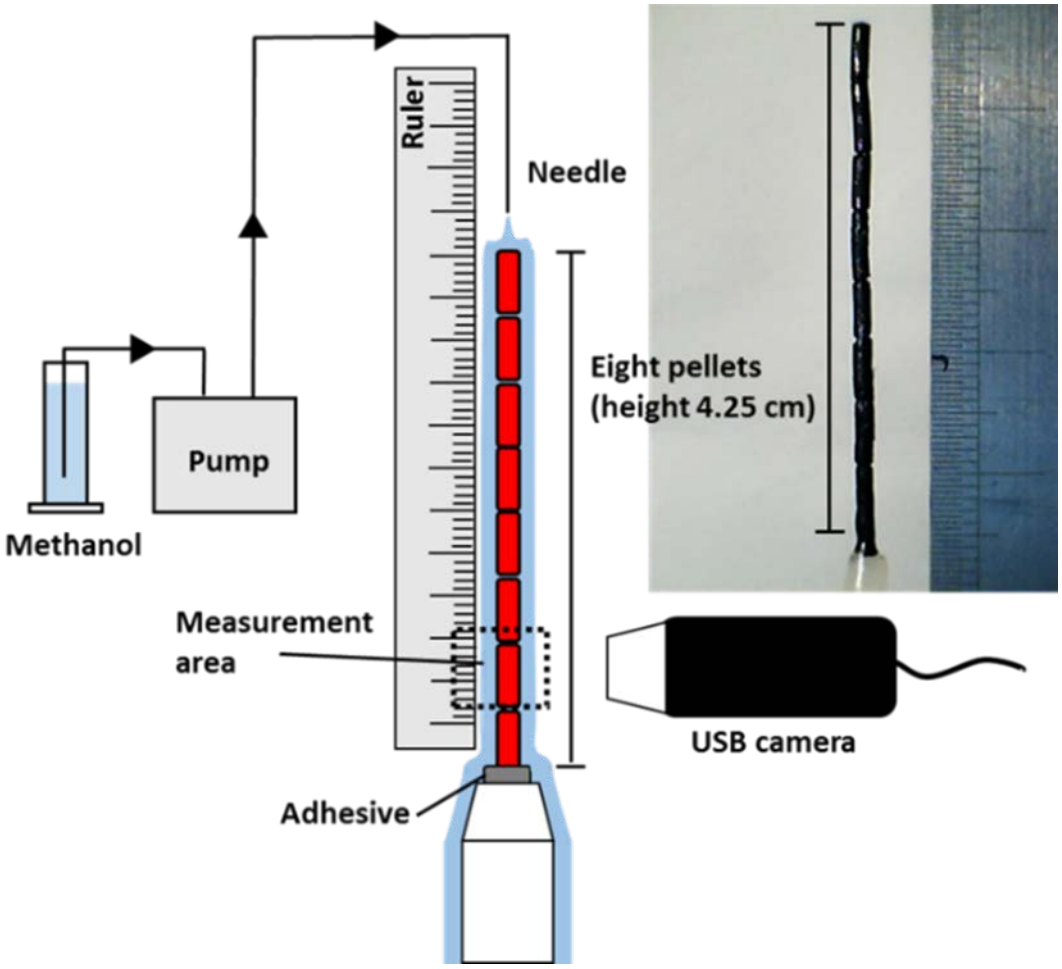

.

Figure 4.6: Schematic of the liquid film experimental setup and a picture of the glued pellets forming the stack before methanol flowed over.

The liquid film thickness over the pellets was determined by post-processing the recorded images via the image analysis software ImageJ.

4.5.2 Modelling liquid film thickness

The film thickness, δ, was modelled via a momentum balance of a film of uniform thickness δ flowing down over an ideal vertical cylinder (the pellet) of radius, r_p. The fluid is assumed to be an incompressible fluid with constant density and viscosity. For a fully developed laminar flow profile of thin films where $\delta \ll r_p$ the flow can be thought of as liquid falling down a vertical slab, and thus the gravitational force and drag forces acting on the fluid can be defined as;

$$F_{gravitional} = wh(\delta - x)\rho g$$

$$F_{drag} = wh\frac{\partial V_z}{\partial x}\Big|_x \mu$$

At steady state ($F_{gravitional} = F_{drag}$) the flow profile can be reduced to;

$$\mu\frac{\partial V_z}{\partial x} = (\delta - x)\rho g \qquad \textbf{(4.4)}$$

Integrating Eq. (4.4) between the no slip condition at the solid-liquid inference $x = 0$ and the air methanol interface $x = \delta$ (where it can be assumed $dV_z / dx = 0$) an expression for the velocity profile in the z direction, V_z can be derived as shown in Eq**.** (4.5);

$$\int_{x=o}^{x=\delta} \partial V_z = \frac{\rho g}{\mu}\int_{x=o}^{x=\delta}(\delta - x)\partial x$$

$$V_z = \frac{\rho g}{\mu}\left[\delta x - \frac{1}{2}x^2\right]_0^{\delta} = \frac{\rho g}{\mu}\left[\delta^2 - \frac{1}{2}\delta^2\right]$$

$$V_z = \frac{\rho g \delta^2}{2\mu} \qquad \textbf{(4.5)}$$

Here g is the gravitational constant, ρ the fluid density, μ the dynamic viscosity and δ the film thickness. Further integration of Eq. (4.5) taking the width of the slab as the circumference of the pellet (width = $2\pi r_p$) yields Eq. (4.6) which describes the film thickness in terms of volumetric flow rate.

$$\varphi = 2\pi r_p \int V_z \, dx$$

$$\varphi = \frac{2\pi r \rho g}{\mu}\int_{x=0}^{x=\delta} \delta x - \frac{1}{2}x^2 \, dx = \frac{2\pi r \rho g}{\mu}\left[\frac{1}{2}\delta x^2 - \frac{1}{6}x^3\right]_0^{\delta}$$

$$\delta = \sqrt[3]{\frac{3\varphi\mu}{2\rho g \pi r_p}} \qquad \textbf{(4.6)}$$

Lin and Liu [190] derived a general laminar velocity profile for any value of δ and r_p;

$$\frac{1}{r}\frac{\partial}{\partial r}\left(-r\frac{dv_z}{dr}\mu\right) = \rho g \qquad \textbf{(4.7)}$$

Integrating Eq. (4.7) between the no slip condition at the solid-liquid inference $r = r_p$ and the air methanol interface $r = r_p + \delta$ (where it can be assumed $dV_z/dr = 0$), the velocity profile flowing in the z direction, V_z can be expressed as;

$$V_z = \frac{\rho g}{4\mu}\left(\left(r_p^2 - r^2\right) + 2\left(r_p + \delta\right)^2 \ln\left(\frac{r}{r_p}\right)\right) \quad \textbf{(4.8)}$$

To derive an expression in terms of the volumetric flow rate, φ, Eq. (4.8) must again be further integrated between $r = r_p$ and $r = r_p + \delta$ giving Eq. (4.9).

$$\varphi = \int 2\pi r\, V_z\, dr$$

$$\varphi = \int 2\pi r \left(\frac{\rho g}{4\mu}\left((r_0^2 - r^2) + 2(r_0 + \delta)^2 \ln\left(\frac{r}{r_0}\right)\right)\right) dr$$

$$\varphi = \frac{\pi\rho g(r_0 + \delta)^2}{2\mu} \int_{r_0}^{r_0+\delta} \left(\frac{r r_0^2}{(r_0 + \delta)^2} - \frac{r^3}{(r_0 + \delta)^2} + 2r \ln\left(\frac{r}{r_0}\right)\right) dr$$

$$\varphi = \frac{\pi\rho g\left(r_p + \delta\right)^4}{\mu}\left(\frac{1}{2}\ln\left(\frac{r_p + \delta}{r_p}\right) - \frac{1}{8}\frac{r_0^4}{\left(r_p + \delta\right)^4} + \frac{1}{2}\frac{r_p^2}{\left(r_p + \delta\right)^2} - \frac{3}{8}\right) \quad \textbf{(4.9)}$$

The full derivation leading to Eq. (4.9) can be found in Appendix A**.** Expanding Eq. (4.9) in powers of $\left(\delta/r_p\right)$, it can be shown that the liquid film thickness is proportional to the cubic root of volumetric flow rate, as can be seen with the slab model. The film thickness δ in Eq. (4.9) was determined for a given flow rate and pellet diameter using the Solver functionality in Microsoft Excel. Figure 4.7 illustrates the momentum balance used for the two geometries modelled.

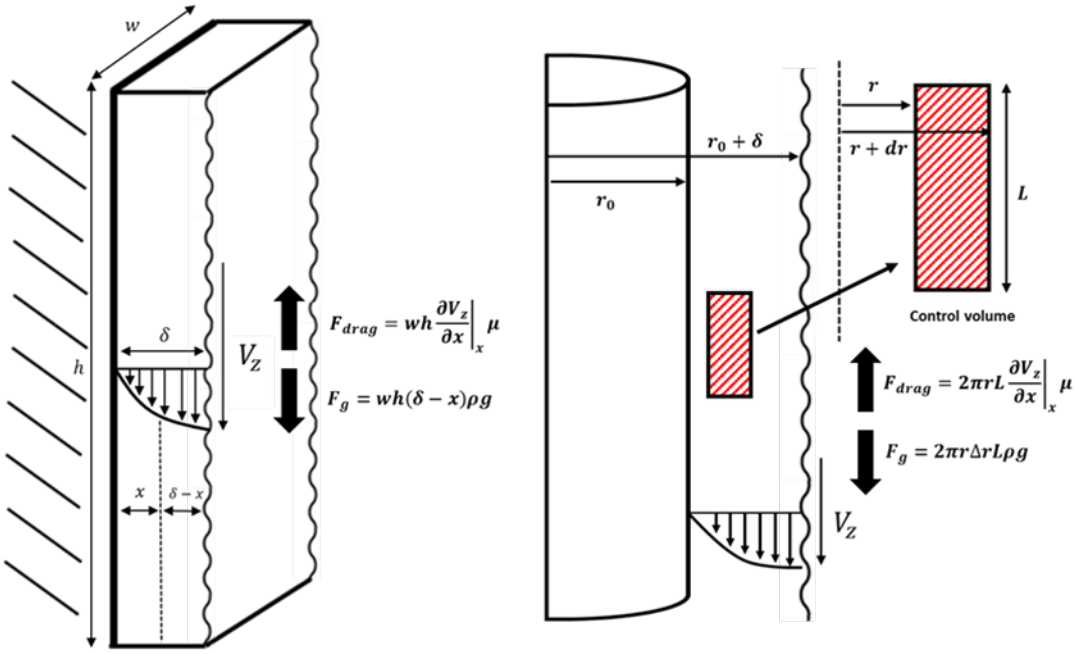

Figure 4.7: Definition sketches used in the slab (when $\boldsymbol{\delta \ll r_p}$) and the general cylinder model to theoretically determine the film thickness.

4.5.3 Liquid film thickness results

Images of the film thickness over the pellet surface at liquid flow rates of 0.2-10 mL/min are illustrated in Figure 4.8. When compared to the initial image taken with no liquid flowing down the pellet, an increase in the overall diameter of the pellet can be observed at all the flow rates investigated. However, it is difficult to identify a clear trend in terms of an increase in film thickness from visual assessment alone.

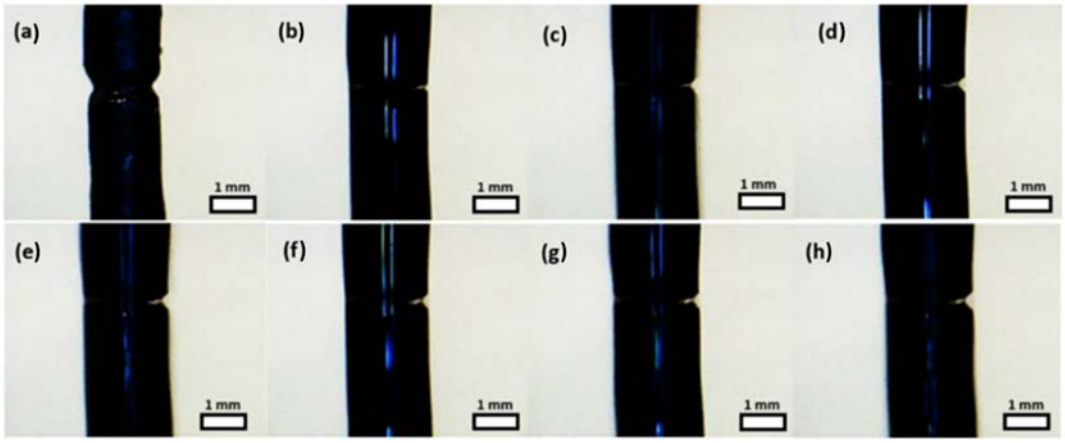

Figure 4.8: Images of the measurement area on the pellet stack showing the liquid film. Liquid flow rates are used in the pictures are as follows; a) no flow, b) 0.23, c) 0.52, d) 1.1, e) 2.8, f) 4.1, g) 5.3 and h) 9.9 mL/min

Figure 4.9 compares the measured film thicknesses to those predicted by the thin film (slab) and the general model. The experimental and modelling results show that the liquid film thickness does indeed increase with flow rate, and although a vertical stack was used the pellet in the bed will also have thicker films at higher flow rates. Therefore, it is highly possible that the thicker films suffer from increased diffusional resistances and thus, represents one of the reasons the uptake rate of the pellet decreases with increased flow rate. Both the thin film (slab) and general model fit the asymptotic nature of the experimental data obtained in this study well, with the thin film (slab) approach appearing to be more suitable at lower flow rates and the general model at higher flow rates. This is consistent with work for liquid flow on thin wires [187], where the disparity between films where δ is of the same order of magnitude as the radius of the wire, Eq. (4.6) and flat films, Eq. (4.9) was experimentally observed.

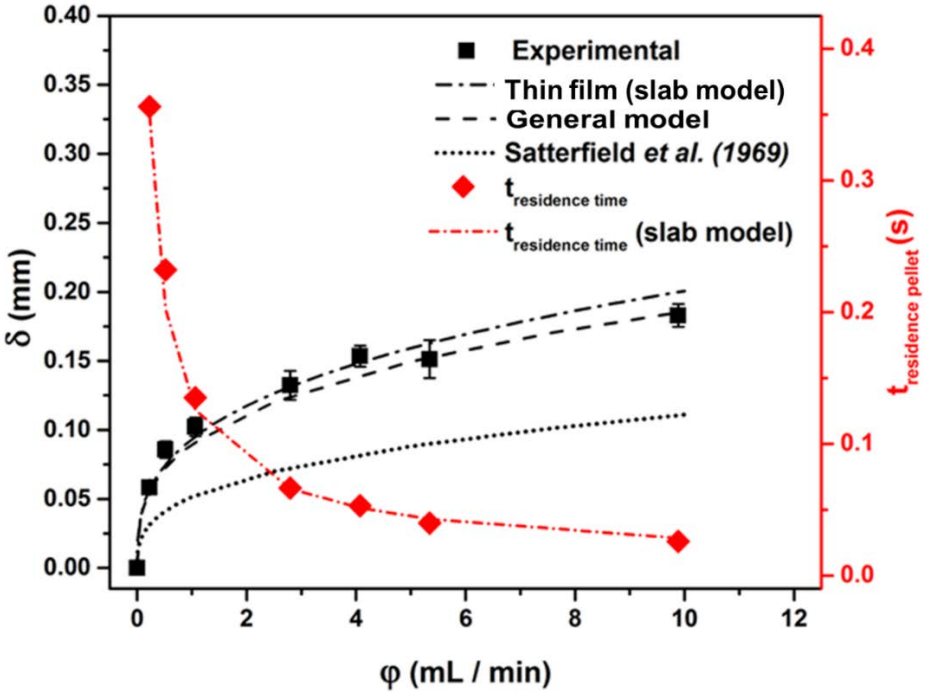

Figure 4.9: Comparison between the experimentally obtained film thicknesses and those calculated from the models for liquid flow rates between 0-10 mL min^{-1} at 1 bara and 21 ^{o}C.

For comparison, the film thickness predicted for flow over spherical catalysts using the model proposed by Satterfield *et al.* is also presented. The predicted film thickness over the pellets is roughly a factor of two larger than films on spherical particles. In relation to the thickness predicted here compared with those for trickle bed reactors in the literature, Tsamatsoulis *et al*. experimentally determined film thicknesses of ~ 0.01 mm for liquid flow over cylindrical pellets of a similar diameter (1.40 mm) used in this work [192]. The authors report that the film thickness remained almost constant with respect to liquid flow rate. The values reported by Tsmatsoulis *et al*. are lower that the film thicknesses determined here, though the phase velocities reported are higher and this would result in thinner liquid films. At the liquid flow rates investigated in the single pellet reactor (0-1 mL/min) the thin film (slab) and general model converge. Thus, for convenience the thin film model (slab), Eq. (4.6) was used to calculate the film thickness of the pellet in the bed.

Using the predicted film thickness from the models, the residence time of the liquid on the pellet as it passes through the single pellet reactor was then estimated. Assuming the pellet to be fully wetted, the residence time, $t_{residence\ pellet}$ can be estimated using Eq. (4.10) and is shown in Figure 4.9 for the thin film model (slab).

$$t_{residence\ pellet} = \frac{A_p \delta}{\varphi} \qquad \textbf{(4.10)}$$

The film thickness at all flow rates investigated is relatively uniform and no significant waves or rippling affects can be seen in any of the images shown in Figure 4.8. To classify which regime the film is operating in, the Reynolds number, Re, is commonly employed [193]. Three flow regimes have been experimentally identified for falling films in the literature, these are as follow;

- $Re_f < 20$ Laminar flow (negligible amount of rippling observed)
- $20 < Re_f < 1500$ Laminar flow (pronounced rippling observed)
- $Re_f > 1500$ Turbulent flow

In this work, the Reynolds number for a falling film is defined as $Re_f = \delta V_z \rho/\mu$. Using Eq. (4.6) from the thin film (slab) and Eq. (4.9) from the general cylinder models derivations, the liquid velocity, V_z was calculated and thus the Reynolds numbers for the experimental results were determined and are shown in Table 4.3. Interestingly, when assuming the system to be a thin film (slab model), the Reynolds number can also be expressed as followed;

$$Re_f = \frac{\delta\rho}{\mu} * \frac{\rho g \delta^2}{2\mu} = \frac{\rho^2 g \delta^3}{2\mu^2} \qquad \textbf{(4.11)}$$

4.6 Effect of film thickness on the pellets' hydrogen uptake rate

If the liquid film is considered to be a stagnant, in which all the resistance to mass transfer of hydrogen is found within (i.e. the gas-liquid and liquid-solid resistances are 'lumped' together), the effect film thickness has on the overall mass transfer rate of hydrogen from the gas-liquid interface to the solid surface can be clearly seen.

Table 4.4: Calculated Reynolds numbers and velocity of the liquid film.

$Q\ (mL/min)$	$\delta\ (mm)$	$V_z\ (m/s)$		Re_f	
		Slab	***Cylinder***	***Slab***	***Cylinder***
0	0	0	0	0.00	0.00
0.23	0.058	0.022	0.023	1.76	1.80
0.52	0.086	0.048	0.050	5.59	5.80
1.10	0.102	0.069	0.072	9.49	9.90
2.80	0.132	0.116	0.122	20.61	21.78
4.10	0.153	0.155	0.166	32.12	34.22
5.34	0.151	0.151	0.161	30.79	32.78
9.90	0.183	0.221	0.238	54.50	58.71

Following the derivation discussed in Section 2.3.1.1 for Whitman two-film theory with no reaction in the film itself the overall mass transfer rate through the film can be expressed as:

$$MTR_{H_2} = \frac{D_{H_2} a}{\delta}\left(C_{H_2,\ L} - C_{H_2,\ S}\right) \quad \textbf{(4.12)}$$

On inspection of Eq. (4.12), the relationship between the mass transfer rate and film thickness can be seen to be inversely proportional. Suggesting that the thicker the liquid film is, the slower the hydrogen will diffuse through it. Having determined a relationship between the film thickness and liquid flow rate ($\delta \propto \sqrt[3]{\varphi}$), the effect the liquid flow rate has on the mass transfer rate of hydrogen was assessed. The system was modelled as a slab to simplify the system and as at the liquid flow rates used the two film thickness models converge.

$$MTR''_{H_2} = \frac{D_{H_2}}{\delta}\left(C_{H_2,\ \mathrm{L}} - C_{H_2,\ S}\right) \quad \textbf{(4.13)}$$

This simple model was not able to reconcile the hydrogen saturated or hydrogen free feeds. However, it was successfully utilised to show the relationship between the liquid flow rate and hydrogen uptake rate for the hydrogen free feed case (where the mass transfer decreased with increasing liquid flow rate). The linear correlation plot between uptake and film thickness/liquid flow rate is illustrated in Figure 4.10.

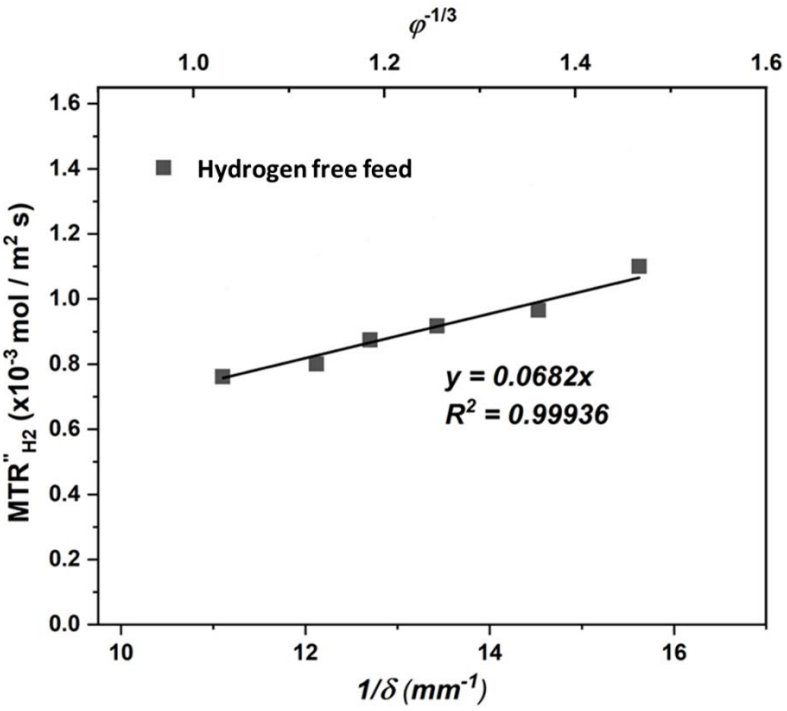

Figure 4.10: Linear correlation plot between the mass transfer rates of hydrogen for the hydrogen free feed and the reciprocal film thickness and liquid flow rate ($\boldsymbol{\varphi}^{-\frac{1}{3}}$).

The plot provides evidence that while the model is clearly too simple to describe the transfer of hydrogen to the pellet and reaction on the catalyst nanoparticles, the increase in liquid film thickness can be directly attributed to the decrease in pellets' overall hydrogen uptake rate. Thicker liquid films result in a larger diffusional distance for the hydrogen to reach the catalyst support and thus, the gas-liquid mass transfer resistance increases resulting in less hydrogen reacting on the catalyst surface. The decrease in the gas-liquid mass transfer coefficient has been attributed as the primary factor in the reduction in uptake rate and thus, conversion in trickle bed reactors [139]. Comparing this result with trends for the gas-liquid mass transfer coefficients for trickle bed reactors in the literature, Stamatiou and Muller compiled values reported from six studies to show that the coefficient decreases with increasing liquid flow rate [108]. The authors do not comment on the reasons

this trend is observed, though it is strongly suspected to be a consequence of an increase in liquid film thickness surrounding the catalyst pellets.

As previously discussed, when a hydrogen saturated feed was used, diffusion from the gas-liquid interface through the bulk of the liquid is not the dominant mass transfer process (though it will still be occurring). As hydrogen is already present in the film, convective transport of hydrogen driven by the bulk flow of the liquid becomes the dominant transfer process and thus, the liquid film thickness does not have a significant detrimental effect on the uptake rate of hydrogen by the pellet. Some evidence of this phenomenon occurring in trickle beds can be found in the literature in studies comparing the reaction rates of diluted and undiluted catalyst beds [108, 194]. When operating diluted packed beds, the inert media still provides a surface for hydrogen to diffuse into the liquid film before it reaches a catalytically active pellet. Therefore, it is postulated that in these circumstances convective transport of hydrogen could be the dominant process supplying hydrogen to the catalyst's supports surface. Yamada *et al.* compared the hydrogen uptake rates between undiluted and beds diluted with inert fines for the hydrogenation of α-methylstryene in a laboratory trickle bed reactor [194]. The authors report that the reaction rate was notably higher when diluted beds were used and reaction rate was independent of the liquid flow rate. When considering the hydrogen saturated feed trends presented in this study, one may expect the reaction rate to have increased if convection was dominant as was observed in the single pellet reactor. However, it is postulated that though at higher liquid velocities the rate at which hydrogen is supplied to the catalyst pellets will increase via convection, the concentration of hydrogen in the liquid will

decrease as a result of the increased resistance to mass transfer over the inert surface before the liquid contacts the pellet. Hence, the reaction rate is observed to neither increase nor decrease with respect to liquid flow rate.

The failure of the model to describe even the hydrogen free feed case suggests that though convective and radial mass transfer are likely responsible for the experimental trends observed, the analysis thus far fails to provide a full picture in describing the phenomena at work supplying hydrogen to the pellet. In the case of the hydrogen free feeds, hydrogen will diffuse into the liquid on any surface present before the pellet, even if it is a non-active surface and hence, there must be a convective contribution to the uptake rate observed. In this system, the glass inert beads provide the surface required for transfer and therefore, hydrogen will be present in the liquid when it encounters the pellet. Moreover, in the saturated feed case the hydrogen concentration in the liquid must decrease as the liquid travels further down the column due to the trickle bed being at atmospheric pressure and the feed saturation occurring at a pressure of 1 barg. To fully quantify the contributions of the two transfer processes it was decided the system would need to be modelled.

4.7 Concluding remarks

By scaling down to a single catalyst pellet, it has been shown that the convective and radial diffusive transfer processes can be isolated and their effects on the hydrogen uptake rate of the pellet observed. The amount of hydrogen present in the feed significantly effects the uptake rate of the pellet due to convective transfer being the dominant transfer process and this significantly increases the catalyst utility. On the other hand, the uptake rate of hydrogen free feeds was significantly impacted by liquid flow, and the fact

that the liquid film thickness was shown to be one of the causes suggests that radial mass transfer is dominant or at the very least limiting in this case. Failure to describe the experimental trends via a simple model highlighted that though the two transfer processes are likely the cause of the trends, qualitative analysis alone is not enough to fully understanding the contributions each has to the pellets uptake rate. It is postulated that the hydrogen concentration in the liquid before it reaches the pellet could vary significantly with flow rate irrespective of the feed conditions. To account for this, a model that can account for hydrogen mass transfer over the inert beds prior to the pellet and the pellet itself will be developed in Chapter 5. Moreover, to fully reconcile the effect hydrogen saturation of the feed had on the hydrogen uptake rate of the pellet, it is hypothesised that inclusion of both the convective and diffuse (normal to the catalyst surface) transport process is required. This would pave the way for quantification of the two transport processes, and offer a methodology to control and manipulate them.

Chapter 5
Modelling and decoupling the convective and radial mass transport processes of hydrogen to the pellet

It was highlighted in the concluding remarks of Chapter 4 that the overall mass transfer rate of the pellet was significantly affected by both the feed conditions and liquid flow rate. As discussed, this was first thought to be attributed to the change in liquid film thickness with respect to liquid velocity, resulting in increased diffusional resistances at higher flow rates. Though this may explain the decrease in the pellet's hydrogen uptake rate when the feed has no hydrogen present, this wasn't thought to account for the increase in uptake rate when hydrogen was present in the liquid feed. Instead, it was hypothesised that by altering the feed conditions and liquid flow rate the concentration of hydrogen at the point where the liquid meets the pellet was being manipulated. Thus, we must consider the two transfer mechanisms operating simultaneously by which the pellet is supplied hydrogen. The first mechanism is the supply of hydrogen from the liquid flowing onto the pellet and is defined here as the convective transfer. Once at the pellet, external (gas-liquid and liquid-solid) and internal (pore diffusion to the catalyst surface) mass transfer will begin to supply hydrogen to the pellet and is the second mechanism defined as the radial transfer. A schematic of the pellet showing the two hydrogen transfer processes is shown in Figure 5.1.

5.1 Aims

The objective of this chapter is to quantitatively evaluate the extent to which the two mechanisms are supplying the pellet with hydrogen via mathematical modelling.

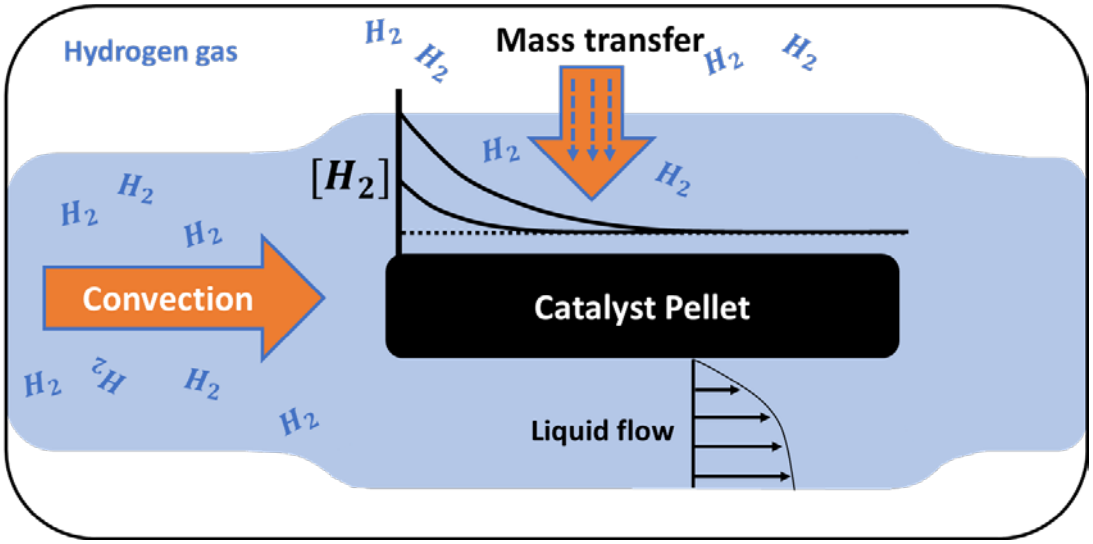

Figure 5.1: Schematic of a pellet illustrating the two transfer mechanisms that the model will decouple; (i) convective transfer of hydrogen from the liquid and (ii) radial diffusion over the catalyst surface.

To achieve this, the single pellet reactor will be split into two sections where mass transfer can occur; (i) the non-active glass beads where no reaction occurs and (ii) the pellet itself where reaction occurs. Thus, a two-stage mass transfer model will be presented that is capable of describing both feed cases and the effect of liquid flow rate. The model will determine the concentration of hydrogen in the liquid film close to the catalyst surface and aim to highlight how the convective and radial diffusion mechanisms affect this film concentration. With this knowledge, it is postulated that the rate of supply of hydrogen to the catalyst surface can be controlled and further manipulated, potentially improving the selectivity or catalyst utility of a reaction independent of scale.

5.2 Modelling trickle bed reactors and catalytic systems

As the chapter discusses the modelling of catalytic systems in continuous flow, a brief literature review will be presented. Work where parameters such as the gas-liquid mass transfer coefficient are calculated experimentally will

not be included here, as experimental methods nor empirical correlations were used to estimate coefficients for the model. Given the complex relationship between the hydrodynamics and mass transfer/kinetics occurring in trickle bed reactors, many authors have attempted to model the hydrodynamics, intraparticle mass transfer and multicomponent mass transfer separately. There are many instances, for example of studies using numerical methods to model flow and hydrodynamic behaviour in trickle bed reactors [120, 195], though these are beyond the scope of this literature review. In addition, the use of 3D models, such as computational fluid dynamics (CFD), which will not form part of the discussion here but of which Wang *et al*. present a detailed overview of the state-of-the-art, have also been used extensively to model flow and mass transfer in trickle bed reactors [44]. Given the breadth of modelling studies present in the literature in relation to the areas stated, this review will solely focus on modelling the mass transfer effects in trickle bed reactors.

One of the first comprehensive mathematical models used to describe the mass transfer effects in a trickle bed reactor was proposed by Satterfield *et al*., who compared several models with the experimental results for the hydrogenation of α-methylstyrene over a stack over spherical pellets [45]. Considering both the diffusional transfer process normal to the pellets' surface and the convective transfer process in the direction of flow, the authors derived a model that incorporated the mixing in the liquid film between pellets. Two extremes were considered in relation to the extent of mixing; (i) a non-mixed model where the hydrogen concentration in the liquid remains constant between pellets and (ii) a mixed model where the hydrogen concentration in the liquid increases to a flow averaged value between pellets.

The models produced significantly different trends like those observed in the uptake rates of hydrogen free and saturated feed presented in Chapter 4, with only the mixed model able to reconcile the experimentally observed, overall reaction rates. Interestingly, the author comments that inefficient mixing was visually observed using a dye experiment, but the mixed model is clearly the more appropriate model to describe the rate data. It is speculated here, that the mixed model accounts for the enhanced convective transfer as a result of the increased hydrogen concentration in the liquid. Banchero *et al*. investigated the hydrogenation of α-methylstyrene in a trickle bed reactor where they considered the initial effect of convection as the liquid encounters the catalyst bed [46]. In this 'entrance' zone, they assume there is a variation in the concentration profile as the catalyst pellets consume the hydrogen dissolved in the liquid feed. The authors determined that the effect of this region on the overall reaction rate is dependent on the length of the bed, accounting for 10% of the overall rate in a relatively small bed (15 cm). As expected, this percentage drops significantly as the length of the bed increases.

Rajashekharam *et al*. proposed a reactor model for the hydrogenation of 2,4-dinitrotoluene that not only incorporated the external and internal mass transfer processes but also the partial wetting and transfer of hydrogen between the dynamic and stagnant potions of liquid in the reactor [196]. Following the methodology set out by Tan and Smith [197], the authors assumed that each catalyst particle could consist of dry, wetted due flowing liquid and wetted due to stagnant liquid zones. An approximate solution for the catalyst effectiveness factor was then determined for each zone. A hydrogen mass balance over the dynamic flowing portion of the liquid was

used to determine the global rate of reaction as a function of reactor length. Many of the mass transfer parameters were determined from correlations found in the literature. The partial wetting model was able to reconcile the experimental global hydrogenation rates reasonably well, showing an increase in reaction rate as the liquid velocity increased. The authors observed that for this chemical system the gas-liquid and liquid-solid mass transfer resistances were comparable, and it was the gas-solid resistance that was most prominent.

Toppinen *et al*. used a different approach to model the mass transfer effects in a trickle bed reactor by deriving and solving the Maxwell-Stefan equations for the system and compared the results to another modelling approach using the effective diffusivity method [198]. Arguing that the intraparticle mass transfer is a facet of the kinetic model, the authors developed a multicomponent reactor model for the gas-liquid and liquid-solid mass transfer coefficients. The Maxwell-Stefan and effective diffusivity models consist of a series of ordinary differential equations representing the mass and energy balances of the flowing phases and the mass and energy balances for transfer between the phases, which were then solved numerically. Rather than use a correlation to determine the two mass transfer coefficients, the authors employed the Newton-Raphson method to numerically approximate unknown variables such as the mass fluxes and species concentration at the interfaces to calculate the gas-liquid and liquid-solid mass transfer coefficients in the model. Though the authors go further by providing a hydrogenation simulation case study, there is no attempt to reconcile experimental data with the rigorous model. Maxwell-Stefan theory is generally accepted to be more a more comprehensive model than Fickian

diffusion, with the inclusion of a thermodynamic correction factor in the Fickian diffusivity coefficient [199]. Though this correction factor accounts for deviations from ideal-behaviour, difficulties approximating the diffusion coefficients limits its use.

5.3 Two stage mass transfer model

The feed initially flows over a nonreactive portion of the bed, resulting in hydrogen mass transfer into the liquid over the surface of the non-active beads. The hydrogen concentration in the liquid will either increase or decrease towards equilibrium (1 bara hydrogen gas pressure) depending on the initial feed conditions. Once the liquid feed reaches the pellet, reaction will occur at the surface of the pellet, resulting in depletion of the hydrogen flowing into the pellet's film from the bead section. Additional hydrogen is simultaneously transferred into the film at the gas liquid interface over the pellets' surface. Thus, the system is treated as two successive mass transfer sections: (i) a bed consisting of 48 glass beads in which the hydrogen concentration moves from the inlet concentration, C_{in}, to the liquid concentration at the point where it reaches the pellet, C_o. Followed by (ii) the cylindrical pellet which we assume is fully wetted with an averaged film thickness along its length.

5.3.1 Liquid saturation with hydrogen on the glass beads

In the section of the bed above the pellet, liquid is held in place between the beads by capillary forces acting near the bead contact points. This portion of the liquid is referred to as the static holdup and is treated as a liquid reservoir that the hydrogen diffuses to via a liquid film (of thickness, δ_b where $V_{film} < V_{reservior}$) flowing over the beads. Here we assume that the film flowing over

a bead (dynamic holdup) can be treated as if it's flowing over a cylinder with the same diameter as the bead and enough mixing occurs around the contact points (illustrated in Figure 5.2). Therefore, the total area of the film on the beads, A_{bs}, is;

$$A_{bs} = N_{bs}\, A_b \tag{5.1}$$

Here, A_b is the surface area of a single glass bead and N_{bs} the total number of beads in the reactor prior to the pellet. If the mass transfer coefficient changes slightly with liquid flow rate, the film mass transfer coefficient k_b can be linearised around a reference point:

$$k_b \approx k_{b.ref} \times \left[1 + \gamma_1 \frac{(\varphi - \varphi_{ref})}{\varphi_{ref}}\right] \tag{5.2}$$

where γ_1 and $k_{b.ref}$ are fitted parameters. The lowest flow rate was arbitrarily chosen as the reference condition φ_{ref} = 0.2 mL min^{-1}.

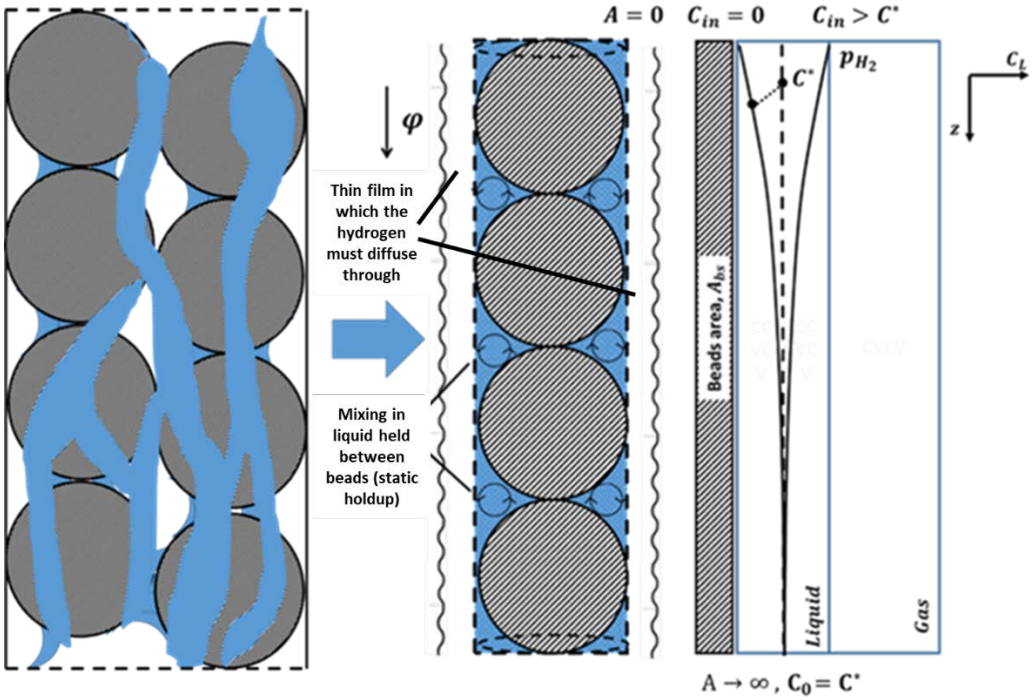

Figure 5.2: Schematic showing the method of modelling mass transfer of hydrogen into the liquid film on the glass beads prior to the catalyst pellet and the concentration profile in the static liquid referred to as the reservoir**.**

An expression of the concentration of hydrogen in the liquid, C_L, is obtained following a one-dimensional steady state mass balance over a section of the surface area in the glass beads section:

$$\varphi \, dC_L = k_b \, (C^* - C_L) \, dA$$

$$\int_{C_0}^{C_{in}} \frac{dC_L}{(C^* - C_L)} = \int_0^{A_{bs}} \frac{k_b}{\varphi} dA$$

$$[-\ln(C^* - C_L)]_{C_0}^{C_{in}} = \left[\frac{A \cdot k_b}{\varphi}\right]_0^{A_{bs}} \quad \textbf{(5.3)}$$

Subject to the boundary condition that at $A = 0$, $C_L = C_{in}$ and $A = A_{bs}, C_L = C_0$, solving Eq. (5.3**)** gives the hydrogen concentration at the point where the liquid reaches the pellet C_o, where C_{in} is the concentration of hydrogen in the liquid feed and C_0 the concentration of hydrogen in the liquid as contacts the pellet

$$C_0 = C^* - (C^* - C_{in})\left(e^{-\frac{k_b A_{bs}}{\varphi}}\right) mol \, m^{-3} \quad \textbf{(5.4)}$$

Here C^* is the equilibrium concentration of hydrogen in methanol obtained using the Henry's constant, H for hydrogen in methanol [200]:

$$P_{H_2}(MPa) = H \, C^*$$

$$\ln(H) = 122.3 - 4815.6\frac{1}{T(K)} - 17.5\ln(T) + 1.4x10^{-7}P_{H2} \quad \textbf{(5.5)}$$

5.3.2 Pellet section: Axial hydrogen concentration profile

The pellet section of the bed was modelled as a plug flow reactor, with mass transfer from the gas phase to the film modelled as diffusion through a stagnant film, and mass transfer from the film to the catalyst surface and the subsequent reaction modelled by a resistance in series model [92]. This assumes the concentrations at the gas liquid interface to be in equilibrium,

and that the flux of hydrogen from the gas liquid interface to the site of reaction reaches steady state instantaneously. It is debatable whether plug flow conditions are prevalent in this scale of reactor in relation to either the liquid or gas phase. Moreover, the extent of axial dispersion (if any) in the single pellet reactor was not experimentally verified. However, plug flow models have been shown to successfully model large scale trickle bed reactors in the literature [201] and thus, plug flow conditions were assumed here. A schematic of the pellet, the modelling methodology and the hydrogen concentration profiles in the liquid can be seen in Figure 5.3. If axial dispersion was experimentally shown to be significant a dispersion model would be more suitable [202] [142]. An alternative approach to modelling non-ideal systems where axial dispersion in the liquid phase causes deviation from plug flow behaviour is the tanks in series model [203].

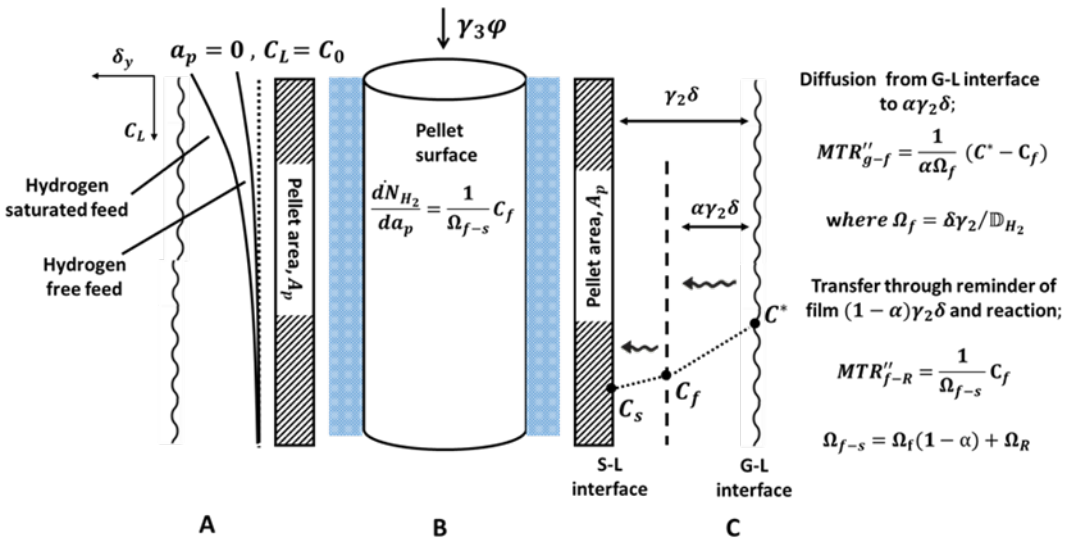

Figure 5.3: Schematic illustrating the modelling approach of the pellet in the bed. Diagram illustrating (A) the hydrogen concentration profile in the liquid film over the pellet, (B) a schematic of the pellet and (C) the method in which the hydrogen concentration in the film close to the surface of the pellet was modelled.

Having passed over the glass beads above, the liquid encounters the pellet with a characteristic hydrogen concentration, C_0, depending on the rate at which the liquid flows through the bed. A fraction, γ_3, of the liquid passes over the pellet, and is assumed to completely cover its' surface. The remainder flows over the glass beads and the walls adjacent to the pellet. The liquid flow results in an averaged film thickness, γ_2, across the length of the pellet. The parameter, γ_2, allows for an average pellet film thickness that is different, but proportional to the observed thickness as described by Eq. (4.6) in Chapter 4.

It is assumed that within the film there is an average film concentration, C_f, that is achieved some distance, $\alpha\,\gamma_2\delta$, from the gas liquid interface at steady state. Thus, α, represents the fraction of the liquid film that forms the gas to liquid film transport resistance, where $\alpha \leq 1$. Therefore, diffusion from the gas liquid interface to the film is then:

$$MTR''_{g-f} = \frac{1}{\alpha\Omega_f}\left(C^* - C_f\right)\frac{mol}{m^2\,s} \qquad \textbf{(5.6)}$$

Where Ω_f is the gas to liquid film transport resistance; $\Omega_f = \delta\gamma_2/\mathbb{D}_{H_2}$ and MTR''_{g-f} is expressed as mol / m^2 (pellet) s . Transport from the film to the catalyst surface and subsequent reaction may be described by a mass transfer in series model with two resistances: (i) diffusion from the film to the surface, Ω_{f-s}, and (ii) chemical reaction, Ω_R (where $\Omega_R = 1\ /\ k''_{obs}$ and k''_{obs} is the observed rate constant per unit area of pellet (s m^{-1})):

$$MTR''_{f-R} = \frac{1}{\Omega_{f-s}}\,C_f\,\frac{mol}{m^2\,s} \text{ with } \Omega_{f-s} = (1-\alpha)\,\Omega_f + \Omega_R\,\frac{s}{m} \qquad \textbf{(5.7)}$$

Here the resistance $(1-\alpha)\,\Omega_f$ describes the flux to the catalyst surface at concentration C_s, as diffusional transport through a liquid film with thickness $(1-\alpha)\,\delta\gamma_2$:

$$MTR''_{f-s} = \frac{1}{(1-\alpha)\Omega_f}\ (C_f - C_s) \qquad \textbf{(5.8)}$$

The hydrogenation of styrene may be described as proceeding via Langmuir adsorption of styrene followed by subsequent hydrogenation on the surface of the palladium [43]. As the styrene conversion is small (~2%) and the process is operated continuously, the reaction rate per unit pellet area is linearised with respect to the hydrogen concentration so $(-R''_S) = \left(-R''_{H_2}\right) = k''_{obs}\ C_s\ \left(\ mol\ /\ m^2_{pellet}\ s\right)$. The mass transfer in series model assumes the rate of change of the concentration, C_s, is small compared to the hydrogen flux. Following the methodology set out by Herskowitz and Abuelhaij it is therefore assumed that the liquid-solid mass transfer rate and reaction rate is equal so that MTR''_{f-s}=$(-R''_s)$ [155]. Therefore Eq. (5.7**)** then follows by elimination of C_s, this is in essence the Bodenstein assumption [108].

$$MTR''_{f-R} = \frac{1}{(1-\alpha)\Omega_f}\ \left(C_f - C_s\right) = \frac{1}{\Omega_R}\ C_s$$

$$MTR''_{f-R}(1-\alpha)\Omega_f = \ \left(C_f - C_s\right), \qquad MTR''_{f-s}\,\Omega_R = \ C_s - 0$$

$$MTR''_{f-R}(1-\alpha)\Omega_f + MTR''_{f-R}\cdot\Omega_R = \ \left(C_f - C_s\right)\ +\ C_s - 0 = C_f$$

$$MTR''_{f-R} = \frac{1}{(1-\alpha)\Omega_f + \Omega_R}\ (C_f)$$

To derive an expression for the hydrogen film concentration, C_f, a differential molar balance was conducted. The molar flow of hydrogen into and out of a portion film over the pellet surface, da_p, was balanced against the radial transfer of hydrogen into the film from the gas phase (Eq. 5.6) and transfer out of the film to react on the surface of the catalyst (Eq. 5.7). A schematic of the differential molar balance is shown in Figure 5. 4.

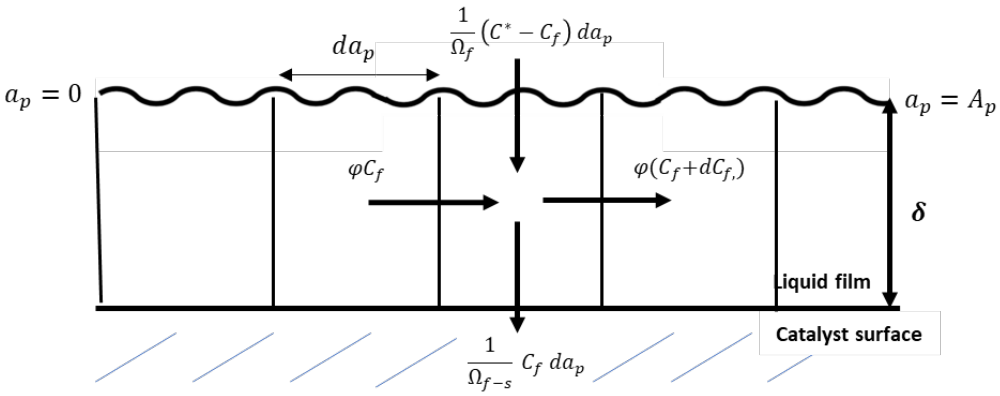

Figure 5. 4: Schematic showing the differential molar balance of a portion of the liquid film used to derive the expression for the film concentration, $\boldsymbol{C_f}$.

$$In = out + radial\ transfer\ in - radial\ tansfer\ out$$

$$\gamma_3 \varphi C_f = \gamma_3 \varphi \left(C_f + dC_f\right) + \frac{1}{\alpha \Omega_f}\left(C^* - C_f\right) da_p - \frac{1}{\Omega_{f-s}} \left(C_f\right) da_p$$

$$\gamma_3 \varphi\, dC_f = \left[\frac{1}{\alpha \Omega_f} \left(C^* - C_f\right) \ - \frac{1}{\Omega_{f-s}}\, C_f \right] da_p \qquad \textbf{(5.9)}$$

Integrating Eq. (5.9**)** over the area of the pellet where $C_f = C_o$ at $a_p = 0$, gives the fluid concentration of hydrogen as a function of the pellet area passed by the fluid:

$$dC_f = \frac{\frac{1}{\alpha \Omega_f} + \frac{1}{\Omega_{f-s}}}{\gamma_3 \varphi} \left[\frac{C^*}{1 + \frac{\alpha \Omega_f}{\Omega_{f-s}}} - \ C_f \right] da_p$$

For simplicity this expression can be written as follows;

$$dC_f = \frac{1}{A_o}\left[C_\infty - \ C_f \right] da_p$$

$$with\ C_\infty = \frac{C^*}{1 + \alpha \Omega_f / \Omega_{f-s}} mol\ m^{-3}\ and\ A_o = \frac{\gamma_3 \varphi}{\frac{1}{\alpha \Omega_f} + \frac{1}{\Omega_{f-s}}} m^{-2}$$

$$\int_0^{C_f} \frac{dC_f}{C_\infty - \ C_f} = \frac{1}{Ao} da_p$$

$$C_f = C_\infty - (C_\infty \ - C_o) e^{-\frac{a_p}{A_o}}\ mol\, m^{-3} \qquad \textbf{(5.10)}$$

5.3.3 Hydrogen uptake rate on the surface of the pellet

The total rate at which hydrogen is consumed by the pellet, $\dot{N}_{H2}$, per unit time (mol/s) is given by integrating the mass transfer to the surface across the whole pellet area, A_p:

$$d\dot{N}_{H2} = \frac{1}{\Omega_{f-s}}\, C_f\, da_p \tag{5.11}$$

Substituting Eq. (5.10**)** into Eq. (5.11**)** and integrating from $C_f = C_o$ at $a_p = 0$ gives;

$$\dot{N}_{H2} = \int_0^{A_P} \frac{1}{\Omega_{f-s}} \left(C_\infty - (C_\infty - C_0) e^{-\frac{a_p}{A_0}} \right) da_p$$

$$\dot{N}_{H2} = \frac{1}{\Omega_{f-s}} \left(C_\infty A_p - (C_\infty - C_0) \int_0^{A_p} e^{-\frac{a_p}{A_0}}\, da_p \right)$$

$$\dot{N}_{H2} = \frac{A_p}{\Omega_{f-s}} \left(C_\infty - (C_\infty - C_0) \frac{A_0}{A_p} \left(1 - e^{-\frac{A_p}{A_0}} \right) \right)$$

$$\dot{N}_{H2} = \frac{A_p}{\Omega_{f-s}} \left[C_\infty - [\, C_\infty - \, C_0] \, \frac{A_o}{A_p} \left(1 - e^{-\frac{A_p}{A_o}} \right) \right] \tag{5.12}$$

In Eq. (5.12)**,** the term in the square brackets represents the characteristic hydrogen concentration in the liquid film;

$$MTR''_{H_2} = \frac{\dot{N}_{H2}}{A_P} = \frac{1}{\Omega_{f-s}} \overline{C_f} \tag{5.13}$$

$$with\ \overline{C_f} = \left[1 - \left[1 - \frac{C_0}{C_\infty} \right] \frac{A_o}{A_p} \left(1 - e^{-\frac{A_p}{A_o}} \right) \right] \times C_\infty$$

$$with\ C_\infty = \frac{C^*}{1 + \alpha \Omega_f / \Omega_{f-s}} mol\, m^{-3}\ and\ A_o = \frac{\gamma_3 \varphi}{\frac{1}{\alpha \Omega_f} + \frac{1}{\Omega_{f-s}}} m^{-2}$$

The key equations and the respective model parameters that are used in the two stage model to calculate the overall mass transfer rate of the pellet are summarised in Table 5.1.

Table 5. 1 Summary of the key equations and parameters used in the two-stage model. Bolded symbols are fitted in the model

Mass transfer over the bead section of the bed	
Estimation of mass transfer coefficient, k_b	
$k_b \approx \boldsymbol{k_{b.ref}} \times \left[1 + \boldsymbol{\gamma_1} \frac{(\varphi - \varphi_{ref})}{\varphi_{ref}}\right]$	$\boldsymbol{k_{b.ref}}$ and $\boldsymbol{\gamma_1}$ are fitted parameters to account for changes in k_b as a function of flow rate, φ. $\boldsymbol{\gamma_1}$ governs the extent the mass transfer into the film is effected by the flow rate (fitted).
Hydrogen concentration at the point where the liquid reaches the pellet C_o	
$C_0 = C^* - (C^* - C_{in})\left(e^{-\frac{k_b A_{bs}}{\varphi}}\right)$	C_{in} accounts for the extent of hydrogen saturation in the feed before entering the bed of bead. Both C^* and C_{in} approximated via Henry's law.
Mass transfer and reaction over the pellet	
Determination of the hydrogen film concentration C_f	
$C_f = C_\infty - (C_\infty - C_o)e^{-\frac{A_p}{A_o}}$	Ω_f is the film resistance and is defined as $\Omega_f = \delta\boldsymbol{\gamma_2}/\mathbb{D}_{H_2}$. Here y_2 is a parameter to account for the increased liquid film thickness in the bed as δ is approximated via a falling film model (fitted).
$C_\infty = \frac{C^*}{1 + \boldsymbol{\alpha}\Omega_f/\Omega_{f-s}}$ and $A_o = \frac{\boldsymbol{\gamma_3}\varphi}{\frac{1}{\boldsymbol{\alpha}\Omega_f} + \frac{1}{\Omega_{f-s}}}$	$\boldsymbol{\gamma_3}$ is the portion of liquid that actually flows onto the pellet, not the wetting efficiency (fitted) $\boldsymbol{\alpha}$ is a parameter that accounts for the portion of the liquid film that forms the mass transfer resistance (fitted) Ω_{f-s} is the film to catalyst surface transport resistance and defined as $\Omega_{f-s} = (1 - \boldsymbol{\alpha})\,\Omega_f + \Omega_R$. Ω_R is the chemical reaction resistance and is estimated from the literature
Overall mass transfer flux of hydrogen, MTR''_{H_2}	
$MTR''_{H_2} = \frac{\dot{N}_{H2}}{A_P} = \frac{1}{\Omega_{f-s}}\overline{C_f}$	$\overline{C_f}$ is the characteristic hydrogen concentration in the film as liquid flows off the pellet, as the surface area of pellet increases this will approach equilibrium

5.4 Determination of model parameters

Before the two-stage mass transfer model could be used to evaluate the convective and radial mechanisms occurring during the hydrogenation of styrene in the atmospheric single pellet reactor, the liquid film thickness and intrinsic rate constant were first determined. The film thickness was estimated from the liquid film thickness experiments described in Chapter 4. At the liquid flow rates investigated the thin film (slab) and general models converge and therefore, for convenience the thin film model (slab), Eq. (4.6), was used to calculate the film thickness in the two-stage model.

5.4.1 Observed rate constant

The intrinsic chemical reaction resistance Ω_R is a function of the observed rate constant, k''_{obs} and thus a value of the rate constant in the absence of pore resistance is required for proper determination of the overall mass transfer rate. It should be noted that k''_{obs} represents the observed reaction rate based on the external area of the pellet and is a function of temperature, and both styrene and hydrogen concentration. Therefore, we assume that these are essentially constant over the surface of the pellet.

To approximate k''_{obs}, the observed rate constant reported by Stamatiou and Muller, who used the 5% Pd/C powder characterised for the hydrogenation of styrene in an agitated slurry reactor [204], was used. Analysis of the nanoparticle size distributions via TEM was discussed in Chapter 3 and showed that the nanoparticles of both the 1% and 5% Pd/C catalysts have a similar size range. Moreover, as palladium is the catalyst used on both supports it was hypothesised that the intrinsic reaction rate on

the surface of the catalyst should be the same. A comparison of the two catalysts and their nanoparticle size distributions is shown in Figure 5.5.

Based on the weight of palladium on the catalyst support and the hydrogen concentration in the fluid, C_f, an observed rate constant at 32 ℃ was determined;

$$\left(-R_{H_2}^{Pd}\right)/C_f = k_{obs}^{Pd} = 0.0273\,\frac{m^3(fluid)}{g(Pd).s} \qquad \textbf{(5.14)}$$

Comparing with the literature, the rate constant is larger than the rate published by Nijhuis *et al*., who reported a rate constant of $0.0086\,\frac{m^3(fluid)}{g(Pd).s}$ for styrene hydrogenation on Pd/C [205]. The lower rate constant is shown to be a result of active pore diffusion by the activation barrier reported by Nijhuis *et al*.

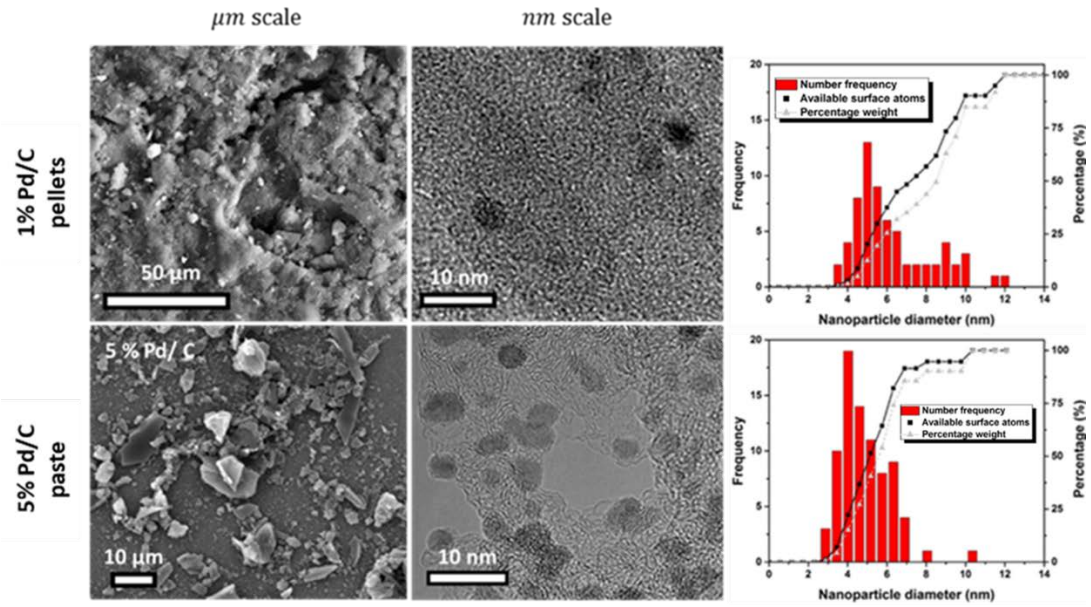

Figure 5.5: SEM, TEM and nanoparticle size distributions of the 1% and 5% Pd/C catalysts SEM image of the catalyst sample (left), TEM image of the palladium nanoparticles (middle) and the corresponding nanoparticle size distribution (right) of the 1% Pd/C pellets (top row) and 5% Pd/C (bottom row). The square and triangle trends represent the total surface atoms and weight of each bin respectively.

The rate is of a similar order of magnitude to the rate reported by Meille *et al.* for α-methylstyrene hydrogenation using palladium on an alumina oxide support ($k_{obs}^{Pd} = 0.0106 \frac{m^3(fluid)}{g(Pd).s}$) [206]. The intrinsic rate constant reported by Herskowitz and Mosseri for α -methylstyrene using 1% palladium on alumina oxide support is also in agreement with these values ($0.0087 \frac{m^3(fluid)}{g(Pd).s}$) when no pore diffusion is present [207]. In comparison with a relatively slower chemical system, Losey *et al*. reported a rate constant of $0.0014 \frac{m^3(fluid)}{g(Pd).s}$ for the hydrogenation of cyclobenzene using a 1% Pd / Al_2O_3 powder catalyst [145]. The authors identified that pore diffusion was significant, limiting the intrinsic reaction rate by approximately 20%.

In the case of the 1% Pd/C pellet, SEM-EDX analysis of the nanoparticles location on the support showed that, though palladium is located on the surface in high concentrations, a significant portion of the palladium is also located within the pore network of the carbon support. Thus, pore resistance could not be neglected. The 5% Pd/C on the other hand, is a fine powder consisting of flat shards of carbon approximately ~30 μm in diameter and is it a reasonable assumption given the particle size that pore resistance is negligible. The SEM-EDX linescan of the pellet interior (Figure 3.9, Column B) shows that the pellets used in this study have an enriched palladium shell approximately 6 μm thick. The reaction rate of hydrogen in this enriched zone of the catalyst, $\left(-R_{H_2}^{Pd}\right)$ is defined as the moles of hydrogen consumed per second per gram of palladium present in the volume of enriched shell ($A_p \delta_{shell}$). Thus, the observed rate constant in the shell, k_{obs}^{Vshell} is defined as;

$$k_{obs}^{Vshell} = Pd_{\%S} \cdot W_p \cdot \frac{k_{obs}^{Pd}}{A_p \delta_{shell}} \quad \textbf{(5.15)}$$

Using Eq. (5.15) the shell rate constant was found to be 2410 $\frac{m^3(fluid)}{m^3(shell).s}$. Here, $Pd_{\%S}$ is the fraction of palladium in the shell (Eq. (3.2)), W_p the quantity of palladium in the pellet (grams), δ_{shell} is the thickness of the enriched shell and k_{obs}^{Pd} is the observed rate constant calculated from Eq. (5.14). Using the effective diffusion rate in Pd/C catalysts $D_{eff} = 2 \times 10^{-9} m^2\ s^{-1}$ determined by Kobayashi and Katsuzawa, the penetration depth of hydrogen into the shell in the presence of the liquid phase can be approximated [208];

$$\frac{1}{M_T} = \frac{\sqrt{D_{eff}/k_{obs}^{V_{sh}}}}{\delta_{shell}} \quad \textbf{(5.16)}$$

Using Eq. (5.16) the penetration depth was found to be ~16% of the enriched film thickness. Therefore, pore diffusion limits the reaction to a 1 μm thick surface layer on the pellet catalyst. The determined penetration depth is in line with models where the reaction is mass transfer limited, where most of the pore's depth is catalytically inactive. Blasi *et al*. modelled the depth of reaction in cylindrical pores and found that when mass transfer limited on average only 23% of the pore depth was used [209]. Moreover, the depth was found to be highly dependent on the unique pore morphology, something their model struggled to describe.

The reaction rate per unit external pellet area, k_{obs}^{S}, results from k_{obs}^{Vsh} by multiplication with the volume ($A_p \delta_{shell}$) of the shell, and division by the total external interface (A_p):

$$k''_{obs} = \frac{1}{M_T} k_{obs}^{Vsh}\ \delta_{shell} = 0.0022\ \frac{m^3(fluid)}{m^2(external\ pellet\ surface).s} \qquad \textbf{(5.17)}$$

This corresponds to a rate constant based on the quantity of palladium present and hydrogen concentration in the liquid of $0.0031\frac{m^3(fluid)}{g(Pd).s}$. Comparing this value with other rate constants found in the literature for systems where porous catalysts have been employed is slightly more challenging due to a distinct lack of information needed to estimate k''_{obs}. It is approximated that Satterfield *et al*. obtained a k''_{obs} value of $5.73x10^{-6}\frac{m^3(fluid)}{g(Pd).s}$ during the hydrogenation of α-methylstryene using 1% Pd/Al_2O_3 pellets at 50 ^oC [45]. This value is significantly lower than the value obtained here, though larger catalyst particles were used, and the authors show that pore diffusion was severely limiting the reaction to the extent that hydrogenation is only occurring in the outermost layers or surface of the catalyst. For comparison, Satterfield *et* al. reported an effectiveness factor and Thiele modulus of 0.00575 and 521 respectively for their catalyst and system. In this work, the respective parameters were determined to be 0.11 and 6.58 which suggests a considerable amount of the palladium contained within the carbon support is not utilised. Herskowitz *et al*. determined and compared the effectiveness factors for a series of spherical and cubic Pd/Al_2O_3 catalyst of different palladium loadings during the hydrogenation of α-methylstryene at 40 ^oC [185]. It is estimated that for 0.75% Pd/Al_2O_3 cubic pellets a k''_{obs} of 0.0057 $\frac{m^3(fluid)}{g(Pd).s}$ was obtained. This result is in the same magnitude as the k''_{obs} obtained here for styrene and interestingly, the authors reported a very similar effectiveness factor value of 0.153. The low effectiveness factors reported both here and the literature are thought to be a consequence of the chemical

system. Styrene and α-methylstyrene are both kinetically very fast and therefore the intrinsic reaction rate is sufficiently fast that only a small portion of the catalyst is utilised by the substrate.

5.4 Modelling the hydrogenation of styrene

The five model parameters $\alpha, \gamma_1, \gamma_2, \gamma_3$ and $k_{b.ref}$ were fitted to the experimental mass transfer rates of hydrogen by minimising the Sum of Squares (SOS). The objective function used to reconcile the model and experimental data is defined as;

$$\frac{\overline{SOS}}{\overline{MTR}_{H2,exp}} \; where \; \overline{SOS} = \frac{\sum_{i=0}^{n}(|y_{exp.i} - y_{calc.i}|)}{n}.$$

The GRG Non-linear engine available in Excel's Solver was utilised to find the local optimal solution starting with initial estimates of the five model parameters. The solver algorithm was ran multiple times until there was no further decrease in objective function. The two-stage model fit is presented for the two feed cases in Figure 5.6 as a function of the liquid residence time on the pellet.. In addition, the absolute values of the fitted and calculated parameters used in the two-stage model are presented in Table 5.2. The model fits both the hydrogen saturated and free feed cases very well, falling within the upper and lower experimental error limits for all but one point. Moreover, for the fitted solution the objective function ($\frac{\overline{SOS}}{\overline{MTR}_{H2,exp}}$) was minimised to 3.22%. This suggests that the relative rate of hydrogen supply by both the liquid (convective) and mass transfer across the pellet surface (radial) are important factors. The predicted MTR''_{H_2} from the model also highlights the asymptotic behaviour the experimental data appears to be moving towards.

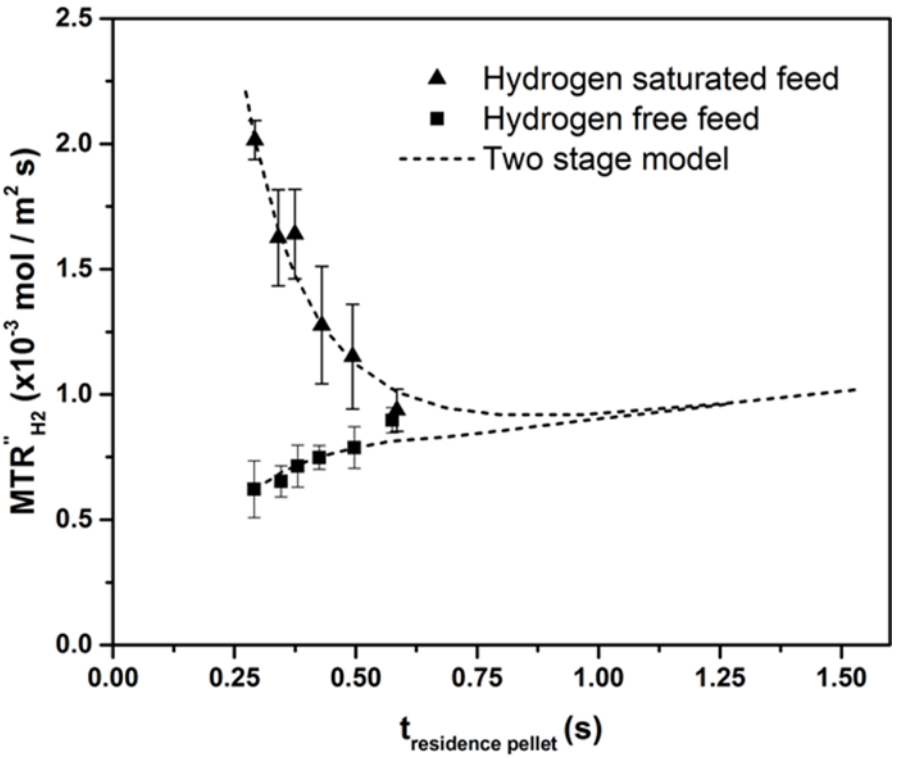

Figure 5.6: Comparison between the measured mass transfer rates of hydrogen and the two stage model for both hydrogen free and saturated feed cases.

Comparing again to Satterfield *et al*, their residence time on a pellet is estimated to range from 0.06 to 0.17 s, significantly shorter than for the single pellet case [45].

Table 5. 2: Upper and lower 95% confidence limits of the two-stage mass transfer model for both hydrogen free and saturated feed cases.

	Pellet film residence time $t_{residence\ pellet}$ (s)	**Experimental MTR''_{H2} (x10^{-3} mol m^{-2} s^{-1})**	**Modelled MTR''_{H2} (x10^{-3} mol m^{-2} s^{-1})**	**Upper 95% confidence interval**	**Lower 95% confidence interval**
Hydrogen saturated feed	0.58	0.94	1.01	1.05	0.97
	0.49	1.15	1.13	1.17	1.09
	0.43	1.28	1.28	1.32	1.23
	0.37	1.64	1.48	1.52	1.43
	0.34	1.63	1.66	1.70	1.61
	0.29	2.02	2.02	2.06	1.97
Hydrogen free feed	0.57	0.90	0.81	0.86	0.77
	0.50	0.79	0.79	0.83	0.74
	0.42	0.75	0.75	0.79	0.71
	0.38	0.71	0.72	0.76	0.68
	0.35	0.65	0.69	0.73	0.65
	0.29	0.62	0.62	0.66	0.57

Based on the model presented here it appears that the film over the spherical pellets was “flushed out” at low temperatures, and thus the system was reaction limited. As the reaction rate increases with temperature, the reaction resistance reduces, and the mass transfer resistances become noticeable. This results in the higher hydrogenation rates observed by Satterfield *et al.* at lower liquid velocities and hence thinner liquid films.

5.4.1 Model fitting evaluation

Given the number of fitting parameters in the model, an assessment was undertaken to ascertain whether other local minima could exist that might cause the model to be interpreted differently. The starting values of $\alpha, \gamma_1, \gamma_2, \gamma_3$ and $k_{b.ref}$ were incrementally changed and the solver run to estimate the parameters from different the starting points. Table 5.3 summarises initial starting point (guess) of each of the parameters, the solver estimation and the value of the objective function once fitted ($\overline{SOS}/\overline{MTR}_{H2,exp}$). The results from the fitting study are graphically shown in Figure 5. 7(a). Twelve runs were attempted with different combinations of initial starting values (or guesses). Visually it appears that there could be at least two solutions across the range investigated (run 3 and 7). However, when the solver estimations are compared the values are very similar and would unlikely lead to different model interpretations. As the initial starting values move too far from the optimal solution (run 7) the solver is unable to find a solution. Of the five parameters fitted, the portion of the liquid film that forms the mass transfer resistance, α, appears to have the most influence on the value of the objective function, as can been observed from the Figure 5. 7(b).

Table 5.3: Initial values of the fitted parameters in model, the values estimated by the Solver once fitted and the objective function value ($\frac{SOS}{\overline{MTR}_{H2,exp}}$). Run 7 represents the optimal solution.

Run	Initial parameter value					Solver estimation after fitting					$\frac{SOS}{\overline{MTR}_{H2,exp}}$ (%)
	$k_{b.ref}$ x10^{-6} m/s	γ_1	γ_2	γ_3	α	$k_{b.ref}$ x10^{-6} m/s	γ_1	γ_2	γ_3	α	
1	0.025	0	0.15	0.2	0.9999999	4.53	-0.227	1.78	0.63	0.967	3.329
2	0.05	0	0.3	0.35	0.99999	4.40	-0.290	1.78	0.61	0.996	3.405
3	0.2	0	0.6	0.45	0.998	4.73	-0.149	1.86	0.65	0.961	3.228
4	0.5	0	0.8	0.5	0.995	4.74	-0.136	1.87	0.65	0.958	3.234
5	1	-0.05	1	0.55	0.99	4.74	-0.152	1.84	0.65	0.949	3.280
6	2	-0.1	1.5	0.6	0.98	4.48	-0.154	1.81	0.65	0.956	3.235
7 (optimal solution)	4.7	-0.16	1.8	0.65	0.966	4.69	-0.156	1.86	0.65	0.970	3.219
8	6	-0.3	2	0.75	0.95	5.93	-0.176	1.99	0.72	0.902	3.474
9	8	-0.6	3	0.85	0.9	7.96	-0.236	2.98	0.89	0.893	4.159
10	10	-0.9	4	0.95	0.85	9.96	-0.317	3.96	0.98	0.909	5.327
11	12	-1	5	0.1	0.8	**No solution found**					
12	14	-1.2	6	0.1	0.75	**No solution found**					

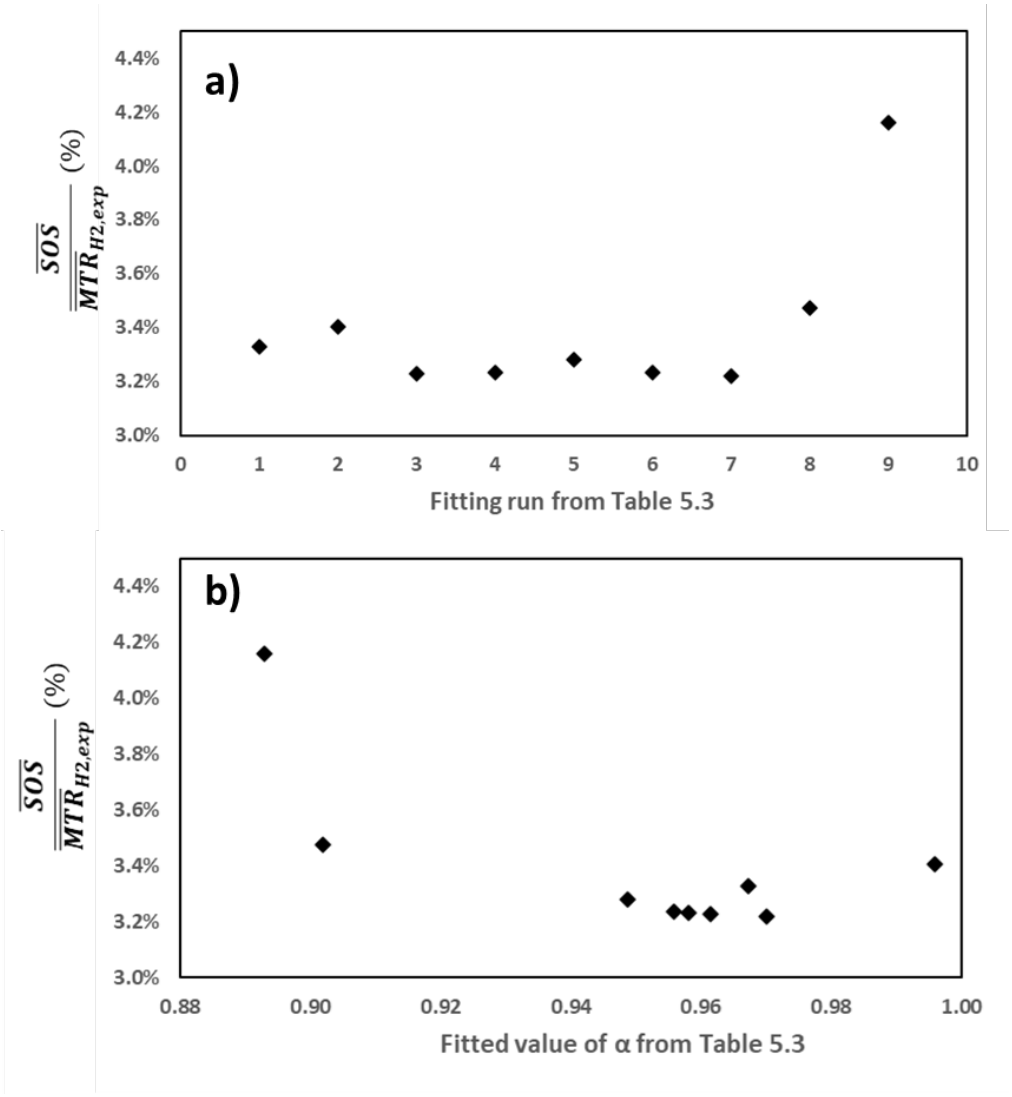

Figure 5. 7: The objective functions ($\frac{\overline{SOS}}{\overline{MTR}_{H2,exp}}$) value of each run in the fitting study outlined in Table 5.3 (a) and as a function of the parameter $\boldsymbol{\alpha}$ (b).

Given the influence $\boldsymbol{\alpha}$ has the on the fitting and final solution obtained, a second study where the portion of the liquid film that forms the mass transfer resistance, α is fixed and $\gamma_1, \gamma_2, \gamma_3$ and $k_{b.ref}$ are fitted using the solver was conducted. Figure 5. 8 shows the value of the objective function at different values of α having fitted the other four parameters. Two local minima can be observed, implying that there are at two possible solutions across the range investigated. However, the second minima point at $\alpha \approx 0$ is a trivial solution, as that would imply that is no convective transfer occurring in the film and this has no physical grounding.

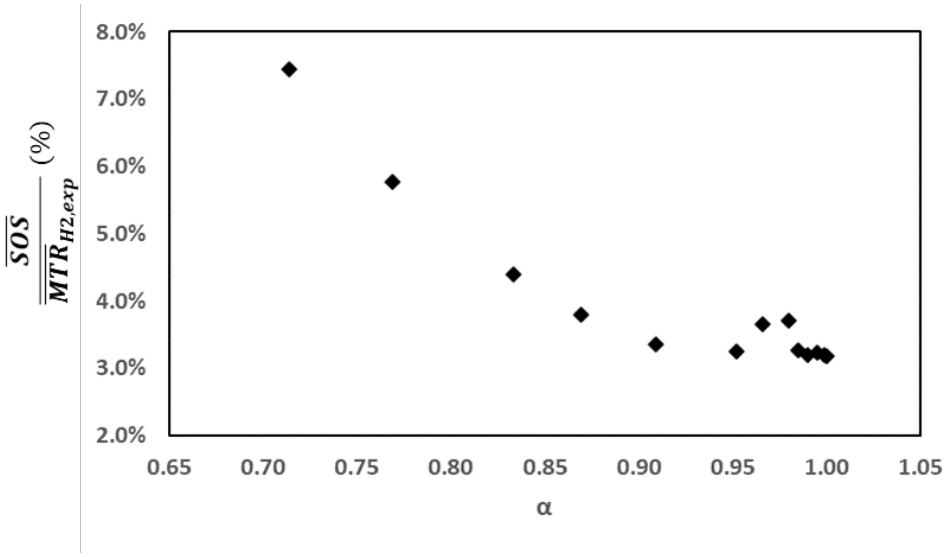

Figure 5. 8: The object function value obtained when the portion of the liquid film that forms the mass transfer resistance, $\boldsymbol{\alpha}$ is fixed and $\boldsymbol{\gamma_1, \gamma_2, \gamma_3}$ and $\boldsymbol{k_{b.ref}}$ are fitted using the solver.

5.4.2 Discussion of fitted and calculated parameters

The absolute values of the fitted and calculated parameters used in the two-stage model are presented in Table 5. 4. Visual observation revealed that liquid was bypassing the pellet and based on the mass transfer data the liquid bypass factor, γ_3, was estimated to be 65%. Whereas this number could not be validated, it is consistent with the observations. The two-stage model indicates that the falling film model is not truly representative of the film thickness around the pellet in the bed, as the thickness proportionality constant, γ_2, suggests the film is almost twice as thick as that predicted by the slab model. It does show, however, that the falling film model gives a reasonable estimate for the relationship between film thickness and flow. It does not account for the additional liquid holdup present on the pellet due to the proximity of the beads, nor are differences in the pellet position considered.

Table 5. 4: Values of the fitting and model parameters used in the two-stage mass transfer model.

	Parameter	Value	Source / Comment
Bead section	$k_{b.ref}$	4.69 x 10^{-6} m/s	Fitted mass transfer coefficient over the beads, defined in Eq. 7.
	γ_1	-0.156	Fitted gradient of the effect of flowrate on mass transfer to beads, defined in Eq. 7.
Pellet section	γ_2	1.86	Fitted ratio of film thickness over a pellet in a bed vs film thickness (δ) over a pellet stack.
	γ_3	65.5 %	Fitted fraction of liquid flowing over the pellet (bypass factor).
	α	0.97	Fitted fraction of the liquid film that forms the mass transfer resistance, defined in Eq. 11.
Mass transfer resistances	$1/\Omega_f$	119-169 x 10^{-6} m/s	Gas to film transport resistance, $\Omega_f = \delta\gamma_2/\mathbb{D}_{H_2}$.
	$1/\Omega_{f-s}$	1350-1520 x 10^{-6} m/s	Film to catalyst surface transport resistance, calculated from Eq. 12.
	$1/\Omega_R$	2200 x 10^{-6} m/s	Chemical reaction resistance, calculated from Eq. 26.

5.4.3 Mass transfer in the bead section

The estimated mass transfer coefficient for the beads section is in the right order of magnitude and as can be seen in Figure 5.9 decreases with increasing liquid velocity. The values are in good agreement when compared to systems involving gas absorption with no subsequent chemical reaction. This is evident when comparing the experimentally derived Sherwood number with the well-established correlation involving the Reynolds and Schmidt numbers for a flat plate, both defined in Eq. (5.18) [210];

$$Sh_{bs} = \frac{k_{b.ref} N_{bs} d_{bs}}{\mathbb{D}_{H_2}} = 0.664\, Re_{bs}^{1/2} Sc^{1/3} \qquad \textbf{(5.18)}$$

$$\text{with } Re_{bs} = \frac{\rho U_{bs} N_{bs} d_{bs}}{\mu} \text{ and } U_{bs} = \frac{\varphi}{2\pi d_{bs}\, \delta_b}$$

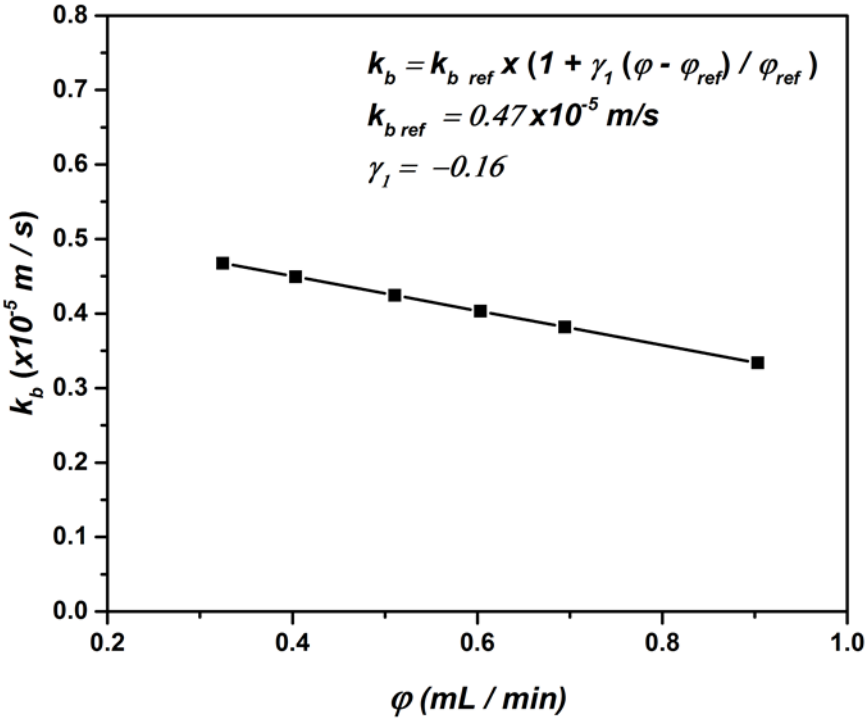

Figure 5.9: The effect of liquid flow rate on the estimated mass transfer coefficient determined by the two-stage model.

Where δ_b is the liquid film thickness over the surface of the beads (considered here as a cylinder as illustrated in Figure 5.3) and is calculated using the general film thickness model (Eq. (4.6)). The experimentally derived and correlated Nusselt numbers were determined to be 40 and 52 respectively, with the difference due to the fact the geometries are different.

The mass transfer rate, $k_{b.ref}$, is used to determine the hydrogen concentration at the point where the liquid contacts the pellet, C_0, as a function of flow rate. The calculated hydrogen concentration at the point where the liquid contacts the pellet is shown in Figure 5.10 for both feed cases and all flow rates used. At lower flowrates, more time is available for mass transfer, and the concentration at the pellet, C_o, approaches equilibrium at the reaction conditions (1 bara). At higher flow rates and short liquid residence times, the system is essentially flushed out and C_o approaches the feed concentration.

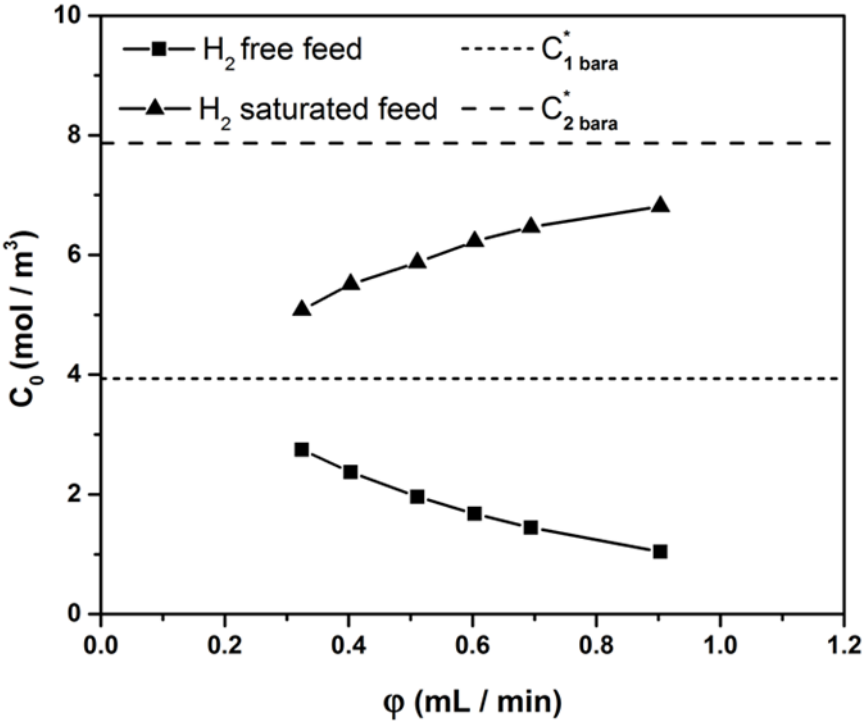

Figure 5.10: The calculated hydrogen concentration in the liquid from the two-stage model when it reaches the pellet, C_0, for the hydrogen saturated and free feed experiments. The dashed and dotted lines represent the saturated feed concentration and the equilibrium concentration of hydrogen in the liquid respectively.

5.4.4 Mass transfer to the pellet

The gas to film mass transfer coefficient ($1/\Omega_f$) was found to be an order of magnitude larger than that of the beads. Moreover, the gas film mass transport resistance barrier consists of 97% of the film. It is suspected that the portion of the film dedicated to the gas-liquid mass transfer resistance would initially be lower when the pellet first contacts the pellet and convective transfer is dominant. As the liquid travels further along the pellet and the hydrogen present in the film prior to contacting the pellet is consumed and the film mass transport resistance barrier will move closer to the surface of the pellet. As the model does not account for any change in the distance the liquid resistance barrier is formed from the pellet, it may be actually underestimating the amount of hydrogen being supplied radially from the gas phase when the liquid initially contacts the pellet.

The calculated mass transfer coefficient is in the same order of magnitude but slightly lower than gas-liquid coefficients reported in the literature [108, 211] for trickle bed reactors investigated at similar superficial liquid flow rates (between 3-4 x 10^{-5} m s^{-1}). The resistance for hydrogen transport from the film to the surface of the catalyst is thus small as the distance to diffuse is small. The corresponding mass transfer coefficient ($1/\Omega_{f-s}$) and the reaction rate constant, k''_{obs} ($= 1/\Omega_R$), are both an order of magnitude larger than the mass transfer rate from the gas phase. Comparing the liquid-solid coefficient with those in the literature, Stamatiou and Muller determined an average specific mass transfer coefficient of 4.72 x 10^{-4} m s^{-1} for the hydrogenation of styrene in a trickle bed reactor who employed the same 1% Pd/C pellets used here [182]. In their system, a very small amount of active catalyst surface was present relative to the total amount of surface area available for gas-liquid mass transfer to occur. Thus, the gas-liquid mass transfer resistance was found to be much lower than the liquid-solid resistance, as the liquid was likely fully saturated on contact with the catalyst pellets. The values determined here are relatively lower than those reported by Herskowitz and Abuelhaija [155]. It is estimated that they obtained liquid-solid coefficients from 2.13-4.80 x 10^{-4} m s^{-1} using Pd/Al_2O_3 catalyst spheres during the hydrogenation of cyclohexene in a trickle bed reactor. The values of the liquid-solid mass transfer coefficient calculated in this work (1.3-1.5 x 10^{-4} m s^{-1}) are slightly lower than both the referenced literature values. This is likely due to the lower liquid velocities used here, resulting in a reduced mass transfer rate. The results obtained here suggest that mixtures of active and inactive catalyst can convert more raw material per unit mass of palladium as a result of additional non active mass transfer area.

The concentration gradient over the pellet is shown in Figure 5.11 for hydrogen free and saturated feed solutions at the maximum and minimum feed flowrates. As the flow progresses along the length of the pellet, L_p, the hydrogen concentration moves to an asymptotic value. If we consider the case of having a very large pellet $(L_p \rightarrow \infty)$ the film concentration reaches C_∞ (Eq. (5.10)). The film reaches equilibrium relatively quickly, but the extent to which the liquid is saturated, C_0, still has a large impact on the overall mass transfer rate as film to catalyst resistance is very small. When the flowrate increases the film will reach the hydrogen concentration of the feed, and the term A_0/A_P tends to zero. As a result, the hydrogen concentration of the film approaches C_o. This will result in the highest hydrogen conversion rates per unit mass of palladium, but the concentration of product downstream will reduce.

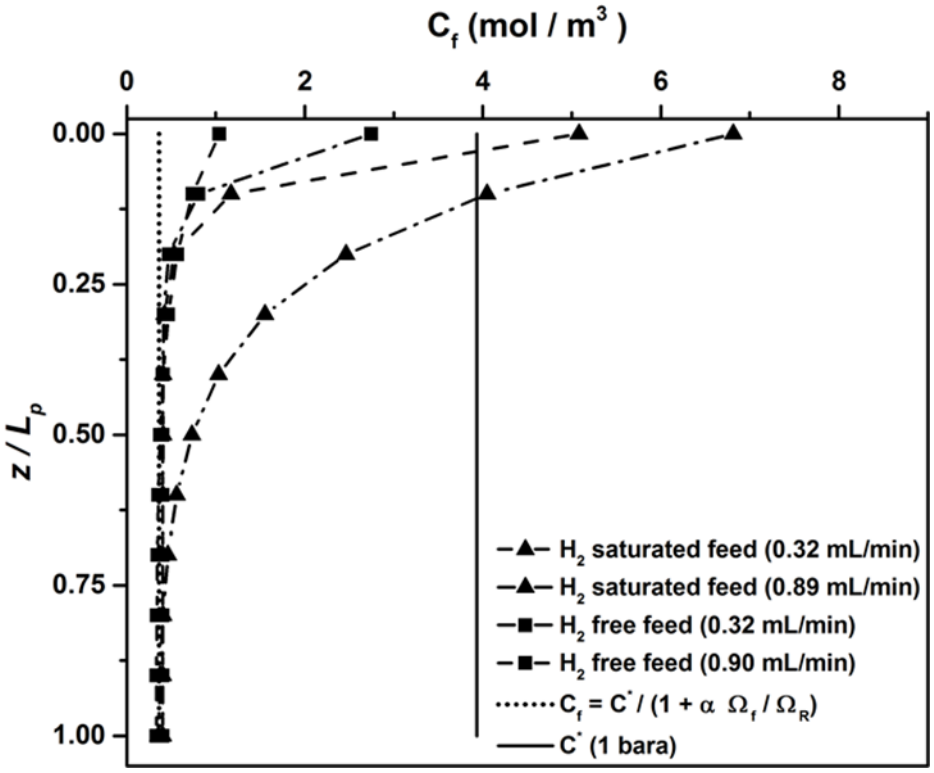

Figure 5.11: Change in concentration of hydrogen in the liquid film over the area of a pellet Calculated using Eq. (5.10) for both hydrogen free and saturated feed solutions at the maximum and minimum feed flowrates. The dotted line highlights the case where $A_p \rightarrow \infty$.

5.5 De-coupling convective and radial mass transfer

One of the final key objectives was to establish the relative contributions of hydrogen transport from (i) convective transport of hydrogen with the liquid flowing onto the pellet MTR''_{conv}, and (ii) radial mass transfer of hydrogen from the gas phase to the liquid film surrounding the pellet, MTR''_{radial}.

The convective transport may be estimated from the concentration difference between the liquid entering the pellet and the liquid leaving the pellet. The radial mass transfer is then the difference between the total mass transfer observed, and the contribution of convection:

$$MTR''_{radial} = MTR''_{H_2} - MTR''_{conv} \qquad \textbf{(5.19)}$$

$$with \quad MTR''_{conv} = \varphi\gamma_3(C_0 - C_f)$$

This simulates the two modes of hydrogen delivery to the pellet for all flowrates and feed conditions. The comparison between the two simulated transport processes is shown in Figure 5.12. The overall mass transfer rate is significantly affected by convective transport, evident by the fact that as the molar flow of hydrogen increases the rate at which hydrogen is consumed increases. As illustrated in Figure 5.8, the film concentration C_f will always eventually reach C_∞, irrespective of the feed conditions or flow rates used.

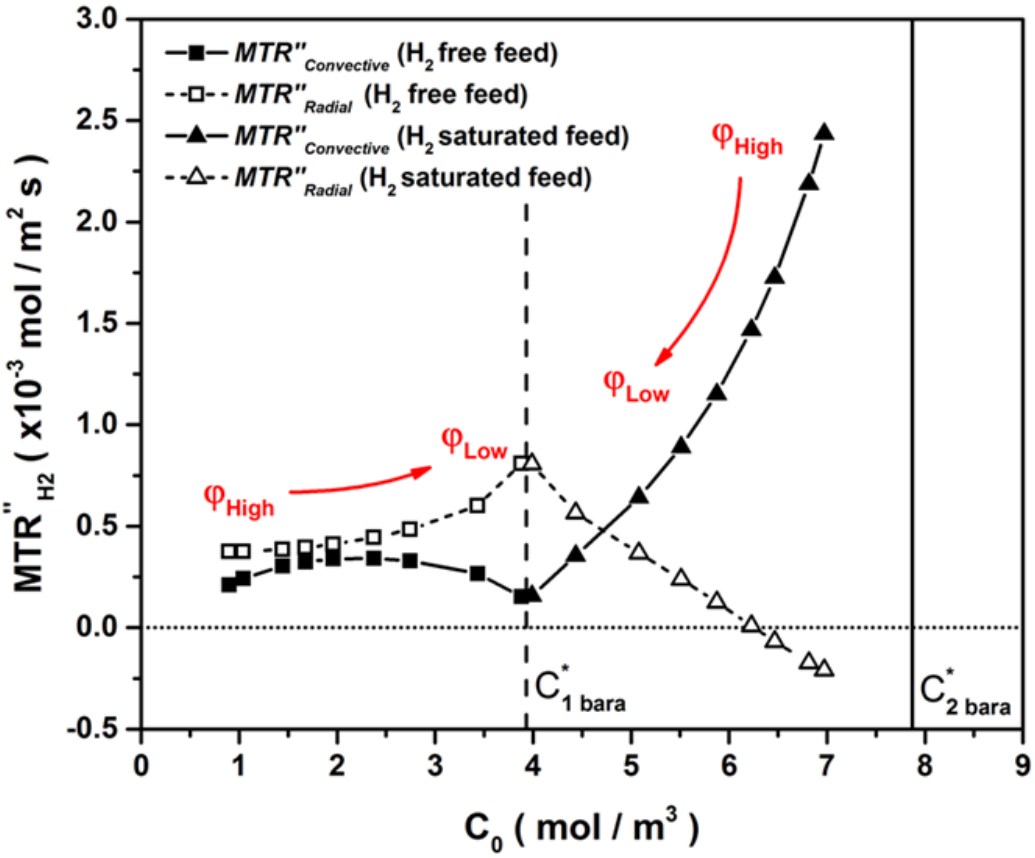

Figure 5.12: The simulated contributions of convective and radial mass transfer of hydrogen the for hydrogen saturated and free feed conditions at the flow rates investigated. φ_{High} and φ_{Low} refer to the velocity of the liquid phase for each feed condition.

Therefore, the differentiator between the two feed conditions is the convective contribution, and it is only at very low flow rates that the convective and radial diffusive contributions for the two feed conditions become comparable. When the liquid feed is saturated with hydrogen the radial diffusive contribution is observed to have a negative impact on the overall mass transfer rate of hydrogen to the pellet at higher liquid flow rates. This is a limitation of the experimental methodology in that the reactor is composed entirely of glass and therefore, the reactor limited to atmospheric pressure. The feed is 'super' saturated with hydrogen at a pressure of 2 bara before passing through and therefore, hydrogen will diffuse from the liquid into the gas phase lowering the hydrogen concentration in the liquid at the point where it contacts the pellet. This in turn will lower the molar flow of hydrogen flowing onto the pellet. This

phenomenon is considered by the first section of the model (non-reactive mass transfer over the beads) and shows that at high liquid flow rates the convection is completely dominating. On the other hand, if limiting the supply of hydrogen to the catalyst is preferential, high liquid flow rate and no feed saturation could be a possible operating regime at the expense of overall conversion.

Decoupling the two transfer processes further highlights the benefits that operating in a convection dominated regime has on the catalyst utility. Whether the feed is prematurely saturated beforehand or inert surface area is added to the bed, both result in an increase in hydrogen uptake per gram of catalyst. This is ultimately achieved by controlling the hydrogen concentration close to the surface of the catalyst pellets. This methodology could be readily extended to many other three phase catalytic processes whereby transport of the gaseous reacting molecules limits the overall rate of reaction. Examples include reactions involving not only the hydrogenation of fine chemicals but hydrogenolysis reactions during hydrodesulfurization, catalytic oxygenation of alcohols such as ethanol and it could even find application in specific bioreactions such as gas synthesis of methanol from hydrogen and carbon monoxide.

5.7 Conclusions

The knowledge of how to better regulate the supply of hydrogen gas to the catalyst and manipulate the mass transfer characteristics, unlocks the potential of trickle bed reactors, making them an attractive technology for the manufacture of fine chemicals in the agrochemical and pharmaceutical industries. Solving this problem paves the way to further understanding and

cracking the complex scale up and selectivity issues involved in three phase reactions whilst capitalising on the benefits continuous processing offers. Having observed and manipulated the contributions of convection and radial diffusion in the scaled down trickle bed reactor in Chapter 4, a novel two-stage mass transfer model has been developed to aid in describing the complex transfer phenomena and reaction kinetics experimentally observed. The model combines the transfer of hydrogen into the liquid over the non-active beads with transfer and chemical reaction over the catalyst pellet to describe the hydrogen concentration in the liquid close the surface of the catalyst. The model was shown to reconcile the experimental hydrogen uptake rates for both hydrogen saturated and hydrogen free feed cases as a function of liquid flow rate. Moreover, the extent to which convection and radial diffusion normal to the catalyst surface were contributing to the overall mass transfer rate of hydrogen were quantified, demonstrating that delivery of hydrogen via radial mass transfer is relatively constant when the convective flux of hydrogen is low. When the convective flux of hydrogen increases (by super saturation of the feed and higher flowrates) the rate of hydrogen consumption increases virtually proportionally to the hydrogen flux, indicating that most of the hydrogen transported by convection is consumed. As the hydrogen concentration in the film on the pellet increases, the radial mass transfer reduces, and even becomes negative when operating a saturated feed at high flowrates.

In terms of process understanding, decoupling the two transfer processes has highlighted the potential advantages operating in convection dominated and radial diffusion dominated regimes could have on continuous heterogenous hydrogenations. The results show that catalyst utility can be

significantly enhanced when operating in a convection dominated regime whilst hydrogen supply to the catalyst can be limited by operating in a diffusion dominated regime, at the expense of overall conversion. Furthermore, in a practical sense this work demonstrates that by controlling the ratio of inactive to catalytically active surface area in a trickle bed reactor, one can control the hydrogen concentration close to the surface of the catalyst pellets.

Although the scaled down single pellet reactor has improved understanding of the transport processes that supply hydrogen to the catalyst surface in trickle bed reactors, the system is still relatively complex and difficult to describe mathematically. This is evident in the fact that five fitting parameters were required, as some of the hydrodynamic properties and mass transfer parameters are difficult to approximate (bypass factor and transfer with no reaction). Moreover, the transfer of hydrogen from the liquid stream to the gas phase at higher feed saturation pressures due to the atmospheric pressure in the reactor is undesirable, unrepresentative of the operation of a trickle bed reactor and adds further complication when analysing the hydrogen uptake rates. It was therefore decided that a methodology of completely removing the catalyst pellet from the bed would be attempted, using a reactor platform that could be pressurised so the effect of hydrogen saturation pressure could be studied to a greater extent. Moreover, it was hypothesised that removing the pellet completely from a packed bed environment decreases the number of parameters needed to mathematically model the system.

Chapter 6
Experimental evaluation of alternative single pellet technologies for heterogenous hydrogenations

The concluding remarks from both Chapter 4 and 5 highlighted that although the approach of evaluating a single pellet in a bed of glass beads successfully enabled isolation and decoupling of the convective and radial diffusive transfer processes, the system was still inherently complex. Having been more of a proof of concept study, the processing conditions were challenging to control, which subsequently made analysis and modelling of the data difficult. This was apparent in the number of unknown parameters that required fitting in order to reconcile the experimental data with the model. Thus, the aim of this chapter is to design novel reactors to enable experimental evaluation of whether alternative methods of presenting a 1% Pd/C single pellet can be used to assess the mass transfer characteristics, improve the process understanding and aid in catalyst testing. By removing the pellet from the packed bed altogether, it was hypothesised that the pressure and hydrodynamics local to the pellet could be more finely controlled, and consequentially allow the assessment of how convection and radial mass transfer processes are affected by the processing conditions. The result reactors were also assessed to determine their ability to; (i) screen the catalytic activity of a number of pellets (ii) and identify to what extent the hydrogen uptake rate varied from pellet to pellet as a function of hydrogen pressure and liquid flow rate. The two alternative reactor platforms that were developed and experimentally evaluated using the styrene case study will be detailed in the next section.

6.1 Reactor design criteria and selection

Initial design ideas fell into two categories depending on the position of the catalyst pellet within the reactor platform. The first category of designs involved enclosing the pellet in a steel pipe of a similar diameter so that the liquid and gas flow was forced over the pellet. Though simple in nature and construction, this type of reactor design was not taken forward. The main reasoning being concerns that the hydrodynamics significantly differ from that of trickle bed reactors, having slug flow characteristics. Therefore, the mass transfer characteristics will differ too, as seen in similar ‘string pellet’ reactors by Bauer *et al*. [82]. Instead, rather than flowing both phases past the pellet in the pipe, the liquid would first be fully saturated with hydrogen gas at a specific pressure. As no hydrogen gas will be present in the reactor, convective transfer will be the primary transport process by which the pellet is supplied with hydrogen. Moreover, this will remove the complex hydrodynamics associated with gas-liquid flow. This reactor technology will be referred to as the ‘dissolved gas reactor’ throughout the rest of this thesis.

The second category of designs focussed on fixing the catalyst in place within a vessel of much larger diameter than the pellet and directly distributing liquid over it. Due to the nature of the liquid flow, this reactor will be referred throughout the rest of this thesis as the ‘falling film reactor’. Though more complex to design and fabricate, this design was chosen for two reasons. The first being that this approach removes the complex hydrodynamic relationship between the gas and liquid phases, as the diameter of the vessel will be large enough that gas velocity or shear would have a negligible impact on the liquid film thickness. The second reason was that the trickling liquid will form a film over the catalyst that is more representative of the liquid film thickness

experiments and the two-stage mass transfer model outlined in Chapter 5. This design comes with several drawbacks that were taken into consideration at the beginning of the design process. The primary concern is that without being able to see into the reactor, one cannot ensure that the liquid is being directly and evenly distributed over the pellet. Therefore, the reactor needed to be designed so that the pellet could always be observed during operation, though this criterion would impact the final design and maximum operating pressure of the reactor considerably. The second drawback of having a large pressurised internal volume relative to the catalyst pellet was the envisioned heating issues, namely being the inability to either consistently heat the pellet to a desired temperature or provide a flow of liquid to the pellet of a constant temperature. Rather than design an elaborate heating mechanism, it was decided that the reactor would be operated at room temperature whilst investigating the hydrogenation of styrene. As seen in Chapter 4, a quantifiable amount of ethylbenzene is detected at ambient conditions (room temperature) using a single catalyst pellet.

The final design consideration was the working pressure range required for the hydrogenations of interest. All the hydrogenations initially planned to be investigated in the reactor are conducted at relatively low pressures (2-8 barg) [43, 182, 204, 212] and therefore, the maximum working pressure would need to be able to accommodate this pressure range.

6.2 Falling film reactor; design, fabrication and operation

Several different designs were proposed before the final reactor design was selected. This section will aim to first describe and justify all the decisions

made in relation to the materials and fabrication of the reactor, followed by the experimental procedure used.

6.2.1 Vessel design

A concept and engineering drawing of the external body of the reactor was generated using the computer aided design software AutoCAD and is shown in Figure 6.1

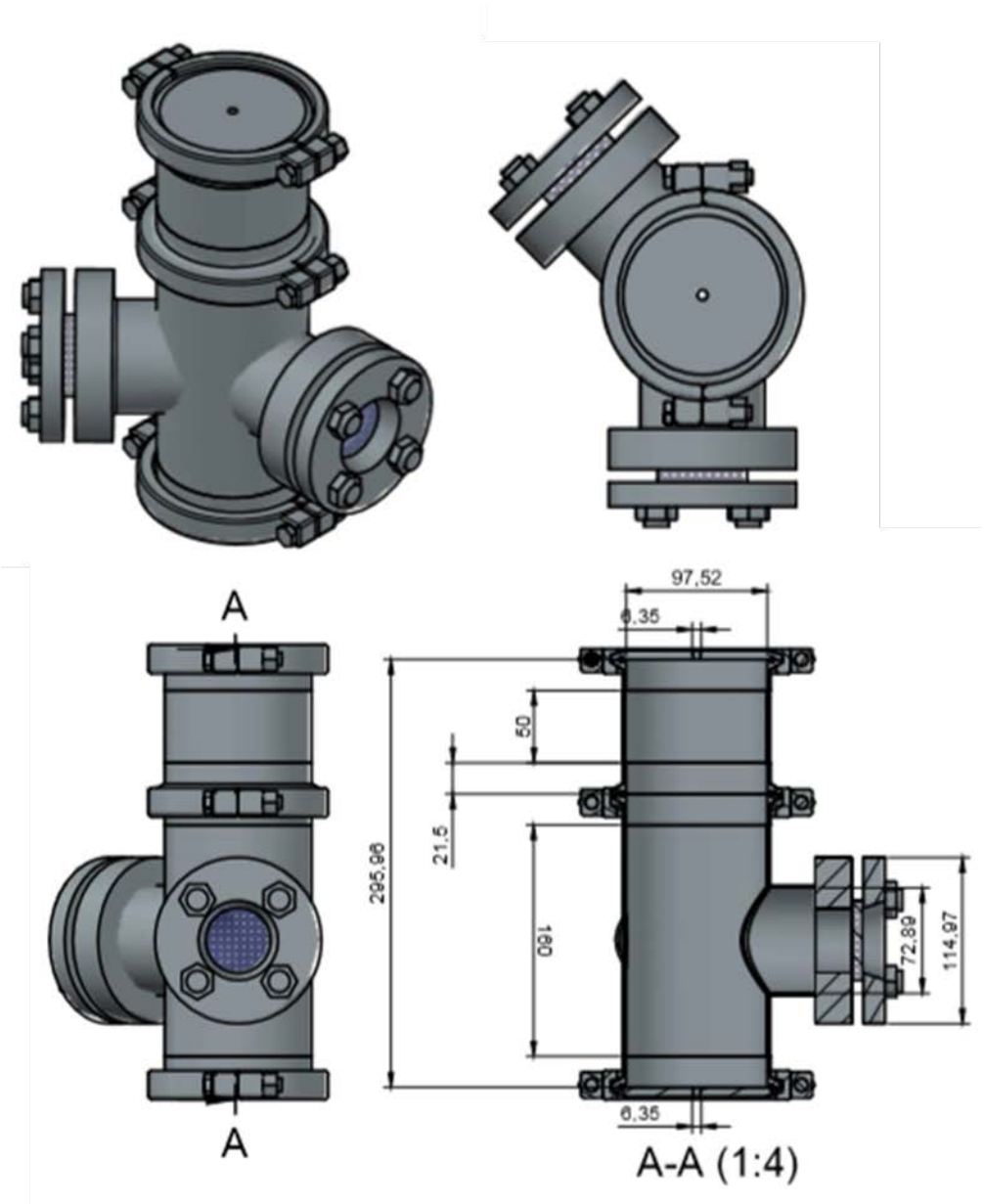

Figure 6.1: Computer aided design drawings showing the design of the falling film reactor. Showing the reactor design (top-left), a top-down view of the reactor (top-right), a side on view (bottom-left) and the corresponding engineering drawing (bottom right). All measurements are in millimetres (mm).

A blank cap, EPDM gasket and tri-clamp were used to seal the top of the second tube and a tri-clamp/EPDM gasket used to join the second tube to the main body of the reactor. A tapped ¼'' NTP hole was machined in the top and bottom blank caps, to allow gas and liquid to enter and exit the reactor. Images of the reactor showing the main reactor body attached to the top tube are shown in Figure 6.2.

6.2.2 Reactor interior and pellet stage

To permanently fix a catalyst pellet within the reactor, several different approaches were considered, from designing a pellet 'harness' to simply gluing the pellet in place. A simple stage to which the pellet could be glued was chosen over more elaborate ideas due to the ease of construction and more versatile practical use.

Figure 6.2: Images of pressurised falling film reactor showing the main body, the second top tube and the sight glass windows.

The concept drawing, engineering drawing and a picture of the fabricated stage in shown in Figure 6.3. The stage was machined from a small steel rod (Ø 6 mm) and attached to a thin piece of steel sheet via a screw. A SS 316L tube (Ø 25.4 mm) was used to mount the stage in the reactor by machining two grooves at one end of the tube that the stage could slot into. This tube was then welded to the bottom blank cap of the main reactor body directly over the ¼'' NTP hole to allow the liquid to escape.

To ensure that the liquid constantly flows over the pellet, a liquid distributor consisting of a Swagelok 1/16'' SS pipe (0.36 mm internal diameter) was placed above the pellet and held in place using a miniature microscopy XY stage purchased from Pro-Lite Technology Ltd. (MKT 30) fitted with a small PTFE bung. To hold the XY stage in place a system rail (SYS 40) was additionally purchased from Pro-lite and attached to the tube holding the pellet stage using Unistrut pipe clips (PCH14-18) purchased from RS components. An image showing the interior tube, pellet stage and liquid distribution system are shown in Figure 6.4.

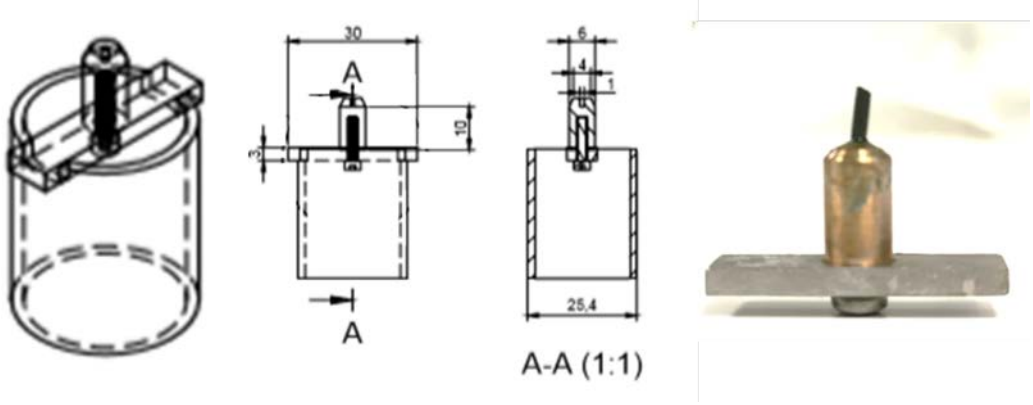

Figure 6.3: Showing a concept drawing of the pellet stage (left), an engineering drawing (centre) and the fabricated stage (right). All measurements are in millimetres (mm).

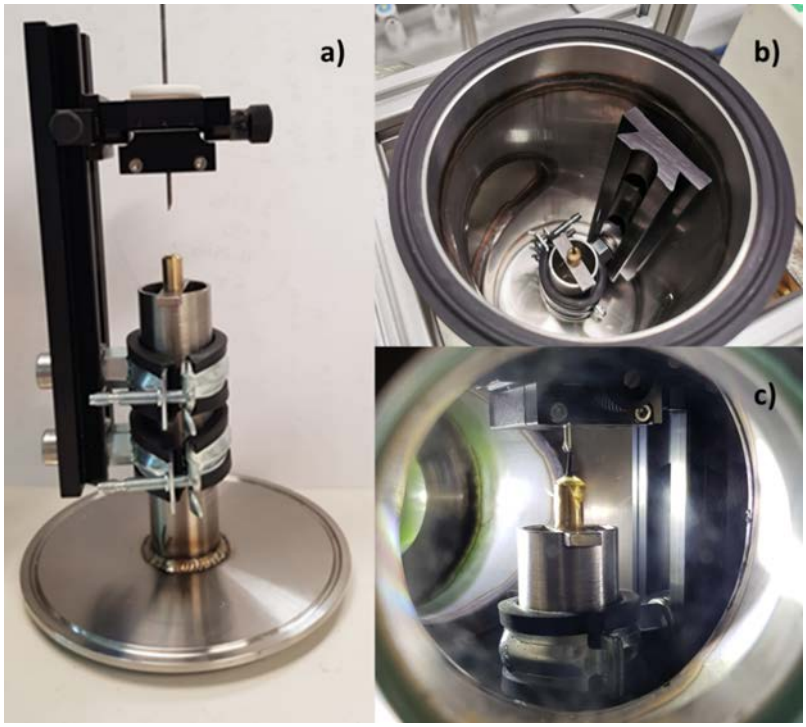

Figure 6.4: The inner tube, pellet stage and liquid distributor system of the pressurised pellet reactor (a), a top-down view into the reactor to see the pellet stage and rail system (b), and a view of the pellet stage through one of the sight glass windows (c).

6.2.3 Reactor platform and rig set-up

The reactor set-up and its corresponding piping and instrumentation diagram (P+ID) are shown in Figure 6.5, and consists of the pressurised pellet reactor module, a liquid saturation device and two gas manifolds (one for each reactor). Starting with the pressurised pellet reactor module first, hydrogen and nitrogen are supplied to the reactor via gas cylinders and the pressure in the vessel is controlled using a regulator (R-1). An adjustable back pressure regulator was added to keep the reactor at the desired pressure, which was monitored using a pressure gauge. Pure solvent or hydrogen saturated solvent was continuously pumped into the reactor via a HPLC pump. The liquid passes over the pellet and exits out of the bottom of the reactor and enters a small gas-liquid separator system consisting of a Swagelok T-piece and a transparent PFA level indicator (Ø 6.35 mm).

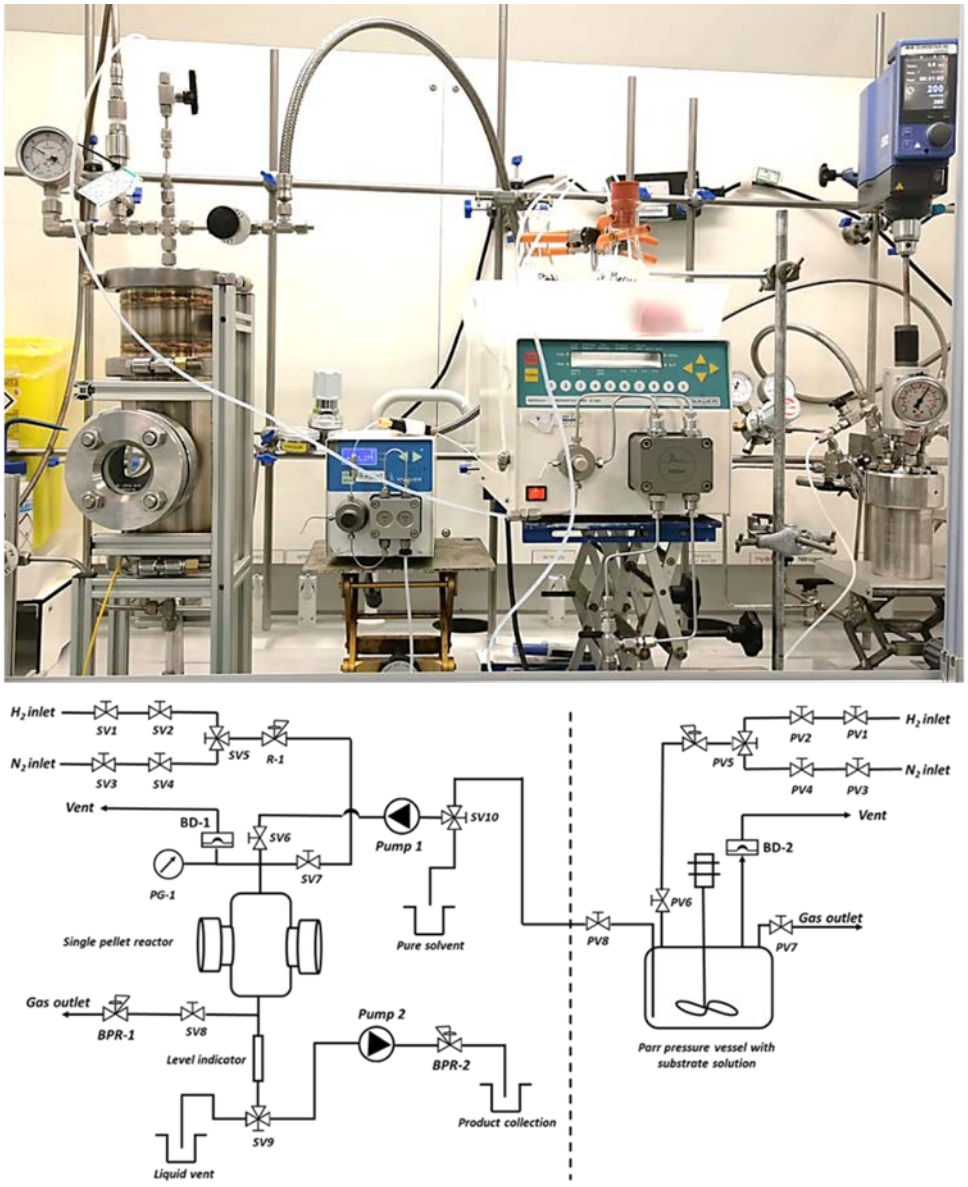

Figure 6.5: The pressurised pellet reactor platform and liquid saturation device with the corresponding process flow diagram. SV/PV refers to a quarter turn valve, BRP a back pressure regulator and R a regulator.

The liquid level is controlled using a second HPLC pump, which is calibrated to continuously remove liquid at the rate at which liquid exits the reactor, thus keeping the liquid level constant. When operating at higher pressures, liquid was observed to flow freely through the pump head and it was difficult to regulate the liquid level throughout the experiment. Thus, a back-pressure regulator was inserted into the setup after the pump to prevent this issue from occurring. A Par autoclave (0.3 L) fitted with a gas entrainment impeller was

used to saturate the liquid with hydrogen before being pumped into the pressurised pellet reactor. The hydrogen and nitrogen pressure in the autoclave was monitored using a pressure gauge and controlled using a regulator. A dip rod was used to pump the saturated solvent into the pressurised pellet reactor. An IKA electronic overhead stirrer (Eurostar 60) was used to ensure the liquid was fully saturated with hydrogen.

6.2.4 Experimental procedure

Before assembling the reactor as shown in Figure 6.5, a single 1% Pd/C pellet was first weighed (10.1 mg) and its dimensions recorded (width = 1.59 mm and length = 6.0 mm). The pellet was then glued vertically to the tip of the stage using Araldite Standard 2-part epoxy adhesive, care was taken to ensure glue covered as little of the pellets' surface as possible. To prevent the pellet from leaning or falling over during the drying period, the tip of a glass Pasteur pipette was carefully removed and used to hold to pellet in place on the stage. The glue was left to dry for approximately 24 hours. Once dry, the stage was placed in the centre of the reactor and the liquid distributor system aligned to ensure that the liquid flowed directly over the pellet. The tip of the distributor was positioned a few millimetres away from the top of the pellet, to create a continuous film of liquid over the pellets' surface. If the liquid freely dropped onto the pellet this would drastically alter the mass transfer characteristics and not be representative of the rivulets of flow in a trickle bed reactor. With the pellet in place the reactor was then sealed.

6.2.3.1 Establishing liquid flow and purging

Liquid flow was established by pumping pure methanol over the pellet at 1 mL/min. Once the liquid level in the PFA tube acting as a level indicator was

visually observed to be steadily rising, the second pump was switched on. The system was left until the methanol stayed at a constant level, observed via the indicator. Whilst flowing methanol, the system was first purged of air using nitrogen by pressurising the reactor to 5 barg, waiting 15 seconds and then depressurising, this step was repeated three times. The system was then purged with hydrogen following the same procedure (5 barg three times). On the final purge the reactor was depressurised after 10 minutes to monitor pressure drop due to lose fittings or poor sealing. If a leak was detected, all fittings were checked and tightened before repeating the pressure test.

6.2.3.2 Catalyst activation and saturating the substrate solution

To activate the catalyst pellet, the reactor was pressurised with hydrogen to the required pressure and methanol flowed over the pellet at 1 mL/min for 30 minutes. Whilst activating the pellet, a solution of styrene (5.62 g, 0.18 M) and n-decane (1.4 g, 0.025 M) in methanol (300 mL) was made up and added to the Par autoclave. The autoclave was purged with nitrogen followed by hydrogen (three times at 5 barg) before being pressurised to the desired pressure. Agitation was initiated to begin saturating the methanol with hydrogen and left to fully saturate for 30 minutes at 1000 rpm.

6.2.3.3 Hydrogenation of styrene

A three-way valve was used to switch the flow from pure methanol to the saturated substrate solution to begin the hydrogenation. A liquid flow rate of 1 mL/min was initially employed for fifteen minutes to ‘flush’ the system with substrate solution before moving to the desired flow rate. Once at a flow rate of interest, the reaction was left to run continuously for a set period to each steady state before sampling started. The amount of time required to reach steady state was estimated experimentally by monitoring the internal standard

and styrene concentration in the outlet stream when there was no catalyst present in the reactor. The estimated time required to reach steady state for each of the flow rates is shown in Table 6.1. For comparison with the scaled down trickle bed reactor presented in Chapter 4, similar liquid flow rates of 0.2, 0.4, 0.6, 0.8, 1.0 and 1.2 mL/min were investigated. Once sampling had begun, the product stream exiting the reactor was sampled at five-minute intervals. Samples were taken and analysed offline via gas chromatography following the method described in Chapter 3.

6.2.3.4 Calibrating liquid flow

The actual liquid flow rate was determined before starting hydrogenations by physically measuring the amount of methanol exiting the reactor over a set time period. The reactor was set up as seen in Figure 6.5, however, the liquid indicator was removed so liquid could pass straight out of the reactor. For each flow rate of interest, liquid was passed through the reactor for fifteen minutes before the mass of liquid exiting the reactor was measured over a sixty second interval, this was repeated three times for each flow rate. Figure 6.6 shows the measured flow rate against the flow rate shown on the pump.

Table 6.1: The investigated flow rates and the corresponding time waited before sampling was started.

Flow rate (mL /min)	Time waited until sampling started (mins)
0.2	45
0.4	40
0.6	35
0.8	25
1.0	15
1.2	15

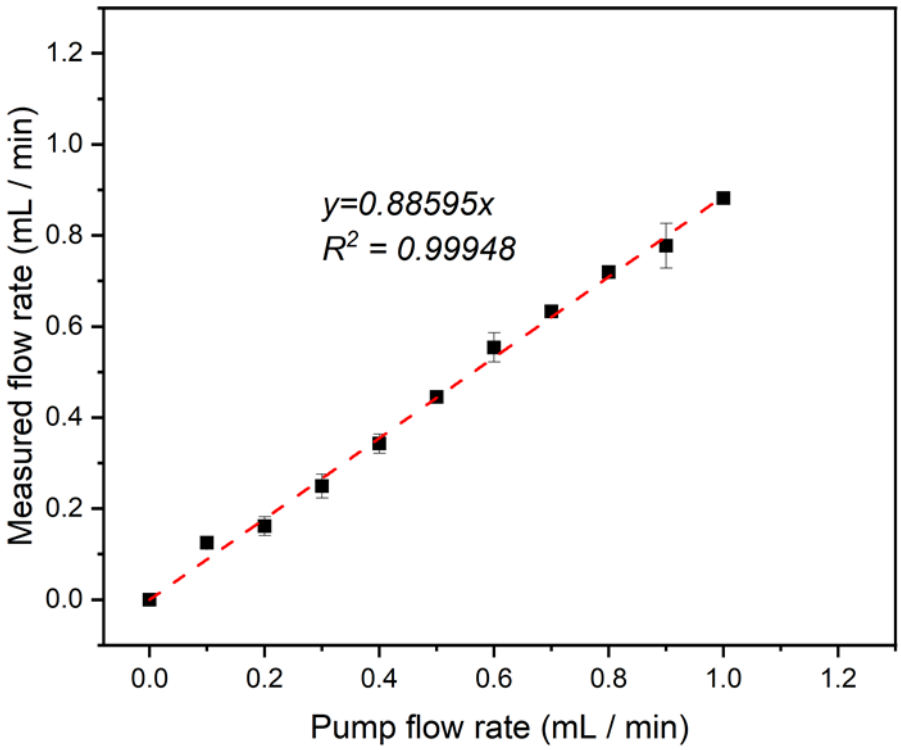

Figure 6.6: The measured liquid flow rate flowing through the pressurised pellet reactor compared to the rate shown on the pump.

The actual rate of flow passing through the reactor is slightly lower for all the flow rates investigated. This is likely attributed to friction along the walls of the pipe slowing the flow of liquid before it reaches the pellet.

6.3 Dissolved gas reactor; experimental methodology

A picture of the reactor platform and the corresponding schematic are shown in Figure 6.7. A single 1% Pd/C pellet was housed in the centre of a 1/8'' Swagelok union (I.D. = 2.3 mm) and held in place using cotton wool, located at both ends of the union. The liquid phase was saturated with hydrogen in a separate stainless steel 316L vessel (1 L), using a makeshift sparger comprising of a 0.25 µm filter fitted to the hydrogen line to assist in fully saturating the liquid, as no agitation device was present. The hydrogen gas pressure in the saturation vessel was maintained using a mass flow controller

and pressure transducer to create an automated feedback loop, where any loss in pressure in the vessel is compensated for by the mass flow controller. The pressure range was limited by the saturation vessels seal to 6.5 barg.

6.3.1 Screening pellets at different pressures

The following experimental procedure was used for all the pellets screened. A single 1% Pd/C pellet's length, diameter and mass were recorded and the pellet was placed in the union, which was then integrated into the rig as shown in Figure 6.7.

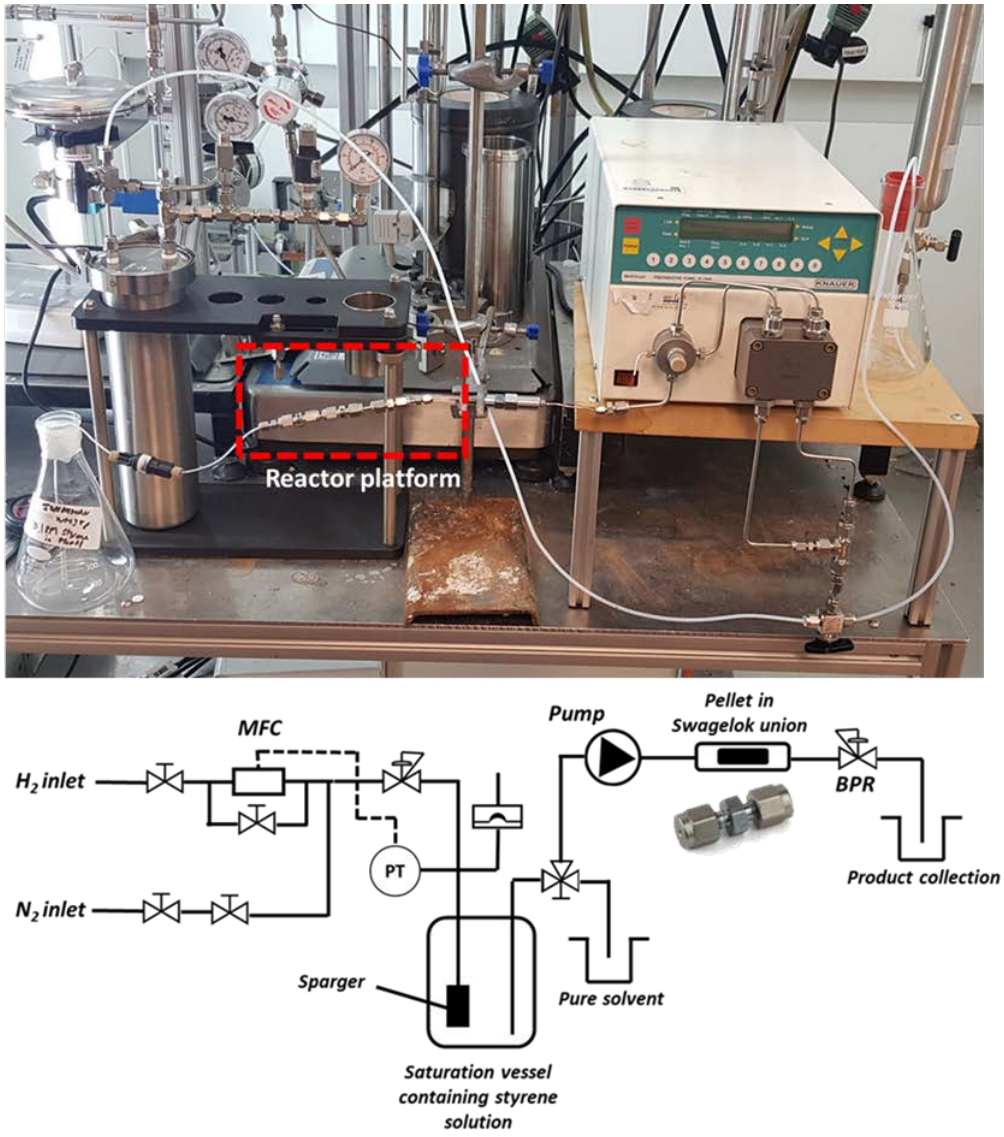

Figure 6.7: Picture of the pellet in a pipe reactor (top) and schematic of the pellet in a pipe reactor (bottom).

A solution of styrene (5.62 g, 0.18 M) and n-decane (1.4 g, 0.028 M) in methanol (300 mL) was placed in the saturation vessel, sealed and pressurised to the desired pressure for 30 minutes. Meanwhile, pure methanol was pumped through the reactor to fully wet the pellet at 0.4 mL/min. Once saturation was complete, pumping from the pure solvent was switched to the saturation vessel to begin the hydrogenation. Transparent piping was employed between the vessel and pump to monitor the liquid flow. Continuous liquid flow was observed throughout the reaction (no slug flow was seen). For every pressure investigated, the reaction was run for 30 minutes before sampling took place, this equates to well over a 100 residence times at the highest flow rate used (due to the small reactor volume), and was thought to be sufficient to reach steady state. Samples were taken every 10 minutes and analysed offline via gas chromatography following the method detailed in Chapter 3.

6.3.2 Effect of flow rate on hydrogen uptake

The experimental procedure followed that of the screening pellets at different pressures, however, the same pellet was used throughout, and the pressure was kept constant at 4 barg for all flow rates used. Four flow rates were investigated; 0.2, 0.4, 0.6 and 0.8 mL/min. The sampling times and method were the same as those outlined in the screening experiments. The liquid flow rate of the product stream was physically measured throughout the reaction at every flow rate used and an average taken.

6.4 Falling film reactor; experimental assessment

The effect of liquid flow rate and hydrogen saturation pressure on the styrene conversion in the falling film reactor is shown in Figure 6.8. Considering first

the effect of increasing flow rate, styrene conversion drops significantly with increasing liquid velocity. It was expected that the decrease in conversion would be relatively small, as observed with the saturated feed case in the pellet in the bed reactor (Chapter 4), however, that is clearly not observed in this system. At high liquid flow rates, the styrene conversions converge at almost zero conversion (0.1 – 0.2%) at all saturation pressures investigated. This implies that at high flow rates there is a physical or chemical mechanism preventing hydrogen from accessing the pellet, irrespective of pressure. As expected, the 4, 5 and 7 bara experiments showed that increased hydrogen saturation results in a higher rate of hydrogen uptake by the pellet and hence a greater styrene conversion.

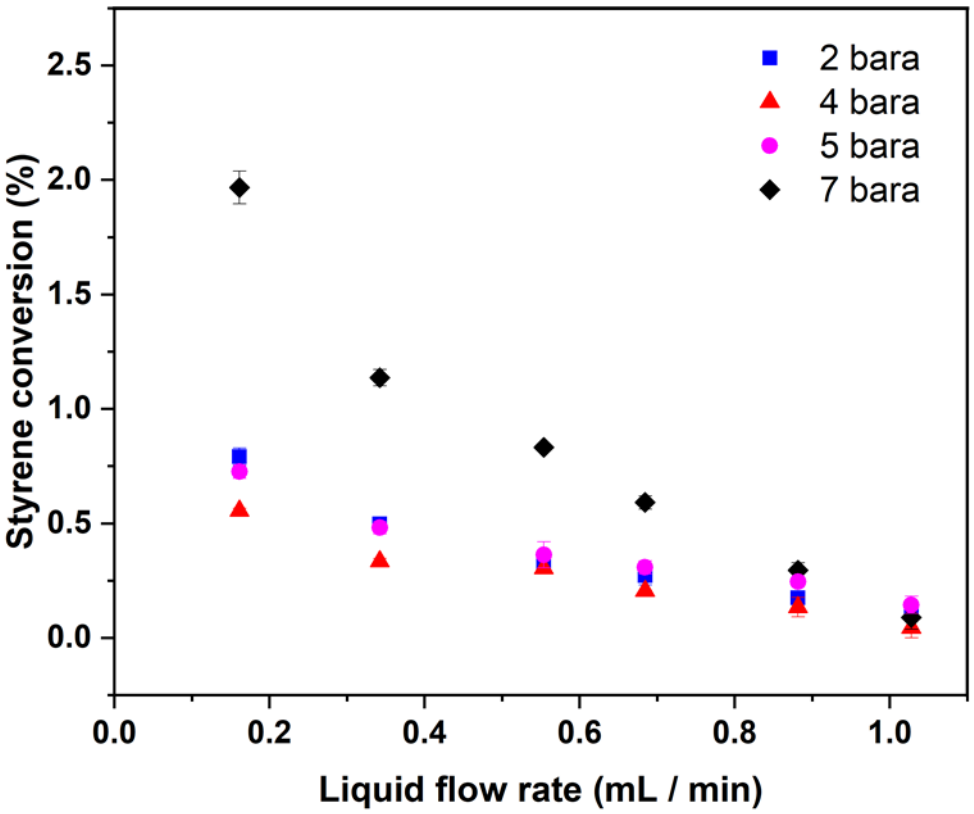

Figure 6.8: Styrene conversion as a function of liquid flow rate at different liquid saturation pressures. Using a 0.18 M styrene solution in methanol saturated with hydrogen, 298 K and a 1% Pd/C 10 mg pellet.

Though at higher liquid flow rates the effect of hydrogen saturation pressure becomes less pronounced, suggesting that even with a higher concentration of hydrogen in the liquid film the supply of hydrogen is being significantly limited. The trend seen at 2 bara saturation pressure appears to be an anomaly, as one would expect the conversion data to be lower than the 4 and 5 bara results. It is difficult to pinpoint the cause of this apparent error and as discussed at a later point the experiment was not able to be repeated.

The results become more interesting when considering the corresponding overall mass transfer flux of hydrogen to the pellet as a function of the liquid residence time over the surface of the pellet. The mass transfer flux of hydrogen to the pellet was determined via a mass balance over the liquid film ($MTR''_{H_2} = \varphi C_{ethylbenzene}$, Eq. (4.3)) and the liquid residence time calculated using the film thickness expression (Eq. (4.6)), both derived in Chapter 4.

$$\tau_{residence\ pellet} = \frac{2\pi r_p L_p \delta}{\varphi} \quad \textbf{(6.1)}$$

The pellet's hydrogen uptake rate as a function of liquid residence time is shown in Figure 6.9 at different hydrogen saturation pressures. The trend observed at all saturation pressures is markedly different to that seen in the saturated feed case in the atmospheric reactor (pellet in the bed). The fact that the hydrogen uptake rate reaches a maximum before a rapid and significant decrease is observed at higher liquid flow rates again suggests that a chemical or physical phenomenon is severely limiting the reaction. If it was the kinetics limiting the reaction, it is thought that the uptake rate would plateau or steadily decrease as the quantity of hydrogen consumed by the pellet would remain constant whilst the rate at which hydrogen is supplied to the pellet

increased (via convection). From a physical transport perspective, the increase in film thickness or diffusional limitations are unlikely to cause such a sharp drop in the uptake rate. It is possible that at higher liquid flow rates the feed begins to bypass or completely miss the pellet, though the pellet is carefully aligned, and liquid flow checked before the experiment. No evidence of liquid spraying was seen throughout the hydrogenation. Moreover, it is not known whether liquid bypassing the pellet would result in the trend seen in Figure 6.9.

More complications were found when trying to repeat the experiment with different 1% Pd/C pellets. Several different pellets were tried, and no ethylbenzene was detected in the gas chromatograph.

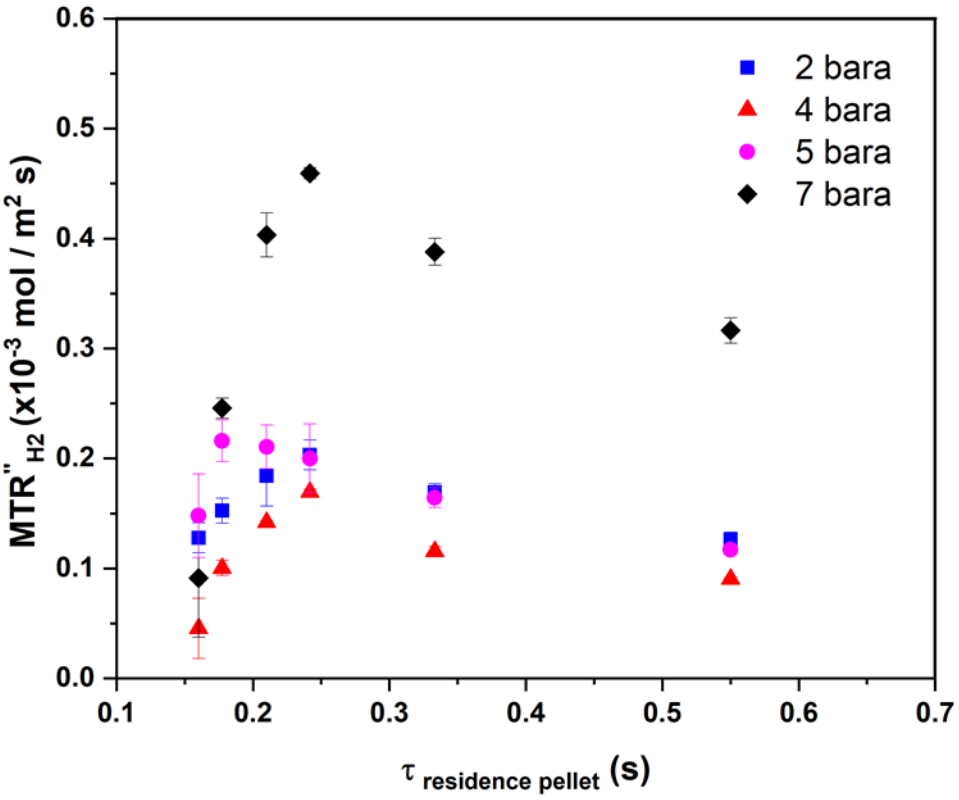

Figure 6.9: The overall mass transfer rate of hydrogen over the pellet area as a function of the liquid residence time over the pellet at different hydrogen saturation pressures. Using a 0.18 M styrene solution in methanol saturated with hydrogen, 298 K and a 1% Pd/C 10 mg pellet.

The ICP-MS results presented in Chapter 3 showed that the palladium loading distribution of the 1% Pd/C pellets was broad, suggesting that direct comparison of the hydrogen uptake rates of individual pellets could lead to erroneous analysis of the results. To circumvent this issue in the packed bed case (Chapter 4) the same 1% Pd/C pellet was used throughout the study. It is possible that the pellets chosen to repeat the experiment here were poorly loaded with palladium and hence no conversion was observed. However, all the catalysts pellet used in the dissolved gas reactor displayed quantifiable catalytic activity and therefore it is unlikely that poor catalyst loading is the cause.

6.5 Dissolved gas reactor; experimental assessment

The effect of hydrogen pressure during liquid saturation on the measured styrene conversion of different 1% Pd/C pellets is illustrated in Figure 6.10.

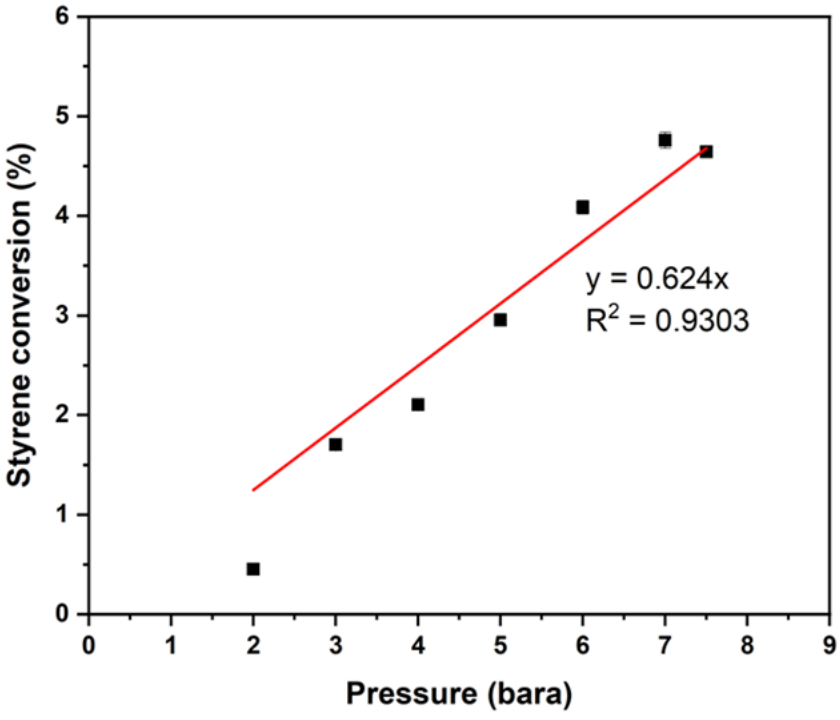

Figure 6.10: Styrene conversion at increasing hydrogen saturation pressures. Each point is a different pellet, 0.18 M styrene solution in methanol, 298 K, methanol saturated with hydrogen 30 mins.

Styrene conversion was observed to increase almost linearly with hydrogen pressure, with all but one pellet (2 bara) appearing to follow this trend. This trend agrees with the hydrogen saturated feed conditions used in the atmospheric scaled down trickle bed reactor (Chapter 4). It is thought the lower styrene conversion seen with the pellet used at 2 bara is a consequence of the pellet being poorly loaded with palladium (< 1% wt/wt), therefore, resulting in a lower observed catalytic activity. This hypothesis could quite easily be tested using ICP-MS analysis to quantify the pellet loading, however, as the technique is intrusive the pellet is unable to be re-used.

Evidence that this result is an anomaly is reinforced when considering the quantity of hydrogen taken up by the pellet from the methanol steam. Figure 6.11 shows the fraction of hydrogen in the liquid stream consumed by the pellet ($\frac{C_{ethylbenzene}}{C^*}$ %) as a function of hydrogen pressure. Interestingly, the pellets all appeared to consume 25-30% of the available hydrogen supply in the liquid irrespective of the hydrogen saturation pressure.

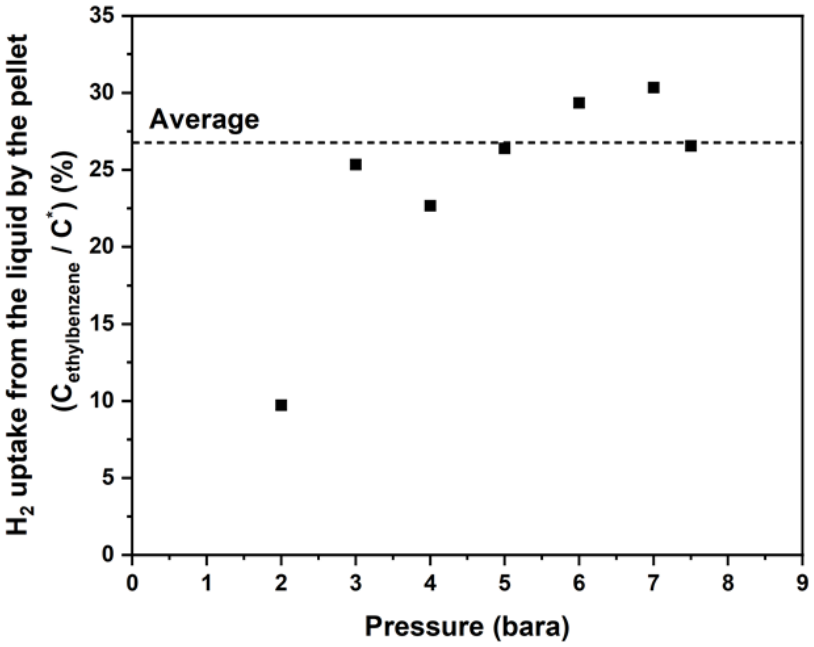

Figure 6.11: Showing the fraction of hydrogen in the liquid stream consumed by the pellet as a function of hydrogen saturation pressure.

However, the pellet used at 2 bara pressure consumed only ≈10% of the available hydrogen in the liquid, significantly lower than the other pellets operating at higher pressures. The fact that amount of hydrogen consumed from the liquid stream by the pellet remains roughly constant across all pressures investigated suggests that hydrogenation here is limited by the intrinsic kinetics on the surface of the palladium nanoparticles.

The overall mass transfer rate, MTR''_{H_2}, was calculated using Eq. (4.3), resulting from a hydrogen mass balance over the liquid stream passing the pellet (derivation can be found in Chapter 4). The uptake rate of each pellet at the different pressures studied is shown in Figure 6.12. Initial observation of the trend suggests that the uptake rate increases almost linearly until 6 bara pressure is reached before the uptake rate appears to plateau. The uptake rate would be expected to eventually reach a plateau (where the increase in hydrogen saturation pressure has no effect on the uptake rate), as the reaction would be limited by the kinetics. It is thought that a plateau in uptake rate has not been reached here. As was previously discussed, the pellet at 2 bara is likely an anomaly and thus, obscures the analysis. It is hypothesised that the trend is linear with respect to hydrogen pressure and the apparent plateau is due to the pellet at 6 bara having a higher than expected uptake rate. It could be possible that the pellet had a greater quantity of palladium, and thus was able to convert more styrene, but this hypothesis would require the pellet to be analysed via ICP-MS to confirm. The linear relationship between the hydrogen uptake rate and the pressure agrees with the results obtained from the atmospheric scaled down trickle bed reactor in the hydrogen saturated feed case.

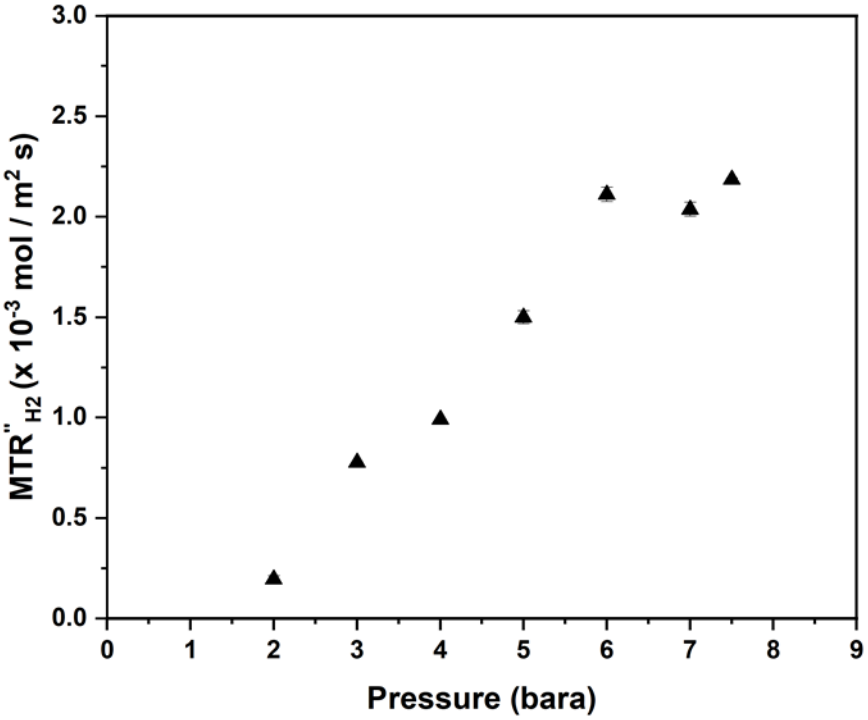

Figure 6.12: Showing the overall mass transfer of rate hydrogen as a function of the hydrogen saturation pressure. Each measurement is a different 1% Pd/C pellet

As initially discussed in the introductory paragraph to this chapter, one of the aims of this investigation was primarily designed to screen and compare the catalytic activity of the pellets. The anomaly at 2 bara shows that randomly selecting pellets under the assumption they are all loaded uniformly complicates analysis when comparing pellet uptake rates. To emphasise this fact, three pellets were independently tested at the same pressure 7.5 bara for comparison, the results can be found in Table 6.2. The hydrogen uptake has the potential to vary greatly between pellets, with no correlation between the mass transfer flux and the pellets' mass or surface area. Suggesting that without a screening process to identify whether a pellets' catalytical activity fits the trend observed during the pressure investigations, analysis of uptake rates using randomly selected pellets may result in erroneous analysis of the results. It should be noted that all the catalyst pellets tested in the convection reactor were catalytically active.

Table 6.2: Comparison of the hydrogen uptake rates of three different pellets at constant pressure (7.5 bara).

Pellet	Mass (mg)	Surface area (m^2)	$MTR''_{H_2}(x10^{-3}\ mol/m^2\ s)$
1	12	$3.1x10^{-5}$	1.59
2	9	$2.4x10^{-5}$	1.72
3	8	$2.7x10^{-5}$	2.07

6.5.1 Effect of liquid flow on the hydrogen uptake of the pellet

To investigate the effect of flow, a pellet from the screening process was selected that best fits the relationship between hydrogen uptake rate and saturation pressure. A suitably high pressure of 5 bara was then chosen, as a decrease in styrene conversion was predicted at higher flow rates and it was feared that if too low a pressure was used conversion may be hard to detect. The styrene conversion as a function of liquid flow rate for the same pellet is shown in Figure 6.13. A similar trend to that seen in the saturated feed case with the atmospheric scaled down trickle bed reactor can be observed, where styrene conversion decreases by a relatively small amount as the flow rate increases from the lowest to the highest flow rate (≈ 0.5%). One would expect the styrene conversion at 0.2 mL/min to be slightly higher or in line with the conversion observed at 0.4 mL/min. However, considering the size of the error bars the lower conversion is thought to be a facet of the experimental methodology, perhaps an irregular flow rate or gas slug in the pipe. The observed relationship between styrene conversion and liquid flow rate can be partly explained by the liquid residence over the pellet surface; higher flow rates resulting in shorter residence times and thus lower conversions. The extent to which the conversion changes will also be affected by mass transfer and diffusion as the flow rate increases/decreases.

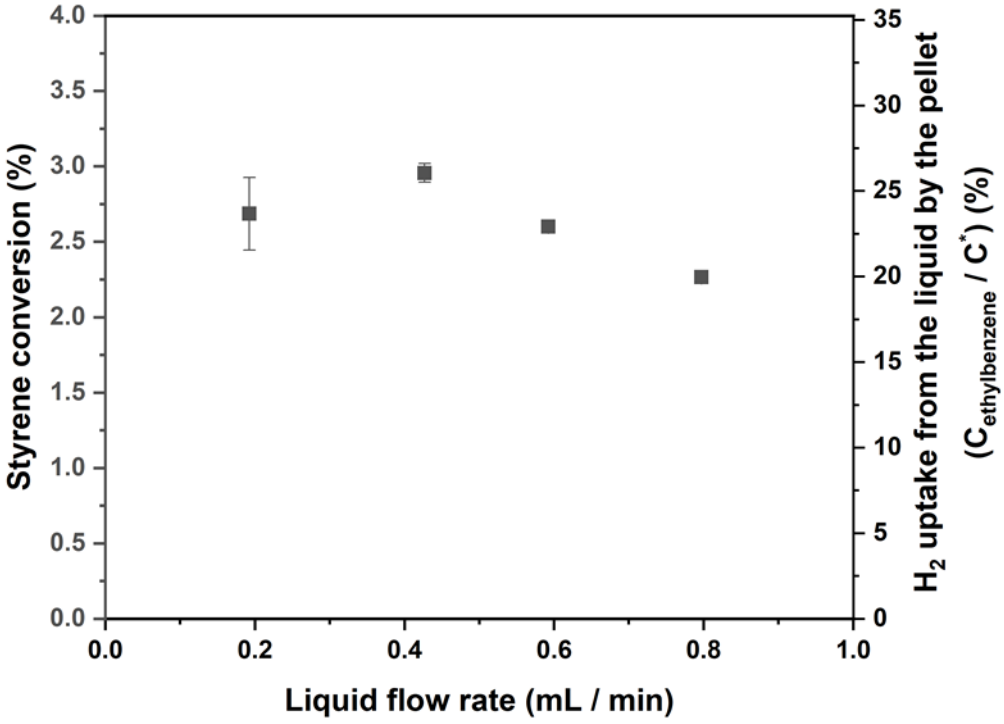

Figure 6.13: The styrene conversion and fraction of available hydrogen consumed as a function of liquid flow rate. The same pellet was used for all flow rates.

The fraction of available hydrogen consumed by the pellet is also presented in Figure 6.13, and highlights again that ~25% of the available hydrogen is consumed. Though the experimental results suggest that the fraction of hydrogen consumed decreases with respect to increasing liquid flow rate. As the flow rate increases, the time the pellet is in contact with the liquid stream decreases and therefore the quantity of hydrogen consumed from the liquid stream ultimately decreases.

The overall mass transfer rate of hydrogen at the different flow rates was investigated and compared with those in the scaled down trickle bed reactor, as a function of the residence time of the liquid flowing over the pellets' surface, $t_{residence\ pellet}$. To approximate the liquid residence time over the surface of the pellet, it was assumed that the pellet rests in the centre of the pipe with liquid flowing horizontally around it. The dimensions of the pellet housing (1/8'' Swagelok union) were taken from the CAD sales drawing [213]

and used to determine the volume around the pellet for the liquid to flow, V_{p-w}, (between the surface of the pellet and the walls of the pipe). Hence, the liquid residence time was calculated as follows;

$$t_{pellet\ residence} = \frac{V_{p-w} - V_p}{\varphi} \qquad \textbf{(6.2)}$$

Where V_p is the pellet volume and φ the volumetric liquid flow rate. Using Eq. (6.2**)**, the residence time of the liquid flowing over the pellet surface was estimated to be between 0.88-3.64 seconds for the flow rates investigated. The overall mass transfer rate of hydrogen as a function of the liquid residence time is shown in Figure 6.14, for comparison the atmospheric scaled down trickled bed reactor mass transfer rates (saturated feed) have also been included. Both datasets show that when convective mass transfer is dominant the hydrogen uptake rate of the pellet improves with increasing liquid flow rate.

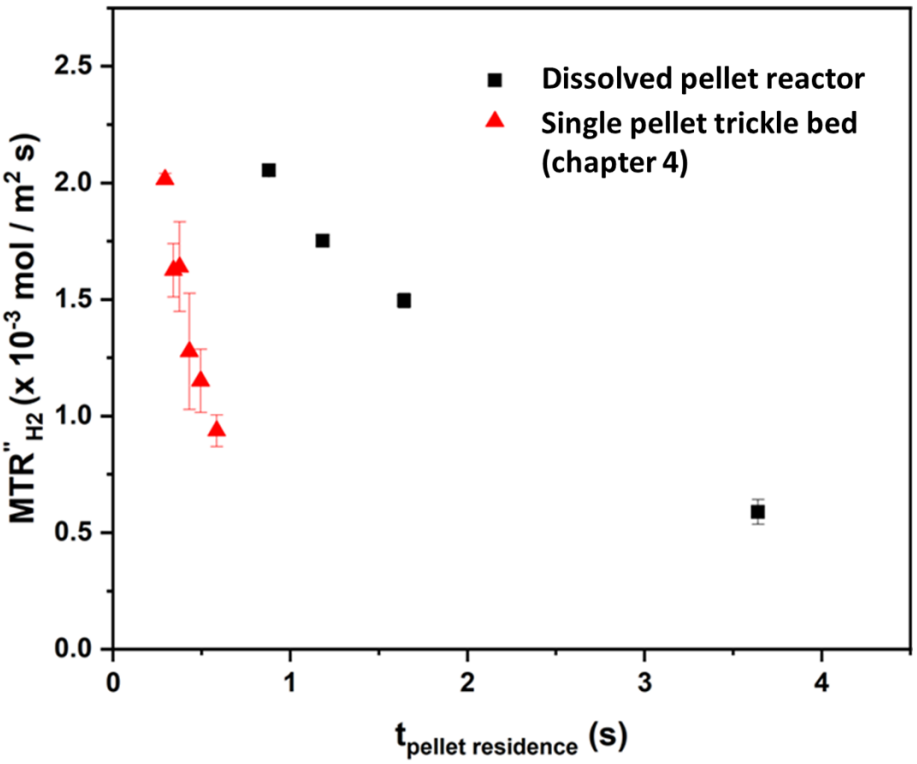

Figure 6.14: The overall mass transfer rate of hydrogen as a function of the liquid residence time over the pellets' surface for the liquid only and scaled down trickle bed reactors.

The uptake rates exhibited by the pellets in the two separate reactor platforms are of the same magnitude, though one might expect the liquid only reactor to have a higher uptake rate due to the higher saturation pressure. Comparing the two trends, the rate at which the mass transfer rate drops is significantly higher for the pellet in the bed. As shown in Chapter 5, this is a direct consequence of operating the reactor at atmospheric pressure; as the flow rate decreases, the concentration of hydrogen decreases in the liquid. Resulting, in a more significant drop in the hydrogen uptake rate of the pellet.

6.6 Dissolved gas reactor; mathematical modelling of the transfer phenomena

With the absence of gas flowing through the pipe and mass transfer prior to the pellet, the two-stage mass transfer model was deemed to be an inappropriate model to describe the liquid only system. It does, however, simplify the system considerably and therefore, a new model was developed to reconcile the effect of pressure and liquid flow on the mass transfer rate experimentally observed. As opposed to the two-stage model, where mass transfer and reaction over the pellet's surface is treated as a plug flow reactor, a boundary layer model was used to describe the liquid only case. Detailed discussion of boundary layer theory can be found in Chapter 2. The modelling approach is illustrated in the schematic shown in Figure 6.15. As the hydrogen saturated liquid flows around the pellet, hydrogen diffuses from the bulk liquid to the palladium surface where the subsequent chemical reaction occurs to form ethylbenzene.

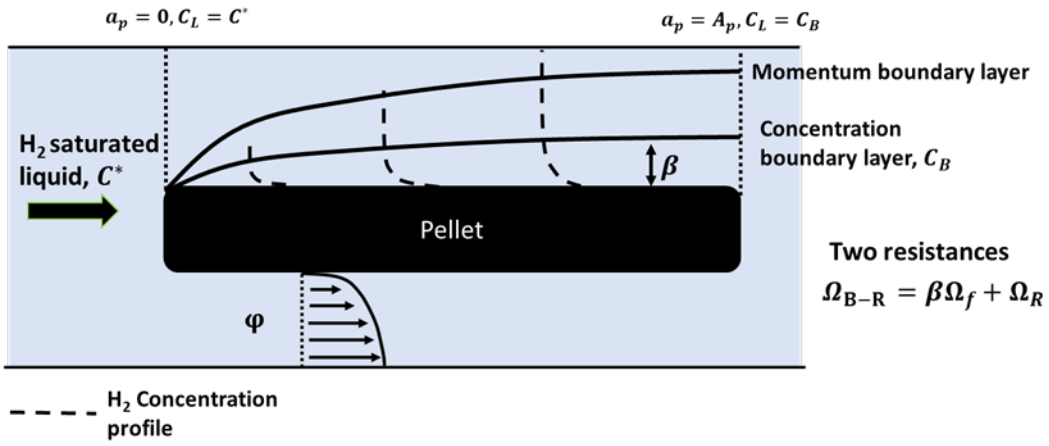

Figure 6.15: Schematic of the pellet in the pipe and the modelling approach used to describe the transport of hydrogen from the liquid to the pellet via convection.

Therefore, it is assumed that there are two resistances occurring in series; (i) a diffusional resistance through the liquid, Ω_f, and (ii) a chemical reaction resistance, Ω_R. Following boundary theory, it is assumed that at steady state a concentration boundary layer is formed at an unknown distance from the pellets' surface. The concentration boundary layer is the distance into the film where a concentration gradient is established between the local surface and bulk liquid concentrations. It is in this portion of the liquid film, β, that diffusion occurs. It is assumed that this boundary concentration, C_B, is averaged across the length of the pellet and it is within this area that diffusional resistance to the palladium surface occurs. Hence, the mass transfer rate of hydrogen from the boundary layer to the palladium surface with subsequent reaction, MTR''_{B-R}, can be expressed as;

$$MTR''_{B-R} = \frac{1}{\Omega_{B-R}} C_B \ \frac{mol}{m^2\ s} \qquad \textbf{(6.3)}$$

Where Ω_{B-R} is the resistance associated with both diffusion and chemical reaction; $\Omega_{B-R} = \beta\Omega_f + \Omega_R$. The $\beta\Omega_f$ term describes the flux of hydrogen from the concentration boundary layer to the palladium surface of concertation, C_s.

$$MTR''_{B-s} = \frac{1}{\beta \Omega_f}(C_B - C_s)\ \frac{mol}{m^2\ s} \tag{6.4}$$

Following the same assumptions used in the two-stage model and detailed in Section 5.3.2, C_s is eliminated and the concentration at the boundary layer, C_B, can be modelled by a differential molar balance over the pellet surface, da_p, yielding:

$$dC_B = \left[-\frac{1}{\Omega_{B-R}} C_B\right] da_p \tag{6.5}$$

Integration of Eq. (6.5**)** across the surface of the pellet where $a_p = 0, C_B = C^*$ yields an expression for the concentration boundary as a function of the area across the surface of the pellet the liquid has travelled.

$$\frac{1}{C_B} dC_B = -\frac{1}{\Omega_{B-R}} da_p$$

$$\int_{C_0}^{C_B} \ln(C_B) = \int_0^{a_p} -\frac{1}{\Omega_{B-R}} da_p$$

$$\ln\left(\frac{C_B}{C^*}\right) = -\frac{A_p}{\Omega_{B-R}}$$

$$C_B = C^* e^{-\frac{A_p}{\Omega_{B-R}}} \tag{6.6}$$

As the reactor is operated in a liquid only regime, convective mass transfer is the only transport process suppling hydrogen to catalyst. Thus, the overall mass transfer rate of the pellet can be expressed as;

$$MTR_{H_2} \cdot A_p = \varphi C^* - \varphi C_B \tag{6.7}$$

Substituting Eq. (6.6**)** into Eq. (6.7**)** gives the overall mass transfer flux of hydrogen to the pellet;

$$MTR''_{H_2} = \frac{\varphi\left(C^* - C^* e^{-\frac{A_p}{\varphi \Omega_{B-R}}}\right)}{A_p} \quad \textbf{(6.8)}$$

The equilibrium concentration of hydrogen in methanol, C^*, was obtained using Henry's constant as described in Section 5.3.1 [200].

6.6.1 Determination of the mass transfer coefficient of the film

As the main transport mechanism suppling the pellet with hydrogen is convective transport from the flowing fluid, a Sherwood correlation was utilised. The averaged mass transfer coefficient of the film along the length of the pellet, k_f, was determined through a correlation for the Sherwood number, Sh, for laminar liquid flow over a flat horizontal plate [193];

$$Sh = \frac{L_p k_f}{D_{H_2}} = 0.664 Re^{0.5} Sc^{0.33} \quad \textbf{(6.9)}$$

$$Re = \frac{\rho U L_p}{\mu} \; and \; Sc = \frac{\mu}{\rho D_{H_2}}$$

Where L_p is the characteristic length (here the length of the pellet), Re the Reynolds number for the liquid flowing between the pellet surface and wall of the pipe and Sc, the Schmidt number. The superficial velocity, U, of the liquid flowing past the pellet was calculated from the difference between the cross-sectional area of the pellet, CSA_{pellet} and pipe, CSA_{pipe};

$$U = \frac{\varphi}{CSA_{pipe} - CSA_{pellet}} \quad \textbf{(6.10)}$$

Table 6. 3 outlines the calculated Reynolds number, Sherwood number and film coefficient. Beginning first with the Reynolds number, the calculated values are very low (< 50) indicating that flow around the pellet is laminar [214].

Table 6. 3: The superficial velocity, Reynolds number, Sherwood number and averaged mass transfer coefficient for the liquid flow rates investigated.

$\boldsymbol{\varphi}\ (\boldsymbol{mL/min})$	$\boldsymbol{U}\ (\boldsymbol{x10^{-3}\,m/s})$	$\boldsymbol{Re}$	$\boldsymbol{Sh}$	$\boldsymbol{k_f}\ (\boldsymbol{x10^{-5}\,m/s})$
$\mathbf{0.19}$	1.46	10.47	7.53	2.43
$\mathbf{0.43}$	3.24	23.22	11.21	3.36
$\mathbf{0.59}$	4.50	32.25	13.21	4.27
$\mathbf{0.80}$	6.10	43.21	15.33	4.96

This is not an unexpected result, as the characteristic length the liquid travels is very short, resulting in a limited time frame for the velocity profile of the liquid to fully develop and transition into a turbulent flow regime (which would be observed if the pellet was infinitely long). The Schmidt number, though not displayed in Table 6. 3 was determined to be ~43. The number gives an indication of the relative magnitudes of the fluid flow (momentum) boundary layer and the concentration boundary layer over the surface of the pellet and suggests that the momentum boundary layer is thicker (*Sc* >1) [215]. This is commonly observed in liquid-solid flow.

In terms of the averaged mass transfer coefficient, k_f, it is difficult to find convective only studies, similar systems such as pellet string reactors almost always involve a gas flow and have been showed to exhibit markedly different hydrodynamics to those observed here. Rather than using a known Sherwood correlation, Haase *et al*. estimated the empirical coefficients by fitting a proposed correlation for the hydrogenation of alpha methyl-styrene obtained in a pellet string reactor [82]. Using their correlation, it is estimated that they obtained Sherwood numbers and averaged liquid mass transfer coefficients for a single pellet in the bed across ranges of 13.43 - 25.05 and 3.36 – 6.27 m/s respectively. The higher mass transfer rates seen in the pellet

string reactor are thought to be a result of the smaller sized catalyst particles or the thin liquid films formed over the surface of the catalyst due to gas flow.

Comparing the averaged mass transfer coefficient calculated here with the gas-liquid coefficient for trickle bed reactors found in the literature, it is apparent that though the values are within the same magnitude (1 – 5x10^{-5} m/s) the trends show very different behaviours. Stamatiou and Muller compared the gas-liquid mass transfer coefficients experimentally obtained in trickle bed reactors and observed that the mass transfer coefficient decreases at higher liquid phase velocities [182]. In the case of trickle beds, though higher flow rates will enhance convection, the liquid film thickness over the catalyst support will also increase resulting in a higher gas-liquid mass transfer resistance. In the pipe reactor, this phenomenon is unlikely to affect the overall hydrogen uptake rate as convection is the only transfer process supplying hydrogen to the catalyst surface and the liquid film is limited to the diameter of the pipe. Hence, an increase in the averaged mass transfer coefficient is observed.

6.6.2 Reduction of styrene at different saturation pressures

Following determination of the averaged mass transfer coefficient, the hydrogen uptake rates at different liquid saturation pressures were modelled. The chemical reaction resistance was calculated following the same procedure outlined in Section 5.4.1 and thus, will not be detailed again here. The percentage of the film in which diffusion from the concentration boundary occurs, β, was fitted to the experimental hydrogen uptake rates by minimising the Sum of Squares $\sum_{i=0}^{n}\left(y_{exp.i} - y_{calc.i}\right)^2$ to successfully model the effect of

pressure. Comparison between the modelled and experimental hydrogen uptake rates is shown in Figure 6.16, including the 95% confidence limits.

From initial observations, the model generally fits the experimental data relatively well for all pressures expect at 2 and 6 bara. It is thought that if the experiment was repeated and the same pellet used throughout, the model would be able to reconcile the experimental data much better, as palladium loading distribution would not be an issue. The result at 2 bara has been extensively discussed earlier in this chapter and can be confidently identified as an anomaly. Interestingly, the model suggests that the flux at 6 bara is also an outlier, and the trend does not in fact begin to plateau between 6 to 7.5 bara. This reinforces the hypothesis stated earlier that a plateauing of the hydrogen uptake rate at the relatively low pressures investigated would be unlikely.

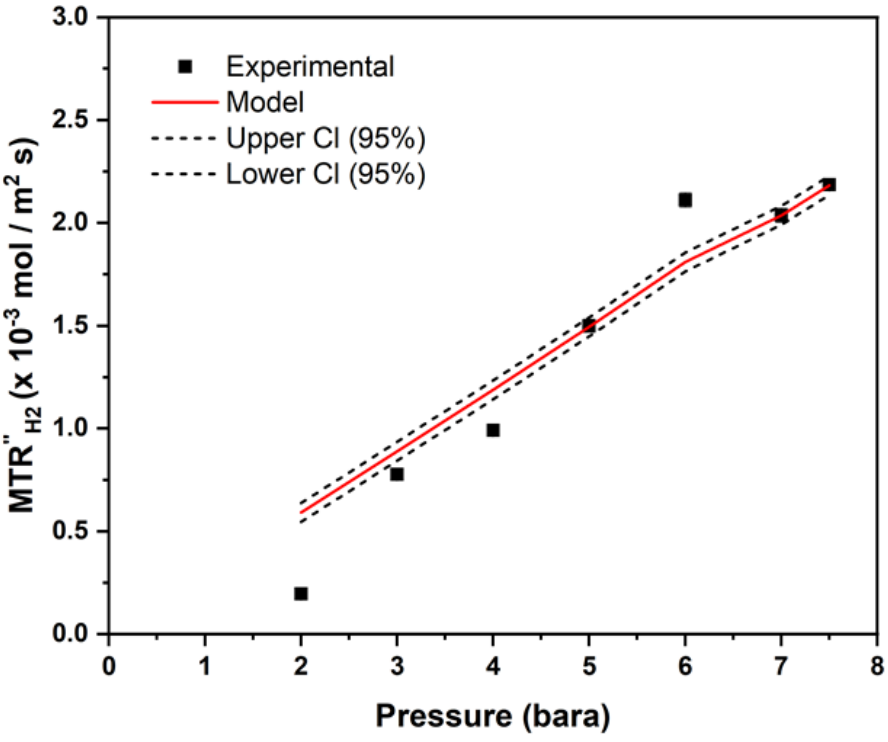

Figure 6.16: Comparison between the fitted convection only model and the experimental mass transfer flux of hydrogen to the pellet at different liquid saturation pressures. The 95% upper and lower confidence limits have also been included.

The calculated and fitted parameters for the convection only model are presented in Table 6.4. The proportion of the film surrounding the pellet in which mass transfer occurs in was determined to be 42.3%. This equates to the concentration boundary being formed at approximately 0.17 mm into the liquid from the catalyst supports' surface. This number is significantly lower than the percentage of the film dedicated for gas-liquid diffusion seen when a pellet was immobilised in a bed ~97%. This makes sense, however, as diffusion is occurring from the gas-liquid interface to the immobilized pellet and, therefore, over a larger portion of the film. For the pellet in the pipe (convection only), the pellets' supply of hydrogen is from the liquid flow only and thus, any hydrogen outside the concentration boundary will by-pass the pellet. Therefore, this suggests that over 50% of the hydrogen flowing past the pellet is not in close enough proximity to diffusive to the catalyst surface. Considering this and the fact that the pellet was able to consume roughly 25% of the hydrogen present in the liquid film irrespective of the saturation pressure, the pellet is significantly more effective at consuming the hydrogen that is actually accessible to it.

Table 6.4: The calculated and fitted parameters used to model the mass transfer flux at different saturation pressures.

Parameters	Value	Comment/source
$\boldsymbol{\beta}$	42.3%	Proportion of the film in which diffusion from the concentration boundary occurs (fitted)
$\mathbf{1/\Omega_R}$	2.2x10^{-3} m/s	Chemical reaction resistance
$\mathbf{1/\Omega_f}$	3.63x10^{-5} m/s	Film resistance from the concentration boundary to the catalyst surface
$\mathbf{1/\Omega_{B-R}}$	8.24x10^{-5} m/s	Resistance associated with both diffusion and chemical reaction

The resistance associated with both diffusion from the concentration boundary and reaction, Ω_{B-R}, is an order of magnitude higher than the liquid film and reaction resistance determined in the pellet in the bed case. Again, this can be explained by the distance into the liquid film at which the boundaries exist. The concentration boundary layer in the convection only case is established further away from the pellets' surface when compared to the liquid boundary of the pellet in the bed (3%). Therefore, the resistance to diffusion will be much lower due to the shorter distance mass transfer is occurring over.

6.6.3 Reduction of styrene at liquid different flow rates

Using the mass transfer coefficients determined in Section 6.6.1 and the chemical reaction resistance calculated for styrene on Pd/C catalyst in Section 5.4.1, the hydrogen uptake rate was modelled at the different liquid flow rates investigated. Again, β was fitted to the experimental hydrogen uptake rates by minimising the Sum of Squares $\sum_{i=0}^{n}\left(y_{exp.i} - y_{calc.i}\right)^2$. Comparison between the modelled and experimental hydrogen mass transfer rates is shown in Figure 6.17 with the 95% confidence limits included. From initial observation, the model fits the experimental trend well with all but one flow rate falling well within the 95% confidence limits. The fact that the model is unable to reconcile the hydrogen uptake rate at the longest residence time (0.2 mL/min liquid flow rate) is thought to be a consequence of experimental error rather than any limitations of the model. As previously discussed, the measured styrene conversion at this flow rate was lower than expected and this would give rise to the lower mass transfer rate the model appears to be unable to reconcile.

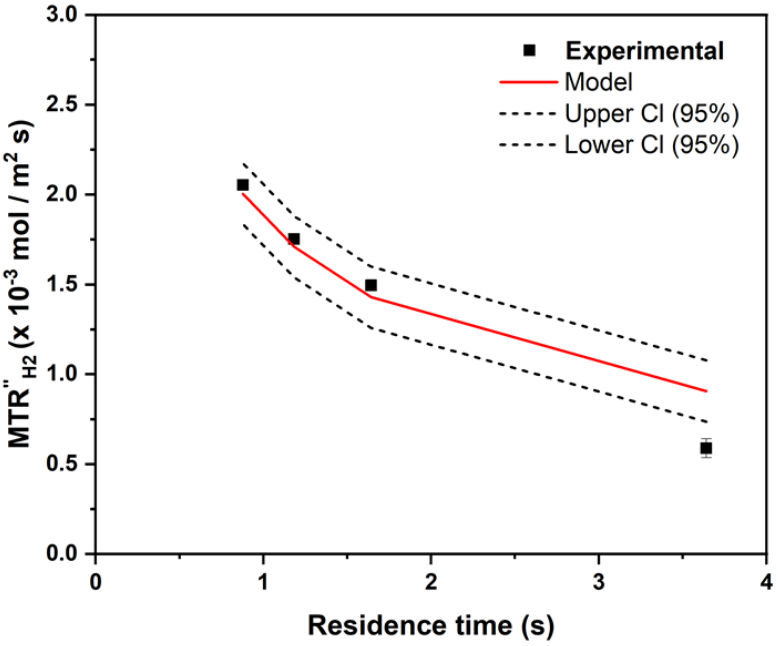

Figure 6.17: The modelled and experimental overall hydrogen mass transfer flux to the pellet as a function of the liquid residence time over the surface of the pellet.

The calculated and fitted parameters used to model the effect of liquid flow are presented in Table 6.5. The proportion of the film in which diffusion from the concentration boundary to the catalyst surface occurs was found to be 44.66%, suggesting that the concentration boundary exists approximately 18 mm from the pellets' surface.

Table 6.5: The calculated and fitted parameters used to model the mass transfer flux at different liquid flow rates.

Parameters	Value	Comment/source
$\boldsymbol{\beta}$	44.66 %	Proportion of the film in which diffusion from the concentration boundary occurs (fitted)
$\mathbf{1}/\boldsymbol{\Omega_R}$	2.2x10^{-3} m/s	Chemical reaction resistance
$\mathbf{1}/\boldsymbol{\Omega_f}$	2.43 – 4.96x10^{-5} m/s	Film resistance from the concentration boundary to the catalyst surface
$\mathbf{1}/\boldsymbol{\Omega_{B-R}}$	5.32 – 10.60x10^{-5} m/s	Resistance associated with both diffusion and chemical reaction

As might be expected this result is very close to the value of β found when the flow rate was held constant and the saturation pressure was investigated. It is hypothesised that the distance at which the concentration boundary exists should change with respect to liquid flow rate, and that as the flow rate increases the proportion of the film dedicated to diffusion decreases. Hence, the mass transfer rate increases. Evidence of this phenomenon can be seen by examining the film resistance from the concentration boundary to the catalyst surface, Ω_{B-R}, which decreases as the liquid flow rate increases. Therefore, it is thought that one of the limitations of the model would be the divergence from experimental reality at very high/low flow rates.

6.7 Evaluation of the two technologies and concluding remarks

The main aims of the chapter, by which the two technologies would be experimentally assessed, can be summarised by the reactor's ability to;

- Investigate convective and diffusive processes to improve process understanding of the hydrogen uptake rate of the pellet,
- Aid in catalyst testing by screening pellets at different pressures and liquid flow rates.

From a practical and scalability perspective, the dissolved gas reactor is operationally a much simpler technology that could be easily modified for use with other chemical systems at various scales. Being akin to a plug flow reactor, by increasing the length and using parallel channels the number of pellets could be sizably increased, though loading would likely be time consuming. In this regard, the falling film reactor would be very challenging to

scale up to even ten pellets, as the gluing process is somewhat arduous and very time consuming. The inability to heat the reactor with ease is also a major drawback, though with additional development the reactor could be redesigned to accommodate for a heating mechanism but this would require significant changes to the overall fabrication.

Their practicality also affects the two technologies abilities to efficiently screen the pellets. The time spent positioning the pellets within the falling film reactor restricts its potential at rapidly screening different catalysts. Moreover, many catalyst forms such as spheres maybe incompatible with the gluing approach required currently. Again, the method by which the catalyst particles are fixed in the reactor could be redesigned, using a ‘basket’ for smaller catalyst particle sizes or a clamp design for the pellets used in this study, but this still might not address the trends seen at higher liquid flow rates (sudden loss of conversion). The dissolved gas reactor on the other hand, is capable of screening different pellets at different processing conditions efficiently and is more compatible with different catalyst sizes.

When investigating the mass transfer characteristics of a single pellet under different processing conditions, the two reactors produced markedly different trends. Though flow over the pellet in the falling film reactor may be more representative of that seen in trickle bed reactors, the effect the processing conditions had on the hydrogen uptake were difficult to explain. Considering the effect of liquid flow, where the mass transfer rate suddenly dropped off at higher liquid flow rates, it was not apparent whether this trend was due to mass transfer limitations, the kinetics or a facet of the reactor design. Moreover, this trend has not been observed to date when compared

to the trickle bed literature and given the failure to reproduce these results with other catalyst pellets, it is difficult to have confidence in the validity of the results. The trends seen with respect to pressure and liquid flow rate in the dissolved gas reactor are relatively simple to explain and correspond well with the trends observed in the scaled down trickle bed reactor in Chapter 5. Though not able to quantify the effect of radial diffusion (no gas phase present), the transport processes are significantly easier to model than in the case of the scaled down trickle bed reactor. With the number of unknown parameters that required fitting to the experimental data reduced to one. Using the dissolved gas reactor, it has been shown that the rate at which hydrogen gas accesses the catalyst surface can be easily manipulated through the liquid flow rate and hydrogen saturation pressure.

In conclusion, following the experimental assessment of the two technologies it is in the authors' opinion that the dissolved gas reactor is the more viable reactor platform for investigating transfer phenomena and screening heterogenous catalysts. In its current state, the falling film reactor requires more development to increase the frequency at which pellets can be tested, which would in turn allow for validation of the results presented in this chapter. Until these issues are solved, this ultimately prevents this technology from being utilised in an academic or industrial setting. The dissolved gas reactor on the other hand has the potential to rapidly screen catalysts and due to its simple design could be easily scalable and is flexible enough to allow investigation of other chemical systems. This, coupled with the ability to manipulate the rate at which hydrogen accesses the pellet through the operating conditions, makes the reactor platform a promising tool in screening for selectivity benefits in more complex chemical systems in future.

Chapter 7
Conclusions & future perspectives

Given the important role mass transfer plays in delivering hydrogen to the catalyst surface in three phase catalytic systems, it is a key parameter in the design and scale up of trickle bed reactors. Traditionally, to obtain the mass transfer characteristics required for the successful scale up of trickle bed reactors, trials have focused on the design of a laboratory scale reactor that is hydrodynamically similar to its commercial scale counterpart. Wall effects, liquid mal-distribution and poor catalyst wetting, all characteristic of laboratory scale reactors, are seldom issues on a commercial scale and thus, need to be removed to obtain representative data useful for scale up. This can be a challenging and time intensive process, where subsequent scale up criterions are undefined and lacking in the general trickle bed literature. Moreover, the complex relationship between the fluid hydrodynamics and mass transfer that exists within the catalyst bed makes the reliable quantification of the mass transfer characteristics difficult.

An alternative method to studying the mass transfer processes that are so critical in the performance of these reactors, is by scaling down to a small number of catalyst pellets. Using bespoke reactor platforms, the conditions within the bed can be more finely controlled and the mass transfer characteristics can be decoupled from the hydrodynamics. This method was selected to successfully scale down to a single catalyst pellet to isolate and measure the convective and diffusive mass transfer processes supplying hydrogen to the catalyst surface in heterogenous hydrogenations in trickle bed

reactors. Moreover, bespoke reactor platforms were fabricated and evaluated to assess their ability to investigate mass transfer in three phase reactions.

7.1 Scaling down to isolate the mass transfer processes

Before any work focussing on bespoke reactor design or system modelling could be undertaken, a proof of concept study was required to demonstrate that a single catalyst pellet could be used to measure hydrogen uptake. An aim from the offset was to reach a balance between ensuring the system was as representative as possible of a trickle bed reactor, whilst having the required control over the systems' operating conditions. This resulted in a design that was able to ensure that the pellet was fully wetted and still exhibited the desired flow regime, but liquid bypassing on the walls and the lack of pressure control within the reactor made the subsequent interpretation and modelling of the results more complex. Designing a scaled down reactor that is fully representative of the packed bed environment and allows for fine control over the hydrodynamic behaviour would likely be very challenging. Another constraint derived from the use of a single catalyst pellet was the palladium loading distribution and how to account for this when comparing pellet uptake rates. Moreover, setting up the experiment and immobilising the pellet in the bed was time consuming and difficult to reproduce, hence the same pellet was used throughout.

The hydrogenation of styrene was shown to be an appropriate case study for the single pellet system, having fast intrinsic kinetic properties with the catalyst of choice. Even so, maximum conversion with the pellet was very low (≈ 2%) and this brings into question whether the methodology could be directly applied to a slower kinetic system. Scaling the system up to increase

catalytic activity and conversion may make it difficult to decouple and model the two transport processes.

The scaling down methodology was successfully utilised to determine two distinct mass transfer regimes, depending on whether the liquid feed is saturated or not before entering the reactor. To the best of the authors knowledge these trends have yet to be isolated and compared in the trickle bed literature. Moreover, a level of control over the rate at which hydrogen is supplied to the catalyst was demonstrated through manipulation of the liquid phase velocity. The significance being that by appropriately selecting the extent to which the liquid feed is saturated with hydrogen, the pellet uptake rate can be increased or decreased with increasing liquid flowrate. In the case of the diffusion limited regime, the increase in liquid film thickness over the pellets' surface was shown to cause the drop in uptake rate with increasing liquid velocity through a combined experimental and modelling approach.

Though able to isolate the regimes that were most dominant (or most limiting), the experimental approach alone was not able to quantify the extent to which each transfer process was suppling hydrogen to the catalyst at a given operating condition. Simple thin or stagnant film mass transfer models were not able to reconcile the experimental data when liquid was hydrogen free or saturated on entering the reactor. Thus, a more comprehensive model was required to obtain the level of process understanding required.

7.2 Modelling the scaled down single pellet reactor and quantifying the convective and diffusive contributions

The design of the scaled down reactor, consisting of inert glass beads and the one pellet, had a strong influence on the modelling approach. The two-stage

model was developed to be able to account for the mass transfer into (and out of) the liquid before it reached the pellet. The concentration of hydrogen in the liquid at the point where it reaches the pellet has a strong effect on the hydrogen concentration profile in the liquid as it flows over the pellet and was estimated via a plug flow model. Due to the lack of experimental methods or correlations to approximate the mass transfer coefficient over the non-catalytically active surface, two fitting parameters where required. Modelling of the convective and radial diffusion over the pellets surface was achieved using the well-established mass transfer resistances in series approach, and by combining the two models the average hydrogen concentration in the film close to the surface of the pellet was approximated. Three fitting parameters were used to reconcile the experimental data, providing evidence that even when scaled down to the one pellet the system is still inherently complex to model. Moreover, to account for pore resistance and to justify the assumptions made in relation to the intrinsic observed rate constant used in the model, detailed catalyst characterisation and interpretation was required.

Using the two-stage model, the amount of hydrogen supplied to the pellet by convection and radial diffusion was decoupled and their individual contributions quantified. With regards to improving the performance of trickle beds, the mass transfer of hydrogen can be significantly improved by enhancing convective transport. This is ultimately achieved by maximising the amount of hydrogen in the liquid as it reaches the pellet, through feed saturation or addition of non-active surface area in the bed. Furthermore, provision of inert surface to increase gas-liquid surface area, enabling more mass transfer to occur has been shown to enhance catalyst productivity per gram of palladium via convective transfer. Convective transfer can be

increased further by manipulating the liquid velocity, though this comes at the expense of reducing product conversion downstream. The rate at which hydrogen is delivered by the two processes only starts to become comparable at low liquid flow rates.

Limitations with the model are thought to centre around application upon increasing scale. Applying the model to a laboratory scale trickle bed reactor containing pellets diluted in inert fines or beads would be challenging, as the two mass transfer stages would be occurring simultaneously across the length of the bed. Moreover, it is not apparent whether the model would be able to describe kinetically slower systems. With a slower system, the uptake rate would naturally be lower and the chemical reaction resistance higher, and it is suspected contributions from convection and diffusion may not be measurable.

Having successfully decoupled the two transport processes and effectively quantified their contribution to the mass transfer rate of hydrogen, the primary objectives and research question of the thesis has been answered. In principle, it is possible on an individual pellet scale to identity, measure and quantify the effects of the two transfer processes. However, quantification is challenging and has required an extensive modelling effort, producing a model that currently may not be suitable to describe the phenomena on scale up. The work highlights three design parameters that can be utilised when trying to control the rate at which hydrogen is supplied to the pellet: (i) hydrogen concentration in the liquid, (ii) liquid flow rate and (iii) addition of non-active surface area. Manipulation of these parameters to limit, maximise or optimise hydrogen uptake of a catalyst has the potential to

improve trickle bed performance. Moreover, knowledge of how to control the hydrogen supply could aid in the design of trickle bed processes for chemical systems where selectivity is key to performance, whether hydrogen rich or hydrogen starved conditions are required.

7.3 Evaluating alternative hydrogenation technologies

Having isolated the transport processes in Chapter 4 and quantified their contributions to the hydrogen uptake rate of the pellet in Chapter 5, the main objectives of the thesis had been met. The final chapter of work focussed on combining the experimental and modelling approaches to evaluate the mass transfer characteristics of two single pellet reactor technologies fabricated in house. To reduce system complexity, the pellet was removed from a ‘packed bed environment’ entirely and instead the single pellet was housed alone, either on a stage or within a narrow pipe, where the hydrodynamics and process conditions could be finely controlled. Furthermore, this removed some of the complexity when attempting to model the system. The main objectives of the study were to assess each technologies ability to; (i) investigate convective and diffusive processes and (ii) efficiently screen pellets (something which the proof of concept single pellet trickle bed reactor was unable to do).

Of the two reactors tested, the dissolved gas reactor was found to be a promising scalable technology for the rapid screening of catalysts that was significantly easier to model when compare to the scaled down trickle bed. Several pellets (>10) were able to be screened under different processing conditions and similar trends were observed to those seen in the scaled down trickle bed. A greater range of hydrogen saturation pressures were able to be

investigated, finding that the pellet on average was able to consume 25% of the available hydrogen in the liquid feed irrespective of the saturation pressure. The pellet's uptake rate increased almost linearly with saturation pressure, suggesting that across the process conditions investigated, the uptake rate of the pellet was still limited by the rate at which hydrogen was being supplied to the pellet.

Due to the design of the reactor, no gas phase was present and thus one is not able to decouple the convective and radial diffusive processes. Moreover, this brings into question how representative the system is when compared to the packed bed environment. As mentioned, the system was successfully modelled, requiring only one fitting parameter to reconcile the experimental data due to the reduction in system unknowns. However, as gas-liquid transfer is not present, it is thought that this model would not be suitable for describing trickle bed reactors.

The falling film reactor, being more complex in design and operation, was unable to effectively screen the pellets and suffered from issues with reproducibility. Trends in the pellet uptake rates differed significantly from those seen in the dissolved gas and scaled down trickle bed reactors. A lack of understanding behind the chemical and/or physical processes causing these trends made interpretation difficult. In addition, the results that were obtained could not be described using the two-stage model. Further development to simplify the method of fixing the pellet in place would significantly reduce the time taken to screen catalysts and improve the possible application of the technology for process understanding.

Despite the limitations of both single pellet technologies, by removing the pellet from the complex environment within the packed bed the common challenges associated with the design of laboratory trickle bed reactors have been negated. Allowing for investigation into the mass transfer characteristics of the pellet in a finely controlled environment, where the uptake rate can be controlled and manipulated via the process conditions. Screening in these reactors before moving to a laboratory trickle bed reactor could give integral process information on both catalyst activity and the preferred mass transfer conditions to give the desired yield or selectivity.

7.4 Future perspectives

Scaling down to study the transport phenomena has been shown to be a suitable approach to quantifying the mass transfer characteristics in trickle bed reactors. By demonstrating the ability to manipulate the convective and diffusive transport processes, this work has built on and supplemented the process understanding available in literature and opens the question of whether this control can be applied to improve reactor performance during selective hydrogenation of fine chemicals at various processing scales.

To facilitate the broader application to heterogenous hydrogenations and other reaction classes, the methodology would have to be validated with other chemical systems. Identification of a potential system that is suitable for the single pellet reactor may be a challenge, but screening at the single pellet scale (where you can finely control the rate at which hydrogen is supplied) would be very beneficial for process development and subsequent scale up. A selective hydrogenation that could be a promising candidate is the hydrogenation of ethyl pyruvate [216, 217]. Enantioselectivity to the desired

S-ethyl lactate (shown in Figure 7.1) has been shown to be enhanced in batch when operating in hydrogen starved conditions, achieved by manipulating gas-liquid mass transfer through agitation intensity to operate in a diffusion limited regime. On scale up to a laboratory scale trickle bed, provision of inert surface area through the addition of fines would enhance the convective uptake of hydrogen and be used to emulate the conditions observed in the single pellet system [194].

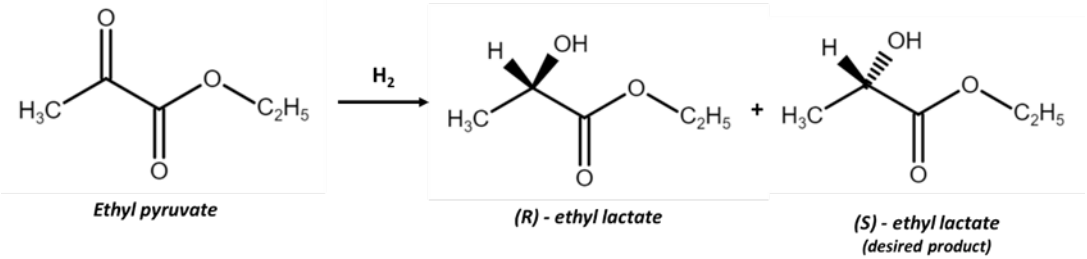

Figure 7.1: Hydrogenation of ethyl pyruvate demonstrating the enantioselectivity to R-ethyl lactate and (S)-ethyl lactate enantiomers.

Another key challenge in relation to the broader application of the methodology is to develop the two-stage model into a general reactor model that can describe the convective and diffusive processes in trickle bed reactors independent of scale. One methodology that is becoming increasingly utilised to model these complex three phase systems is computational fluid dynamics (CFD)[218-220]. Being able to model both the fluid hydrodynamics and the mass transfer, CFD studies can construct 3D models based on the geometry of the reactor and catalyst particles themselves. As can be seen in Figure 7.2, the concentration profile of hydrogen in the liquid film can be visually observed to access convection and diffusion. Though the work referenced here investigated a string of spherical pellets, it is evident that this methodology could be scaled up to mixtures of inactive and catalytically active media in a laboratory trickle bed reactor.

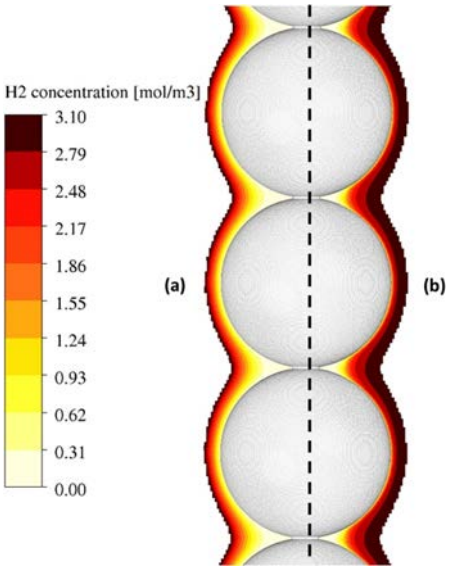

Figure 7.2: CFD simulation of the hydrogen concentration in a liquid layer flowing over a string of catalyst pellets. Showing (a) the concentration profile predicted by pure diffusion and (b) convection-diffusion, taken from Bouras *et al*. (2021).

The advantages of being able to measure and quantify the convective and diffusive mass transfer processes in heterogenous hydrogenations has been demonstrated in this thesis by scaling down to a single catalyst pellet. Through manipulating of the process conditions, the two transport processes can be exploited to give increased catalyst utility and control of the hydrogen concentration close to the catalyst surface. However, these results now need validating with another chemical system (preferably where selectivity is a key performance metric) and the model developing further to be able to describe the convective and diffusive processes independent of scale.

List of References

1. Irfan, M., T.N. Glasnov, and C.O. Kappe, *Heterogeneous Catalytic Hydrogenation Reactions in Continuous-Flow Reactors.* 2011. **4**(3): p. 300-316.
2. Calabrese, G.S. and S. Pissavini, *From batch to continuous flow processing in chemicals manufacturing.* AIChE Journal, 2011. **57**(4): p. 828-834.
3. Braune, S., et al., *Selective nitration in a microreactor for pharmaceutical production under cGMP conditions.* Chemistry Today, 2009. **27**(1): p. 26-29.
4. Hessel, V., C. Knobloch, and H. Lowe, *Review on patents in microreactor and micro process engineering.* Recent Patents on Chemical Engineering, 2008. **1**(1): p. 1-16.
5. Valera, F.E., et al., *The Flow's the Thing… Or Is It? Assessing the Merits of Homogeneous Reactions in Flask and Flow.* Angewandte Chemie International Edition, 2010. **49**(14): p. 2478-2485.
6. Hartman, R.L., J.P. McMullen, and K.F. Jensen, *Deciding Whether To Go with the Flow: Evaluating the Merits of Flow Reactors for Synthesis.* Angewandte Chemie International Edition, 2011. **50**(33): p. 7502-7519.
7. Schaber, S.D., et al., *Economic Analysis of Integrated Continuous and Batch Pharmaceutical Manufacturing: A Case Study.* Industrial & Engineering Chemistry Research, 2011. **50**(17): p. 10083-10092.
8. Westerterp, K.R., E.J. Molga, and K.B. van Gelder, *Catalytic hydrogenation reactors for the fine chemicals industries. Their design and operation.* Chemical Engineering and Processing: Process Intensification, 1997. **36**(1): p. 17-27.
9. Plouffe, P., A. Macchi, and D.M. Roberge, *From Batch to Continuous Chemical Synthesis—A Toolbox Approach.* Organic Process Research & Development, 2014. **18**(11): p. 1286-1294.
10. Doku, G.N., et al., *On-microchip multiphase chemistry—a review of microreactor design principles and reagent contacting modes.* Tetrahedron, 2005. **61**(11): p. 2733-2742.
11. Alsten, J.G.V., M.L. Jorgensen, and D.J. am Ende, *Hydrogenation of a Pharmaceutical Intermediate by a Continuous Stirred Tank Reactor System.* Organic Process Research & Development, 2009. **13**(3): p. 629-633.
12. Sheldon, R.A. and H. van Bekkum, *Fine Chemicals through Heterogeneous Catalysis*. 2008: Wiley.
13. Ranade, V.V., R. Chaudhari, and P.R. Gunjal, *Trickle Bed Reactors: Reactor Engineering and Applications*. 2011: Elsevier Science.
14. Degirmenci, V. and E.V. Rebrov, *Design of catalytic micro trickle bed reactors %J Physical Sciences Reviews.* 2016. **1**(4): p. 20150018.
15. Ende, D.J. and M.T. Ende, *Chemical Engineering in the Pharmaceutical Industry: Active Pharmaceutical Ingredients*. 2019: Wiley.
16. Hou, R., *Catalytic and Process Study of the Selective Hydrogenation of Acetylene and 1,3-Butadiene*. 2017: Springer Singapore.

17. Wang, C., et al., *Product Selectivity Controlled by Zeolite Crystals in Biomass Hydrogenation over a Palladium Catalyst.* Journal of the American Chemical Society, 2016. **138**(25): p. 7880-7883.
18. Mederos, F.S., J. Ancheyta, and J. Chen, *Review on criteria to ensure ideal behaviors in trickle-bed reactors.* Applied Catalysis A: General, 2009. **355**(1): p. 1-19.
19. Gianetto, A. and V. Specchia, *Trickle-bed reactors: state of art and perspectives.* Chemical Engineering Science, 1992. **47**(13): p. 3197-3213.
20. Trambouze, P.J.J.O., G. Science, and T.-r.D.L.I.F.D. Petrole, *Multiphase Catalytic Reactors in the Oil Industry: an Introduction.* 1991. **46**: p. 433-437.
21. Robinson, P.R. and G.E. Dolbear, *Hydrotreating and hydrocracking: fundamentals*, in *Practical advances in petroleum processing*. 2006, Springer. p. 177-218.
22. Pass, G., et al., *Methanol synthesis in a trickle-bed reactor.* 1990. **36**(7): p. 1054-1060.
23. Govindarao, V.M., K.V.J.J.o.A.C. Ramana Murthy, and Biotechnology, *Liquid phase hydrogenation of aniline in a trickle bed reactor.* 1975. **25**(3): p. 169-181.
24. Gallezot, P., et al., *Glucose Hydrogenation on Ruthenium Catalysts in a Trickle-Bed Reactor.* Journal of Catalysis, 1998. **180**(1): p. 51-55.
25. Jarullah, A.T., I.M. Mujtaba, and A.S. Wood, *Improvement of the Middle Distillate Yields during Crude Oil Hydrotreatment in a Trickle-Bed Reactor.* Energy & Fuels, 2011. **25**(2): p. 773-781.
26. Yang, S.H., et al., *Catalytic hydrodenitrogenation of quinoline in a trickle-bed reactor. Effect of hydrogen sulfide.* 1984. **23**(1): p. 20-25.
27. Yui, S.M., E.C.J.I. Sanford, and e.c. research, *Mild hydrocracking of bitumen-derived coker and hydrocracker heavy gas oils: kinetics, product yields, and product properties.* 1989. **28**(9): p. 1278-1284.
28. Levec, J. and J.J.A.J. Smith, *Oxidation of acetic acid solutions in a trickle-bed reactor.* 1976. **22**(1): p. 159-168.
29. Singh, A., K.K. Pant, and K.D.P. Nigam, *Catalytic wet oxidation of phenol in a trickle bed reactor.* Chemical Engineering Journal, 2004. **103**(1): p. 51-57.
30. Hartmans, S. and J.J.B.E. Tramper, *Dichloromethane removal from waste gases with a trickle-bed bioreactor.* 1991. **6**(3): p. 83-92.
31. Jamuna, R. and S.J.B.e. Ramakrishna, *Ethanol fermentation by immobilized cells in a trickle bed reactor.* 1992. **8**(1): p. 61-66.
32. Iliuta, I. and F. Larachi, *Fischer-Tropsch synthesis in vertical, inclined and oscillating trickle-bed reactors for offshore floating applications.* Chemical Engineering Science, 2018. **177**: p. 509-522.
33. Anderson, N.G., *Practical use of continuous processing in developing and scaling up laboratory processes.* Organic Process Research & Development, 2001. **5**(6): p. 613-621.
34. Westerterp, K.R., H.J. Janssen, and H.J. van der Kwast, *The catalytic hydrogenation of 2,4-dinitrotoluene in a continuous stirred three-phase slurry reactor with an evaporating solvent.* Chemical Engineering Science, 1992. **47**(15): p. 4179-4189.
35. Visentin, F., et al., *Study of the Hydrogenation of Selected Nitro Compounds by Simultaneous Measurements of Calorimetric, FT-IR,*

and Gas-Uptake Signals. Industrial & Engineering Chemistry Research, 2006. **45**(13): p. 4544-4553.
36. Sun, H., et al., *Selective hydrogenation of benzene to cyclohexene in continuous reaction device with two reaction reactors in serie over Ru-Co-B/ZrO2 catalysts.* Chinese Journal of Catalysis, 2013. **34**(8): p. 1482-1488.
37. Fishwick, R.P., et al., *Selective hydrogenation reactions: A comparative study of monolith CDC, stirred tank and trickle bed reactors.* Catalysis Today, 2007. **128**(1): p. 108-114.
38. Stüber, F. and H. Delmas, *Partial Hydrogenation in an Upflow Fixed-Bed Reactor: A Multistage Operation for Experimental Optimization of Selectivity.* Industrial & Engineering Chemistry Research, 2003. **42**(1): p. 6-13.
39. Chaudhari, R.V., et al., *Hydrogenation of 1,5,9-cyclododecatriene in fixed-bed reactors: Down- vs. upflow modes.* AIChE Journal, 2002. **48**(1): p. 110-125.
40. Liu, G., et al., *Unsteady-state operation of trickle-bed reactor for dicyclopentadiene hydrogenation.* Chemical Engineering Science, 2008. **63**(20): p. 4991-5002.
41. Liu, G., et al., *Periodically operated trickle-bed reactor for EAQs hydrogenation: Experiments and modeling.* Chemical Engineering Science, 2005. **60**(22): p. 6270-6278.
42. Fernandez-Puertas, E., et al., *Evaluation and Screening of Spherical Pd/C for Use as a Catalyst in Pharmaceutical-Scale Continuous Hydrogenations.* Organic Process Research & Development, 2020.
43. Stamatiou, I.K. and F.L. Muller, *Determination of mass transfer resistances of fast reactions in three-phase mechanically agitated slurry reactors.* AIChE Journal, 2017. **63**(1): p. 273-282.
44. Wang, Y., J. Chen, and F.J.T.C.J.o.C.E. Larachi, *Modelling and simulation of trickle-bed reactors using computational fluid dynamics: A state-of-the-art review.* 2013. **91**(1): p. 136-180.
45. Satterfield, C.N., A. Pelossof, and T.K. Sherwood, *Mass transfer limitations in a trickle-bed reactor.* AIChE Journal, 1969. **15**(2): p. 226-234.
46. Banchero, M., et al., *Conversion rate and mass transfer limitation in trickle bed reactors in the presence of a fast reaction.* Chemical Engineering Science, 2004. **59**(22): p. 5411-5416.
47. Bauer, T. and S. Haase, *Comparison of structured trickle-bed and monolithic reactors in Pd-catalyzed hydrogenation of alpha-methylstyrene.* Chemical engineering journal, 2011. **169**(1): p. 263-269.
48. Hipolito, A., et al., *Single pellet string reactor for intensification of catalyst testing in gas/liquid/solid configuration.* Oil & Gas Science and Technology–Revue d'IFP Energies nouvelles, 2010. **65**(5): p. 689-701.
49. Alpha, S. *Dow And DuPont, Bayer And Monsanto Or Syngenta - Which Will Succeed?* 2016 [cited 2020 29/09/2020]; Available from: https://seekingalpha.com/article/4024476-dow-and-dupont-bayer-and-monsanto-syngenta-which-will-succeed.
50. Geiser, K.G.K., *Materials Matter*. 2001: MIT Press.

51. Heveling, J., *Heterogeneous Catalytic Chemistry by Example of Industrial Applications.* Journal of Chemical Education, 2012. **89**(12): p. 1530-1536.
52. Merriam, W. *Definition of Catalysis*. 2017 [cited 2017 06/10/2017]; Available from: https://www.merriam-webster.com/dictionary/catalysis.
53. Holman, J.S. and P. Stone, *Chemistry*. 2001: Nelson Thornes Limited.
54. Richardson, J.T., *Principles of Catalyst Development*. 2013: Springer US.
55. Carberry, J.J., *Chemical and Catalytic Reaction Engineering*. 2001: Dover Publications.
56. Sheldon, R.A., I. Arends, and U. Hanefeld, *Green Chemistry and Catalysis*. 2007: Wiley.
57. Burrington, J.D., *Industrial Catalysis: Chemistry and Mechanism*. 2016: World Scientific Publishing Company.
58. Hagen, J., *Industrial Catalysis: A Practical Approach*. 2015: Wiley.
59. Smith, G.V. and F. Notheisz, *Heterogeneous Catalysis in Organic Chemistry*. 1999: Elsevier Science.
60. Cao, S., et al., *Size- and shape-dependent catalytic performances of oxidation and reduction reactions on nanocatalysts.* Chemical Society Reviews, 2016. **45**(17): p. 4747-4765.
61. Serp, P. and J.L. Figueiredo, *Carbon Materials for Catalysis*. 2009: Wiley.
62. Hagemeyer, A. and A. Volpe, *Catalysts: Materials*, in *Encyclopedia of Condensed Matter Physics*, F. Bassani, G.L. Liedl, and P. Wyder, Editors. 2005, Elsevier: Oxford. p. 158-165.
63. Afandizadeh, S. and E.A. Foumeny, *Design of packed bed reactors: guides to catalyst shape, size, and loading selection.* Applied Thermal Engineering, 2001. **21**(6): p. 669-682.
64. Averill, B.A., et al., *Catalysis: An Integrated Approach*. 1999: Elsevier Science.
65. Ertl, G., H. Knözinger, and J. Weitkamp, *Preparation of Solid Catalysts*. 2008: Wiley.
66. Rocha, T.C.R., et al., *Promoters in heterogeneous catalysis: The role of Cl on ethylene epoxidation over Ag.* Journal of Catalysis, 2014. **312**: p. 12-16.
67. Koel, B.E. and J.J.H.o.H.C.O. Kim, *Promoters and poisons.* 2008: p. 1593-1624.
68. Faridkhou, A., J.-N. Tourvieille, and F. Larachi, *Reactions, hydrodynamics and mass transfer in micro-packed beds—Overview and new mass transfer data.* Chemical Engineering and Processing: Process Intensification, 2016. **110**: p. 80-96.
69. McGovern, S., et al., *Multiphase flow regimes for hydrogenation in a catalyst-trap microreactor.* Chemical Engineering Journal, 2008. **135**(Supplement 1): p. S229-S236.
70. Britannica, E.o. *Hydrogenation*. 2017 [cited 2017 14/12/2017]; Available from: https://www.britannica.com/science/hydrogenation.
71. Clark, J.H. and D.J. Macquarrie, *Handbook of Green Chemistry and Technology*. 2008: Wiley.
72. Rigas, F. and P. Amyotte, *Hydrogen Safety*. 2012: CRC Press.

73. Liu, Y., et al., *Heterogeneous catalysis for green chemistry based on nanocrystals.* National Science Review, 2015. **2**(2): p. 150-166.
74. Liu, J., A.E. Fitzgerald, and N.S.J.S. Mani, *Reductive amination by continuous-flow hydrogenation: direct and scalable synthesis of a benzylpiperazine.* 2012. **44**(15): p. 2469-2473.
75. Rylander, *Catalytic Hydrogenation in Organic Syntheses*. 2012: Elsevier Science.
76. Chaudhari, R.V. and P.A. Ramachandran, *Three phase slurry reactors.* AIChE Journal, 1980. **26**(2): p. 177-201.
77. McKetta, J.J., *Encyclopedia of Chemical Processing and Design: Volume 46 - Pumps: Bypass to Reboilers*. 1993: Taylor & Francis.
78. Kohler, M.A., *Comparison of mechanically agitated and bubble column slurry reactors.* Applied Catalysis, 1986. **22**(1): p. 21-53.
79. Whitaker, S. and A.E. Cassano, *Concepts and Design of Chemical Reactors*. 1986: Gordon and Breach Science Publishers.
80. Li, H. and A. Prakash, *Heat Transfer and Hydrodynamics in a Three-Phase Slurry Bubble Column.* Industrial & Engineering Chemistry Research, 1997. **36**(11): p. 4688-4694.
81. Edvinsson, R. and A. Cybulski, *A comparative analysis of the trickle-bed and the monolithic reactor for three-phase hydrogenations.* Chemical engineering science, 1994. **49**(24): p. 5653-5666.
82. Haase, S., et al., *Hydrodynamics and mass transfer in three-phase composite minichannel fixed-bed reactors.* Chemical Engineering Science, 2013. **94**: p. 224-236.
83. Wang, T., J. Wang, and Y. Jin, *Slurry Reactors for Gas-to-Liquid Processes: A Review.* Industrial & Engineering Chemistry Research, 2007. **46**(18): p. 5824-5847.
84. Deckwer, W.D. and A. Schumpe, *Improved tools for bubble column reactor design and scale-up.* Chemical Engineering Science, 1993. **48**(5): p. 889-911.
85. Stemmet, C., et al., *Hydrodynamics of gas–liquid counter-current flow in solid foam packings.* Chemical engineering science, 2005. **60**(22): p. 6422-6429.
86. Safinski, T. and A.A. Adesina, *Two-Phase Flow Countercurrent Operation of a Trickle Bed Reactor: Hold-up and Mixing Behavior over Raschig Rings Fixed Bed and Structured Bale Packing.* Industrial & Engineering Chemistry Research, 2012. **51**(4): p. 1647-1662.
87. Trambouze, P., *Countercurrent two-phase flow fixed bed catalytic reactors.* Chemical Engineering Science, 1990. **45**(8): p. 2269-2275.
88. Wu, Y., et al., *Comparison of Upflow and Downflow Two-Phase Flow Packed-Bed Reactors with and without Fines: Experimental Observations.* Industrial & Engineering Chemistry Research, 1996. **35**(2): p. 397-405.
89. Winterbottom, J., et al., *Catalytic hydrogenation in a packed bed bubble column reactor.* Catalysis today, 1999. **48**(1): p. 221-228.
90. Molga, E. and K. Westerterp, *Gas− liquid interfacial area and holdup in a cocurrent upflow packed bed bubble column reactor at elevated pressures.* Industrial & engineering chemistry research, 1997. **36**(3): p. 622-631.

91. Mills, P. and R. Chaudhari, *Multiphase catalytic reactor engineering and design for pharmaceuticals and fine chemicals.* Catalysis Today, 1997. **37**(4): p. 367-404.
92. Levenspiel, O., *Chemical reaction engineering*. 1999: Wiley.
93. Coulson, J.M. and J.F. Richardson, *Chemical Engineering*. 2000: Butterworth-Heinemann.
94. Fick, A., *On liquid diffusion.* Journal of Membrane Science, 1995. **100**(1): p. 33-38.
95. Simons, S. and R.S.o. Chemistry, *Concepts of Chemical Engineering 4 Chemists*. 2007: Royal Society of Chemistry.
96. Lewis, W. and W. Whitman, *Principles of gas absorption.* Industrial & Engineering Chemistry, 1924. **16**(12): p. 1215-1220.
97. Berk, Z., *Food Process Engineering and Technology*. 2013: Elsevier Science.
98. Ruthven, D.M., *Principles of Adsorption and Adsorption Processes*. 1984: Wiley.
99. SINHA, A.P. and P. DE, *Mass Transfer: Principles and Operations*. 2012: PHI Learning.
100. Coulson, J.M., et al., *Chemical Engineering Volume 1: Fluid Flow, Heat Transfer and Mass Transfer*. 1999: Elsevier Science.
101. Cussler, E.L. and E.L. Cussler, *Diffusion: Mass Transfer in Fluid Systems*. 1997: Cambridge University Press.
102. Danckwerts, P.V., *Significance of Liquid-Film Coefficients in Gas Absorption.* Industrial & Engineering Chemistry, 1951. **43**(6): p. 1460-1467.
103. Asano, K., *Mass Transfer: From Fundamentals to Modern Industrial Applications*. 2007: Wiley.
104. Forni, L., *Mass and heat transfer in catalytic reactions.* Catalysis Today, 1999. **52**(2): p. 147-152.
105. Thomas, J.M. and W.J. Thomas, *Principles and practice of heterogeneous catalysis*. 2014: John Wiley & Sons.
106. Thiele, E.W., *Relation between catalytic activity and size of particle.* Industrial & Engineering Chemistry, 1939. **31**(7): p. 916-920.
107. Aris, R., *On shape factors for irregular particles—I: The steady state problem. Diffusion and reaction.* Chemical Engineering Science, 1957. **6**(6): p. 262-268.
108. Stamatiou, I. and F.L. Muller, *Determination of mass transfer resistances in trickle bed reactors.* Chemical Engineering Journal, 2018.
109. Prins, R., A. Wang, and X. Li, *Introduction To Heterogeneous Catalysis*. 2016: World Scientific Publishing Company.
110. Murzin, D.Y., *Thermodynamic analysis of nanoparticle size effect on catalytic kinetics.* Chemical Engineering Science, 2009. **64**(5): p. 1046-1052.
111. Chorkendorff, I. and J.W. Niemantsverdriet, *Concepts of Modern Catalysis and Kinetics*. 2017: Wiley.
112. He, C., et al., *Synergistic catalysis in the Sonogashira coupling reaction: Quantitative kinetic investigation of transmetalation.* 2013. **125**(5): p. 1567-1570.
113. Herskowitz, M. and J. Smith, *Trickle-bed reactors: A review.* AIChE Journal, 1983. **29**(1): p. 1-18.

114. Ramachandran, P.A. and R.V. Chaudhari, *Three-phase catalytic reactors*. 1983: Gordon and Breach Science Publishers.
115. Satterfield, C.N., *Trickle-bed reactors.* AIChE Journal, 1975. **21**(2): p. 209-228.
116. Sie, S. and R. Krishna, *Process development and scale up: III. Scale-up and scale-down of trickle bed processes.* Reviews in Chemical Engineering, 1998. **14**(3): p. 203-252.
117. Boelhouwer, J.G., H.W. Piepers, and A.A. Drinkenburg, *Nature and characteristics of pulsing flow in trickle-bed reactors.* Chemical Engineering Science, 2002. **57**(22): p. 4865-4876.
118. Wu, R., M.J. McCready, and A. Varma, *Influence of mass transfer coefficient fluctuation frequency on performance of three-phase packed-bed reactors.* Chemical Engineering Science, 1995. **50**(21): p. 3333-3344.
119. Lange, R., M. Schubert, and T. Bauer, *Liquid Holdup in Trickle-Bed Reactors at Very Low Liquid Reynolds Numbers.* Industrial & Engineering Chemistry Research, 2005. **44**(16): p. 6504-6508.
120. Stegeman, D., et al., *Residence time distribution in the liquid phase in a cocurrent gas− liquid trickle bed reactor.* Industrial & engineering chemistry research, 1996. **35**(2): p. 378-385.
121. Charpentier, J.C. and M. Favier, *Some liquid holdup experimental data in trickle-bed reactors for foaming and nonfoaming hydrocarbons.* AIChE Journal, 1975. **21**(6): p. 1213-1218.
122. Iliuta, I., et al., *Hydrodynamics and mass transfer in trickle-bed reactors: an overview.* Chemical Engineering Science, 1999. **54**(21): p. 5329-5337.
123. Dudukovic, M.P., F. Larachi, and P.L. Mills, *Multiphase reactors – revisited.* Chemical Engineering Science, 1999. **54**(13): p. 1975-1995.
124. Saez, A. and R. Carbonell, *hydrodynamic parameters for gas-liquid cocurrent flow in packed beds.* AIChE Journal, 1985. **31**(1): p. 52-62.
125. Saez, A., et al., *Static liquid holdup in packed beds of spherical particles.* AIChE journal, 1991. **37**(11): p. 1733-1736.
126. Urrutia, G., et al., *On dynamic liquid holdup determination by the drainage method.* Chemical engineering science, 1996. **51**(15): p. 3721-3726.
127. Dudukovic, M.P., Ž.V. Kuzeljevic, and D.P. Combest, *Three-Phase Trickle-Bed Reactors.* Ullmann's Encyclopedia of Industrial Chemistry, 2014.
128. Maiti, R.N. and K.D.P. Nigam, *Gas−Liquid Distributors for Trickle-Bed Reactors: A Review.* Industrial & Engineering Chemistry Research, 2007. **46**(19): p. 6164-6182.
129. Ravindra, P.V., D.P. Rao, and M.S. Rao, *Liquid Flow Texture in Trickle-Bed Reactors: An Experimental Study.* Industrial & Engineering Chemistry Research, 1997. **36**(12): p. 5133-5145.
130. Maiti, R., P. Sen, and K. Nigam, *Trickle-bed reactors: liquid distribution and flow texture.* Reviews in Chemical Engineering, 2004. **20**(1-2): p. 57-110.
131. van Houwelingen, A.J., C. Sandrock, and W. Nicol, *Particle wetting distribution in trickle-bed reactors.* AIChE journal, 2006. **52**(10): p. 3532-3542.

132. Sederman, A. and L. Gladden, *Magnetic resonance imaging as a quantitative probe of gas–liquid distribution and wetting efficiency in trickle-bed reactors.* Chemical Engineering Science, 2001. **56**(8): p. 2615-2628.
133. Lutran, P.G., K.M. Ng, and E.P. Delikat, *Liquid distribution in trickle-beds. An experimental study using computer-assisted tomography.* Industrial & Engineering Chemistry Research, 1991. **30**(6): p. 1270-1280.
134. Al-Dahhan, M.H. and M.P. Duduković, *Catalyst wetting efficiency in trickle-bed reactors at high pressure.* Chemical Engineering Science, 1995. **50**(15): p. 2377-2389.
135. Llano, J.J., et al., *Determination of wetting efficiency in trickle-bed reactors by a reaction method.* Industrial & engineering chemistry research, 1997. **36**(7): p. 2616-2625.
136. Mears, D.E., *The role of axial dispersion in trickle-flow laboratory reactors.* Chemical Engineering Science, 1971. **26**(9): p. 1361-1366.
137. Iliuta, I., M.C. Iliuta, and F.C. Thyrion, *Gas-liquid mass transfer in trickle-bed reactors: Gas-side mass transfer.* Chemical engineering & technology, 1997. **20**(9): p. 589-595.
138. Last, W. and J. Stichlmair, *Determination of mass transfer parameters by means of chemical absorption.* Chemical engineering & technology, 2002. **25**(4): p. 385-391.
139. Goto, S. and J.M. Smith, *Trickle-bed reactor performance. Part I. Holdup and mass transfer effects.* AIChE Journal, 1975. **21**(4): p. 706-713.
140. Zhang, J., A.R. Teixeira, and K.F. Jensen, *Automated measurements of gas-liquid mass transfer in micropacked bed reactors.* AIChE Journal, 2018. **64**(2): p. 564-570.
141. Evren, V. and A.R. Özdural, *A new technique for the determination of mass transfer coefficients in packed columns for physical gas absorption systems.* The Chemical Engineering Journal and the Biochemical Engineering Journal, 1995. **57**(1): p. 67-71.
142. Turek, F. and R. Lange, *Mass transfer in trickle-bed reactors at low reynolds number.* Chemical Engineering Science, 1981. **36**(3): p. 569-579.
143. Blok, J., C. Koning, and A. Drinkenburg, *Gas-Liquid mass transfer in fixed-bed reactors with cocurrent downflow operating in the pulsing flow regime.* AIChE journal, 1984. **30**(3): p. 393-401.
144. Larachi, F., M. Cassanello, and A. Laurent, *Gas−Liquid Interfacial Mass Transfer in Trickle-Bed Reactors at Elevated Pressures.* Industrial & Engineering Chemistry Research, 1998. **37**(3): p. 718-733.
145. Losey, M.W., M.A. Schmidt, and K.F. Jensen, *Microfabricated Multiphase Packed-Bed Reactors: Characterization of Mass Transfer and Reactions.* Industrial & Engineering Chemistry Research, 2001. **40**(12): p. 2555-2562.
146. Litt, M., *Gas-liquid reactions, P. V. Danckwerts, McGraw-Hill Book Co., New York (1970). 276 pages. $11.50.* AIChE Journal, 1971. **17**(2): p. 509-510.

147. Highfill, W. and M. Al-Dahhan, *Liquid-solid mass transfer coefficient in high pressure trickle bed reactors.* Chemical Engineering Research and Design, 2001. **79**(6): p. 631-640.
148. Zheng, Q., et al., *Operando determination of the liquid-solid mass transfer coefficient during 1-octene hydrogenation.* Chemical Engineering Science, 2017. **171**(Supplement C): p. 614-624.
149. van Houwelingen, A.J. and W. Nicol, *Parallel hydrogenation for the quantification of wetting efficiency and liquid–solid mass transfer in a trickle-bed reactor.* AIChE Journal, 2011. **57**(5): p. 1310-1319.
150. Al-Dahhan, M., W. HighFill, and B.T. Ong, *Drawbacks of the Dissolution Method for Measurement of the Liquid− Solid Mass-Transfer Coefficients in Two-Phase Flow Packed-Bed Reactors Operated at Low and High Pressures.* Industrial & engineering chemistry research, 2000. **39**(8): p. 3102-3107.
151. Cao, E., et al., *Study of Liquid–Solid Mass Transfer and Hydrodynamics in Micropacked Bed with Gas–Liquid Flow.* Industrial & Engineering Chemistry Research, 2021. **60**(29): p. 10489-10501.
152. Speccia, V., G. Baldi, and A. Gianetto, *Solid-Liquid Mass Transfer in Concurrent Two-Phase Flow through Packed Beds.* Industrial & Engineering Chemistry Process Design and Development, 1978. **17**(3): p. 362-367.
153. Joubert, R. and W. Nicol, *Trickle flow liquid–solid mass transfer and wetting efficiency in small diameter columns.* The Canadian Journal of Chemical Engineering, 2013. **91**(3): p. 441-447.
154. Tan, C. and J. Smith, *A dynamic method for liquid-particle mass transfer in trickle beds.* AIChE Journal, 1982. **28**(2): p. 190-195.
155. Herskowitz, M. and M. Abuelhaija, *Liquid-solid mass transfer in a trickle-bed reactor measured by means of a catalytic reaction.* Chemical Engineering Science, 1985. **40**(4): p. 631-634.
156. Sims, W.B., F.G. Schulz, and D. Luss, *Solid-liquid mass transfer to hollow pellets in a trickle bed.* Industrial & engineering chemistry research, 1993. **32**(9): p. 1895-1903.
157. Koptyug, I., et al., *Functional imaging and NMR spectroscopy of an operating gas–liquid–solid catalytic reactor.* Applied Catalysis A: General, 2004. **267**(1-2): p. 143-148.
158. Sederman, A.J., et al., *In situ MRI study of 1-octene isomerisation and hydrogenation within a trickle-bed reactor.* Catalysis letters, 2005. **103**(1-2): p. 1-8.
159. Littlewood, A.B., *Gas Chromatography: Principles, Techniques, and Applications*. 2013: Elsevier Science.
160. Aygün, M., et al., *Magnetically recyclable catalytic carbon nanoreactors.* 2018. **28**(34): p. 1802869.
161. Marsh, H. and F.R. Reinoso, *Activated Carbon*. 2006: Elsevier Science.
162. Lukiyanov, F.A., E.I. Rau, and R.A. Sennov, *Depth range of primary electrons, electron beam broadening, and spatial resolution in electron-beam studies.* Bulletin of the Russian Academy of Sciences: Physics, 2009. **73**(4): p. 441-449.
163. Girard, J., *Principles of Environmental Chemistry*. 2005: Jones and Bartlett Publishers.

164. Reger, D.L., S.R. Goode, and D.W. Ball, *Chemistry: Principles and Practice*. 2009: Cengage Learning.
165. Isaifan, R.J., S. Ntais, and E.A. Baranova, *Particle size effect on catalytic activity of carbon-supported Pt nanoparticles for complete ethylene oxidation.* Applied Catalysis A: General, 2013. **464-465**: p. 87-94.
166. Coq, B. and F.J.C.C.R. Figueras, *Structure–activity relationships in catalysis by metals: some aspects of particle size, bimetallic and supports effects.* 1998. **178**: p. 1753-1783.
167. Barnard, A.S., *Mapping the shape and phase of palladium nanocatalysts.* Catalysis Science & Technology, 2012. **2**(7): p. 1485-1492.
168. Hu, B., et al., *Shape controlled synthesis of palladium nanocrystals by combination of oleylamine and alkylammonium alkylcarbamate and their catalytic activity.* Chemical Communications, 2010. **46**(45): p. 8552-8554.
169. Jin, M., et al., *Palladium nanocrystals enclosed by {100} and {111} facets in controlled proportions and their catalytic activities for formic acid oxidation.* Energy & Environmental Science, 2012. **5**(4): p. 6352-6357.
170. Tian, Y. and J. Wu, *A Comprehensive Analysis of the BET Area for Nanoporous Materials.* AIChE Journal, 2018.
171. Stitt, E.H., *Alternative multiphase reactors for fine chemicals: A world beyond stirred tanks?* Chemical Engineering Journal, 2002. **90**(1): p. 47-60.
172. Gierman, H., *Design of laboratory hydrotreating reactors: Scaling Down of Trickle-flow Reactors.* Applied Catalysis, 1988. **43**(2): p. 277-286.
173. Langsch, R., S. Haase, and R. Lange, *Hydrodynamics and Mass Transfer in a Pellet String Reactor for Gas-Liquid-Solid Reactions.* Chemie Ingenieur Technik, 2013. **85**(5): p. 642-655.
174. Langsch, R., et al., *Investigation of a packed bed in a mini channel with a low channel-to-particle diameter ratio: flow regimes and mass transfer in gas–liquid operation.* Chemical Engineering and Processing: Process Intensification, 2014. **75**: p. 8-18.
175. Kallinikos, L.E. and N.G. Papayannakos, *Intensification of hydrodesulphurization process with a structured bed spiral mini-reactor.* Chemical Engineering and Processing: Process Intensification, 2010. **49**(10): p. 1025-1030.
176. Balder, J.R. and E.E. Petersen, *Application of the single pellet reactor for direct mass transfer studies: I. Mass transfer in porous media.* Journal of Catalysis, 1968. **11**(3): p. 195-201.
177. Balder, J.R. and E.E. Petersen, *Application of the single pellet reactor for direct mass transfer studies: II. Measurement of composition at center of catalyst pellet.* Journal of Catalysis, 1968. **11**(3): p. 202-210.
178. Hegedus, L.L. and E.E. Petersen, *An Improved Single-Pellet Reactor to Study the Interaction of Kinetics with Mass Transfer Effects in Heterogeneous Catalysis.* Industrial & Engineering Chemistry Fundamentals, 1972. **11**(4): p. 579-584.

179. Adaje, J. and M. Sheintuch, *Comparison of multiplicity patterns of a single catalytic pellet and a fixed catalytic bed for ethylene oxidation.* Chemical Engineering Science, 1990. **45**(5): p. 1331-1342.
180. Watson, P.C. and M.P. Harold, *Dynamic effects of vaporization with exothermic reaction in a porous catalytic pellet.* AIChE journal, 1993. **39**(6): p. 989-1006.
181. Colombo, A.J., G. Baldi, and S. Sicardi, *Solid-liquid contacting effectiveness in trickle bed reactors.* Chemical Engineering Science, 1976. **31**(12): p. 1101-1108.
182. Stamatiou, I. and F.L. Muller, *Determination of mass transfer resistances in trickle bed reactors.* Chemical Engineering Journal, 2019. **377**: p. 119808.
183. Holub, R.A., M.P. Duduković, and P.A. Ramachandran, *A phenomenological model for pressure drop, liquid holdup, and flow regime transition in gas-liquid trickle flow.* Chemical Engineering Science, 1992. **47**(9): p. 2343-2348.
184. Al-Dahhan, M.H. and M.P. Dudukovic´, *Pressure drop and liquid holdup in high pressure trickle-bed reactors.* Chemical Engineering Science, 1994. **49**(24, Part 2): p. 5681-5698.
185. Herskowitz, M., R. Carbonell, and J. Smith, *Effectiveness factors and mass transfer in trickle-bed reactors.* AIChE Journal, 1979. **25**(2): p. 272-283.
186. Karimi, G. and M. Kawaji, *An experimental study of freely falling films in a vertical tube.* Chemical Engineering Science, 1998. **53**(20): p. 3501-3512.
187. Grünig, J., T. Skale, and M. Kraume, *Liquid flow on a vertical wire in a countercurrent gas flow.* Chemical Engineering Journal, 2010. **164**(1): p. 121-131.
188. Chyu, M.-C. and A. Bergles, *An analytical and experimental study of falling-film evaporation on a horizontal tube.* Journal of Heat Transfer, 1987. **109**(4): p. 983-990.
189. L. Goren , S., *The Instability of an Annular Thread of Fluid*. Vol. 12. 1962. 309-319.
190. Lin, S. and W. Liu, *Instability of film coating of wires and tubes.* AIChE journal, 1975. **21**(4): p. 775-782.
191. Trifonov, Y.Y., *Wavy liquid film in the presence of co- or counter-current turbulent gas flow.* Thermophysics and Aeromechanics, 2014. **21**(3): p. 319-336.
192. Tsamatsoulis, D., et al., *THE EFFECT OF PARTICLE DILUTION ON WETTING EFFICIENCY AND LIQUID FILM THICKNESS IN SMALL TRICKLE BEDS.* Chemical Engineering Communications, 2001. **185**(1): p. 67-77.
193. Bird, R.B., W.E. Stewart, and E.N. Lightfoot, *Transport Phenomena*. 2007: Wiley.
194. Yamada, H., T. Naruse, and S. Goto, *Trickle bed reactor diluted with fine particles and coiled tubular flow-type reactor for kinetic measurements without external effects.* Catalysis Today, 1999. **48**(1): p. 301-306.
195. Nigam, K.D.P., I. Iliuta, and F.ç. Larachi, *Liquid back-mixing and mass transfer effects in trickle-bed reactors filled with porous catalyst*

particles. Chemical Engineering and Processing: Process Intensification, 2002. **41**(4): p. 365-371.
196. Rajashekharam, M.V., R. Jaganathan, and R.V. Chaudhari, *A trickle-bed reactor model for hydrogenation of 2,4 dinitrotoluene: experimental verification.* Chemical Engineering Science, 1998. **53**(4): p. 787-805.
197. Tan, C.S. and J.J.C.E.S. Smith, *Catalyst particle effectiveness with unsymmetrical boundary conditions.* 1980. **35**(7): p. 1601-1609.
198. Toppinen, S., J. Aittamaa, and T. Salmi, *Interfacial mass transfer in trickle-bed reactor modelling.* Chemical Engineering Science, 1996. **51**(18): p. 4335-4345.
199. Krishna, R. and J.A. Wesselingh, *The Maxwell-Stefan approach to mass transfer.* Chemical Engineering Science, 1997. **52**(6): p. 861-911.
200. Liu, Q., F. Takemura, and A. Yabe, *Solubility of hydrogen in liquid methanol and methyl formate at 20 C to 140 C.* Journal of Chemical & Engineering Data, 1996. **41**(5): p. 1141-1143.
201. Froment, G.F., G.A. Depauw, and V. Vanrysselberghe, *Kinetic Modeling and Reactor Simulation in Hydrodesulfurization of Oil Fractions.* Industrial & Engineering Chemistry Research, 1994. **33**(12): p. 2975-2988.
202. Alvear, M., et al., *Modelling of transient kinetics in trickle bed reactors: Ethylene oxide production via hydrogen peroxide.* Chemical Engineering Science, 2022. **248**: p. 117156.
203. Azarpour, A., N. Rezaei, and S. Zendehboudi, *Performance analysis and modeling of catalytic trickle-bed reactors: a comprehensive review.* Journal of Industrial and Engineering Chemistry, 2021. **103**: p. 1-41.
204. Stamatiou, I., C. Brennan, and F.L. Muller, *Determination of styrene hydrogenation surface kinetics through detailed simulation of the hydrogen uptake curve.* Reaction Chemistry & Engineering, 2019. **4**(8): p. 1477-1485.
205. Nijhuis, T.A., F.M. Dautzenberg, and J.A. Moulijn, *Modeling of monolithic and trickle-bed reactors for the hydrogenation of styrene.* Chemical Engineering Science, 2003. **58**(7): p. 1113-1124.
206. Meille, V., C. de Bellefon, and D. Schweich, *Kinetics of α-Methylstyrene Hydrogenation on Pd/Al2O3.* Industrial & Engineering Chemistry Research, 2002. **41**(7): p. 1711-1715.
207. Herskowitz, M., S.J.I. Mosseri, and E.C. Fundamentals, *Global rates of reaction in trickle-bed reactors: effects of gas and liquid flow rates.* 1983. **22**(1): p. 4-6.
208. Kobayashi, J.-I. and H. Katsuzawa, *The geometrical evaluation of effective diffusion coefficient in the liquid phase for porous bodies consisting of spherical elementary particles.* 1986. **64**(3): p. 419-425.
209. Blasi, J.M., et al., *Modeling reaction–diffusion processes within catalyst washcoats: II. Macroscale processes informed by microscale simulations.* Chemical Engineering Science, 2016. **145**: p. 308-316.
210. McCabe, W.L., *Mass transfer, Thomas K. Sherwood, Robert L. Pigford, and Charles R. Wilke, McGraw-Hill Book Company (1975). 677 pages. $21.50.* 1976. **22**(3): p. 620-621.

211. Metaxas, K. and N. Papayannakos, *Gas-Liquid Mass Transfer in a Bench-Scale Trickle Bed Reactor used for Benzene Hydrogenation.* Chemical Engineering & Technology, 2008. **31**(10): p. 1410-1417.
212. McMillan, L., et al., *The application of a supported palladium catalyst for the hydrogenation of aromatic nitriles.* Journal of Molecular Catalysis A: Chemical, 2016. **411**: p. 239-246.
213. Swagelok. *Stainless Steel Swagelok Tube Fitting, Union, 1/8 in. Tube OD*. 2020 [cited 2020 05/10/2020]; Available from: https://www.swagelok.com/en/catalog/Product/Detail?part=SS-200-6.
214. Gemba, K.J.C.S.U., Long Beach, Experimental report, *Measurement of boundary layer on a flat plate.* 2007.
215. Yan, X.T. and Y. Xu, *Chemical Vapour Deposition: An Integrated Engineering Design for Advanced Materials*. 2010: Springer London.
216. Sun, Y., et al., *A re-examination of pressure effects on enantioselectivity in asymmetric catalytic hydrogenation.* Journal of the American Chemical Society, 1996. **118**(6): p. 1348-1353.
217. Blaser, H.-U., et al., *Kinetic Studies of the Enantioselective Hydrogenation of Ethyl Pyruvate Catalyzed by a Cinchona Modified Pt/Al2O3Catalyst.* Journal of Catalysis, 1998. **173**(2): p. 282-294.
218. Dasgupta, S. and A. Atta, *Computational insights on intensification of hydrodenitrogenation in a trickle bed reactor using periodic flow modulation.* Chemical Engineering and Processing - Process Intensification, 2020. **157**: p. 108135.
219. Reyes-Antonio, C.A., et al., *Analysis of the effect of hydrodynamics over the activity and selectivity of the oxidative dehydrogenation of propane process in a packed bed reactor through CFD techniques.* Fuel, 2020. **280**: p. 118510.
220. Bouras, H., et al., *CFD modeling of mass transfer in Gas-Liquid-Solid catalytic reactors.* Chemical Engineering Science, 2021. **233**: p. 116378.
221. Swinley, J. and P. de Coning, *A Practical Guide to Gas Analysis by Gas Chromatography*. 2019: Elsevier Science.
222. Scott, R.P.W., *Chromatographic Detectors: Design: Function, and Operation*. 1996: Taylor & Francis.
223. Venn, R.F., *Principles and Practice of Bioanalysis*. 2000: Taylor & Francis.
224. Thomas, R., *Practical Guide to ICP-MS: A Tutorial for Beginners*. 2003: Taylor & Francis.
225. Vanhaecke, F. and P. Degryse, *Isotopic Analysis: Fundamentals and Applications Using ICP-MS*. 2012: Wiley.
226. Ul-Hamid, A., *A Beginners' Guide to Scanning Electron Microscopy*. 2018: Springer International Publishing.
227. Inkson, B.J., *2 - Scanning electron microscopy (SEM) and transmission electron microscopy (TEM) for materials characterization*, in *Materials Characterization Using Nondestructive Evaluation (NDE) Methods*, G. Hübschen, et al., Editors. 2016, Woodhead Publishing. p. 17-43.
228. Egerton, R., *Physical Principles of Electron Microscopy: An Introduction to TEM, SEM, and AEM*. 2011: Springer US.

229. Steele, W.A., G. Zgrablich, and W. Rudzinski, *Equilibria and Dynamics of Gas Adsorption on Heterogeneous Solid Surfaces*. 1996: Elsevier Science.
230. Condon, J.B., *Surface Area and Porosity Determinations by Physisorption: Measurement, Classical Theories and Quantum Theory'*. 2006: Elsevier Science.
231. Rouquerol, J., et al., *Recommendations for the characterization of porous solids (Technical Report).* Pure and Applied Chemistry, 1994. **66**(8): p. 1739-1758.

List of Abbreviations

AAS	Atomic adsorption spectroscopy
BET	Brunauer–Emmett–Teller theory
BJH	Bayer-Joyner-Halenda theory
CDE	Cyclododecene
CDT	1,5,9 cyclododecatriene
CFD	Computational fluid dynamics
CSA	Cross-sectional area
CSTR	Continuously stirred tank reactor
EAQs	2-ethylanthraquinones
EDX	Energy dispersive X-ray analysis
FID	Flame ionisation detector
ICP-MS	Inductively coupled plasma – mass spectroscopy
LHSV	Liquid hourly space velocity
MRI	Magnetic resonance imaging
Pd	Palladium
Pd/C	Palladium on activated carbon
PLSR	Partial least squares regression
PSD	Particle size distribution
P+ID	Piping and instrumentation diagram
RTD	Residence time distribution
SEM	Scanning electron microscopy
SS	Stainless steel
TEM	Transmission electron microscopy
TBR	Trickle bed reactor

Appendix A
Mathematical derivations

The following section is dedicated to the full mathematical derivations that are not shown but referenced in the main body of text.

A.1 Chapter 3 deviations

The following derivations were used calculate number of surface atoms and bulk atoms in the different nanoparticle geometries

A.1.1 Number of surface atoms

As discussed in the main body of text, for a face centred cubic palladium unit cell, the number of atoms per nm^2 can be expressed as;

$$N_{atoms\ per\ nm^2} = \frac{2}{(l_{unit})^2}$$

Cube;

For a cubic nanoparticle of size, L_p, the surface area can be defined as that of a simple cube;

$$A_{cube} = 6\ x\ A_{face} = 6\ x\left(L_{np}\right)^2$$

Therefore, the number of surface atoms, N_s, can be expressed as;

$$N_s = 6\left(L_{np}\right)^2 x\ \frac{2}{(l_{unit})^2} = 12\left(\frac{L_{np}}{l_{unit}}\right)^2$$

Tetrahedron;

In terms of a tetrahedron shaped nanoparticle, the surface area is a sum of the four equilateral triangles' areas;

$$A_{tet} = 4\ x\frac{1}{2}\mathrm{x\ L_{edge}\ x}\left(\frac{L_{edge}\sqrt{3}}{2}\right) = \sqrt{3}L_{edge}^2$$

If the length of the particle is taken as the tetrahedrons height;

$$L_{np} = \sqrt{\frac{2}{3}}L_{edge}$$

Therefore, the area in terms of the particle length is;

$$A_{tet} = \sqrt{3}\ x\left(\sqrt{\frac{3}{2}}L_p\right)^2 = \frac{3\sqrt{3}}{2}L_{np}^2$$

And the number of surface atoms;

$$N_s = \frac{3\sqrt{3}}{2} L_{np}^2 \, x \frac{2}{(l_{unit})^2} = \, 3\sqrt{3} \left(\frac{L_{np}}{l_{unit}}\right)^2$$

Octahedron;

For an octahedral shaped nanoparticle the length of the particle, L_{np}, can be defined in terms of the edge length, L_{edge} by:

$$\left(\frac{L_{np}}{2}\right)^2 = \left(\frac{1}{2} L_{edge}\right)^2 + \left(\frac{1}{2} L_{edge}\right)^2$$

$$\frac{1}{\sqrt{2}} L_{np} = L_{edge}$$

The surface area of an octahedron consists of eight identical faces and thus can be defined as;

$$A_{Oct} = 8 * \frac{1}{2} * \left(L_{edge}\right) * \left(\frac{L_{edge}\sqrt{3}}{2}\right) = 2\sqrt{3} \, \left(L_{edge}\right)^2$$

$$A_{Oct} = 2\sqrt{3} \, \left(\frac{1}{\sqrt{2}} L_{np}\right)^2 = \sqrt{3}\left(L_{np}\right)^2$$

Therefore for an octahedron, N_s, equals;

$$N_s = \sqrt{3}\left(L_{np}\right)^2 * \frac{2}{(l_{unit})^2} = 2\sqrt{3}\left(\frac{L_{np}}{l_{unit}}\right)^2$$

Cuboctahedron;

For a nanoparticle with regular cuboctahedron geometry, the surface area is a sum of the six faces and eight triangles where;

$$A_{face} = 6L_{edge}^2$$

$$A_{triangle} = 8\left(\frac{1}{2} L_{edge}\right)\left(\frac{L_{edge}\sqrt{3}}{2}\right) = 2\sqrt{3} L_{edge}^2$$

Hence the surface area can be expressed as;

$$A_{cubo} = A_{face} + A_{triangle} = L_{edge}^2\left(2\sqrt{3} + 6\right)$$

$$\left(\frac{L_{edge}}{2}\right)^2 = \, \left(\frac{1}{2} L_{np}\right)^2 + \, \left(\frac{1}{2} L_{np}\right)^2$$

$$L_{edge} = \frac{1}{\sqrt{2}} \, L_{np}$$

$$A_{cubo} = \frac{1}{2} L_{np}^2\left(2\sqrt{3} + 6\right)$$

Therefore, the number of surface atoms in a cuboctahedron is;

$$N_s = \frac{1}{2} L_{np}^2\left(2\sqrt{3} + 6\right) * \frac{2}{l_{unit}^2} = (2\sqrt{3} + 6)\left(\frac{L_{np}}{l_{unit}}\right)^2$$

A.1.2 Total number of atoms

In terms of palladium atoms per nm^3, there are four equivalent atoms per unit cell and therefore;

$$N_{atoms\ per\ nm^3} = \frac{4}{(l_{unit})^3}$$

Sphere;

For a spherical nanoparticle the volume can be expressed as;

$$V_{Sphere} = \frac{4}{3}\pi\left(\frac{d_p}{2}\right)^3 = \frac{1}{6}\pi d_p^3$$

Therefore, the total number of atoms in the nanoparticle is defined as;

$$N_{bulk} = \frac{1}{6}\pi d_p^3\ x\frac{4}{(l_u)^3} = \frac{2}{3}\pi\left(\frac{d_p}{l_{unit}}\right)^3$$

Cube;

For the cubic geometry, the volume is equal to;

$$V_{cubic} = L_{np}^3$$

Hence, the total number of atoms is;

$$N_{bulk} = L_{np}^3\ x\frac{4}{(l_{unit})^3} = 4\left(\frac{L_{np}}{l_{unit}}\right)^3$$

Tetrahedron;

For tetrahedron geometry, the volume is defined as;

$$V_{tet} = \frac{L_{edge}^3}{6\sqrt{2}}$$

In terms of the particle size, L_p;

$$V_{tet} = \frac{1}{6\sqrt{2}}\left(\sqrt{\frac{3}{2}}L_{np}\right)^3 = \frac{1}{6\sqrt{2}}\ x\frac{3\sqrt{6}}{4} = \frac{\sqrt{3}}{8}L_{np}^3$$

Therefore, the total number of atoms is equal to;

$$N_{bulk} = \frac{\sqrt{3}}{8}L_p^3\ x\frac{4}{(l_{unit})^3} = \frac{\sqrt{3}}{2}\left(\frac{L_{np}}{l_{unit}}\right)^3$$

Octahedron;

For the octahedron geometry, the volume is defined as;

$$V_{oct} = \frac{\sqrt{2}}{3}L_{edge}^3$$

In terms of the particle length;

$$V_{oct} = \frac{\sqrt{2}}{3}\left(\frac{1}{\sqrt{2}}L_{np}\right)^3 = \frac{\sqrt{2}}{3}x\frac{\sqrt{2}}{4}L_{np}^3{}^3 = \frac{1}{6}(L_{np})^3$$

Therefore, the total number of atoms is;

$$N_{bulk} = \frac{4}{(l_{unit})^3}\ x\ \frac{1}{6}(L_{np})^3 = \frac{2}{3}\left(\frac{L_{np}}{l_{unit}}\right)^3$$

Cuboctahedron;

The volume of a cuboctahedron is given by;

$$V_{cubo} = \frac{5\sqrt{2}}{3}L_{edge}^3$$

In terms of the particle length, L_{np};

$$L_{edge} = \frac{1}{\sqrt{2}}\ L_{np}$$

$$V_{cubo} = \frac{5\sqrt{2}}{3}\left(\frac{1}{\sqrt{2}}L_{np}\right)^3 = \frac{5\sqrt{2}}{3}\left(\frac{\sqrt{2}}{4}\right)(L_{np})^3 = \frac{5}{6}(L_{np})^3$$

Therefore, the number of bulk atoms is;

$$N_{bulk} = \frac{4}{(l_{unit})^3}\ x\ \frac{5}{6}(L_{np})^3 = \frac{10}{3}\left(\frac{L_{np}}{l_{unit}}\right)^3$$

A.2 Chapter 4 derivations

A.2.1 Derivation of liquid film thickness flowing down over an ideal vertical stack of pellets

$$V_z = \frac{\rho g}{4\mu}\left((r_0^2 - r^2) + 2(r_0+\delta)^2\ln\left(\frac{r}{r_0}\right)\right)$$

To derive an expression in terms of the volumetric flow rate the above equation must be further integrated between $r = r_0$ and $r = r_0 + \delta$;

$$\varphi = \int 2\pi r\ V_y\ dr$$

$$\varphi = \int 2\pi r\left(\frac{\rho g}{4\mu}\left((r_0^2 - r^2) + 2(r_0+\delta)^2\ln\left(\frac{r}{r_0}\right)\right)\right)dr$$

$$\varphi = \frac{\pi\rho g(r_0+\delta)^2}{2\mu}\int\left(r\frac{(r_0^2 - r^2)}{(r_0+\delta)^2} + 2r\ln\left(\frac{r}{r_0}\right)\right)dr$$

$$\varphi = \frac{\pi\rho g(r_0+\delta)^2}{2\mu} \int_{r_0}^{r_0+\delta} \left(\frac{r r_0^2}{(r_0+\delta)^2} - \frac{r^3}{(r_0+\delta)^2} + 2r \ln\left(\frac{r}{r_0}\right) \right) dr$$

The solution to the integral in the form of $\int x\, ln(x/a)\, dx$ can be found from a table of integrals and is as follows;

$$\int_{x_1}^{x_2} x\, Ln(x/a) dx = \int_{x_1}^{x_2} xLn(x) - xLn(a)\, dx$$

$$= \left[\frac{1}{2} x^2\, Ln(x/a) - \frac{1}{4} x^2 \right]_{x_1}^{x_2}$$

$$\varphi = \frac{\pi\rho g(r_0+\delta)^2}{2\mu} \left[\frac{1}{2} \frac{r^2 r_0^2}{(r_0+\delta)^2} - \frac{1}{4} \frac{r^4}{(r_0+\delta)^2} + r^2 \ln\left(\frac{r}{r_0}\right) - \frac{1}{2} r^2 \right]_{r_0}^{r_0+\delta}$$

$$\varphi = \frac{\pi\rho g(r_0+\delta)^2}{2\mu} \left[\frac{1}{2} \frac{(r_0+\delta)^2 r_0^2}{(r_0+\delta)^2} - \frac{1}{4} \frac{(r_0+\delta)^4}{(r_0+\delta)^2} + (r_0+\delta)^2 \ln\left(\frac{r_0+\delta}{r_0}\right) - \frac{1}{2}(r_0+\delta)^2 \right]_{r_0}^{r_0+\delta}$$

$$- \left[\frac{1}{2} \frac{r_0^2 r_0^2}{(r_0+\delta)^2} - \frac{1}{4} \frac{r_0^4}{(r_0+\delta)^2} + r_0^2 \ln\left(\frac{r_0}{r_0}\right) - \frac{1}{2} r_0{}^2 \right]_{r_0}$$

$$\varphi = \frac{\pi\rho g(r_0+\delta)^4}{2\mu} \left[\frac{1}{2} \frac{r_0^2}{(r_0+\delta)^2} - \frac{1}{4} \frac{(r_0+\delta)^4}{(r_0+\delta)^4} + \ln\left(\frac{r_0+\delta_s}{r_0}\right) - \frac{1}{2} \right]_{r_0}^{r_0+\delta}$$

$$- \left[\frac{1}{2} \frac{r_0^4}{(r_0+\delta)^4} - \frac{1}{4} \frac{r_0^4}{(r_0+\delta)^4} - \frac{1}{2} \frac{r_0^2}{(r_0+\delta)^2} \right]_{r_0}$$

$$\varphi = \frac{\pi\rho g(r_0+\delta)^4}{2\mu} \left[\frac{r_0^2}{(r_0+\delta)^2} - \frac{1}{4} + \ln\left(\frac{r_0+\delta}{r_0}\right) - \frac{1}{2} \right]_{r_0}^{r_0+\delta}$$

$$- \left[\frac{1}{4} \frac{r_0^4}{(r_0+\delta)^4} \right]_{r_0}$$

$$\varphi = \frac{\pi\rho g(r_0+\delta)^4}{\mu} \left(\frac{1}{2} \ln\left(\frac{r_0+\delta}{r_0}\right) - \frac{1}{8} \frac{r_0^4}{(r_0+\delta)^4} + \frac{1}{2} \frac{r_0^2}{(r_0+\delta)^2} - \frac{3}{8} \right)$$

A.3 Chapter 5 derivations

A.3.1 Derivation for hydrogen concentration in the liquid at the point where the liquid contacts the pellet

For the determination of the hydrogen concentration in the liquid at the point where the liquid contacts the pellet, following a steady state mass balance over a section of the inert bed of glass beads;

$$\varphi \, dC_L = k_b \, (C^* - C_L) \, dA$$

$$\int \frac{dC_L}{(C^* - C_L)} = \int \frac{k_b}{\varphi} dA$$

$$-\ln(C^* - C_L) = \frac{A \cdot k_b}{\varphi}$$

$$[-\ln (C^* - C_0]_{C_L = C_0} - [-\ln (C^* - C_{in}]_{C_L = C_{in}} = \left[\frac{A_p \cdot k_b}{\varphi}\right]_{A = A_{bs}}$$

$$\frac{C^* - C_0}{C^* - C_{in}} = e^{-\frac{A_{bs} \cdot k_b}{\varphi}}$$

$$C^* - C_0 = (C^* - C_{in}) e^{-\frac{A_{bs} \cdot k_b}{\varphi}}$$

$$C_0 = C^* - (C^* - C_{in}) e^{-\frac{A_{bs} \cdot k_b}{\varphi}}$$

A.3.2 Derivation for hydrogen concentration in the liquid over the surface of the pellet

For determination of the film concentration over the surface of the pellet;

$$\gamma_3 \varphi \, dC_f = \left[\frac{1}{\alpha \Omega_f} \left(C^* - C_f\right) \; - \frac{1}{\Omega_{f-s}} \, C_f \right] da_p$$

Subject to the boundary conditions $C_z = C_o$ at $a = 0$ this can be integrated to find C_f:

$$dC_f = \frac{1}{\gamma_3 \varphi} \left[\frac{1}{\alpha \Omega_f} \, C^* - \left(\frac{1}{\alpha \Omega_f} + \frac{1}{\Omega_{f-s}}\right) C_f \right] da_p$$

$$dC_f = \frac{\frac{1}{\alpha \Omega_f} + \frac{1}{\Omega_{f-s}}}{\gamma_3 \varphi} \left[C^* - \left(1 + \frac{\alpha \Omega_f}{\Omega_{f-s}}\right) C_f \right] da_p$$

$$dC_f = \frac{\frac{1}{\alpha\Omega_f} + \frac{1}{\Omega_{f-s}}}{\gamma_3 \varphi}\left[\frac{C^*}{1+\frac{\alpha\Omega_f}{\Omega_{f-s}}} - C_f\right] da_p$$

$$\int_0^{C_f} \frac{dC_f}{\frac{C^*}{1+\frac{\alpha\Omega_f}{\Omega_{f-s}}} - C_f} = \frac{\frac{1}{\alpha\Omega_f} + \frac{1}{\Omega_{f-s}}}{\gamma_3 \varphi}\, da_p$$

$$\frac{\frac{C^*}{1+\frac{\alpha\Omega_f}{\Omega_{f-s}}} - C_f}{\frac{C^*}{1+\frac{\alpha\Omega_f}{\Omega_{f-s}}} - C_0} = e^{-\frac{a_p}{A_0}} \; where \; A_0 = \frac{\gamma_3 \varphi}{\frac{1}{\alpha\Omega_f} + \frac{1}{\Omega_{f-s}}}$$

$$C_f = \frac{C^*}{1+\frac{\alpha\Omega_f}{\Omega_{f-s}}} - \left(\frac{C^*}{1+\frac{\alpha\Omega_f}{\Omega_{f-s}}} - C_0\right) e^{-\frac{a_p}{A_0}}$$

A.3.3 Derivation for the hydrogen uptake rate of the pellet

The actual amount of hydrogen consumed inside the pellet $\dot{N}_{H2}$ is given by the reaction at the surface:

$$d\dot{N}_{H2} = \frac{1}{\Omega_{f-s}}\, C_f\, da_p$$

Integrating over the whole pellet area:

$$\dot{N}_{H2} = \int_0^{A_P} \frac{1}{\Omega_{f-s}} \left(\frac{C^*}{1+\frac{\alpha\Omega_f}{\Omega_{f-s}}} - \left(\frac{C^*}{1+\frac{\alpha\Omega_f}{\Omega_{f-s}}} - C_0\right) e^{-\frac{a_p}{A_0}}\right) da_p$$

$$\dot{N}_{H2} = \frac{1}{\Omega_{f-s}} \left(\frac{C^*}{1+\frac{\alpha\Omega_f}{\Omega_{f-s}}} A_p - \left(\frac{C^*}{1+\frac{\alpha\Omega_f}{\Omega_{f-s}}} - C_0\right) \int_0^{A_p} e^{-\frac{a_p}{A_0}}\, da_p\right)$$

$$Using \int_0^{A_p} e^{-\frac{a_p}{A_o}}\, da_p = A_o \left(1 - e^{-\frac{A_p}{A_o}}\right)$$

$$\dot{N}_{H2} = \frac{1}{\Omega_{f-s}} \left(\frac{C^*}{1+\frac{\alpha\Omega_f}{\Omega_{f-s}}} A_p - \left(\frac{C^*}{1+\frac{\alpha\Omega_f}{\Omega_{f-s}}} - C_0\right) A_0 \left(1 - e^{-\frac{a_p}{A_0}}\right)\right)$$

$$\dot{N}_{H2} = \frac{A_p}{\Omega_{f-s}} \left(\frac{C^*}{1 + \frac{\alpha\Omega_f}{\Omega_{f-s}}} - \left(\frac{C^*}{1 + \frac{\alpha\Omega_f}{\Omega_{f-s}}} - C_0 \right) \frac{A_0}{A_p} \left(1 - e^{-\frac{a_p}{A_0}} \right) \right)$$

$$\dot{N}_{H2} = \frac{A_p}{\Omega_{f-s}} \left[C_\infty - [\, C_\infty - \; C_0] \; \frac{A_o}{A_p} \left(1 - e^{-\frac{A_p}{A_o}} \right) \right]$$

$$MTR''_{H2} = \frac{\dot{N}_{H2}}{A_p} = \frac{C_\infty}{\Omega_{f-s}} \left[1 \; - \left[\, 1 - \; \frac{C_0}{C_\infty} \right] \; \frac{A_o}{A_p} \left(1 - e^{-\frac{A_p}{A_o}} \right) \right]$$

$$with \quad C_\infty = \frac{C^*}{1 + \alpha\Omega_f / \Omega_{f-s}} \; and \; A_o = \frac{\gamma_3 \varphi}{\frac{1}{\alpha\Omega_f} + \frac{1}{\Omega_{f-s}}}$$

Appendix B
Analytical methods

This appendix briefly documents the theory and operating principles of the analytical techniques used for and characterisation the 1% Pd/C pellets, 5% Pd/C paste and the unloaded carbon pellets.

B.1 Gas chromatography

Gas-liquid chromatography was used as the main analysis method for quantifying the styrene conversion and is a well-established technique in the separation and quantification of mixtures of volatile compounds [159]. A sample of the mixture of interest is vaporised and injected into a stream of inert gas known as the carrier gas, which forces the analytes through the instrument. Separation is achieved using a chromatographic column containing a liquid that is bonded to an inert solid support within the column, which the analytes of interest adsorb onto as they pass through the column. The established equilibrium between the mobile gas phase and stationary bonded liquid phase dictates the rate at which the compounds move through the column, and thus column length, temperature and flow rate all effect the separation process [221]. As different compounds interact with the stationary phase to different extents, the individual components are retained in the column for varying amounts of time and thus can be separated out. This concept is illustrated in Figure B. 1. Having separated in the column, the carrier gas transports the compounds to a detector for quantification. In this case, the detector used was a flame ionisation detector, which will be briefly described here.

B.1.1 Flame ionisation detector

The flame ionisation detector (FID) is one of the most widely used universal detectors due to its simple operation, ease of use and reliability [222]. Fundamentally, the detector works by measuring the ions produced by the column eluent stream as it combusts in the flame. The ions produced in the flame are collected using a cylindrical electrode surrounding the flame by applying a high voltage between the jet and electrode.

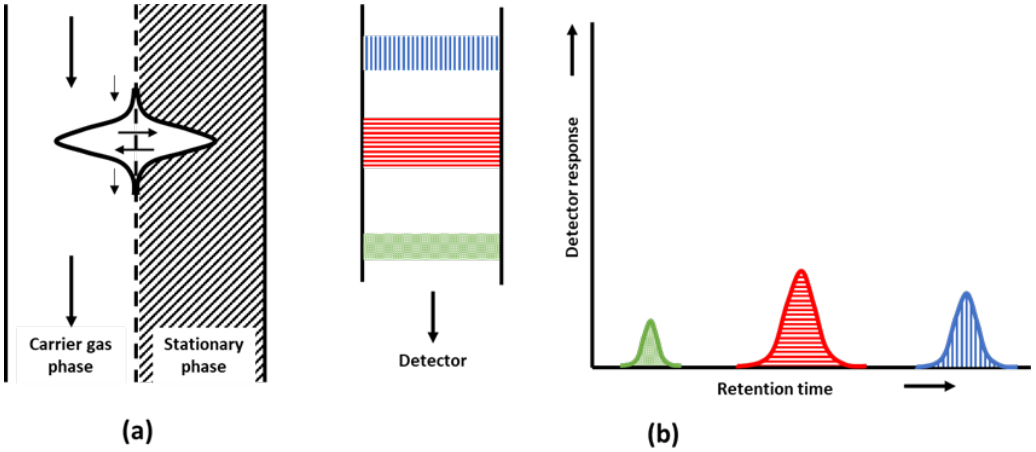

Figure B. 1: Graphic illustrating; (a) the partitioning of a compound between the mobile carrier gas phase and the liquid bonded stationary phase and (b) the separation of three compounds in the column and the resulting chromatogram.

An amplifier is used to amplify the resulting current and the output fed to a recorder or data acquisition system. A schematic of a typical FID is presented in Figure B.2. The advantages of the FID are as follows [223];

- Universal for organic analytes with a similar response for most
- Wide linear range
- Rapid response and very small effective detector volume (able to tolerate a large range of carrier gas flow rates).
- High sensitivity whilst being robust and easy to operate

The disadvantages associated with the FID are that the technique is destructive and non-selective.

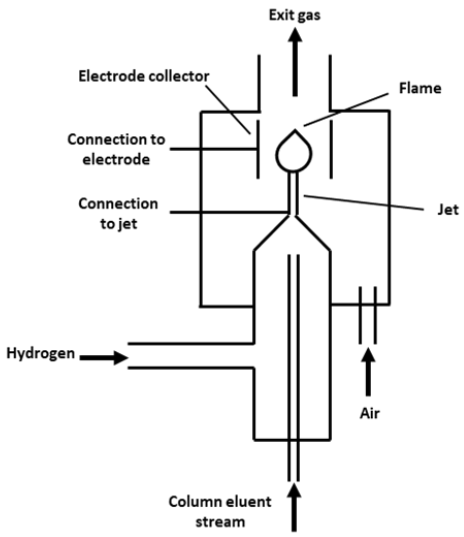

Figure B.2: Schematic drawing of a typical flame ionisation detector [222]

B.2 Inductively coupled plasma – mass spectrometry

Inductively coupled plasma – mass spectrometry (ICP-MS) is a highly sensitive and fast trace element analysis technique [224]. Capable of multielement quantification, ICP-MS offers detection limits in the sub parts per trillion and quantification in the parts per million range. Though there are many ICP-MS designs available, all share the following basic components; a nebuliser, spray chamber, plasma torch, mass separation device and detector. A schematic of a typical ICP-MS is illustrated in Figure B.3.

In terms of the basic operating principle, the liquid sample is first converted into a fine aerosol via the nebuliser and the fine droplets are separated from the larger droplets in the spray chamber before being injected into the plasma torch. The plasma torch itself, is a high temperature plasma discharge (≈ 10,000 K) sustained by the constant ionisation of the argon gas and used to generate positively charged ions. The generated ions are then directed into the mass-spectrometer via the sampler and skimmer cones by a series of electrostatic lenses known as the ion optics. The ions of interest are then filtered by their mass to charge ratio in the mass separation device before reaching the detector.

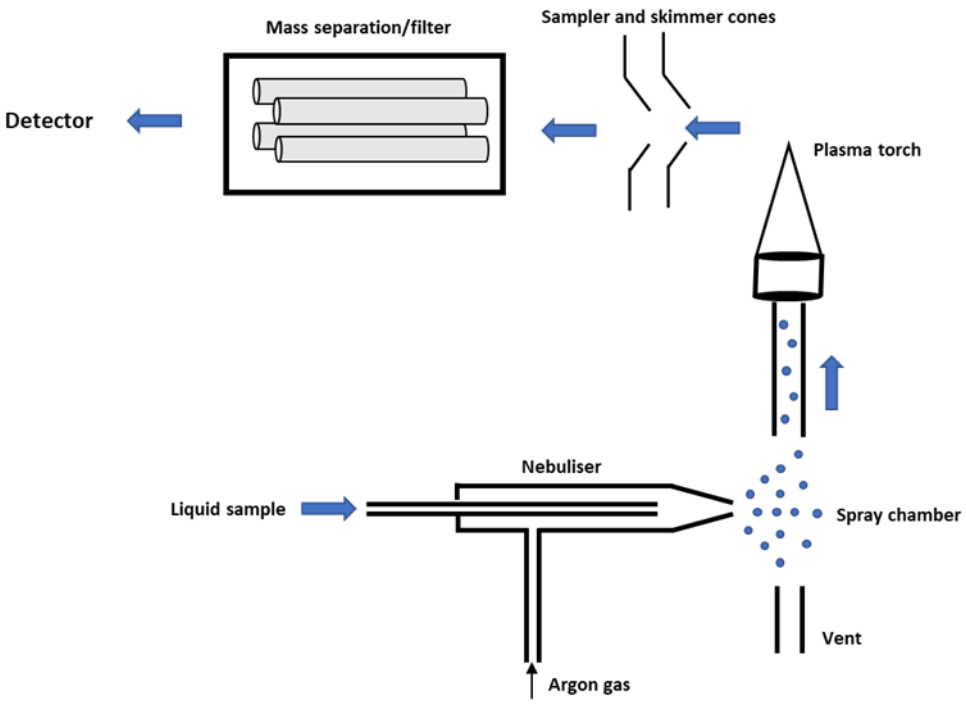

Figure B.3: Schematic showing the basic instrumental components of ICP-MS.

There are numerous designs of mass separation devices with their own principals of operation, but they all have the same purpose. Four common types are; time of flight, quadrupole, magnetic sector and collision cell technology, each having their own advantages and disadvantages [225].

B.3 Scanning electron microscopy

Scanning electron microscopy (SEM) is a widely used non-destructive imaging technique that produces an image by scanning a high energy electron beam across the surface of the sample [226]. Due to their short wavelengths, electrons are capable of resolving much finer material details than optical lights, and hence SEM can resolve features smaller than 1 nm in dimension. Thus, SEM is a very useful technique for investigating the material surface or near surface features, though it is not able to probe the internal structure.

A typical SEM instrument consists of three sections; (i) the electron column, (ii) specimen chamber and (iii) the electron controls. The three sections and the associated components are illustrated in Figure B.4.

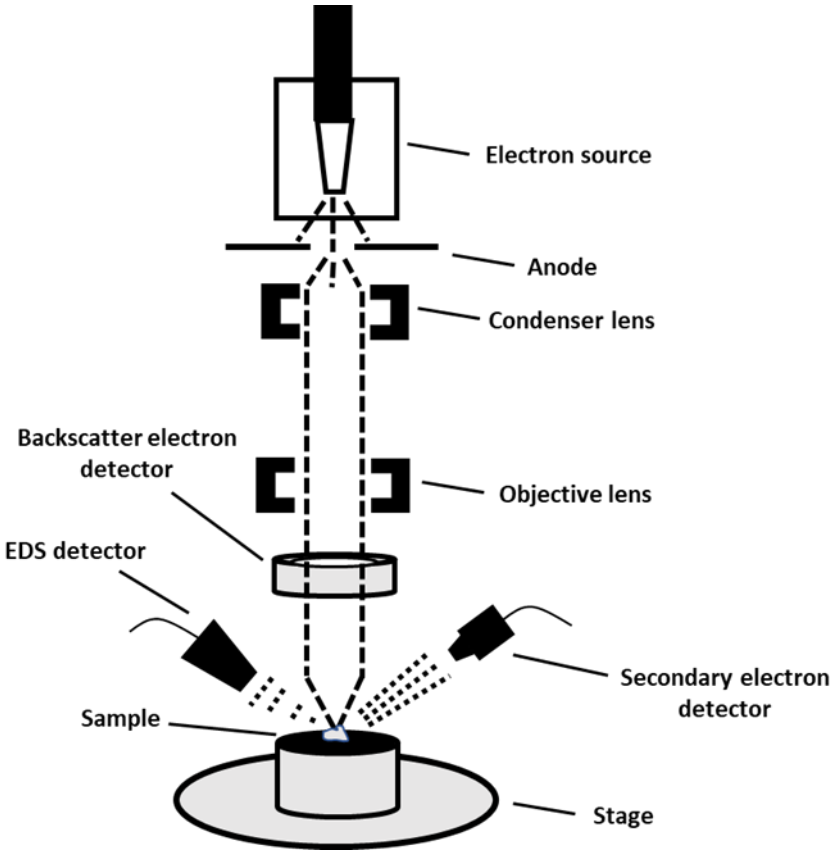

Figure B.4: Schematic of a SEM showing the basic components involved in producing an image.

To produce an image, an electron gun located at the upper section of the column generates a beam of electrons that is focussed into a small diameter probe that scans the surface of the sample. As the electrons penetrate into the sample, they interact with the orbitals of atoms in the sample and generate secondary elections, backscattered electrons and characteristic X-rays. The particles are collected by a detector and processed, giving information in relation to the sample. The secondary electrons in particular are used to generate the SEM image.

B.3.1 Energy dispersive using X-ray analysis

As the electron beam strikes the surface, electrons from the beam strike the inner shell electrons within the atoms of the sample and cause their ejection from the atom [163]. The vacancy in the orbital created by this interaction is then filled by an electron in a higher energy orbital, which loses energy as it drops to the lower energy orbital. The loss of energy is released in the form of an X-ray photon, whose energy is equal to the difference between the two energy levels and is detected by the energy dispersive detector (EDS). The photon energies are characteristic of the energy level being filled of a particular element in the sample and therefore the element in the sample can be identified from the characteristic X-ray produced. Moreover, the intensity of the photons being emitted is directly proportional to the concentration of the element present in the sample. A schematic of the electron-sample interaction is presented in Figure B.5.

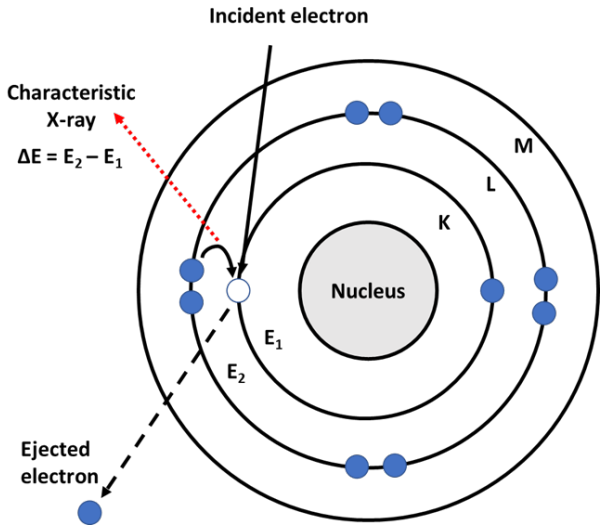

Figure B.5: Schematic showing the electron – sample interaction that produces the characteristic X-rays measured in SEM-EDX.

B.4 Transmission electron microscopy

Transmission electron microscopy (TEM) also utilises electrons to form an image, however, unlike SEM the electrons are transmitted through the sample and detected [227]. As the electrons are transmitted through the sample TEM is heavily used for the analysis of internal microstructure and the evaluation of nanostructures. The requirement of transmission restricts the sample geometry greatly. Many TEM sample holders limit the samples to roughly 3 mm in diameter and a maximum thickness of 200 µm in the incident beam direction, however, the thickness is dependent on the material being analysed. A schematic of the TEM showing the basic components is presented in Figure B.6 and can generally be split into three sections; the illumination system, specimen stage and imaging system [228]. The illumination system consists of an electron gun that produces a beam of electrons via thermionic emission from a tungsten filament. Condenser lenses then focus the beam onto the sample and can be operated to determine the diameter of the beam. The objector lenses focus the beam to form the image and the projector lenses magnify the image on the detector.

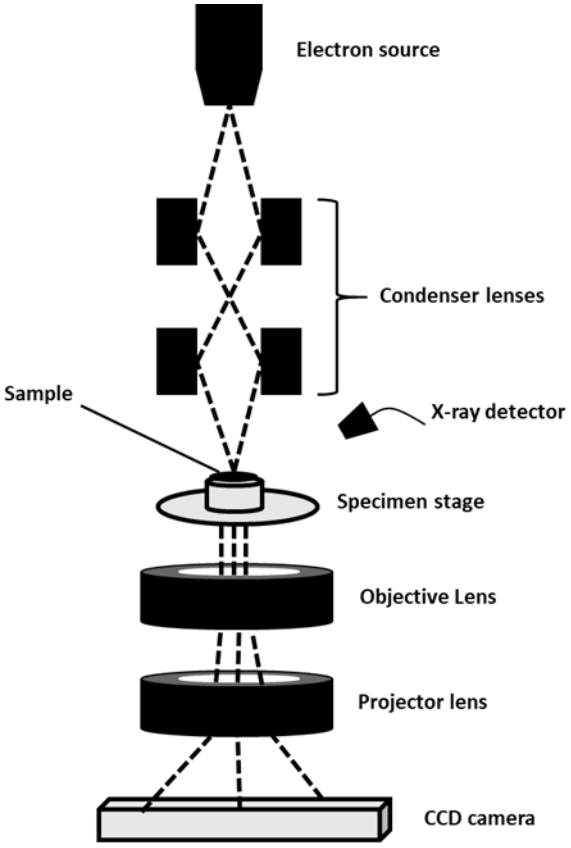

Figure B.6: Schematic of a TEM showing the primary components [163].

Electrons that are successfully transmitted through the sample are focussed by a set of lenses to form the image, which is typically recorded on a digital electron detector that converts incoming electrons into an electron pulse per pixel.

B.5 Brunauer, Emmett and Teller Gaseous Nitrogen adsorption

The Brunauer, Emmett and Teller (BET) isotherm is an extension of the Langmuir isotherm in that it accounts for multilayer adsorption and can extract the monolayer capacity of a material and thus determine the specific surface area of a material [98]. The BET model is based on a number of idealised assumptions [229];

- Gas behaves as a perfect gas.
- The surface is characterised by N_s number of active sites.
- Absorbed molecules are treated as classical objects adsorbed onto the active sites.
- Adsorption can take place on the active sites present on the surface or directly on top of molecules already adsorbed.
- Only the first layer of molecules interacts with the surface, all other layers have interparticle interaction with the same energy as would apply in the liquid state.
- The adsorbed molecules do not interact laterally.

Following the assumptions presented a linearised form of the BET isotherm can be derived [230];

$$\frac{1}{v\left[\left(\frac{p_0}{p}\right)-1\right]} = \frac{c-1}{v_m c}\left(\frac{p}{p_0}\right) + \frac{1}{v_m c} \qquad \textbf{(B.1)}$$

Where v is the absorbed gas volume, v_m the monolayer absorbed gas volume, p is the equilibrium pressure of the gas, p_0 the saturated pressure of the gas and c the BET constant. By plotting the left-hand side of Eq. (B.1) vs $\frac{p}{p_0}$ the BET constant for the material can be obtained and thus so can the monolayer volume. The specific surface area (SSA) can then be calculated.

$$SSA = n_m N_A a \quad \textbf{(B.2)}$$

Where n_m is the number of moles of the molecules adsorbed in the monolayer, N_A is Avogadro's number and a the cross-sectional area of the adsorbed molecule (nitrogen is usually used, and thus a is taken as 16.2 x10^{-20} m).

In terms of the experimental determination of the monolayer volume, the volumetric method was used. A more thorough explanation of the operational procedure is available in the literature [230] but essentially, routine de-gassing of the sample is first undertaken before a tube containing the sample of interest is immersed in liquid nitrogen. The adsorbing gas (nitrogen) is then first released into a volume closed off from the sample and the pressure recorded. This volume is then shut off from the nitrogen supply and then admitted to the sample tube. The pressure drop is monitored and by knowing the volume of the tube without the sample, one can determine the amount of gas adsorbed. The process is then repeated at increasing gas pressures.

B.5.1 Bayer, Joyner and Halenda method

The Bayer, Joyner and Halenda (BJH) method is an analysis of the pore size distributions based on the Kelvin equation which relates the relative nitrogen pressure to the size of the pores where capillary condensation takes place at higher values of $\frac{p}{p_0}$ (where the isotherm plateaus as the pore is filled) [161]. This idealised model assumes that the porous solid consists of cylindrical capillaries that have uniform cross-sections and are closed at one end [231];

$$r_k = \frac{2\sigma V_m}{RTln\left(\frac{p}{p_0}\right)} \quad \textbf{(B.3)}$$

Where r_k is the radius of the equivalent meniscus in the pore, σ the surface tension, V_m the molar volume of the liquid condensate. If the radius of the pore r_{pore}, can then be determined from r_k and the thickness of the monolayer adsorbed on the wall of the pore, t_m;

$$r_{pore} = r_k + t_m \quad \textbf{(B.4)}$$